UNIVERSITÉ DE SHERBROOKE
Faculté de génie
Département de génie chimique et de génie biotechnologique

Développement, validation et application de modèles de bilan de populations sur des réacteurs à écoulement de bulles

Development, Validation and Application of Population Balance Models in Eulerian Approach for Bubbly Flow Reactors

Thèse de doctorat
Specialité: génie chimique

Ehsan Askari Mahvelati

Sherbrooke (Québec) Canada

November 2018

JURY MEMBERS

Pierre Proulx

Supervisor

Martin Désilets

Examiner

Sébastien Poncet

Examiner

Alberto Passalacqua

Examiner

RÉSUMÉ

Dans l'optique d'optimiser et de concevoir des réacteurs à écoulement de bulles, il est nécessaire de prédire le comportement et les propriétés des bulles dans le temps et l'espace. En temps normal, la distribution de taille des bulles est bien définie et les bulles s'écoulent de manière uniforme et homogène. Toutefois des agrégats et les grosses bulles se forment rapidement si le l'écoulement n'est plus homogène. Il possible d'appuyer l'analyse de ces systèmes à l'aide de modèles mathématiques d'écrivant l'évolution de la distribution du volume, de la taille et d'autres propriétés dans le réacteur.

La présente thèse explore l'application d'un de ces modèles mathématiques, appelés modèle de bilans des populations (PBM) [1], dans différents cas impliquant deux colonnes à bulles rectangulaires et une cellule d'électrolyse. Les travaux ont été effectués à l'aide d'un ensemble d'outils numériques libres en CFD [2], mécanique des fluides numérique appelé OpenFOAM. C'est dans cet ensemble que la méthode des classes (CM) [3] et des méthodes basées sur la quadrature des moments (QBMM) [4] furent implémentées pour être comparées, par la suite, avec d'autres méthodes de bilans des populations précédemment publiées.

La méthode de quadrature étendue des moments (EQMOM) [5], dans cette thèse, mène à une amélioration de la prédiction des échanges gazeux, lorsque comparés aux résultats en laboratoire. De plus, la méthode permet la reconstruction des distributions statiques des bulles, ce qui s'avère particulièrement utile pour une modélisation précise des écoulements dans les cellules d'électrolyse.

Une application plus complexe de l'implémentation des solveurs CFD-PBM àaussi été faite dans un bioréacteur de 3 litres en présence d'une hélice marine placée sur l'axe. Dans ce cas, l'effet combiné de la fission et de la coalescence des bulles a été pris en compte. L'écoulement tridimensionnel est réalisé en utilisant des référentiels multiples (MRF) [6], une méthode bien établie dans la modélisation de réacteur de ce type. Le modèle a été utilisé pour prédire la distribution du gaz, le diamètre moyen de Sauter (d32), la fonction de densité (NDF), l'oxygène dissous et l'évolution de l'écoulement. Les résultats de la simulation numérique impliquant 4 vitesses de rotation concordent de manière satisfaisante aux résultats obtenus en laboratoire.

Mots-clés : écoulement de bulles; colonnes à bulles; modèle de bilans des populations; la méthode de quadrature étendue des moments; transfert de masse; électrode d'évolution de gaz

1. Population Balance Model
2. Computational Fluid Dynamic
3. Method of Classes
4. Quadrature-based Moments Method
5. Extended Quadrature Method of Moments
6. Multiple Reference Frame

ABSTRACT

In order to optimize and design new bubbly flow reactors, it is necessary to predict the bubble behavior and properties with respect to the time and location. In gas-liquid flows, it is easily observed that the bubble sizes may vary widely. The bubble size distribution is relatively sharply defined, and bubble rises are uniform in homogeneous flow; however bubbles aggregate, and large bubbles are formed rapidly in heterogeneous flow. To assist in the analysis of these systems, the volume, size and other properties of dispersed bubbles can be described mathematically by distribution functions. Therefore, a mathematical modeling tool called the Population Balance Model (PBM) is required to predict the distribution functions of the bubble motion and the variation of their properties. In the present thesis, three different types of reactors are modeled using the open-source Computational Fluid Dynamic (CFD) package OpenFOAM. Furthermore, the Method of Classes (CM) and Quadrature-based Moments Method (QBMM) are described, implemented and compared using the developed CFD-PBM solver. These PBM tools are applied in two bubbly flow cases: bubble columns (using a Eulerian-Eulerian two-phase approach to predict the flow) and a water electrolysis reactor (using a single-phase approach to predict the flow). The numerical results are compared with measured data available in the scientific literature. It is observed that the Extended Quadrature Method of Moments (EQMOM) leads to a slight improvement in the prediction of experimental measurements and provides a continuous reconstruction of the Number Density Function (NDF), which is helpful in the modeling of gas evolution electrodes in the water electrolysis reactor. In the last case of the project, oxygen distribution in a laboratory scale (3 liters) bioreactor in the presence of an axial impeller is modeled using the CFD-PBM solver. The combined effect of the bubble breakup and coalescence in the tank is accounted for EQMOM. The three-dimensional simulation is made using a Multiple Reference Frame (MRF), a well-established method for the modeling of mixers. The model is used to predict the spatial distribution of gas phase fraction, Sauter mean bubble diameter (d32), NDF, Dissolved Oxygen (DO) evolution and flow structure. The numerical results are compared with experimental data and good agreement is achieved. The results are discussed based on four rotational speeds of impeller with different volumetric mass transfer coefficients.

Keywords: bubbly flow; population balance model; extended quadrature moment method; bubble column; gas evolution electrode; gas-liquid stirred tank; mass transfer

I would like to dedicate this thesis to my beautiful wife, Molood, for all of her love and support, to my mother, Mehri Moghaddam, to my father, Mohsen Askari and to my little brother, Amir-Saman Askari, who have always loved me unconditionally, to my friends, Ehsan Madadi-Kandjani as a talented researcher, Hasan Basir and Babak Rohani as professional chemical engineers in petrochemical industry.

ACKNOWLEDGEMENTS

I would like to sincerely thank my thesis supervisor, Professor Pierre Proulx, for his valuable insights, recommendations and support. Fruitful discussions with OpenQBMM team in Iowa State University under supervision of Professor Alberto Passalacqua are gratefully acknowledged, as well. I would like also to extend my thanks to Gabriel St-Pierre Lemieux for his assistance in C++ and Python programming.

I would like to thank Hydro-Québec and The Natural Sciences and Engineering Research Council of Canada (NSERC) which funded this project.

TABLE OF CONTENTS

LIST OF FIGURES

LIST OF TABLES

LIST OF SYMBOLS

Symbole	Definition
a	interfacial area, m^{-1}
C_D	drag coefficient, $-$
C_l	lift coefficient, $-$
C_{ν_m}	virtual mass coefficient, $-$
c_f	increase coefficient of surface area, $-$
D	diffusion coefficient, $\mathrm{m}^2 \cdot \mathrm{s}^{-1}$
d	bubble diameter, m
d_o	sparger orifice, m
d_{32}	Sauter mean diameter, m
Eo	Eotvos number, $-$
f	friction coefficient for flow around bubbles, $-$
f_i	volume fraction of bubble class i, $-$
F	Faraday constant, $\mathrm{C} \cdot \mathrm{mol}^{-1}$
$\mathbf{g}$	acceleration vector due to gravity, $\mathrm{m} \cdot \mathrm{s}^{-2}$
H	Henry's constant, $\mathrm{Pa} \cdot \mathrm{kg}^{-1} \cdot \mathrm{m}^3$
$\overline{\overline{I}}$	unit tensor, $-$
K_L	mass transfer coefficient, $\mathrm{m} \cdot \mathrm{s}^{-1}$
k	turbulent kinetic energy, $\mathrm{J} \cdot \mathrm{kg}^{-1}$
n	number density of bubbles, m^{-3}
$\mathbf{N}$	angular velocity, $\mathrm{rad} \cdot \mathrm{s}^{-1}$
p	pressure, Pa
p_c	coalescence efficiency or collision probability, $-$
P_{O_2}	partial pressure of oxygen, Pa
$\mathbf{r}$	position vector, m
$\mathbf{R}$	interphase force, $\mathrm{N} \cdot \mathrm{m}^{-3}$
Re	Reynolds number, $-$
Sc	Schmidt number, $-$
Sh	Sherwood number, $-$
t	Time, s
$\mathbf{U}$	average velocity of phase, $\mathrm{m} \cdot \mathrm{s}^{-1}$
We	Weber number, $-$
Y	local mass fraction of oxygen, $-$

Symbole	Definition
Greek Symbols	
α	Volume fraction, $-$
β	constant, 2.05
ϵ	Turbulent kinetic energy dissipation rate, $\mathrm{m}^2 \cdot \mathrm{s}^{-3}$
μ	dynamic viscosity, $\mathrm{N} \cdot \mathrm{s} \cdot \mathrm{m}^{-2}$
λ	eddy size, m
ρ	density, $\mathrm{kg} \cdot \mathrm{m}^{-3}$
σ	surface tension, $\mathrm{N} \cdot \mathrm{m}^{-1}$
ζ	internal variable, $-$
ν	kinematic viscosity, $\mathrm{m}^2 \cdot \mathrm{s}^{-1}$
ξ_{ij}	size ratio, $\mathrm{d}_i/\mathrm{d}_j$
$\Gamma(a, x)$	incomplete Gamma function, $-$
η	diameter ratio, $\mathrm{d}_i/\mathrm{d}_j$
$\overline{\overline{\tau}}$	stress tensor, $\mathrm{kg} \cdot \mathrm{m}^{-1} \cdot \mathrm{s}^{-2}$
Subscripts	
ag	aggregation
br	breakage
c	continous phase
d	dispersed phase
eff	effective
G	gas phase
L	liquid phase
m	mixture
i	phase number
lam	laminar
t	turbulent

LIST OF ACRONYMS

Acronyme	Definition
CFD	**C**omputational **F**luid **D**ynamics
FVM	**F**inite **V**olume **M**ethod
TFM	**T**wo **F**luid **M**odel
PBM	**P**opulation **B**alance **M**odelling
CM	**C**lasses **M**ethod
MOM	**M**ehods **O**f **M**oments
QMOM	**Q**uadrature **M**ethods **O**f **M**oments
DQMOM	**D**irect **Q**uadrature **M**ethods **O**f **M**oments
EQMOM	**E**xtended **Q**uadrature **M**ethods **O**f **M**oments
QBMM	**Q**uadrature **B**ased **M**oments **M**ethods

CHAPTER 1

Introduction

1.1 Background

Bubbles have considerable importance in numerous natural physical processes and chemical industries. Boiling, floatation and dissolution are only a few of the phenomena and operations in which bubbles play a significant role. Chemical and metallurgical engineers rely on bubbles for such operations as distillation, absorption, floatation and water electrolysis. Mechanical engineers have studied the bubble behavior in electromachining and boiling. In all these phenomena and processes, there is interaction between bubbles themselves on one hand, and between bubbles and carrier fluid on the other. In many cases, transfer of mass and/or heat is also of importance. Interactions between bubbles and fluids and collisions among bubbles themselves form the subject of this research.

Experimental equipment for studying bubbly flow reactors are not provided easily and are expensive. Therefore, modeling and simulation methods have been used by many researchers to predict the performance of gas-liquid reactors. Recently, the new generation of powerful processors have brought significant progress in numerical methods and the calculation of the characteristics of multiphase flow. This provides the opportunity for investigating complex flow problems. Computational Fluid Dynamics (CFD) method that combines many advantages such as recent advancements in computers, less expensive equipments, flexibility and safety is an important design tool to study transport phenomena in process equipments. Compared to experimental methods, it might contribute to complete information with relatively low cost and high speed as well as its flexibility and safety. In fact, the system (reactor) parameters in terms of geometry and operational conditions can be designed, redesigned and improved using CFD without a substantial cost.

OpenFOAM (Open source Field Operation And Manipulation) is an object-oriented C++ framework that can be freely used to model the flow field, turbulence, heat transfer and reactions as well as develop a variety of CFD solvers for academic studies and industrial applications with a focus on finite volume discretization. The OpenFOAM toolkit also includes many different tutorials, stand-alone solvers and post-processing programs. The existence of a group of object classes allow the programmer to manipulate geometries,

physical models and discretization techniques at a comprehensive level of coding. They empower CFD engineers customizing various algorithms and implementing cutting-edge tools and mathematical models. The open source nature of OpenFOAM brings a substantial amount of free power through flexibility to its user. Along with that power, an enormous complexity is involved for those CFD engineers that are used to work with Graphical User Interface (GUI) and do not usually handle such an abundant choice of simulation parameters. Therefore, the use of OpenFOAM comes also with the value of a much better understanding of the methods used to solve as well as the constitutive equations. This aspect that can be negative in an industrial environment but can becomes very positive in the context of the development of an expertise expected in a Ph.D. thesis.

In the computational treatment of multi-phase flows, simulation methods can be chosen on a per-phase basis. As each simulation method (Eulerian and Lagrangian) has its own strengths and weaknesses, each combination of these methods has its own set of characteristics. The relative size between the mesh and the particles as well as the physics involved determine the method of simulation. When bubble is large compared to the computational grid, Volume of Fluid (VOF) is method of choice. This method resolves the interface between the phases. If the bubbles are smaller than the grid size, then unresolved methods are better suited. This can be either the Eulerian-Eulerian method – in short Euler-Euler – or the Eulerian- Lagrangian method. The Euler-Lagrange method treats the suspending phase as a continuum and the dispersed phase is accounted for by solving Newton's second law of motion for each particle. The choice whether to use the Euler-Euler method or the Euler-Lagrange method is mainly based on the computational cost associated with the number of dispersed particles and the need to resolve particle-particle interactions.

One of the main problems in modeling of multiphase dispersion is the prediction of bubble size distribution in E-E framework. There are two types of categories to predict the polydisperisty. First one is entitled as global polydisperse models in which a spatially-varying field of bubble sizes is considered and it can globally account for the polydispersity of the bubbles in addition to the phase continuity equation. Although global polydisperse models yield a non-constant bubble size through the system, they obtain a local monodispersed size distribution and by applying this model, the local probability distribution of the bubble size is not considered. Second category is called local polydisprese which covers detailed models and gives more information on the secondary phase behavior with more computational demand. The current work focused on the most used methods of local polydisperse models including Classes Method (CM) and Quadrature-based Method of Moments (QBMM).

1.2 Problem statement

The main challenge is to predict how the number of particles (bubbles) inside a bubbly flow reactor, could be predicted by population balance modelling. Another issue is the continuous bubble size distribution through the liquid phase. In order to optimize and enhance the bubbly flow reactors, the evolved bubbles should be under control because the presence of bubbles has favourable and unfavourable effects. For instance in an electrochemical reactor consisting of gas evolving electrodes, the bubbles have a resistive film for electric current flow and also for the ions heading to electrode to participate in electrode reaction. On the other hand, the bubble can play role as a turbulence promoter and producer of convection over the electrode surface. In case of bubbles evolution, optimization is possible when the bubbles behaviour including their size and numbers are completely modelled, simulated and then predicted.

OpenFOAM is a helpful tool to develop and implement the models studying the above-mentioned problem. In comparison with commercial CFD software, OpenFOAM provides an environment to customize the existing models with constant bubble size and improve them into the ones which can consider the polydispersity of the bubbles. Not only it is possible to modify the conventional OpenFOAM solvers linked to the newer models, but the special boundary and initial conditions could also be implemented in the proposed problem.

However, to the author' best knowledge, very few publications [1–4] can be found in the literature that discuss the issue of population balance modelling in order to predict flow pattern in electrochemical cells. Most of the previous relevant studies do not take into account gas-liquid flow and consequently, the size variation of bubbles in electrolytic gas evolution.

In this work, CM, QMOM and EQMOM techniques that improve population balance modelling are implemented. The method of classes, while intuitive and accurate, is computationally intensive due to the large number of classes required to finely discretize the Number Density Function (NDF). Compared with CM, the QMOM can consider a wide range of bubble sizes with a reduced number of equations for the moments of the NDF. However, in some evaporation and combustion problems (Nguyen et al. [5], Yuan et al. [6]), the value of the NDF for null internal coordinates such as size, velocity, mass and temperature needs to be known, which is not the case if the QMOM method is used. DQMOM solves the equations for weights and abscissae directly. Shortcomings related to

the conservation of moments affect DQMOM approach since weights and abscissas are not conserved quantities (Yuan et al. [6]). In order to overcome these limitations, Yuan et al. [6] introduced the Extended Quadrature Method of Moments (EQMOM), which enables the shape of NDF to be reconstructed from a moment set using continuous kernel density functions instead of Dirac delta functions.

Our project presents a novel view of integration of CFD multiphase model, population balance model, turbulence model, mass transfer model in bubbly flow reactors. The inspection of the model and study of integrated population balance models are made with reference to experimental data for bubbly flow in three different reactors, a bubble column, a gas-liquid stirred tank and water electrolysis reactor.

1.3 Objectives

Generally, the principal subject of the project is development, validation and application of a CFD-PBM solver to model and simulate the gas-liquid flow inside a bubble column, an electrochemical reactor and gas-liquid stirred tank. The detailed objectives are classified as follows:

- Objective 1

  To obtain and couple the closure equations consisting of continuity equation, two-fluid model equations, mass transfer equations, population balance equations, turbulence equations and then develop the relevant and adequate boundary conditions.

- Objective 2

  To model, simulate and validate the gas-liquid flow involving the bubbles, as a dispersed phase, and liquid phase, as water in bubble column, with Eulerian-Eulerian approach and using population balance modelling.

- Objective 3

  To compare the implemented population balance models (CM, QMOM, DQMOM

and EQMOM) using the developed CFD-PBM solver.

– Objective 4

To apply CFD-PBM solver for an water electrolysis reactor neglecting growth term and compare the experimental bubble size distribution with simulated ones.

– Objective 5

To take into account the two-phase mass transfer in the gas-liquid stirred tank, examine the impact of rotational speeds of impeller on bubble size distribution and predict the volumetric mass transfer coefficients.

1.4 Present contribution

This study makes a contribution to CFD modeling of the polydisperse flows as follows:

1. Development of new and strong coupling among the physical models using OpenFOAM. A full integration through fluid flow of the dispersed phase and continuous phase, two-phase mass transfer and the turbulence induced by bubbles are established.
2. The implementation and comparison of local population balance models and the application of a novel technique called the extended quadrature method of moments "EQMOM".
3. The achievement of the continuous bubble size distribution with the reduced computational demand.
4. The implementation and prediction of volumetric mass transfer coefficients in oxygen absorption.

1.5 Thesis outline

The remainder of this work is organized as follows:

The Chapter 2 presents the mathematical models indicating the backgrounds of Computational Fluid Dynamics (CFD) for two-phase flows.

The Chapter 3 shortly explains the essence of the population balance model approach. Different solution techniques are highlighted in this part. A popular mechanism of bubble coalescence and break-up model is discussed in this chapter, as well.

In Chapter 4, a brief definition of the numerical methods used in CFD in general is discussed, and some background information on OpenFOAM specifically.

In Chapter 5 and 6, the numerical results obtained for the bubble columns and the electrochemical cell are presented, comparing them to the experiments for validation purposes.

The Chapter 7 and 8 are dedicated to the implementation, validation, and application of new CFD-PBM solver coupled with two-phase mass transfer library, for a gas-liquid stirred tank.

Finally, Chapter 9 devoted to the presentation of results, discussion and conclusion.

CHAPTER 2

Multi-phase modelling

2.1 Introduction

Two phase flows, or in general multiphase flows, are mixture consisting of immiscible phases which flow simultaneously in the system. Multiphase flows can be categorized according to the state of the different phases:

- Gas-liquid mixture
- Gas-solid mixture
- Liquid-liquid mixture

Fig. 2.1 [7] exhibits typical multiphase flow regimes in vertical and horizontal tubes.

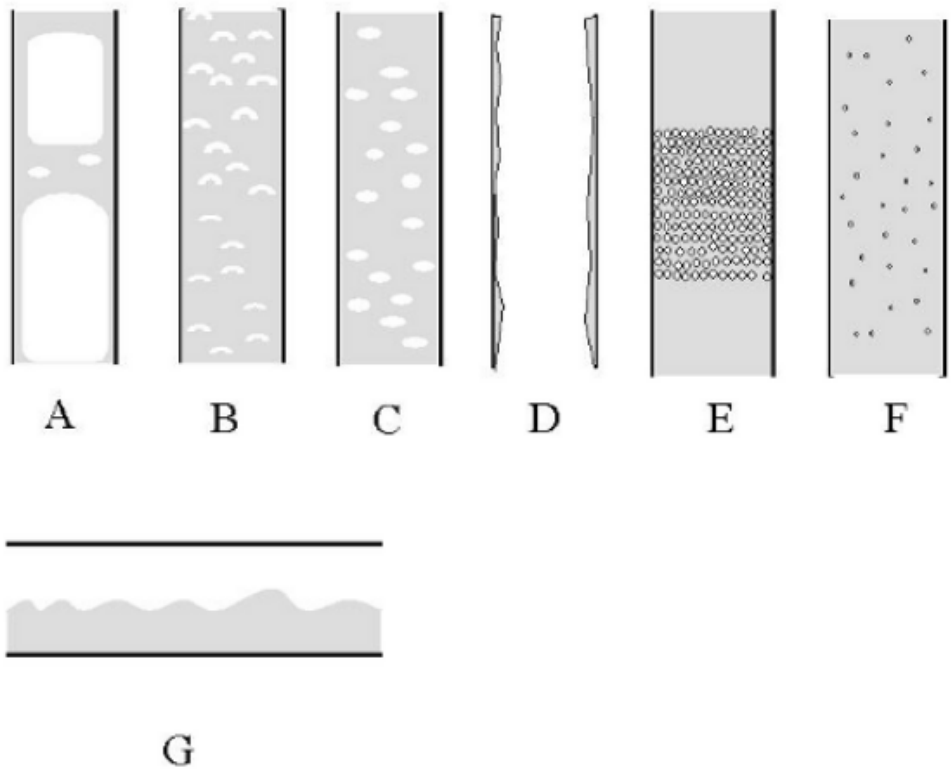

Figure 2.1 Multiphase flow regimes. A: Slug flow. B: Bubbly flow. C: Droplet flow. D: Annular flow. E: Packed and porous fixed bed. F: Particulate flow. G: Stratified free flow [7]

Examples of typical reactor flows are listed below [7]:

- Single phase fluid flows (single phase reactors, i.e., laminar and turbulent flows).
- Flow through porous beds of solids (fixed bed reactors, i.e., continua of gas; three phase fixed beds, i.e., continua of gas through a porous fixed solid and trickling liquids on the solid surface).
- Granular flows (fluidized bed reactors, i.e., discrete particles in a continuous gas phase).
- Bubbly flows (two phase bubble columns, stirred tank reactors, waste water treatment, i.e., bubbles in liquid).
- Slurries (i.e., discrete particles in liquid).
- Complex multiphase flows (e.g., slurry bubble columns and stirred tank reactors i.e., bubbly flows in slurries; three phase fluidized beds, i.e., liquid droplets and particles in continuous gas) where many phases interact simultaneously.

Today, the understanding and modeling of multiphase flows has become essential because of their existence in various industries such as petroleum, mining, chemical and biotechnology. Bubbly flow is a hot topic in the field of multiphase flow. The dispersion of the bubbles in the continuous phase plays an important role in numerous processes. In bubbly flow reactors, the structure of the fluid flow, enhancement of reactions and heat transfer heavily undergo many important changes due to the presence of bubbles.

Bubble column is not a simple device to investigate bubbly flows. Deckwer [8] says: "bubble column reactors are mass transfer and reaction devices in which one or several gases are brought into contact and react with the liquid phase itself or with a component dissolved or suspended in it".

There are three operating states in the bubbles column as follows [8]:

- **homogeneous flow**: In this regime, the bubbles are uniformly distributed in the liquid when gas levels are low. The bubble size distribution is relatively sharply defined and rises uniformly through the column

– **heterogeneous flow**: If the gas flow rate is increased, homogeneous state will be changed to heterogeneous one through the column. This type of flow is referred to as heterogeneous and is quite common as a result of the high gas rates frequently adopted in industry.

– **Slug flow**: A special situation arises in narrow column as generally used for laboratory work: the large bubbles in the heterogeneous zone are stabilized by the tube wall and move upwards through the column in a piston-like manner. These elongated bubbles (known as slug) fill practically the whole cross-section and continue growing by collecting smaller bubbles continuously throughout their upward journey. The slug flow is most likely occur in tall appliances with column diameter around 20 cm or less. Slug flow should be strictly avoided in both laboratory and pilot plant. For instance, in oil industry slug flow can create problems such as emergency shutdown of the platform due to void periods and reduction of mass transfer efficiency caused large bubbles.

Fig. 2.2. demonstrates the regimes explained above.

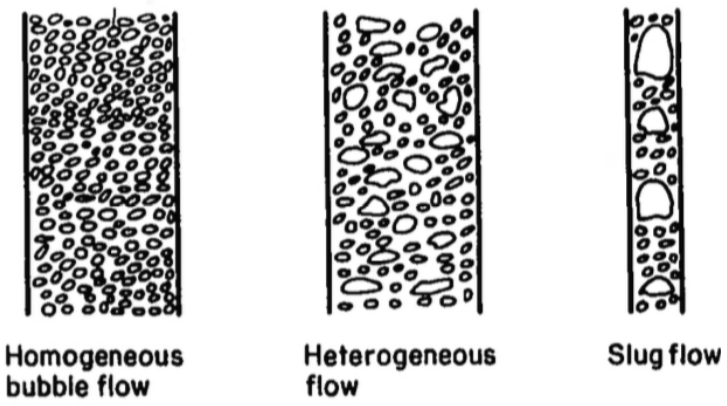

Figure 2.2 Operating states in bubble columns [8]

The scope of two-phase physical system is divided to following different categories [9]:

– ***Macro scale***: Processes or phenomena that are referred to as macro scale are taking place on a scope which is comparable to the physical domain under consideration. The global flow pattern within the selected reactors in this thesis is taking place on the macro scale.

- ***Micro scale***: Processes of phenomena on the micro scale involve the smallest entities of the physical system which have a significant contribution to overall process under consideration. In water electrolysis reactor of the current work the interaction between bubbles and continuous fluid and turbulent eddies is clearly on the micro scale.

- ***Meso scale***: The meso scale is inbetween macro and micro scales. The interaction between a swarm of bubbles and the surrounding flow field might fall in the meso scale.

The main goal of the current research is to apply the proposed CFD model in industrial apparatus. For this model to be computationally and industrially usable, the micro scales cannot be resolved. For dispersed flow systems, three different computational strategies can be developed depending on the scales resolved by the model formulation [7]:

1. The *Eulerian-Lagrangian models* for very dilute flows where small discrete particles are considered in the control volume. The Lagrangian approach which tracks each particle separately by its own equation of motion through continuous phase (Fig.2.3). The translation motion of the particle is governed by Newton's law. The benefit of the Lagrangian approach is the fact that each particle has its own motion equation, and it is relatively comfortable to obtain a distribution of particle sizes. But this approach has limitations. If our systems contain many particles (for instance a typical stirred-tank which includes 10^8 particles), the problem will computationally become too large.

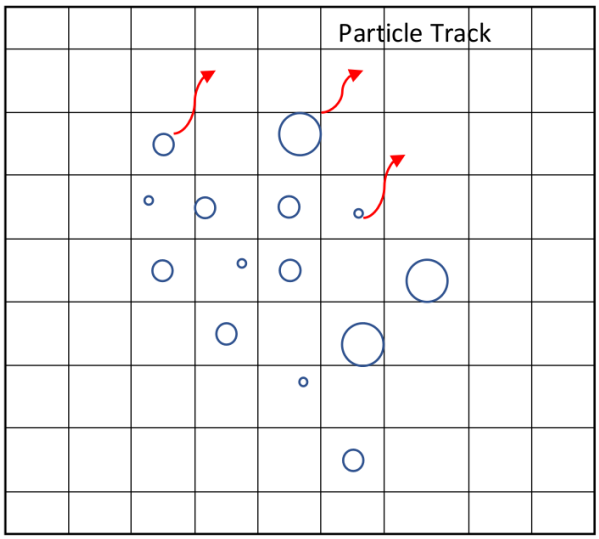

Figure 2.3 Schematic of Lagrangian approach

2. The *High resolution methods* for multiphase flows containing any number of particles where the model equations are formulated considering very small control volumes. Since the mesh size is smaller than particles in this approach (Fig.2.4), high resolution methods is usually able to track the interface between phases. Therefore, the relative size of fluid particles with respect to the control volumes is large enough so the particles can in principle be resolved. The disadvantage of this method is the heaviness of its computational time. The pertinent high resolution methods, often referred in the literature on multiphase reactors modelling, are The Marker and Cell (MAC) method [10] , the simplified MAC method [11], the volume of fluid (VOF) method [12], the level set (LS) front capturing method [13–15], and finally the front tracking method [16, 17].

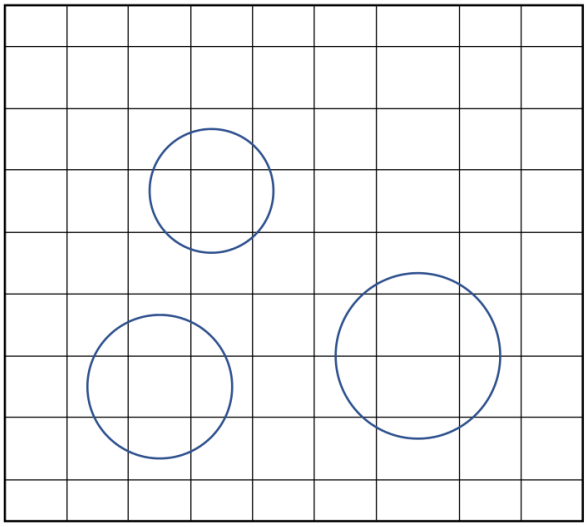

Figure 2.4 Schematic of High resolution methods where mesh size is smaller than bubble diameter to capture the interface

One very fundamental example of multiphase flows is that of a single gas bubble rising and deforming in a viscous liquid which can be achieved by the volume of fluid (VOF) method [12]. Simulation of this system, is an adequate step to conduct thorough investigation of complex flows such as bubbly flows because this initial system has effective simplicity. The geometry scale, numerical parameters and mesh information are summarized in Table 2.1.

Fig.2.5 indicates how the bubble gravity center position varies according to time. In the first moments, the trend is changed to linear. Theoretically, the slope of the line expresses the terminal velocity of the bubble. Visually, the gravitational motion

Characteristic	information
Geometry	cylinder (r=1.2 cm; h= 6 cm)
Solver	interFoam
Number of mesh	251'796
Bubble diameter	8 mm
time step	adjustable ($\delta t_0 = 10^{-8}$)

Table 2.1 The short description of the simulation system to model a rising bubble in the stagnant liquid

through the liquid is illustrated in Fig.2.6 that mirrors the shape of the bubble become ellipsoidal through the rising movement. The calculation of the terminal velocity (=0.14 m/s, slope in Fig.2.5) provides the appropriate criteria in order to compare with Grace regime map[18]. By contrast, the shape is verified by using terminal velocity value and calculation of Eötvös number, Reynolds number and Morton number as following table:

Name	Formulation	Value
Eötvös number (Eo)	$\frac{g\Delta\rho d^2}{\sigma}$	10
Reynolds number (Re)	$\frac{\rho d u_t}{\mu}$	12
Morton number (Mo)	$\frac{g\Delta\rho\mu^4}{\rho^2\sigma^3}$	0.122

Table 2.2 The calculation of dimensionless numbers related to bubble shape based on Grace map [18]

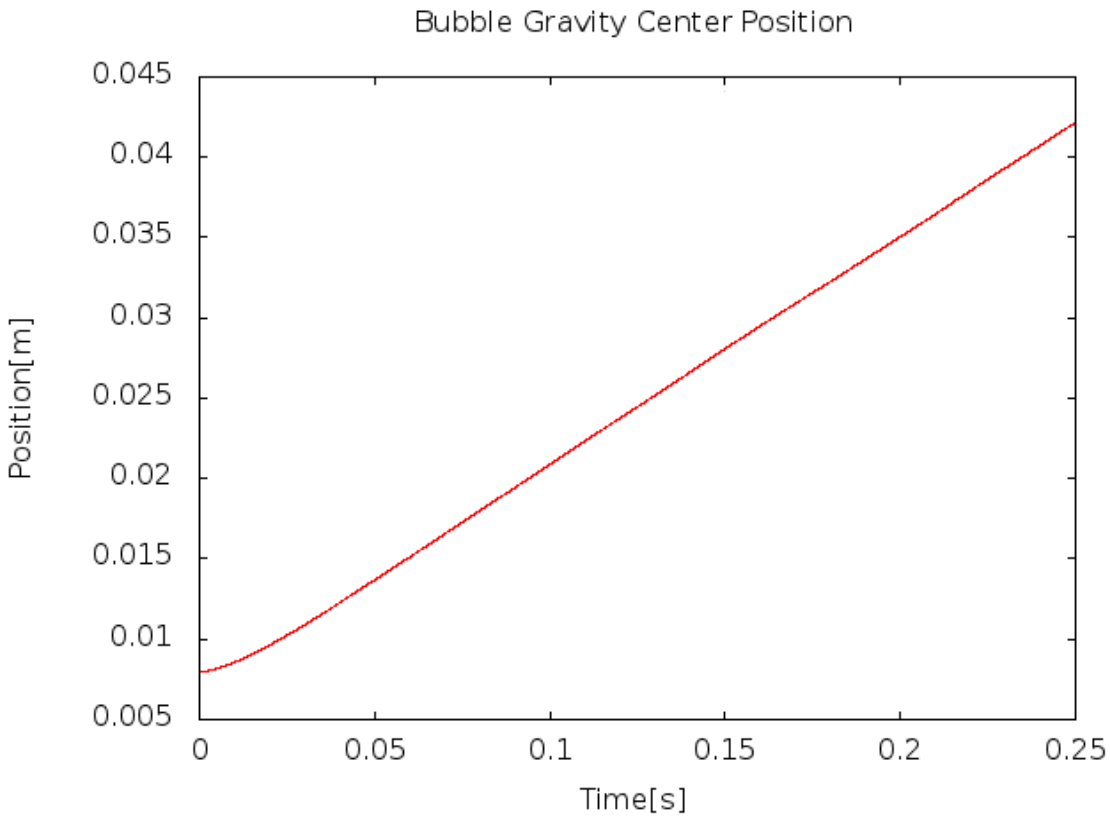

Figure 2.5 The variation of rising bubble location against the time in stagnant liquid

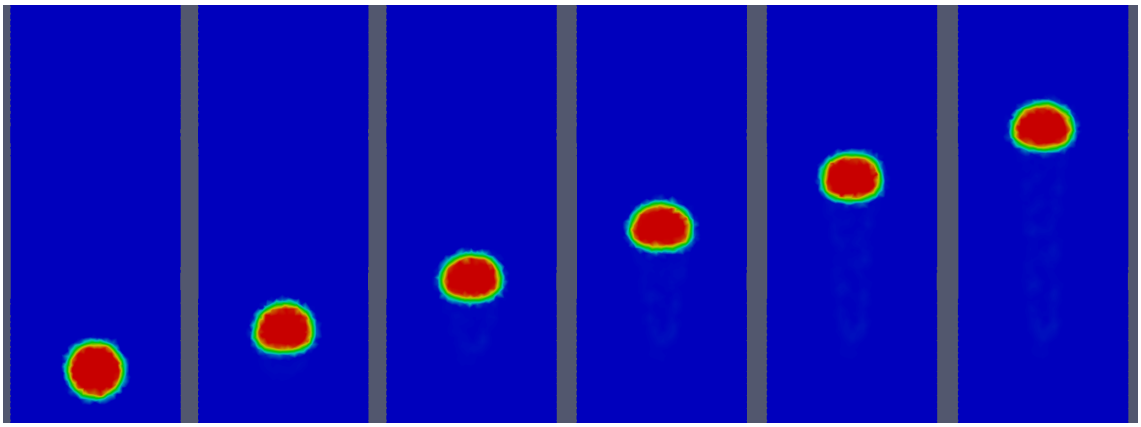

Figure 2.6 The visual motion of the bubble in stagnant liquid

3. The *Eulerian-Eulerian* model is applied when a relatively large number of particles with a continuous phase in the control volume exists in the system (Fig.2.8). In dense flow, the particle motion is controlled by collisions. E-E approach is under the

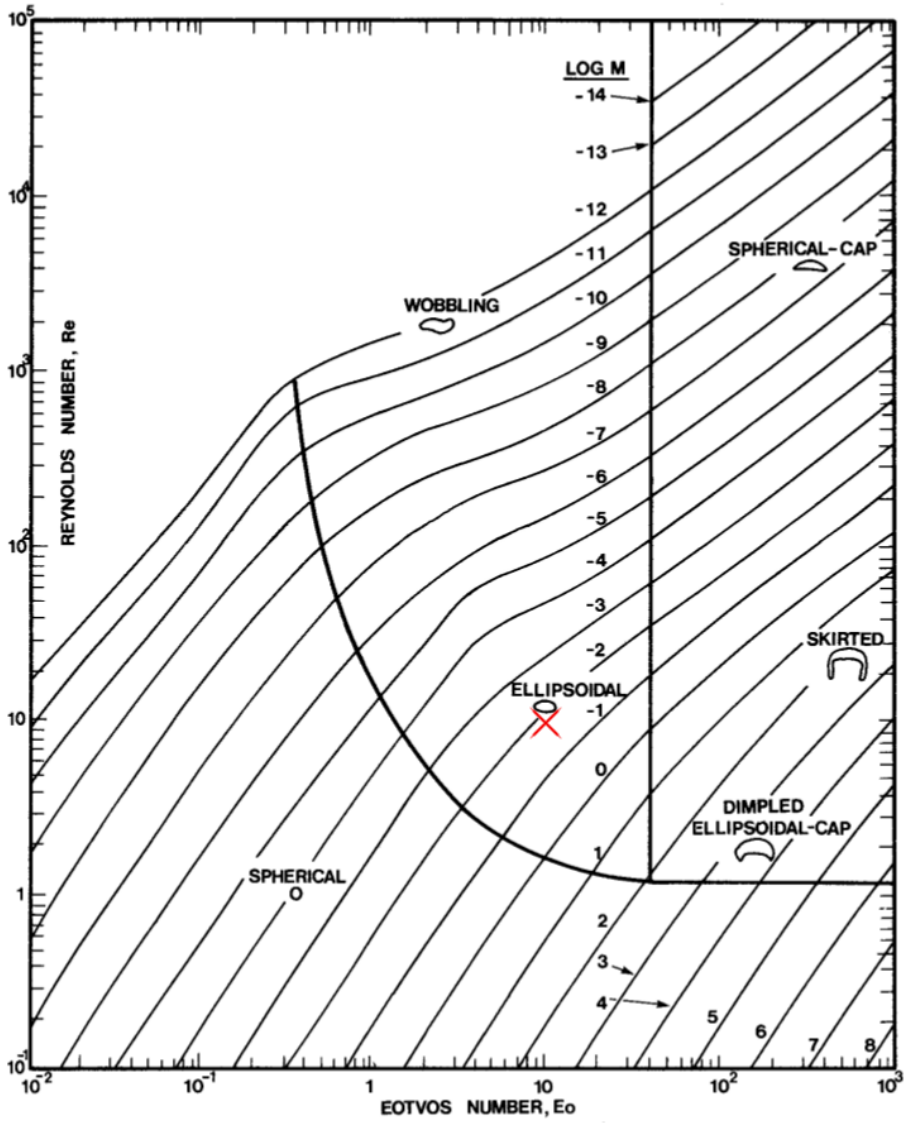

Figure 2.7 Validation of the model based on terminal velocity of the bubble and Grace map [18]

category of macro scale strategy [19]. There are different types of Eulerian averaging procedures (e.g., time averaging, volume averaging or ensemble averaging). Some advantages of this approach is that in principle it can be used in industrial systems due to its lower computational time. This method requires an adequate closure relation for the interfacial coupling terms and polydispersity of the bubbles.

As mentioned earlier, the goal of the current investigation is to develop the models being applicable and usable in industrial scale. Hence, we concentrate on mathematical

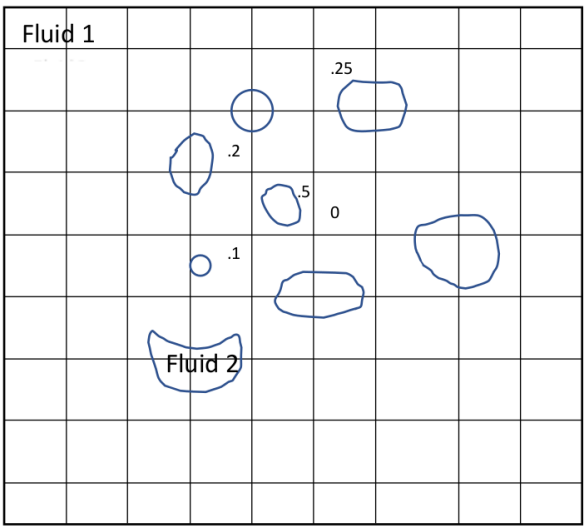

Figure 2.8 Schematic of Eulerian approach (small numbers show the fractional volume occupied by gas in each cell)

descriptions of Eulerian-Eulerian approach. Furthermore, special attention is paid to the topics of interfacial momentum transfer, turbulence modelling and mass transfer within two-phase modelling in particular, and the modelling strategies for poly-disperse flows.

2.2 Eulerian-Eulerian approach (E-E)

The present thesis deals with a mathematical model named "Two-Fluid" for two fluids and "Multi-fluid" for more than two fluids. This approach is also well known as Eulerian-Eulerian (E-E) in the literature. The mathematical form of two-fluid equations resembles the single phase Navier-Stokes equations but the two-fluid equations contain a term referred to mass and momentum exchange between phases. In the Euler-Euler approach, the existing phases behave as interpenetrating continum and the velocity and pressure fields of the dispersed (secondary) and continuous (primary) phases are solved as well as their the volume fractions in the same spatial location at the same time. Discrete entities (particles, bubbles) are effectively represented by a continuum (fluid). The derivation of the balance equations is based on a homogenization technique (e.g., time averaging, volume averaging or ensemble averaging), and is well documented in the literature [20–24]

The governing equations for multiphase flow are gained by multiplying the local governing equations with the indicator function and applying the ensemble average. Thus, we gain governing equations for the ensemble averaged flow fields [23, 25].

Governing Equations

Averaged phase momentum and continuity equations:

The Eulerian description of multiphase flow is not limited to two phases, however, for reasons of simplicity, we limit ourselves to the case of two phases. The continuity and momentum equations for each phase i are given by [23, 26]:

$$\frac{\partial}{\partial t}\left(\rho_{\mathrm{i}}\alpha_{\mathrm{i}}\right)+\nabla\cdot\left(\alpha_{\mathrm{i}}\rho_{\mathrm{i}}\mathbf{U}_{\mathrm{i}}\right)=0 \tag{2.1}$$

$$\frac{\partial}{\partial t}\left(\rho_{\mathrm{i}}\alpha_{\mathrm{i}}\mathbf{U}_{\mathrm{i}}\right)+\nabla\cdot\left(\alpha_{\mathrm{i}}\rho_{\mathrm{i}}\mathbf{U}_{\mathrm{i}}\mathbf{U}_{\mathrm{i}}\right)=-\alpha_{\mathrm{i}}\nabla p+\nabla\cdot\left(\alpha_{i}\bar{\bar{\tau}}_{\mathrm{effi},i}\right)+\mathbf{R}_{\mathrm{i}}+\mathbf{F}_{\mathrm{i}}+\alpha_{\mathrm{i}}\rho_{\mathrm{i}}\mathbf{g} \tag{2.2}$$

$$\bar{\bar{\tau}}_{\mathrm{effi},i}=\left(\mu_{\mathrm{lam},i}+\mu_{\mathrm{t},i}\right)\left(\nabla\mathbf{U}_{i}+\nabla\mathbf{U}_{i}^{T}\right)-\frac{2}{3}\left(\rho_{i}k_{i}+\left(\mu_{\mathrm{lam},i}+\mu_{\mathrm{t},i}\right)\nabla\cdot\mathbf{U}_{i}\right)\bar{\bar{I}} \tag{2.3}$$

where the subscript i denotes the phase, α is the phase fraction, $\bar{\bar{\tau}}_{\mathrm{effi},i}$ is the Reynolds stress tensor, $\mathbf{R}_{\mathrm{i}}$ is the averaged inter-phase momentum transfer term. The term $\mathbf{F}_{\mathrm{i}}$ expresses the centrifugal forces applied in the rotating reference frame for the MRF model.

The MRF approach

The simulations of gas-liquid stirred tank in this work were carried out using the multiple reference frame (MRF) method, also referred to as frozen rotor approach. The main feature of the MRF method is that the actual rotation of the impeller within the stirred tank is not resolved. Instead, the domain is separated into two parts (Figure. 2.9): 1- an inner cylindrical region containing the rotating zone and, 2- an outer zone excluding rotating volume (frozen zone). For the rotating zone, the $\mathbf{F}_{i}$ is activated in the governing equations (Eq.2.2). The MRF model is written as:

$$\mathbf{F}_{\mathrm{i}}=-2\alpha_{\mathrm{i}}\rho_{\mathrm{i}}\mathbf{N}\times\mathbf{U}_{\mathrm{i}}-\alpha_{\mathrm{i}}\rho_{\mathrm{i}}\mathbf{N}\times\left(\mathbf{N}\times\mathbf{r}\right) \tag{2.4}$$

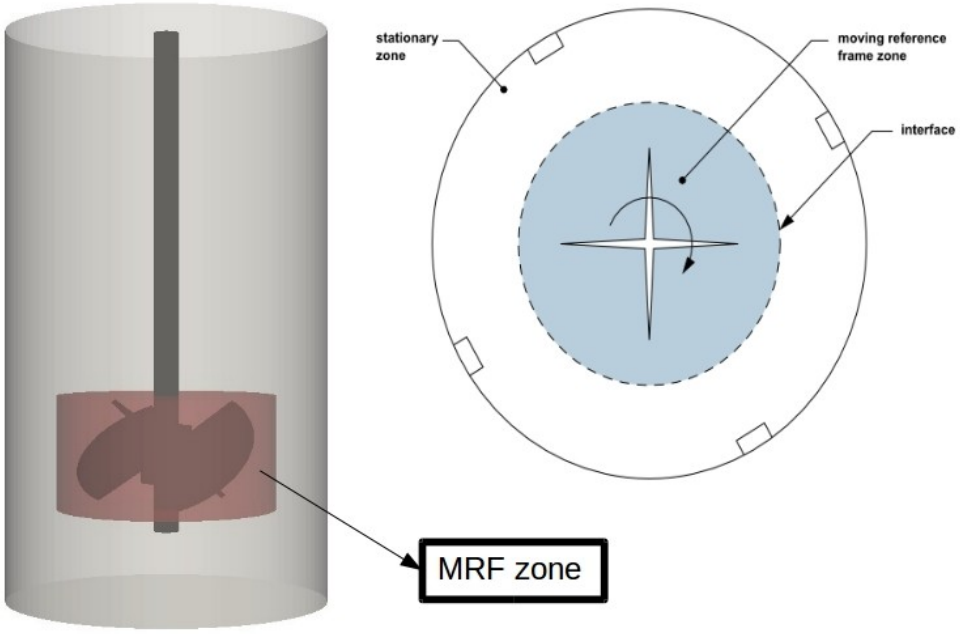

Figure 2.9 Schematic of rotating zone and frozen zone in a stirred tank

The main advantage of the MRF method is that there is no mesh motion involved. Resolving the rotation of the impeller would require a rotation of the inner zone relative to the outer zone (sliding mesh approach) [9]. Modifying the mesh during the simulation is costly in terms of computational time. The major disadvantage of this method is a rather poor temporal resolution of the results since the periodic variation caused by the moving impeller is neglected [9]. This difficulty can cause an issue in turbo machinery but it has achieved convincing results in reactors with impellers (Chapter 6 and 7). This approach is used when only global flow characteristics are of interest or to gain an initial flow estimate for a subsequent sliding mesh simulation [27].

Inter-Phase momentum transfer

Conservation law of momentum transfer leads to zero momentum exchange between phases, i.e. $\sum \mathbf{R}_i = 0$. In E-E approach, the instantaneous inter-phase momentum transfer term is decomposed into its components indicating their different physical meanings:

$$\mathbf{R}_{\mathrm{G}} = -\mathbf{R}_{\mathrm{L}} = \mathbf{R}_{\mathrm{G,drag}} + \mathbf{R}_{\mathrm{G,lift}} + \mathbf{R}_{\mathrm{G,vm}} + \mathbf{R}_{\mathrm{G,O}} \tag{2.5}$$

where the subscript G denotes the dispersed phase. Dispersed Phase Element (DPE) is generally applied for bubbles, droplets and particles, and in this case it mirrors the total bubbles. The inter-phase momentum transfer is determined by assembling the forces acting

on the DPEs. In DPEs generic term, particles could be referred to bubbles. $\mathbf{R}_{\mathrm{G,drag}}$, $\mathbf{R}_{\mathrm{G,lift}}$, $\mathbf{R}_{\mathrm{G,vm}}$ and $\mathbf{R}_{\mathrm{G,O}}$ represent the instantaneous drag, lift, virtual mass and other forces like Basset and turbulent dispersion forces. Turbulent dispersion force is caused by the interaction between turbulent eddies of the liquid and the bubbles. Basset and turbulent dispersion forces are not taken into account in most studies and their importance is not very striking [19].

In most two-fluid calculations the following functional forms are utilized:

$$\mathbf{R}_{\mathrm{G,drag}} = \frac{3}{4}\rho_{\mathrm{L}}\alpha_{\mathrm{G}}\frac{C_{\mathrm{D}}}{d_{32}} \mid \mathbf{U}_{\mathrm{G}} - \mathbf{U}_{\mathrm{L}} \mid (\mathbf{U}_{\mathrm{G}} - \mathbf{U}_{\mathrm{L}}) \tag{2.6}$$

$$\mathbf{R}_{\mathrm{G,lift}} = \alpha_{\mathrm{G}} C_{\mathrm{l}} \rho_{\mathrm{L}} \mathbf{U_r} \times (\nabla \times \mathbf{U_L}) \tag{2.7}$$

$$\mathbf{R}_{\mathrm{G,vm}} = \alpha_{\mathrm{L}} C_{\mathrm{vm}} \rho_{\mathrm{L}} \big(\frac{D_L \mathbf{U_L}}{Dt} - \frac{D_G \mathbf{U_G}}{Dt}\big) \tag{2.8}$$

where, $\mathbf{U_r} = \mathbf{U_L} - \mathbf{U_G}$ is the relative velocity, and $\frac{D_i}{Dt}$ stands for the substantive derivative which is defined as:

$$\frac{D_i}{Dt} = \frac{\partial}{\partial t} + \mathbf{U}_{\mathrm{i}} \cdot \nabla \tag{2.9}$$

The coefficient C_D, C_L and $C_{\nu m}$ are usually determined, empirically. Fig.2.10 exhibits how the forces are imposed on bubbles.

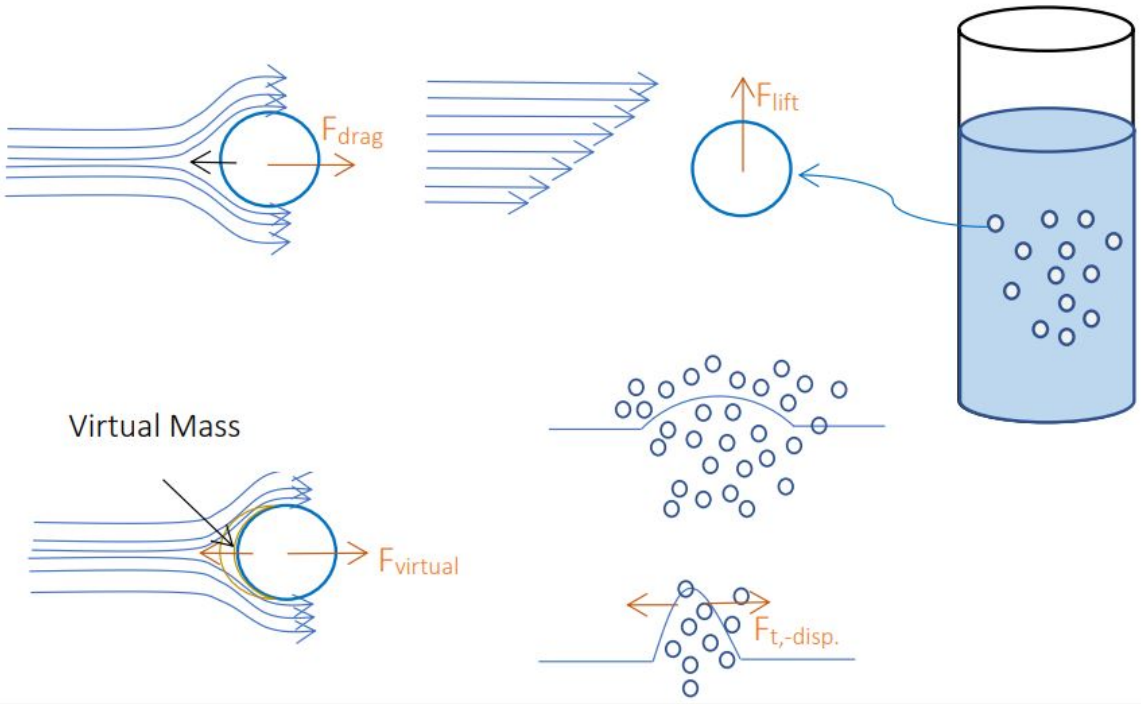

Figure 2.10 Schematic of interfacial forces on bubbles: (a) drag, (b) lift, (c) virtual mass and (d) turbulent dispersion

2.2.1 Drag models

The drag acts as a hydrodynamic resistance to the motion of the particle through continuous phase. The drag force is due to shear stress. In the other words, drag is a hydrodynamic friction between the liquid phase and the dispersed phase. In this section we will list a selection of the most well-known drag models that are used for gas-liquid systems.

Schiller-Naumann

The Schiller and Naumann [28] drag model is one of the most widely used in CFD and it is usually applied for spherical bubbles.

$$C_D = \begin{cases} \frac{24}{\mathrm{Re}}\left(1 + 0.15\mathrm{Re}^{0.687}\right) & \mathrm{Re} \leq 1000 \\ 0.44 & \text{otherwise} \end{cases} \tag{2.10}$$

where the Reynolds number corresponds to bubbles as follows:

$$\mathrm{Re} = \frac{d\mathbf{U_r}}{\nu_L} \tag{2.11}$$

In Eq.2.11, d, $\mathbf{U}_r$ and ν_L are bubble diameter, relative velocity and kinematic viscosity of continuous phase, respectively.

Tomiyama

Tomiyama [29] proposed drag correlations for bubbles in liquids with a varying degree of contamination with surfactants:

$$C_D = \max\left[\min\left\{\frac{16}{\mathrm{Re}}(1+0.15\mathrm{Re}^{0.687}), \frac{48}{\mathrm{Re}}\right\}, \frac{8}{3}\frac{\mathrm{Eo}}{\mathrm{Eo}+4}\right] \tag{2.12}$$

for a clean liquid;

$$C_D = \max\left[\min\left\{\frac{24}{\mathrm{Re}}(1+0.15\mathrm{Re}^{0.687}), \frac{72}{\mathrm{Re}}\right\}, \frac{8}{3}\frac{\mathrm{Eo}}{\mathrm{Eo}+4}\right] \tag{2.13}$$

for a slightly contaminated liquid; and

$$C_D = \max\left[\frac{24}{\mathrm{Re}}(1+0.15\mathrm{Re}^{0.687}), \frac{8}{3}\frac{\mathrm{Eo}}{\mathrm{Eo}+4}\right] \tag{2.14}$$

for fully contaminated liquids.

where Eo is the Eötvös number and Re is Reynolds number of bubble (Eq.2.11)

The Eötvös number is the ratio of buoyancy force to surface tension as follows:

$$\mathrm{Eo} = \frac{g(\rho_L - \rho_G)d^2}{\sigma} \tag{2.15}$$

Tomiyama [29] drag model takes into account the effects of fluid properties, bubble diameter and gravity.

Ishii-Zuber

The drag force of non-spherical bubbles are greater than spherical ones. The Ishii-Zuber drag model [30] is for those gas-liquid systems in which bubble deformation is not negligible.

$$C_{D,cap} = \frac{8}{3} \tag{2.16}$$

$$C_{D,ellipse} = \frac{2}{3}\sqrt{\mathrm{Eo}} \tag{2.17}$$

$$C_{D,sphere} = \frac{24}{\mathrm{Re}}(1 + 0.15\mathrm{Re}^{0.687}) \tag{2.18}$$

$$C_D = \max(C_{D,\mathrm{sphere}}, \min(C_{D,\mathrm{ellipse}}, C_{D,\mathrm{cap}})) \tag{2.19}$$

2.2.2 Lift models

Lift force is transverse to the direction of motion and is due to pressure and velocity gradients which push bubbles toward center or wall. When the liquid flow is non-uniform or rotational, bubbles also experience a lift force. Lift forces are primarily responsible for inhomogeneous radial distribution of the dispersed phase hold up and it could be more important to include their effects in CFD simulation. Actually, two types of lift force exist:

- Constant non-dimensional lift coefficient C_L
- Function of bubbles Etovos number and bubble Reynolds number

Constant coefficient

A constant value of C_L (=0.5 [23]) is usually applied in case of mono-disperse systems where the system does not exhibit bubble coalescence and breakup.

Tomiyama model

The Tomiyama lift model is reported in [31] and computes the lift force coefficient depending on the bubble's size and shape. The shape is considered by using a modified Eötvös number Eo_d :

$$C_L = \begin{cases} \min(0.288\tanh(0.121\mathrm{Re}), f(\mathrm{Eo}_d)) & \mathrm{Eo}_d < 4 \\ f(\mathrm{Eo}_d) & 4 \leq \mathrm{Eo}_d \leq 10.7 \end{cases} \tag{2.20}$$

where Eo_d and $f(\mathrm{Eo}_d)$ are:

$$\mathrm{Eo}_d = \frac{g(\rho_L - \rho_G)d_H^2}{\sigma} \tag{2.21}$$

$$f(\mathrm{Eo}_d) = 0.00105{\mathrm{Eo}_d}^3 - 0.0159{\mathrm{Eo}_d}^2 - 0.0204\mathrm{Eo}_d + 0.474 \tag{2.22}$$

The modified Eötvös number is defined by using the maximum horizontal dimension of a bubble as characteristic length d_H and the maximum vertical dimension of a bubble (d_V). E is the aspect ratio for spheroidal bubbles in a fully contaminated system (e.g. tap water):

$$E = \frac{d_V}{d_H} \tag{2.23}$$

Tomiyama et al. [31] showed d_H is evaluated by following empirical correlation:

$$E = \frac{1}{1 + 0.163\mathrm{Eo}^{0.757}} \tag{2.24}$$

2.2.3 Virtual mass models

Mass force is typically a inertia force and is produced by bubbles and it is resulted from the acceleration of the liquid surrounding the bubbles. Generally, numerical studies use constant virtual mass coefficient. Marschall [32] showed the virtual mass coefficient for spherical bubbles is constant and it equals to $C_{vm} = 0.5$. Use of adequate mass coefficient leads to accurate data in bubble columns, especially at the sparger region. However, Tabib et. al. [33] reported acceleration and deceleration of liquid is restricted to small bubble column. In other words, mass force could be neglected inside in the bubble columns that have a diameter greater than 0.15 m.

2.3 Turbulence in Multiphase Flows

There are various types of multiphase flows such as liquid-liquid, solid-liquid and gas-liquid systems. This diversity provides separated turbulent models for each individual multiphase flow. In fact, the diversity of multiphase flows leads to different strategy to develop turbulent models in multiphase systems [34]. The main focus of the current thesis is on bubbly flow and consequently, here, turbulence models applicable in bubbly flows are shortly described.

There are several possible approaches to the simulation of turbulent flows. These methods are Direct Numerical Simulation (DNS), Large-Eddy simulation (LES) and Reynolds Averaged Navier Stokes (RANS). LES and DNS are the best choices to provide an accurate resolution. However, LES and DES techniques are very expensive computationally and usually require expensive High Performance Computing (HPC) systems and long run times due to the need for intensive mesh refinement. RANS approach is more favorable because it does deal with small mesh size and it is simply implemented providing a satisfying accuracy in modelling flows. Furthermore, it is by far the preferred method for industrial flows since it has shown that it can predict the flow satisfactory for a wide variety of flows with relatively low computational cost.

One of the most important RANS-based turbulence models is k-ϵ which solves two equations: one for the turbulence kinetic energy (k-equation) and one for the turbulence kinetic energy dissipation rate (ϵ-equation). It is very popular and it has been the most widely used and validated turbulence model for many industrial applications [35]. Wall functions are implemented in the model which lowers the resolution requirements for its use, and also, it has demonstrated very good convergence behavior. The k-ϵ model is not suited for flows containing large adverse pressure gradients and in a variety of important cases such as unconfined flows, jet flows and flows exhibiting curved boundary layers [36].

This section covers the most popular turbulence models based on Reynolds Averaged Navier-Stokes (RANS) multiphase turbulence models. The following models originate from $k - \epsilon$ framework.

2.3.1 Standard k-ϵ

In multi-phase simulations the standard $k-\epsilon$ turbulence model is used in a general multi-phase formulation. As the secondary phase is dilute and the primary phase is clearly continuous, the dispersed k-ϵ turbulence model is used and solves the standard k-ϵ equations for the primary phase. The governing equations are denoted as follows [37]:

$$\frac{\partial}{\partial t}(\alpha_c \rho_c k) + \nabla.(\alpha_c \rho_c \mathbf{U}_c k) - \nabla.\left[\alpha_c \frac{\mu_t}{\sigma_k}\nabla k\right] = \alpha_c P_k - \alpha_c \rho_c \epsilon \tag{2.25}$$

$$\frac{\partial}{\partial t}(\alpha_c \rho_c \epsilon) + \nabla.(\alpha_c \rho_c \mathbf{U}_c \epsilon) - \nabla.\left[\alpha_c \frac{\mu_t}{\sigma_\epsilon}\nabla \epsilon\right] = \alpha_c \frac{\epsilon}{k}(C_{\epsilon 1} P_k - C_{\epsilon 2}\rho_c \epsilon) \tag{2.26}$$

here, P_k represents the rate of production of turbulence kinetic energy given as follows:

$$P_k = 2\nu_c^{\text{eff}}(\nabla \mathbf{U}_c \cdot \text{dev}(\nabla \mathbf{U}_c + (\nabla \mathbf{U}_c)^T)) \tag{2.27}$$

where dev shows the deviatory component defined as

$$\text{dev}\mathbf{T} = \mathbf{T} - \frac{1}{3}(\text{tr}(\mathbf{T})) \tag{2.28}$$

$\mathbf{T}$ is a second rank tensor and tr is the trace of this tensor.

The turbulent viscosity μ_t is expressed by:

$$\mu_t = \rho C_\mu \frac{k^2}{\epsilon} \tag{2.29}$$

with the model constants

$$C_{\epsilon 1} = 1.44 \quad C_{\epsilon 2} = 1.92 \quad C_\mu = 0.09 \quad \sigma_{k=1.0} \quad \sigma_\epsilon = 1.3$$

In OpenFOAM, there is a class called "continuousGasKEpsilon". The name does not state gas is continuous phase. In fact, this class applies k-ϵ model for the gas phase supporting phase inversion. In the limit that the gas phase fraction approaches zero a contribution from the other phase is blended into the k and ϵ equations up to the phase fraction of alphaInversion at which point phase inversion is considered to have occurred and the model reverts to the pure single-phase form. OpenFOAM repository says: "This model is

unpublished and is provided as a stable numerical framework on which a more physical model may be built."

2.3.2 Lahey k-ϵ

The Lahey k-ϵ turbulence model [38] is a derivation of the standard k-ϵ turbulence model and an extension of the standard k-ϵ model to account for the effect of the dispersed phase on the turbulence of the continuous phase. This effect is referred to as bubble induced turbulence (BIT). This model considers the velocity fluctuations induced by liquid displacement due to the relative velocity and liquid eddies which may be formed behind the bubbles. The model equations are only written for the liquid phase:

$$\frac{\partial}{\partial t}(\alpha_c \rho_c k) + \nabla.(\alpha_c \rho_c \mathbf{U}_c k) - \nabla.\left[\alpha_c\left(\mu + \frac{\mu_t}{\sigma_k}\right)\nabla k\right] = \alpha_c P_k - \alpha_c \rho_c \epsilon + S_{i,k} \tag{2.30}$$

$$\frac{\partial}{\partial t}(\alpha_c \rho_c \epsilon) + \nabla.(\alpha_c \rho_c \mathbf{U}_c \epsilon) - \nabla.\left[\alpha_c\left(\mu + \frac{\mu_t}{\sigma_\epsilon}\right)\nabla \epsilon\right] = \alpha_c \frac{\epsilon}{k}(C_{\epsilon 1} P_k - C_{\epsilon 2}\rho_c \epsilon) + S_{i,\epsilon} \tag{2.31}$$

The additional source terms $S_{i,k}$ and $S_{i,\epsilon}$ are introduced to account for the influence of the other phase (i.e. inter-phase turbulent interaction)

$$S_{i,k} = \frac{k}{C_{\epsilon 2}\epsilon} S_{i,\epsilon} \tag{2.32}$$

$$S_{i,k} = \rho_c C_p \left[1 + {C_D}^{4/3}\right] \alpha_c \frac{|\mathbf{U}_r|^3}{d} \tag{2.33}$$

where d is bubble diameter and the model constants are written as:

$$C_{\epsilon 1} = 1.44 \quad C_{\epsilon 2} = 1.92 \quad C_\mu = 0.09 \quad \sigma_{k=1.0} \quad \sigma_\epsilon = 1.3 \quad C_p = 0.25$$

2.3.3 Mixture k-ϵ

The mixture k-ϵ is applied when the secondary phase is not dilute and has high phase fraction (more than 10%), In this case, turbulence is simultaneously dictated by the continuous phase and dispersed phase. The use of one set of equations for k and ϵ is suggested for the mixture of the continuous and disperse phases [39].

The transport equations for k_{m} and ϵ_{m} are:

$$\frac{\partial}{\partial t}\left(\rho_{\mathrm{m}} k_{\mathrm{m}}\right)+\nabla\cdot\left(\rho_{\mathrm{m}}\mathbf{U}_{\mathrm{m}} k_{\mathrm{m}}\right)-\nabla.\left[\frac{\mu_{t,m}}{\sigma_k}\nabla k_{\mathrm{m}}\right]=P_{k,m}-\rho_{\mathrm{m}}\epsilon_{\mathrm{m}}+S_k^{\mathrm{m}} \tag{2.34}$$

$$\frac{\partial}{\partial t}\left(\rho_{\mathrm{m}}\epsilon_{\mathrm{m}}\right)+\nabla\cdot\left(\rho_{\mathrm{m}}\mathbf{U}_{\mathrm{m}}\epsilon_{\mathrm{m}}\right)-\nabla.\left[\frac{\mu_{t,m}}{\sigma_\epsilon}\nabla\epsilon_{\mathrm{m}}\right]=\frac{\epsilon_m}{k_m}\left(C_{\epsilon 1}P_{\mathrm{k,m}}-C_{\epsilon 2}\rho_{\mathrm{m}}\epsilon_{\mathrm{m}}\right)+S_\epsilon^{\mathrm{m}} \tag{2.35}$$

$$S_k^{\mathrm{m}}=\frac{k_m}{C_{\epsilon 2}\epsilon_m}S_\epsilon^{\mathrm{m}} \tag{2.36}$$

with the model constants

$$C_{\epsilon 1}=1.44 \quad C_{\epsilon 2}=1.92 \quad C_\mu=0.09 \quad \sigma_{k=1.0} \quad \sigma_\epsilon=1.3 \quad C_P=0.25$$

where m refers to the mixture of the two phases. The mixture quantities appearing in the equations are defined by:

$$\rho_m=\alpha_c\rho_c+\alpha_d\rho_d \tag{2.37}$$

The mixture properties can be related to those of the continuous and dispersed phases as follows:

$$k_m=\left(\alpha_c\frac{\rho_c}{\rho_m}+\alpha_d\frac{\rho_d}{\rho_m}C_t^2\right)k_c \tag{2.38}$$

$$\epsilon_m=\left(\alpha_c\frac{\rho_c}{\rho_m}+\alpha_d\frac{\rho_d}{\rho_m}C_t^2\right)\epsilon_c \tag{2.39}$$

$$\mathbf{U}_m = \frac{\alpha_c \rho_c \mathbf{U}_c + \alpha_d \rho_d \mathbf{U}_d C_t^2}{\alpha_c \rho_c + \alpha_d \rho_d C_t^2} \tag{2.40}$$

$$\mu_m^t = \frac{(\alpha_c \rho_c \mu_c^t + \alpha_d \rho_d \mu_d^t C_t^2)\rho_m}{\alpha_c \rho_c + \alpha_d \rho_d C_t^2} \tag{2.41}$$

$$P_{k,m} = \alpha_c P_{k,c} + \alpha_d P_{k,d} \tag{2.42}$$

$$S_k^{\mathrm{m}} = S_k^{\mathrm{c}} + S_k^{\mathrm{d}} = -A_d(2\alpha_d(C_t - 1)^2 k_c + \eta \nabla . \alpha_d . \mathbf{U}_r) \tag{2.43}$$

$$\mu_d^t = C_t^2 \left(\frac{\nu_c}{\nu_d} \frac{\rho_d}{\rho_c} \right) \mu_c^t \tag{2.44}$$

The basic relations between the turbulent quantities of the mixture and the turbulence quantities of the individual phases are based on the turbulence response coefficient C_t, which is the ratio between the r.m.s. values of the velocity fluctuations of the dispersed and the continuous phase [39].

$$C_t = \frac{\mathbf{U}_d'}{\mathbf{U}_c'} \tag{2.45}$$

What remains to clarify is how the turbulence response coefficient C_t is determined. The turbulence response coefficient is modified to account for the influence of the dispersed phase's volume fraction α_d [19, 39].

$$C_{t,0} = \frac{3 + \beta}{1 + \beta + 2\rho_d/\rho_c} \tag{2.46}$$

$$\beta = \frac{2 A_d L_e^2}{\rho_c \nu_c Re_t} \tag{2.47}$$

Here, ν_c is the kinematic laminar viscosity of the continuous phase, L_e is the eddy length scale obtained by $L_e = C_\mu({k_c}^{0.5}/\epsilon_c)$, A_d is a drag related coefficient given by $A_d = (3\alpha_d \rho_c C_d |\mathbf{U}_r|)/4d$. The turbulence Reynolds number is expressed as:

$$Re_t = \frac{\mathbf{U}'_c L_e}{\nu_c} \tag{2.48}$$

where $\mathbf{U}'_c$ is calculated from $\sqrt{2k_c/3}$.

To account for the functionality of the turbulence response coefficient against phase fraction, C_t is defined [39]:

$$C_t(\alpha_d) = 1 + (C_{t,0} - 1)e^{-f(\alpha_d)} \tag{2.49}$$

$$f(\alpha_d) = 180\alpha_d - 4.71 \times 10^3 \alpha_d^2 + 4.26 \times 10^4 \alpha_d^3 \tag{2.50}$$

Using the definition of turbulence response coefficient, the relations between k and ϵ for primary phase and secondary phase are given as follows:

$$k_d = C_t^2 k_c \tag{2.51}$$

$$\epsilon_d = C_t^2 \epsilon_c \tag{2.52}$$

2.3.4 Wall functions

In high turbulent regime, the universal behavior of near-wall flows called "wall functions" is applied. By wall functions, the turbulence model are not allowed to integrate the equations of k-ϵ for the regions closed to walls. The mean velocity at a point which its dimensionless distance (ratio of distance of the point from solid wall to boundary layer thickness) from solid wall is between 30 and 500, satisfies the log-law. In this region, the rate of turbulence production equals the rate of dissipation. By using these assumptions and the eddy viscosity equation, the wall functions can be developed as [40]:

$$u^+ = \frac{\mathbf{U}}{u_\tau} = \frac{1}{\kappa} ln(E y_p^+) \quad k = \frac{u_{\tau^2}}{\sqrt{C_\mu}} \quad \epsilon = \frac{u_\tau^3}{\kappa y} \tag{2.53}$$

Where the local wall shear stress (through u_τ) is related to the mean velocity, turbulence kinetic energy and rate of dissipation. Von Karman's constant $\kappa = 0.41$ and wall roughness parameter $E = 9.8$ for smooth walls [40].

It is necessary to use large number of mesh points to resolve all the details in the turbulent layer. The "wall functions" are introduced to capture the effect of the wall boundaries. The implementation of wall boundary conditions in turbulent flows starts with the evaluation of

$$u^+ = \frac{\Delta y_p}{\nu}\sqrt{\frac{\tau_w}{\rho}} \tag{2.54}$$

where Δy_p is the distance of the near-wall node P to the solid surface. A near-wall flow is taken to be laminar if $y^+ \leq 11.63$. The wall shear stress is assumed to be entirely viscous in origin. If $y^+ > 11.63$ the flow is turbulent and the wall function approach is used [40]. The exact value of $y^+ = 11.63$ is the intersection of the linear profile and the log-law, so it is obtained from the solution of [40] (Figure. 2.11):

$$u^+ = \frac{1}{\kappa} ln(E y_p^+) \tag{2.55}$$

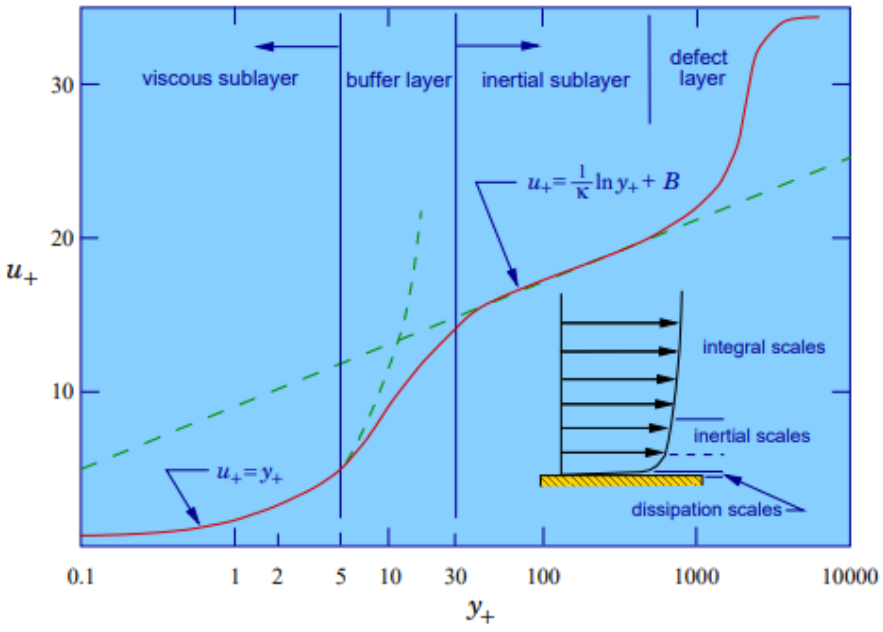

Figure 2.11 Schematic of wall function procedures

2.4 Interphase species mass transfer

Interphase species mass transfer can occur across a phase interface (between a gas and a liquid, or between a liquid and a solid) depending directly on the concentration gradient of the transporting species in the phases. For example,

- evaporation of a liquid into a gaseous mixture including its vapor, such as the evaporation of liquid water into a mixture of air and water vapor.

- absorption/dissolution of a dissolved gas in a liquid from a gaseous mixture. For example, the absorption of oxygen by water from air.

The interphase species mass transfer can be solved in Eulerian model subject to the following conditions [41]:

- Both phases consist of mixtures with at least two species, and at least one of the species is present in both phases.

- The two mixture phases are in contact and separated by an interface.

- Species mass transfer can only occur between the same species from one phase to the other. For example, evaporation/condensation between water liquid and water vapor.

- For the species involved in the mass transfer, the mass fractions in both phases must be determined by solving transport equations.

To model interphase species mass transfer, phase species transport equations are solved along with the phase mass, momentum and energy equations. The transport equation for, the local mass fraction of species p in phase i, is [41]:

$$\frac{\partial}{\partial t}(\rho_i \alpha_i Y_i^p) + \nabla \cdot (\alpha_i \rho_i \mathbf{U}_\mathrm{i} Y_i^p) = \quad \nabla \cdot (\alpha_i \left[\rho_i {D_{i,m}}^p + \tfrac{\mu_t}{Sc_t} \right] \nabla Y_i^p) + \alpha_i R_i^p + \dot{M} \qquad (2.56)$$

where i denotes the ith phase, and n is the number of phases in the system. α_i , ρ_i , and $\mathbf{U}_i$ are the phase fraction, density, and velocity for the ith phase. R_i^p is the source/sink term accounting for chemical reactions, $\dot{M}$ denotes the net volumetric of mass transfer between phases, $D_{i,m}^p$ is the mass diffusion coefficient for species p in the mixture on phase i. Sc_t is

the turbulent Schmidt number ($= \frac{\mu_t}{\rho D_t}$) where μ_t is the turbulent viscosity and D_t is the turbulent diffusivity. All physical properties of the mixture are calculated by the weight average of each species.

Here, $\dot{M}$ is formulated depending on the direction of the mass transfer, mirrors the source term for mass transfer of the species between phase i and phase j. The volumetric rate of species mass transfer is assumed to be a function of mass concentration gradient of the transported species:

$$\dot{m}_i^p = k_i A_p \left(\rho_{i,e}^p - \rho_i^p \right) \tag{2.57}$$

where k_i is the volumetric mass transfer coefficient between the phases, and A_p is the interfacial area which establishes the link among population balance, E-E and mass transfer, ρ_i^p is the mass concentration of species in phase i, and $\rho_{i,e}^p$ is the equilibrium mass concentration of species p in phase i. In order to solve the species mass transfer it is necessary to determine appropriate values for k_i and $\rho_{i,e}^p$.

CHAPTER 3

Population balance modelling

3.1 Introduction

In most practical applications of multiphase flow, the polydispersity should be taken into account in the secondary phase. Mono-disperse flows are rare in industrial multiphase applications. The polydispersity models are more accurate and realistic approaches which improves the fluid dynamics modeling in multiphase systems. For example, in a monodisperse bubbly flow, every bubble has exactly the same size, shape, and chemical composition, while in a polydisperse bubbly flow, each bubble may have a different characteristic size, which changes its velocity relative to the continuous phase and the other bubbles in its vicinity [34]. Additionally, in polydisperse multiphase flows, the properties of the disperse-phase elements is changed. This fact leads to a very complex modeling task. The coalescence of bubbles, for instance, leads to a higher rise velocity and enhancing the turbulence in the liquid phase. Due to these reasons, the mono-dispersity cannot be a precise assumption, and population balance models which bring polydispersity concept to the CFD modeling, become important.

In this chapter, a short description of population balance modelling, which comes along Eulerian-Eulerian approach, is given. Furthermore, the bubble interactions including coalescence and breakage are explained.

3.2 Population Balance Approach

Particles have a huge impact on behaviour of the flow in a particular system. The size distribution of secondary phase, which may be constituted of gas bubbles, liquid drops or solid particles, can evolve in conjunction with the transport of the secondary phase in this type of flow system. The particulate flow processes may include a combination of different phenomena such as nucleation, growth, dispersion, dissolution, aggregation or coalescence, and breakage or break-up creating the dispersion. To investigate the effects of

the particles, a balance equation based on population balance approach could be considered to better examine the behaviour of the population of particles. The population balance method which is also stated as the balance in the particles population, is coupled with momentum, mass and energy balance equations. Nowadays, the coupling of computational fluid dynamic and population balance models is increasingly utilized to predict how the particles properties, such as size, are distributed. Properties distributions of particles help to improve crystallization, precipitation, and polymerization process of materials. It widely applies in various industries including pharmaceutical, agriculture, chemical products, coagulation and break the flocs [1], addition and degradation of polymers [42].

Number Density Function

The dispersed phase includes discrete elements. Each element is generally identified by a number of properties known as "coordinates". If the coordinates become specified, the elements will be distinguished, thus the term used in early publications on population balance where the authors referred to "a balance of countable entities" [43]. There are two kinds of coordinates, internal and external. External coordinates correspond to the physical space coordinates. However, internal coordinates correspond to the properties of the elements, for instance, their momentum (or velocities), their enthalpies (or temperatures), their volumes, surface area or sizes. Fig. 3.1 [42] shows the external and internal variables visually. Based on Eulerian-Eulerian approach, the dispersed phase is represented by number density function (NDF). The NDF provides information about how the population of elements inside a control volume varies through the proposed properties which can be size, volume, temperature, mass and etc.

The evolution of the size distribution of a particle population, which may consist of solid particles, bubbles or droplets, is described studying the changes in space and time of the Number Density Function (NDF) $n(\zeta; \mathbf{x}, t)$. Here, ζ indicates the internal coordinate representing the size of the discrete element of the disperse phase, $\mathbf{x}$ is the position vector in physical space and t is time.

Assuming the velocity of the disperse phase is known, the evolution of the NDF is defined by the population balance equation (Marchisio et al. [44, 45], Marchisio and Fox [46],

1. Floc is a small, loosely aggregated mass of flocculent material suspended in or precipitated from a liquid

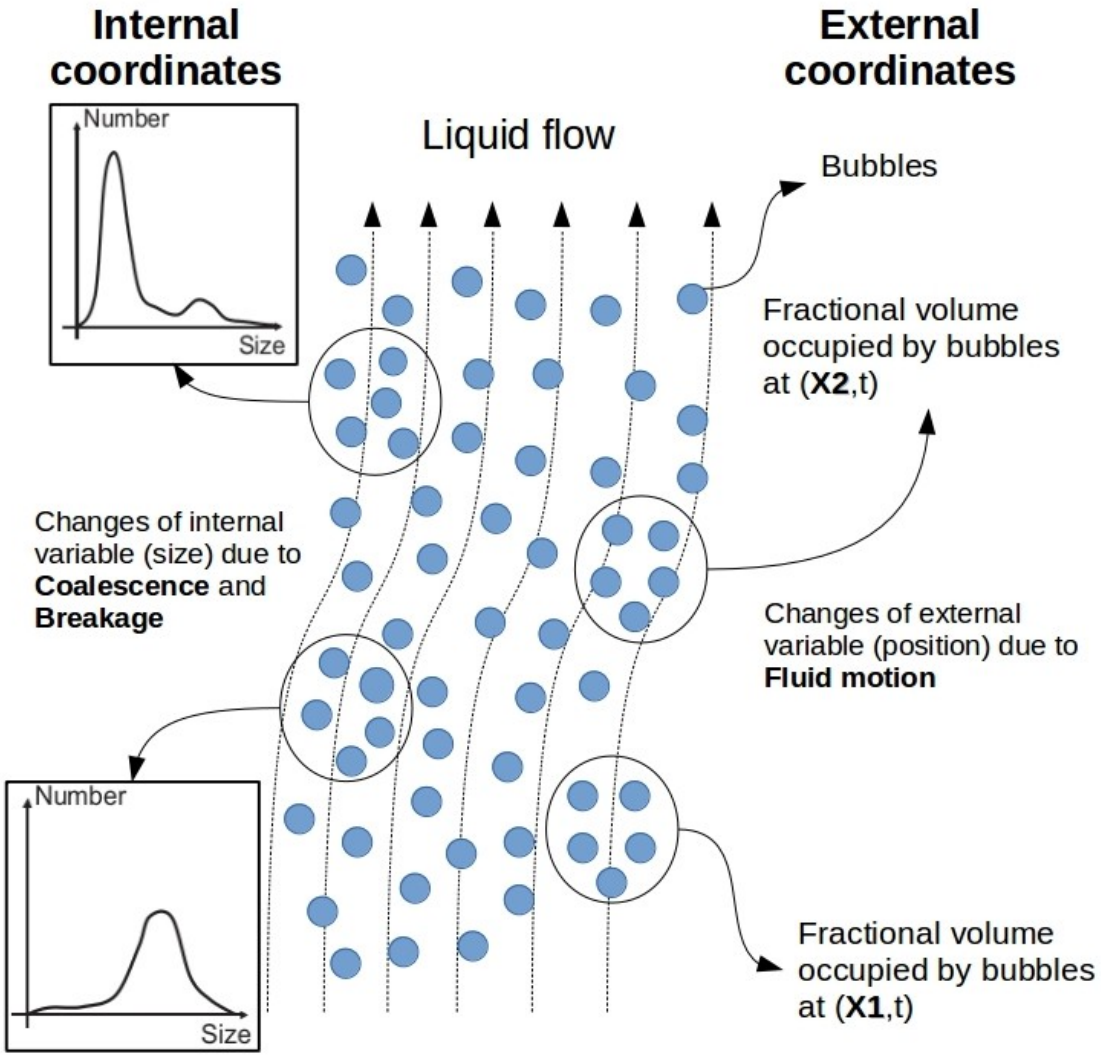

Figure 3.1 Internal and external coordinates of population balance for gas-liquid flow ($\mathbf{x}$= spatial location, t=time)

Ramkrishna [47]):

$$\begin{aligned}\frac{\partial n(\zeta;\mathbf{x},t)}{\partial t}+\nabla_{\mathbf{x}}\cdot[\mathbf{U}_G n(\zeta;\mathbf{x},t)]-\nabla_{\mathbf{x}}\cdot[\Gamma\nabla_x n(\zeta;\mathbf{x},t)]\\ +\nabla_{\zeta}\cdot[G(\zeta)n(\zeta;\mathbf{x},t)]=\overline{B}_{ag}(\zeta;\mathbf{x},t)-\overline{D}_{ag}(\zeta;\mathbf{x},t)\\ +\overline{B}_{br}(\zeta;\mathbf{x},t)-\overline{D}_{br}(\zeta;\mathbf{x},t)+N(\zeta;\mathbf{x},t),\end{aligned} \tag{3.1}$$

where $\mathbf{U}_G$ is the velocity of the disperse phase, Γ is the diffusivity and $G(\zeta)$ the continuous rate of change in the space of internal-coordinates. The first term of Eq.3.1 represents accumulation; the second term describes convection; and the third diffusion in physical space. The source terms $\overline{B}_{\mathrm{br}}(\zeta;\mathbf{x},t)$, $\overline{B}_{\mathrm{agr}}(\zeta;\mathbf{x},t)$, $\overline{D}_{\mathrm{br}}(\zeta;\mathbf{x},t)$ and $\overline{D}_{\mathrm{ag}}(\zeta;\mathbf{x},t)$ are birth rate due to breakage, birth rate due to coalescence, death rate due to breakage and death rate due to coalescence, respectively. Finally, $N(\zeta;\mathbf{x},t)$ is the rate of change of the NDF due to nucleation. In the present study, the NDF has the form of being length-based and $G(\zeta)$ is defined as the growth rate.

Bubbles may nucleate when the liquid is supersaturated with gas. When the dissolved gas concentration reaches a critical value, bubbles nucleate. This critical value might be theoretically obtained from Classical Nucleation Theory (CNT) (Abraham [48]). The nucleation theory provides information about the generation of nuclei (the formation of a cluster of molecules after reaching some critical size) per unit time and volume of the liquid as a function of the local parameters (homogenous nucleation). The bubbles can grow in size if the liquid is saturated with dissolved gas. The remaining gas is transported into the liquid on a molecular level and gives rise to supersaturation that causes an increase of the growth of bubbles that move through liquid. In this case, the growth term is included in the PBE as a source term. In some systems such as a gas-evolving electrode, bubble growth and nucleation terms might be treated as boundary conditions, since the sources of nucleation are usually irregularities of the electrode surfaces, and once a nucleus exists, the bubble growth occurs on the electrode surface in a concentration boundary layer (heterogeneous nucleation). Gas bubbles develop at nucleation sites on the electrode surface, grow in size until they reach a critical break-off diameter and detach into the electrolyte afterwards (Nierhaus [49], Tomasoni [50]). In other words, the bubble formation happens on the electrode. Consequently, it can be described by means of a boundary condition (an ingoing flux boundary).

Growth, nucleation and diffusivity were not taken into account in the example applications presented in this work, since the focus is on bubble coalescence and breakage. Therefore,

the final form of the evolution equation of the NDF is:

$$\frac{\partial n(\zeta;\mathbf{x},t)}{\partial t}+\nabla_{\mathbf{x}}\cdot[\mathbf{U}_G n(\zeta;\mathbf{x},t)] = \overline{B}_{ag}(\zeta;\mathbf{x},t)-\overline{D}_{ag}(\zeta;\mathbf{x},t)+\overline{B}_{br}(\zeta;\mathbf{x},t)-\overline{D}_{br}(\zeta;\mathbf{x},t). \quad (3.2)$$

The breakage and coalescence source terms are modeled as (Marchisio et al. [44, 45], Marchisio and Fox [46]):

$$\overline{B}_{\mathrm{ag}} = \frac{\zeta^2}{2}\int_0^{\zeta} \frac{\beta\left(\left(\zeta^3-\zeta'^3\right)^{1/3},\zeta'\right)}{\left(\zeta^3-\zeta'^3\right)^{2/3}} n\left(\left(\zeta^3-\zeta'^3\right)^{1/3};\mathbf{x},t\right) n(\zeta';\mathbf{x},t)d\zeta', \quad (3.3)$$

$$\overline{D}_{\mathrm{ag}} = n(\zeta;\mathbf{x},t)\int_0^{\infty} \beta(\zeta,\zeta')n(\zeta';\mathbf{x},t)d\zeta', \quad (3.4)$$

$$\overline{B}_{\mathrm{br}} = \int_{\zeta}^{\infty} a(\zeta')b(\zeta|\zeta')n(\zeta;\mathbf{x},t)d\zeta', \quad (3.5)$$

$$\overline{D}_{\mathrm{br}} = a(\zeta)n(\zeta;\mathbf{x},t). \quad (3.6)$$

Here, ζ as internal variable is size L, $\beta(\zeta,\zeta')$ is the coalescence rate between bubbles of size ζ and ζ'; $a(\zeta)$ is the break-up frequency of a bubble with size ζ; $b(\zeta|\zeta')$ represents daughter distribution function generated from the breakup of a bubble of size ζ'.

3.2.1 Class Method (CM)

The class method [47] solves the particle number density, directly. In CM, the particle size distribution divided into a series number of classes of discrete sizes. For each class, the equation of the number density of particles is solved and coalescence and breakup rates are transformed into birth and death rates for each class. The population balance equation for the ith bubble class without nucleation and growth terms is represented as:

$$\frac{\partial n_i}{\partial t} + \nabla.(\mathbf{U}_G n_i) = (\overline{B}_{i,agr} - \overline{D}_{i,agr} + \overline{B}_{i,br} - \overline{D}_{i,br}) \quad (3.7)$$

where n_i is the number of the bubbles from the group i per unit volume, $\overline{B}_{br}$, and $\overline{B}_{agr}$ are the birth rates caused by breakup and coalescence, respectively, and $\overline{D}_{agr}$ and $\overline{D}_{br}$ the relevant death rates.

$$n_i = \frac{\alpha_i}{\nu_i} \tag{3.8}$$

where ν_i is volume bubble of class i.

$$\sum \alpha_i = \alpha_G \tag{3.9}$$

where α_G is the volume fraction of the dispersed phase.

$$f_i = \frac{\alpha_i}{\alpha_G} \tag{3.10}$$

$$\sum f_i = 1 \tag{3.11}$$

where f_i is the bubble volume fraction of the group of size i.

To solve population balance equation using the scalars f_i, Eq.3.7 is changed to the following equation:

$$\frac{\partial \alpha_G f_i}{\partial t} + \nabla.(\alpha_G \mathbf{U}_G f_i) = \overline{B}_{i,agr} - \overline{D}_{i,agr} + \overline{B}_{i,br} - \overline{D}_{i,br} \tag{3.12}$$

As Eq.3.12 shows, all particles move with a same velocity (U_G). This approach is called by homogeneous MUSIG model (The multi-size-group)[51]. The MUSIG model approximates the continuous particle size distribution by M number of size fraction. If the large range of particle sizes is considered in multiphase flow, the number of conservation equations may become impractical. To overcome mentioned problem, the simplified class method is performed that can be categorized based on homogeneous and inhomogeneous MUSIG models. In a system with substantial large particles, the inhomogeneous MUSIG model developed by Krepper et al. [52] is more feasible. In homogeneous MUSIG model, the whole diameter range of dispersed phase is divided into M size groups and only one common momentum equation is solved for all size groups. Alternatively, in the inhomogeneous MUSIG model the dispersed phase is first divided into N velocity groups where each group is characterized by its own velocity field. Furthermore, each velocity group j is divided into a number of sub-size groups M_j, j=1, 2, ... N.

Method of classes calculates the Sauter Mean Diameter d_{32} as follows:

$$d_{32} = \frac{\sum_i f_i}{\sum_i f_i/d_i} \tag{3.13}$$

The Sauter mean diameter which is relied on active surface area, represents the average particle size in each computational cell (control volume). In fact, the ratio of the total volume of the particles over total surface area of the particles in control volume is the Sauter mean diameter.

Source terms:

The coalescence and breakage are expressed in the source terms of the transport equations (class fraction). In CM the source terms are as follows:

$$\overline{S}_i = \overline{B}_{i,agr} - \overline{D}_{i,agr} + \overline{B}_{i,br} - \overline{D}_{i,br} \tag{3.14}$$

Breakage and aggregation may create bubbles with volume ν such that $x_i < \nu < x_{i+1}$. This bubble must be split by assigning respectively fraction γ_i and γ_{i+1} to x_i and x_{i+1}. The following limitations preserve the number balance and mass balance.

$$\begin{cases} \gamma_i x_i + \gamma_{i+1} x_{i+1} = \nu \\ \gamma_i + \gamma_{i+1} = 1 \end{cases} \tag{3.15}$$

Ramkrishna [47] has also reported the birth in class i due to coalescence in this way:

$$\begin{aligned} \overline{B}_{i,agr} = & \sum_{k=0}^{n} \sum_{j=0}^{n} \left[\theta(x_{i-1} < x_j + x_k < x_i) \times (1 - \frac{1}{2}\delta_{jk}) \right] \\ & \times \gamma_{i-1}(x_j + x_k)\beta(x_k, x_j) \frac{36\alpha_g^2}{\pi^2} \frac{f_j f_k}{(d_j d_k)^3} \\ & + \sum_{k=0}^{n} \sum_{j=k}^{n} \left[\theta(x_i < x_j + x_k < x_{i+1}) \times (1 - \frac{1}{2}\delta_{jk}) \right] \\ & \times \gamma_i(x_j + x_k)\beta(x_k, x_j) \frac{36\alpha_g^2}{\pi^2} \frac{f_j f_k}{(d_j d_k)^3}, \end{aligned} \tag{3.16}$$

where θ is a test function expressed as:

$$\theta(\varphi) = \begin{cases} 0 & \varphi \text{ is false} \\ 1 & \varphi \text{ is true} \end{cases}. \tag{3.17}$$

and:

$$\gamma_{i-1}(\nu) = \frac{\nu - x_{i-1}}{x_i - x_{i-1}}, \quad \gamma_i(\nu) = \frac{x_{i+1} - \nu}{x_{i+1} - x_i}. \tag{3.18}$$

The death rates $\overline{D}_{i,agr}$ in class i due to coalescence are defined as follows:

$$\overline{D}_{i,agr} = \frac{36 f_i \alpha_G^2}{\pi^2 d_i^3} \sum_{k=0}^{n} \beta(x_i, x_k) \frac{f_k}{d_k^3}, \tag{3.19}$$

while the birth rate $\overline{B}_{i_{br}}$ in class i due to break-up writes:

$$\overline{B}_{i_{br}} = \frac{6\alpha_G}{\pi} \sum_{k=i}^{n} b(x_k|x_i) a(x_k) \pi_{i,k} \frac{f_k}{d_k^3}, \tag{3.20}$$

and the death rate $\overline{D}_{i,br}$ in class i due to break-up:

$$\overline{D}_{i,br} = \frac{6\alpha_G f_i}{\pi d_i^3} a(x_i), \tag{3.21}$$

where:

$$\pi_{i,k} = \int_{x_{i-1}}^{x_i} \frac{\nu - x_{i-1}}{x_i - x_{i-1}} p(\nu, \nu_k) d\nu + \int_{x_i}^{x_{i+1}} \frac{x_{i+1} - \nu}{x_{i+1} - x_i} p(\nu, \nu_k) d\nu \tag{3.22}$$

The mentioned integrals are solved by the Gaussian quadrature integration as follows:

$$\begin{aligned} \pi_{i,k} \simeq & \sum_{j=1}^{5} \frac{(1+W_j)^3}{(j+1)^2 p_5^2 p(W_j)} p\left(\frac{x_i - x_{i-1}}{2}(1+W_j) - x_{i-1}, x_k \right) + \\ & \sum_{j=1}^{5} \frac{(1+W_j)^2 (1-W_j)}{(j+1)^2 p_5^2 p(W_j)} p\left(\frac{x_{i+1} - x_i}{2}(1+W_j) - x_i, x_k \right) \end{aligned} \tag{3.23}$$

P_n is a Legendre polynomial and can be formulated using the recurrence relation:

$$P_n = \frac{(2n-1)xP_{n-1} - (n-1)P_{n-2}}{n}; \quad P_0 = 1; \quad P_1 = x \tag{3.24}$$

W_j is the weighting function of the orthogonal polynomials as shown in Table 3.1. If j equals five, adequate accuracy is achieved.

W_1	W_2	W_3	W_4	W_5
$\sqrt{\frac{35+2\sqrt{70}}{63}}$	$\sqrt{\frac{35-2\sqrt{70}}{63}}$	0	$-\sqrt{\frac{35-2\sqrt{70}}{63}}$	$-\sqrt{\frac{35+2\sqrt{70}}{63}}$

Table 3.1 Values of weights used in Gaussian quadrature.

3.2.2 Method of Moments (MOM)

Randoph and Larson [53] and Hulburt and Katz [54] introduced the Method of Moments (MOM) and Standard Method of Moments (SMOM). These methods are limited to specific growth rate expression, breakage and aggregation kernels. Hence, their applications are restricted. The methodology is described as follows:

In the absence of convection in physical space due to bubble velocity, breakage and aggregation, Eq.3.2 could be simplified as following equation:

$$\frac{\partial n_L}{\partial t} = -\frac{\partial}{\partial L}(G(L)n_L) \tag{3.25}$$

where $G(L)$ is named by growth function.

If integer moments are considered, their definition is:

$$M_k = \int_0^\infty n(L;\mathbf{x},t)L^k dL, \quad k = 0, 1, \ldots \tag{3.26}$$

If we perform the moment transform, we will have:

$$\frac{\partial M_k}{\partial t} = k\int_{\Omega_\zeta} L^{k-1}G(L)n_L dL \tag{3.27}$$

If the growth function has a special shape, i.e. $G(L) = \beta_0 + \beta_1 L$:

$$\frac{\partial M_k}{\partial t} = k\int_{\Omega_\zeta} L^{k-1}(\beta_0 + \beta_1 L)n_L dL \tag{3.28}$$

which equals to:

$$\frac{\partial M_k}{\partial t} = k\beta_0 M(k-1) + k\beta_1 M(k) \tag{3.29}$$

Mathematically, the above correlations state that existence of high order growth term (for example $\dot{L} = \beta_0 + \beta_1 L + \beta_2 L^2$) results in using high order moments and complex equations. For example, Hulburt and Katz [54] considered orthogonal Laguerre Polynomials for growth function as follows:

$$G(L) = \frac{\beta}{L}, L > 0 \tag{3.30}$$

Likewise, we can obtain for the first four moments:

$$\frac{\partial M_0}{\partial t} = 0 \tag{3.31}$$

$$\frac{\partial M_1}{\partial t} = k\beta M_{-1} \tag{3.32}$$

$$\frac{\partial M_2}{\partial t} = k\beta M_0 \tag{3.33}$$

$$\frac{\partial M_3}{\partial t} = k\beta M_1 \tag{3.34}$$

The moments of even order can be calculated explicitly but for the rest of the moments, it is not possible because M_1 needs M_{-1}. If the series expansion of n_L is implemented, the moment M_{-1} can be specified through the other moments [54]:

$$M_{-1} = \frac{{M_0}^2 M_1}{2{M_1}^2 - M_0 M_2} \tag{3.35}$$

Now, if Eq.3.35 is substituted for M_{-1}, a closed system of equation is reached.

The range of the MOM is very limited. If the growth law, coalescence and breakage models are not constant or linear (lack of analytical solution), MOM cannot be suitable choice. Nowadays, this method is not favoured because the closure requirements are very severe and relied upon the choice of the first lower-order of moments.

3.2.3 Quadrature-based Moments Method (QBMM)

Quadrature-based Moment Methods (QBMM) consider the evolution of a set of moments of the NDF. Using Eq. 3.26, evolution equations for the moments of the NDF including advection due to physical space and source terms read:

$$\frac{\partial M_k(t,x)}{\partial t} + \nabla \cdot [\mathbf{U}_G M_k(t,x)] = S^k \tag{3.36}$$

By solving Equation (3.36) for a set of at least four moments, the Sauter mean diameter $d_{32} = m_3/m_2$ can be calculated. The following list explains separately the methods which are in the family of QBMM method.

1- Quadrature Method of Moments (QMOM)

As mentioned earlier, if the growth or source term does not have a determined shape, a closed system of equations will not be available in the case of the moments. Firstly, McGraw [55] introduced QMOM method. In this technique, the unknown NDF is represented by a weighted summation of Dirac delta distributions $\delta(L - L_\alpha)$[55]:

$$n(L) \approx \sum_{\alpha=1}^{N} W_\alpha \delta(L - L_\alpha) \tag{3.37}$$

where W_i are non-negative weights of each kernel density function, L_i are the corresponding quadrature abscissae and N is the number of kernel density functions to approximate the NDF.

The approximation of n_L with respect to the complicated source term, substituted with one approximation which considers the integral through n-point Gaussian quadrature [56], i.e.,

$$\int_\Omega S(L) n_L dL \approx \sum_{i=1}^{N} S(L_i) W_i(t,x) \tag{3.38}$$

where $S(L)$ is a given function (k=0, 1, 2, ...). Hence, we will have the approximation for the moments M_k. Based on the moments of n_L:

$$M_k = \sum_{i=1}^{N} L_i^k W_i(t,x), \qquad k = 0, 1, 2, ..., 2N-1 \tag{3.39}$$

As above Eq.3.39 shows, there are $2N$ unknowns on the right-hand side namely, W is weight, L is abscissae. We have the simplified transformed equation:

$$\frac{\partial M_k(t,x)}{\partial t} + \nabla.(\mathbf{U}^{(k)} M_k(t,x)) = S^{(k)} \tag{3.40}$$

where is the $S^{(k)}$ is the source term of moment of order k and $\mathbf{U}^{(k)}$ is the k^{th} moment velocity written as:

$$\mathbf{U}^{(k)} = \frac{\sum_{i=1}^{N} u(L_i) W_i L_i^k}{\sum_{i=1}^{N} W_i L_i^k} \qquad k = 0, ..., 2N-1 \tag{3.41}$$

If bubbles travel with same velocity in each computational cell, $\mathbf{U}^{(k)}$ equals to velocity of dispersed phase ($= \mathbf{U}_{\mathrm{G}}$).

The approach of QMOM provides a solution using the given moments, at each time step to calculate the related weights and abscissas (in our case, size). Having weights and abscissas, enables us to approximate the integral including the source term. Fig.3.2 shows the procedures of QMOM. QMOM method requires an algorithm in order to calculate weights and abscissas. Two kinds of different algorithms which are product-difference algorithm (PDA) suggested by McGraw [55] and Wheeler algorithm used by Marchisio and Fox [57], could be separately used. As the QMOM procedures presents, we need six moments ($2N$) for three nodes ($N = 3$) which means three bubble sizes L_1, L_2 and L_3 weighted by W_1, W_2 and W_3. Computationally, it is not expensive to track few points of the distribution and this approach leads to obtain the accurate statistics. In Fig.3.3, the nodes have been visually determined within a special Bubble Distribution Function.

2- Direct Quadrature Method of Moments (DQMOM)

Basically, DQMOM was suggested in 2005 to compute problems containing more than one internal variable by Marchisio and Fox [58]. DQMOM does not solve a system for the equations of the moments. However, it rather uses equations for the weight and abscissas, directly. If the function of n_L is defined based on a combination of Dirac delta distributions:

$$n_L(t,x,L) \approx \sum_{i=1}^{n} W_i(t,x)\delta(L - L_i(t,x)). \tag{3.42}$$

Thus, the transport equation for weights and abscissas are as follows:

$$\frac{\partial}{\partial t} W_i + \nabla.(UW_i) = a_i \tag{3.43}$$

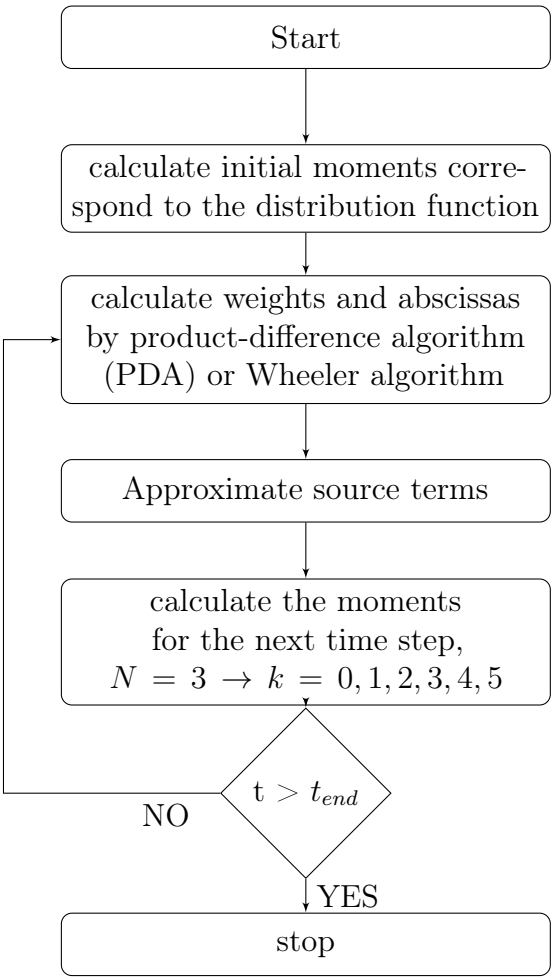

Figure 3.2 QMOM algorithm

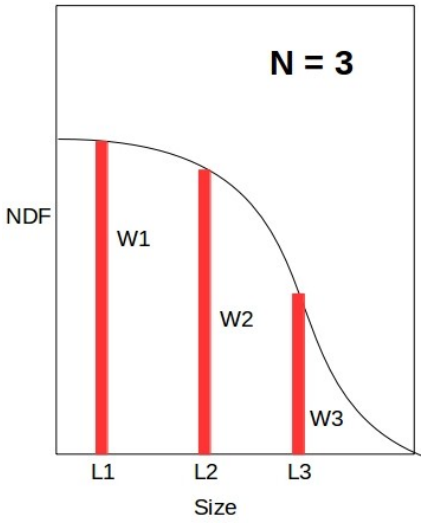

Figure 3.3 Nodes description as weights and abscissas

$$\frac{\partial}{\partial t}L_i + \nabla.(UL_i) = b_i \tag{3.44}$$

where a_i and b_i could be calculated by the solution of linear system, $AX = B$ which is obtained as:

$$(1-k)\sum_{i=1}^{N} L_i^k a_i + k\sum_{i=1}^{N} L_i^{k-1} b_i = S^{(k)} \tag{3.45}$$

For instance, for $N = 2$, we can write:

$$\begin{bmatrix} 1 & 1 & 0 & 0 \\ 0 & 0 & 1 & 1 \\ -L_1^2 & -L_2^2 & 2L_1 & 2L_2 \\ -L_1^3 & -L_2^3 & 3L_1^2 & 3L_2 \end{bmatrix} \begin{bmatrix} a_1 \\ a_2 \\ b_1 \\ b_2 \end{bmatrix} = \begin{bmatrix} S^{(0)} \\ S^{(1)} \\ S^{(2)} \\ S^{(3)} \end{bmatrix}$$

Fig.3.4 is the algorithm for DQMOM which describes the method, briefly. High number of classes in CM method provide accurate results but high computational effort is required, as well. By contrast, quadrature methods, like DQMOM, represents adequately the population without the large computational effort associated with such a large number of additional equations. On other words, as the number of classes used in the method of classes is increased, the advantage of the quadrature methods becomes more important. Selma showed that with a relatively low number of classes it is still much more efficient (computationally) to use DQMOM compared to CM [59].

Source terms in QMOM and DQMOM:

Source term related to the moment methods (QMOM and DQMOM), can be structured as follows:

$$\overline{S}^{(k)} = \overline{B}_{ag,k} - \overline{D}_{ag,k} + \overline{B}_{br,k} - \overline{D}_{br,k} \tag{3.46}$$

where $B_{agr}^{(k)}$ and $D_{agr}^{(k)}$ are the k^{th} birth and death rates because of coalescence and $B_{br}^{(k)}$ and $D_{br}^{(k)}$ are the k^{th} birth and death rates because of the breakage of the bubbles. The source term are formulated as [60]:

$$\overline{B}_{ag,k} = \frac{1}{2}\sum_{\alpha=1}^{N} W_\alpha \sum_{\beta=1}^{N} W_\beta (L_\alpha^3 + L_\beta^3)^{k/3} \beta(L_\alpha, L_\beta), \tag{3.47}$$

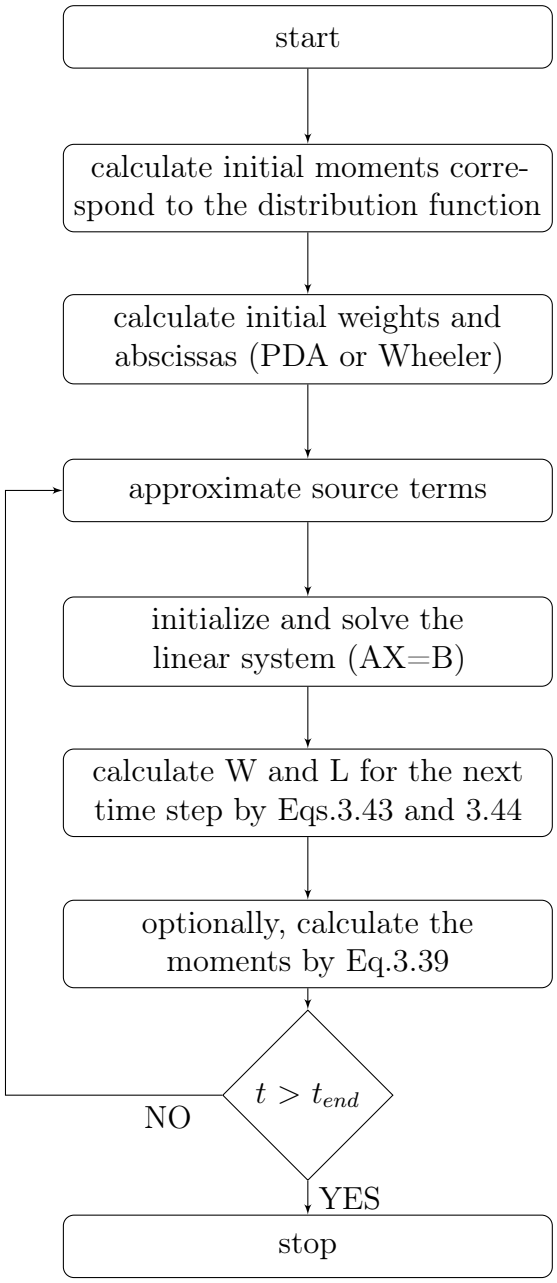

Figure 3.4 DQMOM Algorithm

$$\overline{D}_{ag,k} = \sum_{\alpha=1}^{N} W_\alpha L_\alpha^k \sum_{\beta=1}^{N} W_\beta \beta(L_\alpha, L_\beta), \tag{3.48}$$

$$\overline{B}_{br,k} = \sum_{\alpha=1}^{N} W_\alpha \overline{b}_\alpha^{(k)} a(L_\alpha), \tag{3.49}$$

$$\overline{D}_{br,k} = \sum_{\alpha=1}^{N} W_\alpha L_\alpha^k a(L_\alpha), \tag{3.50}$$

where the N is the number of weights w_α, and the corresponding abscissae L_α are determined from the first $2N$ integer moments of the NDF. $\beta_{\alpha\beta}$ is the aggregation kernel for the bubbles of size L_α and L_β; a_α is the breakage kernel for the bubble size of L_α; and $\overline{b}_\alpha^{(k)}$ represents daughter bubble distribution function. It should be pointed out that $\frac{1}{2}$ in Eq.3.47 is to correct for the redundancy. In other words, 2 is the number of times identical pairs have been considered in the interval of integration.

3- Extended Quadrature Method of Moments (EQMOM):

CM is intuitive, accurate and computationally intensive due to the large number of classes required to finely discretize the Number Density Function (NDF) with a large number of classes. Compared to CM, the QMOM can consider a wide range of bubble sizes with a reduced number of equations for the moments of the NDF. However, in some evaporation and combustion problems (Nguyen et al. [5], Yuan et al. [6]), the value of the NDF for null internal coordinates needs to be known, which is not the case if the QMOM method is used. DQMOM solves the equations for weights and abscissas directly. Shortcomings related to the conservation of moments affect the DQMOM approach since weights and abscissas are not conserved quantities (Yuan et al. [6]). In order to overcome these limitations, Yuan et al. [6] introduced the Extended Quadrature Method of Moments (EQMOM), which enables the shape of NDF to be reconstructed from a moment set using continuous kernel density functions instead of Dirac delta functions.

In comparison with QMOM, the Extended Quadrature Method of Moments (EQMOM) provides a smooth, non-negative NDF that gives the first $2N + 1$ moments with one additional moment. Four types of univariate EQMOM, including: Gaussian distribution, log-normal distribution, Gamma distribution and Beta distribution, can be found in literature [57]. To take example, kernel density function using log-normal distribution is considered as follows:

$$\delta_\sigma(L, L_i) = \frac{1}{L\sigma\sqrt{2\pi}} \exp\left(- \frac{(L - L_i)^2}{2\sigma^2} \right) \tag{3.51}$$

The kernel density function is introduced like:

$$n(\zeta) \approx \sum_{i=1}^{N} W_i \delta_\sigma(\zeta, \zeta_i) \tag{3.52}$$

The value of σ is specified by fixing one additional moment. EQMOM uses the integer moments that can be expressed as:

$$M_k = e^{k\mu + k^2\sigma^2/2} \tag{3.53}$$

In order to obtain the N weights, N abscissas and σ^2, Fig.3.5 illustrates the iterative method. In comparison with QMOM algorithm, EQMOM algorithm requires an additional moment because of an extra unknown variable, σ^2.

As mentioned in above algorithm, by setting $z = e^{\sigma^2/2}$ and $\chi_i = e^{\xi_i}$ the following equations are used:

$$M_k^* = M_k z^{-(2k)^2} \tag{3.54}$$

$$M_{2N}{}^* = \sum_{i=1}^{N} W_i \chi_i^{2N} \tag{3.55}$$

$$J_{2N}(z) = M_{2N} - z^{(2N)^2} M_{2N}{}^* \tag{3.56}$$

The EQMOM approach approximates the unknown NDF with a weighted sum of smooth, non-negative kernel density functions $\delta_\sigma(L, L_\alpha)$ (Nguyen et al. [5], Yuan et al. [6]):

$$n(L) \approx p_N(L) = \sum_{\alpha=1}^{N} W_\alpha \delta_\sigma(L, L_\alpha) \tag{3.57}$$

Source terms in EQMOM:

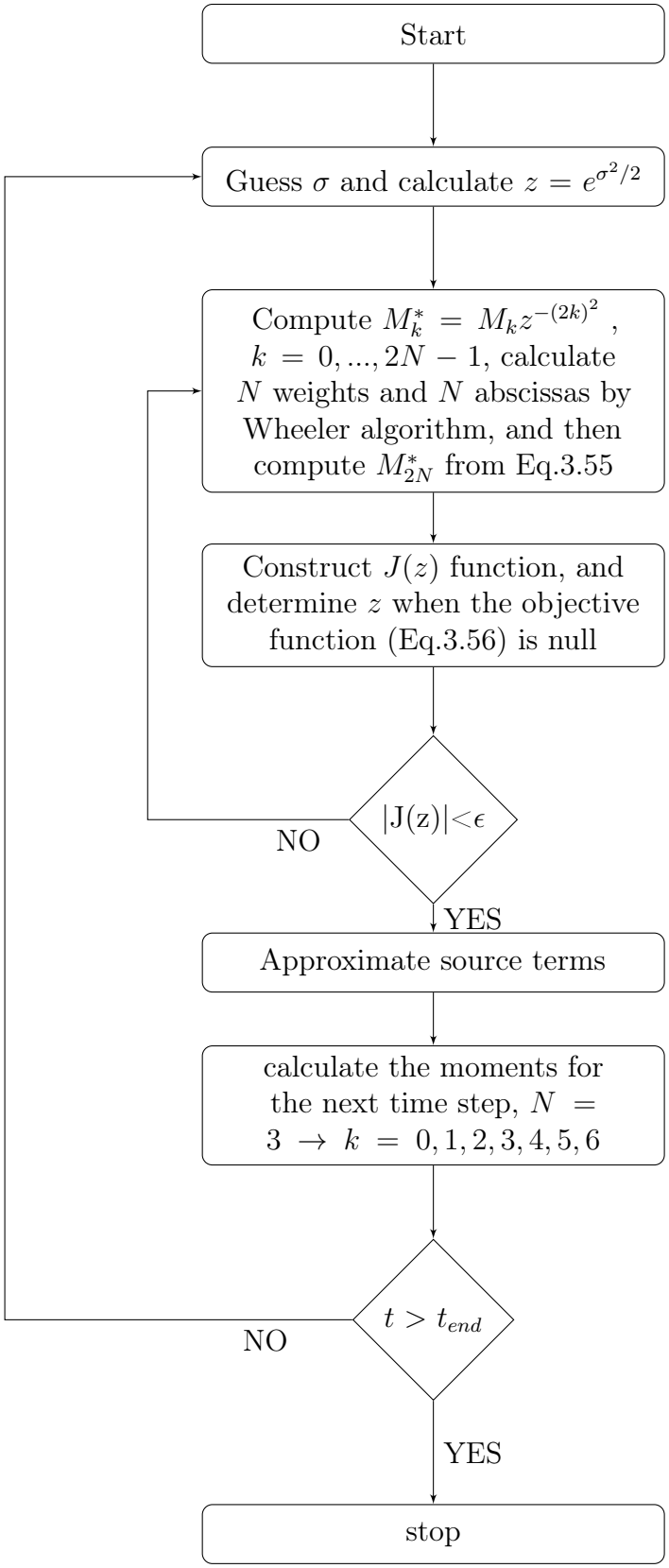

Figure 3.5 EQMOM algorithm

Source terms are closed in terms of the primary and secondary quadratures found with the EQMOM procedure, leading to:

$$\overline{B}_{ag,k} = \frac{1}{2}\sum_{\alpha_1=1}^{N}\sum_{\gamma_1=1}^{N_\alpha} W_{\alpha_1} W_{\alpha_1\gamma_1} \sum_{\alpha_2=1}^{N}\sum_{\gamma_2=1}^{N_\alpha} W_{\alpha_2} W_{\alpha_2\gamma_2} (L_{\alpha_1\gamma_1}^3 + L_{\alpha_2\gamma_2}^3)^{k/3} \beta_{\alpha_1\gamma_1\alpha_2\gamma_2}, \tag{3.58}$$

$$\overline{D}_{ag,k} = \sum_{\alpha_1=1}^{N}\sum_{\gamma_1=1}^{N_\alpha} L_{\alpha_1\gamma_1}^k W_{\alpha_1} W_{\alpha_1\gamma_1} \sum_{\alpha_2=1}^{N}\sum_{\gamma_2=1}^{N_\alpha} W_{\alpha_2} W_{\alpha_2\gamma_2} \beta_{\alpha_1\gamma_1\alpha_2\gamma_2}, \tag{3.59}$$

$$\overline{B}_{br,k} = \sum_{\alpha_1=1}^{N}\sum_{\gamma_1=1}^{N_\alpha} W_\alpha W_{\alpha\gamma} \overline{b}_{\alpha\gamma}^{(k)} a_{\alpha\gamma}, \tag{3.60}$$

$$\overline{B}_{br,k} = \sum_{\alpha_1=1}^{N}\sum_{\gamma_1=1}^{N_\alpha} W_\alpha W_{\alpha\gamma} L_{\alpha\gamma}^k a_{\alpha\gamma}, \tag{3.61}$$

where the N primary weights W_α, the corresponding primary abscissae L_α, together with the parameter σ are determined from the first $2N+1$ integer moments of the NDF. The $2N_\alpha$ quantities $W_{\alpha\gamma}$, called secondary weights and abscissae, respectively, are computed using the standard Gaussian quadrature formulae for known orthogonal polynomials to the kernel NDF (Nguyen et al. [5], Yuan et al. [6]). $\beta_{\alpha_1\gamma_1\alpha_2\gamma_2}$ is the aggregation kernel for the bubbles of sizes $L_{\alpha_1\gamma_1}$ and $L_{\alpha_2\gamma_2}$; $a_{\alpha\gamma}$ is the breakage kernel for the bubbles sizes of $L_{\alpha\gamma}$; and $\overline{b}_{\alpha\gamma}$ represents the daughter distribution function.

3.2.4 Daughter distribution function for QBMM

The daughter distribution function can be estimated by this equation [61]:

$$\overline{b}_i^{(k)} \approx L_i^k \frac{m^{\frac{k}{3}} + n^{\frac{k}{3}}}{(m+n)^{\frac{k}{3}}} \tag{3.62}$$

where m and n are the representative of the mass ratios between two bubble breakage. In other words, if a bubble breaks into two bubbles, we will have $m = \frac{mass_1}{mass_2}$ and $n = \frac{mass_2}{mass_1}$.

For instance, if two bubbles have the same volume (symmetric breakage), m and n equal to 1. Therefore:

$$\overline{b}_i^{(k)} \approx 2^{\frac{(3-k)}{3}} L_i^k \tag{3.63}$$

3.2.5 Bubble coalescence and break-up models

Here, only models which have been frequently used in gas liquid systems in the literatures are described. For more details about other coalescence and breakage models, the reader is referred to literature review of Liao and Lucas [62, 63].

Referring to the balance equation which contains a transient term, a convection term and four source terms due to binary bubble coalescence and breakage, the overal equation is expressed as [7]:

$$\frac{\partial n_i}{\partial t} + \nabla.(\mathbf{U}_{\mathrm{G}} n_i) = \overline{B}_{br,i} - \overline{D}_{br,i} + \overline{B}_{agr,i} - \overline{D}_{agr,i} \qquad \left(\frac{1}{sm^3}\right) \tag{3.64}$$

where n_i is the number density with units m^{-3}, $\mathbf{U}_{\mathrm{G}}$ is the velocity of carrier flow and the source terms express the bubble number birth and death rates per unit dispersion volume for bubbles of size d_i at time t due to coalescence and breakage, respectively. The source terms are assumed to be functions of bubble size d_i, bubble number n_i and time t. The birth of bubbles of size d_i due to coalescence happen between all bubbles of size smaller than d_i. Hence, the birth rate for bubbles of size d_i or $B_{agr}(i)$, can be calculated by summing all coalescence events that form a bubble of size d_i. This gives [7]:

$$\overline{B}_{agr}(i) = \sum_{d_j=d_{min}}^{d_i/2} \Omega_{agr}(d_j : d_i - d_j) \qquad \left(\frac{1}{sm^3}\right) \tag{3.65}$$

where d_{min} is the minimum bubble size and depends on the minimum eddy size in the system. The source term definition implies that bubbles of size d_j coalesce with bubbles of size (d_i - d_j) to form bubbles of size d_i. In other words, $\Omega_{agr}(d_j : d_i - d_j)$ represents an individual coalescence event, the bubble of size d_j is coalesced with the bubble of size $d_i - d_j$. The upper limit of the sum stems from symmetry considerations or to avoid counting the coalescence between the same pair of bubble sizes twice.

Similarly, the death of bubbles of size d_i due to coalescence originates from coalescence between two bubbles in class d_i or between one bubble in class d_i and other bubbles. Hence, the bubble death rate for bubbles of size d_i, D_{agr}, can be calculated by [7]:

$$\overline{D}_{agr}(i) = \sum_{d_j=d_{min}}^{d_{max}-d_i} \Omega_{agr}(d_j : d_i) \qquad \left(\frac{1}{sm^3}\right) \tag{3.66}$$

where d_{max} is the maximum bubble size in the system. The upper limit indicates that the bubble size formed by coalescence will not exceed d_{max}.

The birth of bubbles of size d_i due to breakage derived from the breakage of all bubbles larger than d_i. The breakage birth rate, B_{br}, can be obtained by summing all the breakage events that form the bubbles of size d_i [7]:

$$\overline{B}_{br}(i) = \sum_{d_j=d_i}^{d_{max}} \Omega_{br}(d_j : d_i) \qquad \left(\frac{1}{sm^3}\right) \tag{3.67}$$

The death of bubbles of size d_i due to breakage as result of breakage of the bubbles within this class, writes then:

$$\overline{D}_{br}(i) = \Omega_{br}(d_i) \qquad \left(\frac{1}{sm^3}\right) \tag{3.68}$$

In accordance with the work of Prince and Blanch [64] all the macroscopic source terms determining the death and birth rates could be defined as the product of a collision density and a probability. Thus modeling of bubble coalescence means modeling of a bubble-bubble collision density and a coalescence probability, whereas modeling of bubble breakage means modeling of an eddy-bubble collision density and a breakage probability. Models for the collision densities were derived assuming that the mechanisms of the bubble-bubble and eddy-bubble collisions are analogous to collisions between molecules as in the kinetic theory of gases [7].

Models for the Binary Bubble Coalescence Rate Sink, $\Omega_{agr}(d_i : d_j)$

For the coalescence between bubbles of class, d_i, and bubbles of class, d_j, the binary coalescence rate sink is expressed as [7]:

$$\Omega_{agr}(d_i : d_j) = \omega_{agr}(d_i : d_j) p_C(d_i : d_j) \qquad \left(\frac{1}{sm^3}\right) \tag{3.69}$$

Models for the Bubble-Bubble Collision Density, $\omega_{agr}(d_i : d_j)$

There are various mechanisms of bubble coalescence, Prince and Blanch [64] have considered three mechanisms of bubble collision. Bubbles can collide due to [59]: (i) the random motion in a turbulent flow, (ii) to the different rise velocity and (iii) to the mean shear in the flow field.

A primary cause of bubble collisions is the fluctuating turbulent velocity of the liquid phase. Collision takes place by a mechanism analogous to particle collisions in an ideal gas. The turbulent collision rate proposed by Prince and Blanch [64] for use in the framework of macroscopic population method is given as,

$$\omega^T_{agr}(d_i : d_j) = 0.088\pi n_i n_j (d_i + d_j)^2 \epsilon^{1/3} (d_i^{2/3} + d_j^{2/3})^{1/2} \qquad \left(\frac{1}{sm^3}\right) \tag{3.70}$$

where n_i and n_j are the number density for the bubbles of class i and j, respectively. Additionally, ϵ is turbulent kinetic energy dissipation rate.

Collisions may result from the difference in rise velocities of bubbles of different sizes. The buoyancy collision density $\omega^B_C(d_i : d_j)$ has been expressed by Prince and Blanch [64]:

$$\omega^B_{agr}(d_i : d_j) = n_i n_j \frac{\pi}{4} \left(\frac{d_i + d_j}{2}\right)^2 |\nu_{r,di} - \nu_{r,dj}| \qquad \left(\frac{1}{sm^3}\right) \tag{3.71}$$

where $\nu_{r,di}$ is the rise velocity of the particle.

The third contribution to the collision rate results from laminar shear in the liquid phase. Collisions occur in this situation due to the development of a gross circulation pattern in a reactor at sufficiently high gas rates. This mechanism of collision will not play a significant role at the relatively low gas rates employed. The functional form of the collision rate due to laminar shear is expressed by Prince and Blanch [64]:

$$\omega^{LS}_{agr}(d_i : d_j) = n_i n_j \frac{4}{3} \left(\frac{d_i + d_j}{2}\right)^3 \left(\frac{d\nu_c}{dr}\right) \qquad \left(\frac{1}{sm^3}\right) \tag{3.72}$$

where ν_c is the continuous phase circulation velocity. The term $\frac{d\nu_c}{dr}$ is the average shear rate.

The net coalescence frequency of bubbles of diameter d_i and d_j is then calculated by summing three different bubble collisions as mentioned multiplied by a coalscence efficiency (probablity) [64]:

$$\Omega_{agr}(d_i : d_j) = \left[\omega_{agr}^{T} + \omega_{agr}^{B} + \omega_{agr}^{LS}\right] p_{agr}(d_i : d_j) \qquad \left(\frac{1}{sm^3}\right) \tag{3.73}$$

Each collision cannot result in the coalescence event. Therefore, the definition of coalescence efficiency is required. In order to consider whether a collision leads to coalescence events or not, it is necessary to define a collision efficiency or collision probability. The coalescence probability p_{agr} of Hagesather et al. [65] is written as:

$$p_{agr}(d_i, d_j) = \exp(-C\frac{0.75(1+\eta_{ij}^2)(1+\eta_{ij}^3)^{1/2}}{(\rho_G/\rho_L + 0.5)^{1/2} + (1+\eta_{ij})^3})We_{ij}^{1/2} \tag{3.74}$$

where $C = 0.5$, $\eta_{ij} = \frac{d_i}{d_j}$,$u_{ij} = (u_i^2) + u_j^2)^{1/2}$, $u_i = \beta^{1/2}(\epsilon d_i)^{1/2}$ and β equals 2.05 [66]. In addition, u_i, u_j are bubble velocities and σ is surface tension.

Models for the Macroscopic Breakage Rate Source, $\Omega_{br}(d_i, d_j)$

A breakage density stems from the product of an eddy-bubble collision probability density $\omega_{br,\lambda}^{T}(d_i, \lambda$ and a breakage efficiency $p_{br}(d_i : d_j, \lambda)$, which both depends on the eddy size (λ) [7].

The individual rate breaking a parent bubble of size d_i into the daughter size classes d_j is expressed as [7]:

$$\Omega_{br}(d_i : d_j) = \int_{\lambda_{min}}^{d} \omega_{br}^{T}(d_i, \lambda) p_{br}(d_i : d_j, \lambda) d\lambda \qquad \left(\frac{1}{sm^3}\right) \tag{3.75}$$

The eddy-bubble collision probability density $\omega_{br}^{T}(d_i, \lambda)$ has units $(1/sm^3[m])$. The upper integration limit for the eddy size is based on the model assumption that only eddies of size smaller than or equal to the bubble diameter can cause bubble breakage [67].

The breakage density of one particle of size d_i that breaks into particles of sizes d_j and $(d_i^3 - d_j^3)^{1/3}$ is given by [67]:

$$\Omega_{br}(d_i : d_j) = 0.861\alpha_L n_i (\frac{\epsilon}{d_i^2})^{\frac{1}{3}} \int_{\xi_{min}}^{1} \frac{(1+\xi)^2}{\xi^{11/3}} Exp(-\frac{12 c_f \sigma}{2\rho_L \epsilon^{2/3} d_i^{5/3} \xi^{11/3}}) d\xi \tag{3.76}$$

The increase energy in the surface area is obtained by:

$$c_f = f_{BV}^{2/3} + \left(1 - f_{BV}^{2/3}\right)^{2/3} - 1 \tag{3.77}$$

where f_{BV} is breakage volume fraction which equals to $\frac{\nu_j}{\nu_i}$, ξ is the ratio of eddy size to bubble size (dimensionless eddy size) when a bubble splits into two equal bubbles, f_{BV} amounts to 0.5 [67]. This expresses the breakage rate of sizes d_j which splits into d_i and $d_j - d_i$, $\xi_{min} = \frac{\lambda_{min}}{d}$, $\frac{\lambda_{min}}{\lambda_d} = 11.4 - 31.4$.

In this model no probability density is required, and it could be written as [68, 69]:

$$\begin{aligned}\Omega_{br}(d_i : d_j) = -\frac{18}{11}\frac{0.923\alpha_L\alpha_G f_i}{\pi b^{8/11} d_j^3}\left(\frac{\epsilon}{d_j^2}\right)^{1/3}\left(\Gamma(8/11, t_m) - \Gamma(8/11, b) + 2b^{3/11}\right. \\ \left.(\Gamma(5/11, t_m)\Gamma(5/11, b)) + b^{6/11}(\Gamma(2/11, t_m) - \Gamma(2/11, b))\right)\end{aligned} \tag{3.78}$$

where

$$b = \frac{12 c_f \sigma}{2\rho_L \epsilon^{\frac{2}{3}} d_j^{5/3}} \tag{3.79}$$

$$t_m = b(\xi_{min}/d_j)^{-11/3} \tag{3.80}$$

In above equations, terms which include t_m in the gamma function could be neglected when the flow regime corresponds high Reynolds number flows [70].

$$Re = high \longrightarrow t_\infty \simeq \infty$$

CHAPTER 4

Methodology

4.1 Introduction

The main core of the current work is about the investigation of appropriate mathematical set of equations concerning fluid flow, population balance and mass transfer. The governing equations are usually complex partial differential equations. This section expresses the methodology which was followed to solve the mathematical equations and validate the developed model. Basically, it indicates which set of methods could be implemented to reach the specific goal. The methodology of the project is split into four divisions: 1 - Theoretical modeling, 2 - Computational Fluid Dynamic, 3 - Algorithm and 4 - Software.

4.2 Theoretical modelling

In mathematical modelling, each term of the equations has a special meaning for the description of the system characteristics. In our case, the governing equations consist of continuity equation, Navier-Stokes multi-phase flow equations (two-fluid), k-epsilon equations, mass transfer equations and population balance equations. The whole set of equations describes the physical behaviour of our system.

4.3 Computational Fluid Dynamic (CFD)

The differential equations of momentum, mass transfer, and population balance in this study, form a system of coupled non-linear partial elliptic differential equations. The equations have no known general analytical solution. The equations can, however, be discretized and solved numerically. The advent of high-speed, large-memory computers, the evolution of precise numerical algorithm, and developments in complex flow phenomena have enabled

CFD to obtain numerical solutions of flows of industrial interests. CFD obtains numerical solution through three steps: discretization of the flow domain, discretization of the partial differential equations, and solving of an algebraic system of equations that results from the discretization process. Of the solution used in CFD codes, the Finite Volume Method (FVM) and Finite Element Method (FEM) are the most common. The flow domain is divided into small subregions known as control (finite) volumes in FVM and very small but finite-sized elements in FEM. FVM and FEM use a systematic numerical method for solving PDEs and are usually applied for irregular and complex CAD geometries. However, the mathematics behind the finite-element method is massive and thus its implementation is difficult.

The finite volume method uses the integral form of the conservation equations. Integration is carried out for each finite or control volume (CV). Therefore, FVM is based on the fact that many physical laws are conservation laws. This requires approximation of surface and volume integrals. The surface integration process requires values of variables at one or more faces and/or corners. Since variables are evaluated and stored at the centre of each CV or cell, methods of interpolating values of variables at faces or corners from the CV centers are required [71].

4.3.1 Finite Volume Method (FVM)

This section describes briefly the fundamentals of the finite volume discretisation. The technique has been explained by many authors [40, 71–74] and is applied in the current thesis. The Finite Volume Method is an adequate choice to discretize the complex Partial Differential Equations (PDE) of applications involving fluid flow and heat and mass transfer. In the field of CFD, Finite Volume Method (FVM) is more popular because of these following reasons [74]:

– Conservative: some of the terms in the conservation equation are turned into face fluxes and evaluated at the finite volume faces. Because the flux entering a given volume is identical to that leaving the adjacent volume, the FVM is strictly conservative.

– Adaptable to complex geometry: FVM can be formulated in the physical space on unstructured polygonal meshes.

– Easy implementation of boundary conditions: the unknown variables are evaluated at the centroids of the volume elements, not at their boundary faces.

The general transport equation is the starting point to explain the FVM [71],

$$\underbrace{\int_{V_P} \frac{\partial \rho\phi}{\partial t} dV}_{\text{temporal derivative}} + \underbrace{\int_{V_P} \nabla \cdot (\rho \mathbf{U} dV)}_{\text{convective term}} - \underbrace{\int_{V_P} \nabla \cdot (\rho \Gamma_\phi \nabla \phi \; dV)}_{\text{diffusion term}} = \underbrace{\int_{V_P} S_\phi(\phi) dV}_{\text{source term}} \tag{4.1}$$

The goal is to solve the general transport equation for the transported quantity ϕ in a given domain, with given boundary conditions and initial conditions. Next, the solution domain is divided into arbitrary control volumes such as the one illustrated below.

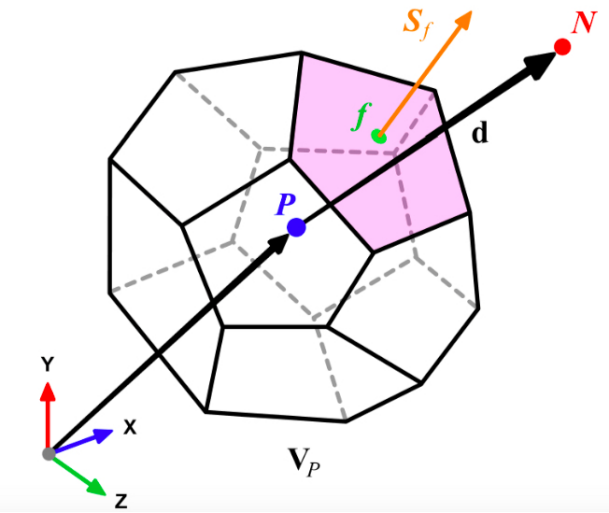

Figure 4.1 An arbitrary control volume in finite volume method

In the control volume illustrated, the centroid is given by

$$\int_{V_P} (x - x_P) dV = 0 \tag{4.2}$$

In the same way, the centroid of face f is given by

$$\int_{S_f} (x - x_P) dS = 0 \tag{4.3}$$

If the Gauss's theorem is used [71]:

$$\int_{V_p} \nabla \cdot a dV = \oint_{\partial V_p} d\mathbf{S}.a \tag{4.4}$$

where ∂V_P is a closed surface bounding the control volume V_P and dS represents an infinitesimal surface element with associated normal $\mathbf{n}$ pointing outward of the surface ∂V_P.

Notice that

$$\mathbf{n}dS = d\mathbf{S} \tag{4.5}$$

Integrating in space each term of the general transport equation and using Gauss theorem, yields to the following discrete equations for each term [71]:

Convective term:

$$\underbrace{\int_{V_P} \nabla \cdot (\rho \mathbf{U} dV)}_{\text{convective term}} = \underbrace{\oint_{\partial V_P} d\mathbf{S} \cdot (\rho \mathbf{U} \phi)}_{\text{convective flux}} = \sum_f \int_f d\mathbf{S} \cdot (\rho \mathbf{U} \phi)_f \approx \sum_f \mathbf{S}_f \cdot (\rho \mathbf{U} \phi)_f \tag{4.6}$$

Diffusion term:

$$\underbrace{\int_{V_P} \nabla \cdot (\rho \Gamma_\phi \nabla) dV}_{\text{diffusion term}} = \underbrace{\oint_{\partial V_P} d\mathbf{S} \cdot (\rho \Gamma_\phi \nabla \phi)}_{\text{diffusion flux}} = \sum_f \int_f d\mathbf{S} \cdot (\rho \Gamma_\phi \nabla \phi)_f \approx \sum_f \mathbf{S}_f \cdot (\rho \Gamma_\phi \nabla \phi)_f \tag{4.7}$$

Source term:

$$\int_{V_P} S_\phi(\phi) dV = S_c V_P + S_P V_P \phi_P \tag{4.8}$$

According to "negative-slope linearization of the source term" rule, the coefficient S_p must always be less than or equal to zero.

Gradient term:

$$(\nabla\phi)_P = \frac{1}{V_P}\sum_f (\mathbf{S}_f\phi_f) \tag{4.9}$$

Temporal term:

$$\int_{V_P} \frac{\partial\rho\phi}{dt} dV = \left(\frac{\partial\rho\phi}{\partial t}\right)_p V_p \tag{4.10}$$

As was mentioned, variables are computed and stored at the centroid of the control volumes. The face values appearing in the convective and diffusive fluxes have to be computed by some form of interpolation from the centroid values of the control volumes at both sides of face f.

4.3.2 Interpolation schemes (convective flux)

Linear interpolation

The linear interpolation scheme is also known as central differencing and it is second order accurate [40]. However, it may generate oscillatory solutions (unbounded solutions). The face values appearing in the convective flux can be computed as follows:

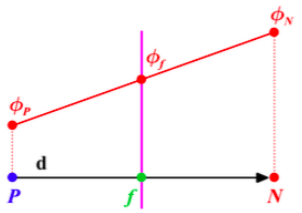

$$\phi_f = f_x\phi_P + (1 - f_x)\,\phi_N$$

$$f_x = \frac{fN}{PN} = \frac{|\,\mathbf{x}_f - \mathbf{x}_N\,|}{|\,\mathbf{d}\,|}$$

Figure 4.2 A simple schematic of linear interpolation scheme

Upwind scheme

This type of interpolation scheme is known as upwind differencing and it is first order accurate [40, 75]. This scheme is bounded but it causes numerical diffusion problem. Numerical diffusion means the gradients of the scalar variable through computational domain is smoothed and the resolution is not very accurate.

The face values appearing in the convective flux can be computed as follows:

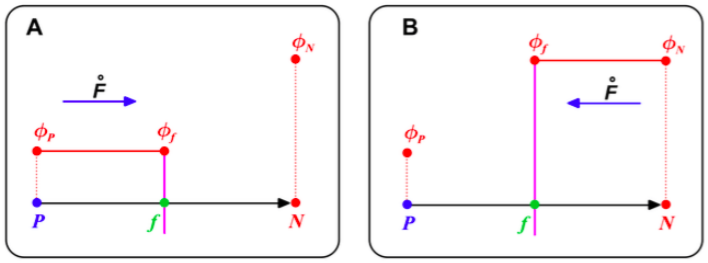

$$\phi_f = \begin{cases} \phi_f = \phi_P & \text{for} \quad \mathring{F} \geq 0, \\ \phi_f = \phi_N & \text{for} \quad \mathring{F} < 0. \end{cases}$$

Figure 4.3 A simple schematic of upwind interpolation scheme

4.3.3 Interpolation schemes (diffusion flux)

The face values appearing in the diffusive flux depends on mesh quality (Fig.4.4). Mesh quality is described using following factors [76]:

1. orthogonal mesh:
   a central difference approximation of the first order derivative is employed. This type of approximation is second order accurate.
2. non-orthogonal mesh
   In this case, the approach consists of orthogonal contribution and non-orthogonal contribution. This type of approximation is second order accurate but involves a larger truncation error. It also uses a larger numerical stencil [1], which makes it less stable. The face gradient of the non-orthogonal contribution is computed by using

1. Stencil is a geometric arrangement of a nodal group following a numerical approximation routine

linear interpolation from the gradient of the control volumes centroid, computed using Gauss theorem.

3. skew mesh

   In the case of a skew mesh, a correction should be introduced in order to maintain second order accuracy and avoid unboundedness.

   Generally, in order to maintain second order accuracy, and to avoid unboundedness, we need to correct non-orthogonality and skewness errors by using mesh refinement. Hexahedral mesh generation can be a solution to minimize the non-orthogonality and skewness errors.

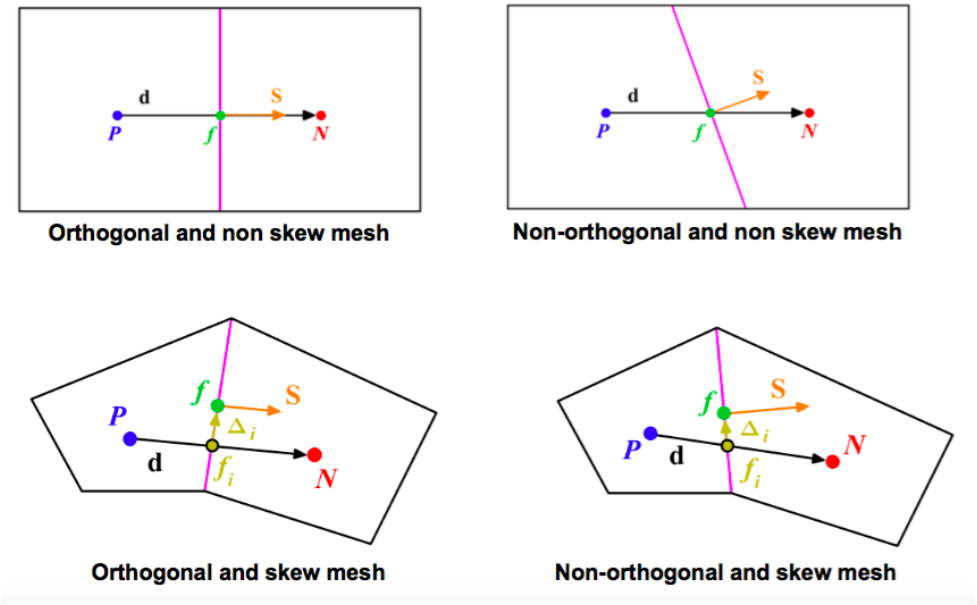

Figure 4.4 A schematic of the criteria concerning on mesh quality

4.3.4 Linear algebraic equations

The semi-discrete general transport equation is rewritten as follows:

$$\left(\frac{\partial \rho\phi}{\partial t}\right)_P V_P + \sum_f \mathbf{S}_f \cdot (\rho \mathbf{U}\phi)_f - \mathbf{S}_f \cdot (\rho\Gamma_\phi \nabla\phi)_f = S_C V_P + S_P V_P \phi_P \tag{4.11}$$

The semi-discrete general transport equation is evaluated in time as follows:

$$\int_t^{t+\Delta t}\left[\left(\frac{\partial \rho\phi}{\partial t}\right)_P V_P + \sum_f \mathbf{S}_f \cdot (\rho \mathbf{U}\phi)_f - \mathbf{S}_f \cdot (\rho\Gamma_\phi \nabla\phi)_f\right] dt = \int_t^{t+\Delta t} (S_C V_P + S_P V_P \phi_P) dt \tag{4.12}$$

At this stage, we can use any time discretization scheme, e.g., Crank-Nicolson, Euler implicit, forward Euler, backward differencing, Adams-Bashforth.

After spatial and temporal discretization by using Eq.4.12, in every control volume V_P of the domain, a system of linear algebraic equations for the transported quantity ϕ is assembled which can be solved by using any iterative or direct method.

4.3.5 Algorithm

The models described in the present work were solved using the OpenFOAM library. Two-fluid model and single-phase flow libraries in OpenFOAM (twoPhaseEulerFOAM, reactingtwoPhaseEulerFoam and pimpleFoam) were customized in order to couple the PBE approaches to the two-phase flow model for simulation of bubbly flows in bubble columns and oxygen absorption in gas-liquid stirred tank, and to the single-phase flow model (dilute system) for simulation of an electrochemical cell. The equations are solved iteratively, relying on the semi-implicit PIMPLE (merged PISO-SIMPLE) approach provided by OpenFOAM, which is a combination of the PISO (Pressure Implicit with Split Operator) and SIMPLE (Semi Implicit Method for Pressure Linked Equations) procedures (Fig.4.5).

4.4 Software

4.4.1 SALOME

SALOME is an open-source software which enables Foam users to use a generic platform for Pre-and Post-Processing in numerical simulation. It relies on an open and flexible architecture made of reusable components. In fact, the CAD geometry could be programmed integrating with Python console in Salome. The SALOME is distributed under the terms

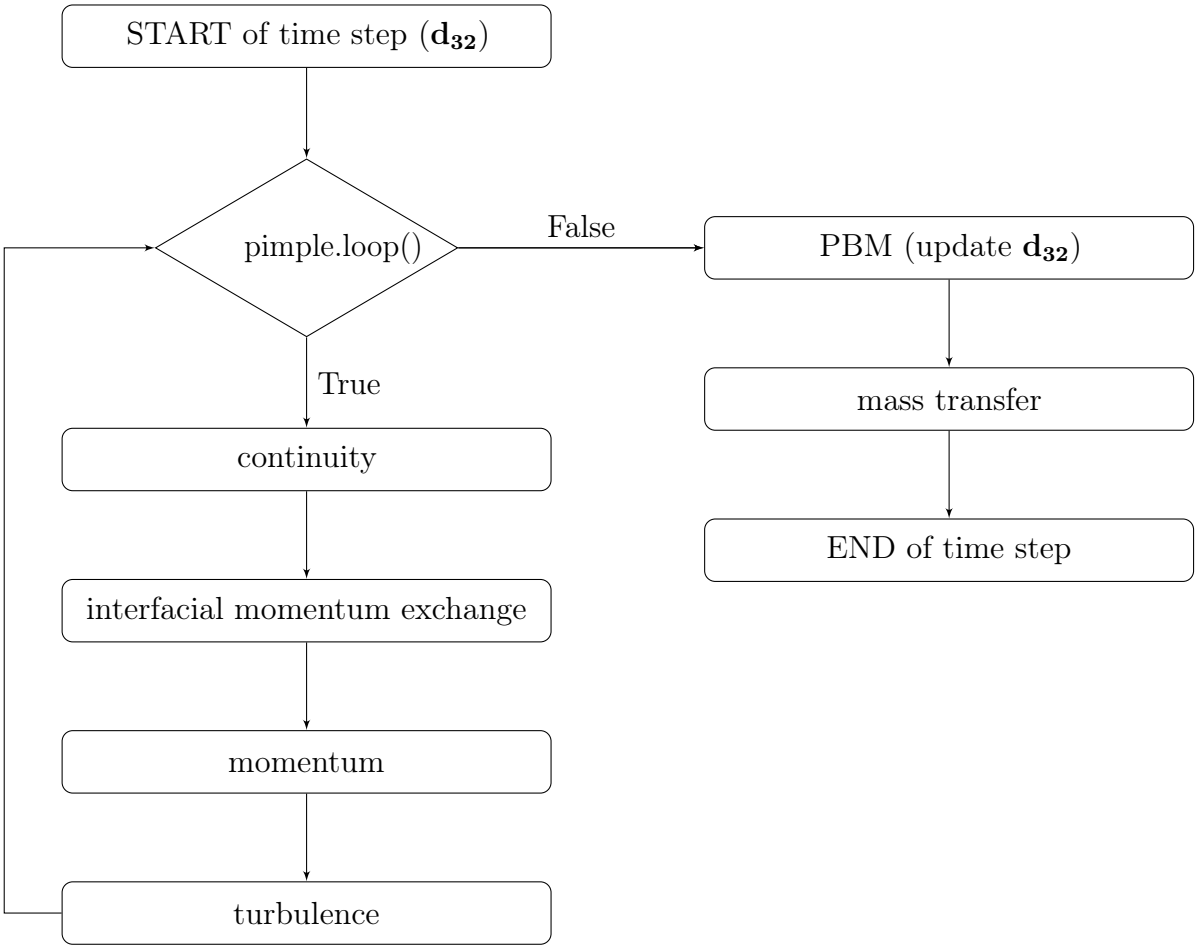

Figure 4.5 Solution algorithm in the OpenFOAM solver

of the GNU General Public License (GPL) license. Salome can be used as software for drawing the CAD geometry and mesh generation (structured and unstructured) for flow domain [77].

4.4.2 OpenFOAM

OpenFOAM as user

The use of the OpenFOAM tool for Computational Fluid Dynamic (CFD) is widely spread across industrial and academic environments. Compared to using propriety CFD codes, the advantage of using OpenFOAM lies in the Open-Source General Public License (GPL) which allows the user to freely use and freely modify a modern advanced CFD code [76].

The information with their path directories which can be given to OpenFOAM, are briefly as follows:

1. Mesh information: **constant/polyMesh**
2. Boundary conditions and initials conditions: **0/**
3. Physical properties (e.g. density, gravity, diffusion coefficient, viscosity, etc): **constant/**
4. Physics involve (e.g. turbulence modeling, mass transfer, etc): **constant/** and/or **system/**
5. Spatial and temporal schemes (accumulation, diffusive,convective, gradient and source terms): **system/fvSchemes**
6. Solution of the linear system of discrete algebraic equations: **system/fvSolution**.
7. Set runtime parameters and general instructions on how to run the case (such as time step and maximum CFL number): **system/controlDict**.
8. Additionally, we may set sampling and functionObjects for postprocessing. This information is contained in the specific dictionaries contained in the directory **system/**

OpenFOAM as programmer

Basically, OpenFOAM is a C++ library. Users can create new solvers with some knowledge of programming and physics of the problem. OpenFOAM source code includes many precompiled libraries. The core of OpenFOAM source code is in *src* directory which

contains the source code for all the libraries, and is divided in different subdirectories each of them with several libraries. In order to understand these libraries and the remainder OpenFOAM code, it is necessary to know C++ concepts such as inheritance, classes, typedefs, templates, namespaces, etc.

The developed solver of the current thesis is on the basis of original OpenFOAM 4.0 solver called: **twoPhaseEulerFOAM** which is a solver for two-phase problems. This solver as well as bubbleFoam is based on the PhD thesis of Henrik Rusche [19]. **twoPhaseEulerFoam** is based on the PIMPLE algorithm.

lookupObject() is allocated to establish the link between population balance library and other libraries of the solver. The **lookupObject()** method is templated since we can register anything with the mesh. Thus, at compile-time the method and the compiler do not know exactly which data types it is going to handle. The templated method is implemented once for the template parameter, and when we use the method, we simply replace the template parameter with the actual type, as in **lookupObject<volScalarField>("p")**. The compiler then does the rest of the work and generates the appropriate code. We could resolve this issue without templates by using function overloading at the price of massive code duplication and poor maintainability.

Calibration and Development of QMOM

As first step, the QMOM approach is implemented as a separated library **diameterModel** through the original solver of OpenFOAM "**twoPhaseEulerFOAM**". The calibration of the solver is based on case 1 used in [44] concerning the constant breakage and aggregation kernels, symmetric fragmentation and 3 nodes (Fig.4.6).

4.4.3 blockMesh

blockMesh generates block-structural hexahedral meshes which are then converted into the arbitrary unstructured format of OpenFOAM. Generating grids with **blockMesh** for complex geometries is often a very tedious and difficult task and sometimes impossible. Therefore, only simple meshes are typically generated using **blockMesh**.

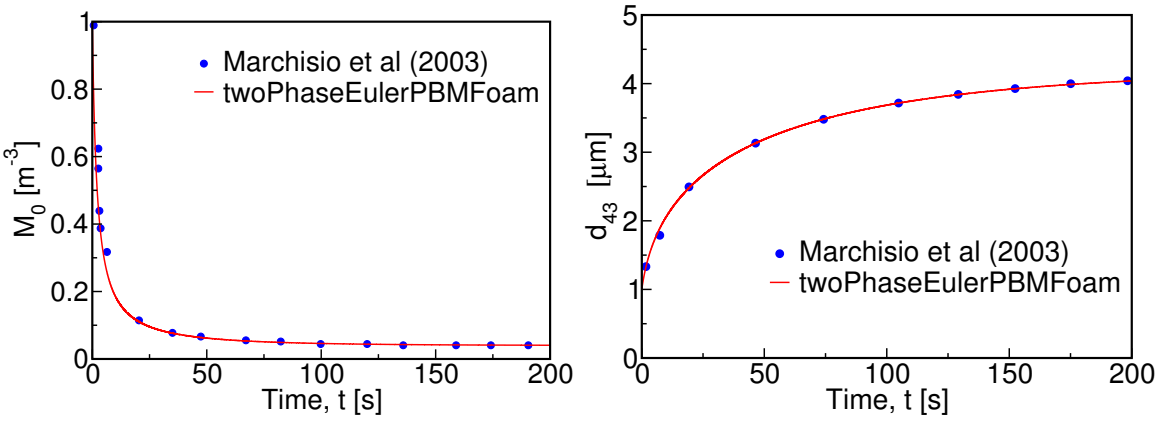

Figure 4.6 (a) Total particle number density (m_0) and (b) mean crystal size evolution (d_{43}) obtained with the rigorous solution (Marchisio et al. [44]) and QMOM approximation developed in the OpenFOAM solver for the zero-dimension case.

4.4.4 snappyHexMesh

snappyHexMesh, also referred to as snappy, is a meshing tool that is able to mesh the space around an arbitrary triangulated surface, e.g. an STL surface-mesh. snappyHexMesh can only be used in conjunction with blockMesh, since it requires a background mesh. With **snappyHexMesh**, hexa-dominant meshes can be generated easily, needing only two things: a hexahedral background mesh and secondly one or more geometries in a compatible surface format (e.g. STL) [76].

4.4.5 Python

Python is an interpreted, high-level, general-purpose programming language widely available on all commonly used platforms. In this project, some parts corresponding to post-processing have been accomplished using **Python**.

4.4.6 OpenQBMM

Turbulent multiphase flows can be described by solving a generalized population balance equation, whose unknown is the number density function (NDF). To reduce the computational cost, transport equations are obtained for the moments of the NDF. These equations are closed using Gaussian quadrature formulae, which allow the calculation of the source terms in the moment transport equations. OpenQBMM [78] allows the NDF to be reconstructed either with a weighted sum of Dirac delta functions or of non-negative kernel density functions, in case a continuous form of the approximate NDF is desired for accuracy.

In this work, the implementation of the EQMOM approach into the open-source toolbox for computational fuid dynamics (CFD) OpenFOAM is achieved by Open Quadrature-based Moment Methods (OpenQBMM) [78].

Calibration and Development of EQMOM

The EQMOM approach is implemented as a separated library **diameterModel** through the link between the original solver of OpenFOAM "**twoPhaseEulerFOAM**" and OpenQBMM. The calibration of the solver is based on case 1 used in [79] concerning on the constant breakage and aggregation kernels, symmetric fragmentation, 3 primary nodes and 20 secondary nodes (Fig.4.7).

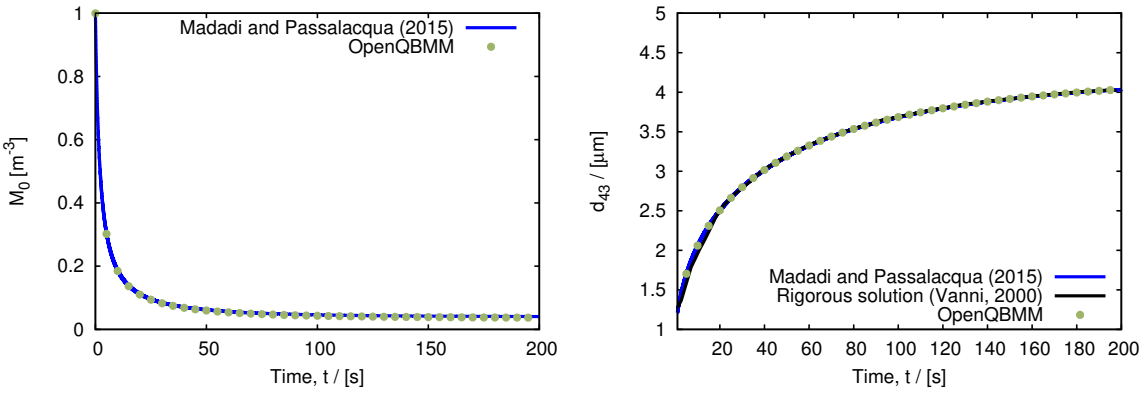

(a) (b)

Figure 4.7 (a) Total particle number density (m_0) and (b) mean crystal size evolution (d_{43}) obtained with the rigorous solution ([79]) and EQMOM approximation developed in the OpenFOAM solver for the zero-dimension case.

4.4.7 Paraview

Paraview is open-source, multi-platform data analysis and visualization application. ParaView can be used as Post-Processing toolkit in order to examine and visualize data which is resulted from OpenFOAM. ParaView uses the visualization Toolkit (VTK) as the data processing and rendering engine and has a user interface written using Qt [80].

4.5 Equipments

One of the most necessary tools for a numerical simulation project is availability to high-performance computers. Moreover, to confirm the simulated data, the presence of the comprehensive experimental data plays a vital role to reach the final goals of the project. For these aims, following equipments are needed:

4.5.1 Mammouth parallel 2

The current project is extremely computer extensive because there are numerous complex partial differential equations. The number of mesh will also be enormous because the CAD geometry is huge. Additionally, several simulations should be performed in order to investigate the mesh dependency, simulate various cases with different operational conditions and optimize the reactor. The researches of the Sherbrooke University has the chance to operate with *Mammouth Parallel 2* supercomputer which belongs to *Calcul Quebec*. Mammouth super computer possess 39168 CPU cores, 1588 SGIC2112-4G3, 20 SGIH2106-G7 and 2 SGIH2106-G7 compute nodes. The operating system of Mammouth is CentOS 6.4, the theoretical peak performance of the system is 240.3 TFLOP/s and the total memory of the system is 57.6 TB [81].

4.5.2 Prototype and equipments of collecting data

The major concern of each CFD project is to get access to the experimental data because if the model is not validated with reliable data, the performed simulations will not have any credibility, academically. In the current work, the relevant experimental data were extracted from the literature and some of them including oxygen concentration evolution in mixer tank were obtained in the laboratory.

CHAPTER 5

Hydrodynamic Study of a Water Electrolysis Reactor Using CM

5.1 Avant-propos

Auteurs et affiliation :

Ehsan Askari : Étudiant au doctorat*

Pierre Proulx : Professeur*

* Université de Sherbrooke, Faculté de Génie, Département de Génie Chimique et de Génie Biotechnologique

Titre français :

Étude hydrodynamique d'une cellule électrolytique avec une approche eulérienne couplée avec un modèle de bilan de populations.

Contribution au document :

Dans cet article, un modèle CFD-PBM est proposé pour prédire la distribution de la taille des bulles dans un réacteur d'électrolyse de l'eau appelé électrode à disque rotatif inversé (IRDE).

Résumé français :

Les écoulements gaz-liquide sont communs dans les appareils électrochimiques. Ces écoulements sont par exemple présents dans un réacteur électrolytique qui vise à séparer l'hydrogène et l'oxygène de l'eau. Un réacteur électrolytique est composé de deux électrodes possédant une différence de potentiel, une cathode et une anode, connectées par de l'eau saline. Les électrodes utilisées pour de l'électrolyse de l'eau sont de type "Gas-evolving". Cela signifie qu'à la surface de ce type d'électrodes, les bulles de gaz sont générées par une réaction électrochimique hétérogène. Les gaz produits, l'hydrogène et l'oxygène, sont donc des produits secondaires de la réaction. Pour produire et optimiser de nouveaux réacteurs électrochimiques, il est nécessaire d'étudier le comportment des bulles et l'évolution de

leurs propriétés dans le temps et l'espace. Dans les écoulements de deux phases, gaz-liquide, la taille des bulles est facilement observable. La taille, le volume et les autres propriétés des bulles peuvent être décrits mathématiquement par des fonctions de distribution. Il est donc possible d'utiliser des outils de modélisation mathématique pour prédire ces propriétés. Les fonctions de distribution sont obtenues avec un programme de résolution numérique implantées dans la boîte à outils de modélisation numérique d'écoulement dynamique (CFD) OpenFOAM. Le programme de résolution numérique utilise des modèles d'équilibre de populations (PBM) couplés à un modèle d'écoulement deux phases Euler-Euler. Les résultats obtenus pour la modélisation d'une électrode à disque inversé (IRDE) sont en accord avec les résultats expérimentaux.

5.2 Hydrodynamic Study of a Water Electrolysis Reactor Using Eulerian Approach Coupled with Population Balance Model

In many electrochemical devices such as water electrolysis reactor, gas-liquid flow exist in the system. A water electrolysis reactor is used to separate electrochemically hydrogen and oxygen from the water molecule. In principle, water electrolysis reactors are composed of two electrodes of sufficient different polarity, cathode and anode, which are conductively connected by water. The electrodes of water electrolysis reactor are gas-evolving types. In such gas-evolving electrodes, gas bubbles are generated by a heterogeneous electrochemical reaction at the surface of the electrode. The produced gases, hydrogen and oxygen, are thus indirect consequences of the reactions. In order to optimize and design new electrochemical reactors, it is necessary to carry out research to predict the bubble behaviour and properties with respect to the time and location, individually. In two-phase flows including liquid and bubbles, it is easily observed that the bubble sizes may vary widely. As a matter of fact, volume, size and other properties of dispersed bubbles can be described mathematically by distribution functions. Therefore, a mathematical modeling tool is required to predict the distribution functions of the bubble motion and variation of their properties. The proposed solver, implemented in the open-source Computational Fluid Dynamic (CFD) package OpenFOAM (Open Source Field Operation And Manipulation), deals with Population Balance Modelling (PBM) coupled to the two-phase flow modelling by an Euler-Euler

approach within an Inverted Rotating Disk Electrode (IRDE). The results were validated showing a good agreement with experimental data and discussed.

5.2.1 Introduction

In the last few years there has been a growing interest in two-phase flows as it can be observed in applied research to various industries such as petroleum, chemical and biotechnology. In presence of two phase flows, the particles dispersed in the continuous phase play an important role in the process. Gas evolving electrodes represent a special case of two phase flow which consider liquid as continuous phase and gas as dispersed phase [50]. In this system, dispersed particles (bubbles) are generated by a heterogeneous reaction. Here, the evolved bubbles at the electrode are responsible for mass transfer enhancement.

Gas evolution at one or both electrodes is a physical process often subsequent to the electrochemical reaction. This event interferes with the electrochemical and physical process at the electrode in several aspects [50]. Gas-evolving electrodes are characterized by the formation of a gaseous phase on the electrode surface during electrolysis as an indirect consequence of the electrochemical reaction [50]. The most important electrochemical industries work with gas evolution electrodes with production of O_2, H_2, Cl_2 and CO_2, but also CO and of gaseous fluorine compounds [50]. The corresponding process is related to many industries such as water electrolysis, the production of chlorine and its inorganic, organic and aluminum compounds. In some of these process the gases are the products, in other cases they are undesired by-products.

Experimental equipments for studying electrochemical reactors, including gas evolution electrodes in electrochemical industries are not provided easily and they are too expensive [50]. Therefore, numerical modelling has been widely considered to predict reactor performance. This provides the opportunity for investigating complex flow problems with having less limitations. CFD combines these advantages and it has been proved to be an important design tool to study transport phenomena in electrochemical reactors [82]. Experimental methods combined with CFD can generate sufficient information with relatively low cost and high speed. A further major advantage of the CFD over experimental methods is its flexibility, as it typically enables changing system geometry and system condition without incurring appreciable cost.

H. van Parys et al. [83] presented two models using Eulerian-Lagrangian approach to simulate the hydrodynamic behaviour of bubbly flow for a gas evolving process. Their models predict the continuous electrolyte phase, while the trajectory of the bubbles is tracked. The diameter of bubbles is formed proportional to the local supersaturation [2]. Maciel et al. [3] reported a new model for gas-evolving electrodes. In their work, the supersaturation of dissolved gas is relied on the gas evolution reaction with using an empirical correlation for current density. They claimed that the model predicts enhanced gas bubble evolution in stagnant zones where the dissolved gas is accumulated.

The gas bubbles, which exist at the nucleation sites, block the electrode and shrink the active surface, while the bubbles that are detached into the electrolyte solution change the conductivity of the electrolyte. Additionally, momentum exchange occurs between the bubbles and the surrounding electrolyte, affecting the motion of solution [3]. The bubbles have a resistive film for electric current flow and also for the ions heading to electrode to participate in electrode reaction.

As one of the process having the gas evolution electrodes, considerable attention has been recently paid to water electrolysis process which is utilized in many applications like electroplating, electrowinning and hydrogen production. One of the first example of two phase flow modelling for water electrolysis reactor composed of gas evolution electrode is presented in [84]. They reported an improved model able to couple the electrical and thermal phenomena with hydrodynamics in the electrolyzer, which was designed a priori for computational optimization of a future pilot cell.

S. Charton et al. [85] investigated the effect of the two-phase parameters associated with hydrogen bubbles production in a filter-press cell. They considered parameters such as electrolyser orientation, forced convection flow and bubbles sizes. Nierhaus et al. [86] provided an hydrodynamic model for Inverted Rotating Disk Electrode (IRDE). By two-way momentum coupling, their Eulerian-Lagrangian model could track hydrogen bubbles produced on cathode. In most cases, such as the results obtained by Charton [85] and Jomard [84], monodisperse bubble size was assumed. However, Nierhaus et al. [86] considered bubble size distribution in their study. A key limitation of their study was the Eulerian-Lagrangian approach. In Eulerian-Lagrangian method, problem arise when the number of dispersed particles is high [19]. The benefit of the Lagrangian approach is the fact that each particle has its own motion equation, and it is relatively comfortable to obtain a distribution of particle sizes. But this approach has limitations. If the system contains many particles (for instance a typical stirred-tank which includes 10^8 particles), the problem will become computationally heavy. On the other side, in case of high phase

fractions (greater than 10 %), the coupling between the particles and the liquid phase can lead to the numerical stability problem [19].

The main challenge is to predict how the number of particles (bubbles) and the time distribution of their sizes, inside an electrochemical reactor, could be predicted by population balance modelling. In order to optimize and enhance the efficiency of the electrochemical reactors, the evolved bubbles should be under control, since the presence has favourable and unfavourable effects, such as a resistive film for the electric current flow and ions supply heading to electrode to participate in electrode reaction. The bubble can also play role as a turbulence promoter and producer of convection over the electrode surface [1]. In case of bubbles evolution, optimization will be possible, when the size and number of bubbles are completely modelled, simulated and then predicted.

In comparison with commercial CFD software, OpenFOAM provides an environment to customize the current solvers to new one which handles the polydispersity of the bubbles. Not only it provides the possibility to modify the existing models with constant bubble size, but special boundary and initial conditions could also be implemented for the proposed problem [87]. However, to the authors' best knowledge, very few publication [1, 3, 4, 83] can be found in the literature that discuss the issue of two phase modelling for prediction of flow pattern in electrochemical cells.

Most of the previous simulation only focused on lagrangian framework [86] which can not be an adequate choice in simulation of industrial electrochemical cells. The literature suffers from the lack of considering the size variation of the produced bubbles provided by Eulerian-Eulerian approach in electrolytic gas evolution. In this study, class method (CM) technique as population balance model is implemented into the existing Euler-Euler two-phase solver (dense system) and single-phase solver (dilute system) of OpenFOAM. The effect of coalescence due to laminar shear rate among evolved bubbles in a water electrolysis reactor is taken into account. The results identify the bubble size distribution of Inverted Rotating Disk Electrode (IRDE).

The paper is organized as follows. First, Inverted Rotating Disk Electrode (IRDE) is described. Then modelling method is explained. After that, modelling results are validated by comparing them to experimental data. The simulation results are presented and discussed afterwards. The paper is ended with few conclusions.

5.2.2 Inverted Rotating Disk Electrode (IRDE)

In order to study gas-liquid flow in electrochemical reactors consisting of gas evolution electrodes, a water electrolysis reactor has been chosen as physical problem for the present work. The purposes of this decision are based on the sake of simplicity and availability of experimental data in literature. It was decided to investigate the Inverted Rotating Disk Electrode (IRDE) proposed by Van Parys et al. [2] which is composed of three electrodes as follows:

1. Reference electrode: Ag/AgCl saturated with KCl
2. Counter electrode: Platinum grid
3. Working electrode (Rotating electrode): made by embedding a platinum rod in an insulating Poly Vinylidene Fluoride (PVFD) cylinder.

The electrolyte is based on 0.1 M Sodium Sulphate (Na_2SO_4) to adjust the $pH = 2.5$. As Fig.5.1 indicates, the counter and reference electrodes are situated in the upper part of the reactor and working electrode is positioned on top of the platinum rod. In fact, the working electrode (rotating electrode) is a circular plate ($D = 4mm$) which is the part of top circular area ($D = 18mm$) in a PVFD cylinder. The reactor is equipped with O-ring in lower part to avoid electrolyte leakage. The device is composed of a waterjacket to keep a constant temperature and control it, as well. When the circuit is closed with the electrodes configuration, and a potential difference is externally operated between the electrodes, electrochemical reactions take place, hydrogen bubbles are evolved in the working electrode (cathode) and oxygen bubbles are generated in the anode. Production of hydrogen bubbles upon cathode causes an unfavourable electrode coverage. To overcome this problem, the reactor has been designed with rotating cathode. The rotation prevents cathode from the bubbles accumulation in its surface due to free rising of bubbles. In other words, the circular movement results in more detachment between particles and cathode. In this study, we put aside the influence of the anode, for the reason that experimental bubble distribution are only available over cathode and hydrogen particles. Consequently, the impact of oxygen bubbles are not taken into account in simulation.

Since the pH of electrolyte solution is 2.5, the half reaction for cathode is:

$$2H^+ + 2e^- \longrightarrow H_{2(g)} \tag{5.1}$$

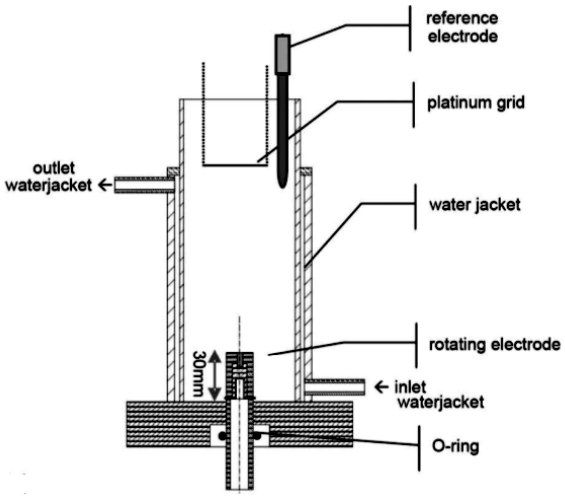

Figure 5.1 Schematic of IRDE reactor [83]

In order to check hydrodynamics, calculation of the mass flux of hydrogen is required. This point is where electrochemical part intersects the hydrodynamic part. Hydrogen mass flux is calculated by measured current density I as follows [86]:

$$\dot{m}_{H_2} = \frac{M_{H_2} I}{n_{H_2} F} = 1.5 \times 10^{-10} \quad \frac{kg}{s} \tag{5.2}$$

where $M_{H_2} = 2.016\ g/mol$ denotes the molecular weight of hydrogen, $F = 96,485\ C/mol$ is the Faraday constant, $n_{H_2} = 2$ expresses the number of exchanged electrons in cathode reaction (Eq.5.1) and $\dot{m}_{H_2}$ mirrors hydrogen mass flux, kgs^{-1}. In the current work, it is assumed that limiting current density is independent of the effect of the bubbles.

5.2.3 Numerical modelling

In this work, two approaches are applied depending on the amount of gas hold-up: 1-single-phase and 2- two-phase. IRDE system is a dilute type due to presence of low gas phase fraction. Therefore, the flow field can be calculated with a single-phase approach to solve population balance equations and reduce the complexity of computation. The developed solver is able to deal with either dilute system (IRDE) or dense system (industrial scale).

Two-phase strategy is implemented using Eulerian-Eulerian (E-E) framework. E-E is utilized in which both the continuous and dispersed phase equations can be defined by using Eulerian conservation equations. This method, which is based on macroscopic equations, is also commonly called "Two-Fluid" approach for two fluid and "Multi-fluid" approach for more than two fluids [19]. The mathematical form of two-fluid equations resemble the single phase Navier-Stokes equations, except for the presence of a term referred to mass and momentum exchange between phases. In the Euler-Euler approach, the different phases behaves as interpenetrating continum [19]. The concept of volume fraction is introduced based on the fact that the volume of a phase cannot be occupied by the other phases. The volume fractions are assumed to be continuous functions of space and time and their summation equals to one [19]. Conservation equations for each phase are expressed to obtain a set of equations which have similar structure for all phases.

Governing equations of fluid flow modeling

The single-phase equations including continuity and momentum in order to apply for dilute system are written as follows:

– Continuity equation (dilute system):

$$\frac{\partial \rho}{\partial t} + \nabla \cdot (\rho \mathbf{U}) = 0 \tag{5.3}$$

– Momentum equation (dilute system):

$$\frac{\partial}{\partial t}(\rho \mathbf{U}) + \nabla \cdot (\rho \mathbf{U}\mathbf{U}) = -\nabla p + \nabla \cdot \bar{\bar{\tau}}_{\text{effi}} \tag{5.4}$$

The Eulerian description of multi-phase flow is not limited to two phases, however, for reasons of simplicity, we limit ourselves to the case of two phases. The continuity and momentum equations for each phase i are given by [19]:

– Continuity equation:

$$\frac{\partial}{\partial t}(\rho_{\text{i}} \alpha_{\text{i}}) + \nabla \cdot (\alpha_{\text{i}} \rho_{\text{i}} \mathbf{U}_{\text{i}}) = 0.0 \tag{5.5}$$

– Momentum equation:

$$\frac{\partial}{\partial t}(\rho_{\text{i}} \alpha_{\text{i}} \mathbf{U}_{\text{i}}) + \nabla \cdot (\alpha_{\text{i}} \rho_{\text{i}} \mathbf{U}_{\text{i}} \mathbf{U}_{\text{i}}) = -\alpha_{\text{i}} \nabla p + \nabla \cdot (\alpha_i \bar{\bar{\tau}}_{\text{effi},i}) + \mathbf{R}_{\text{i}} + \mathbf{F}_{\text{i}} + \alpha_{\text{i}} \rho_{\text{i}} \mathbf{g} \tag{5.6}$$

$$\bar{\bar{\tau}}_{\text{effi},i} = (\mu_{\text{lam},i} + \mu_{\text{t},i}) \left(\nabla \mathbf{U}_i + \nabla \mathbf{U}_i^T \right) - \frac{2}{3} \left(\rho_i k_i + (\mu_{\text{lam},i} + \mu_{\text{t},i}) \nabla \cdot \mathbf{U}_i \right) \bar{\bar{I}} \tag{5.7}$$

– Inter-phase momentum transfer:

Conservation law of momentum transfer for two phase systems dictates zero momentum exchange between phases, i.e. $\sum \mathbf{R}_i = 0$. In E-E approach, the instantaneous inter-phase momentum transfer term is decomposed into its components indicating their different physical meanings:

$$\mathbf{R}_{\text{G}} = -\mathbf{R}_{\text{L}} = \mathbf{R}_{\text{G,drag}} + \mathbf{R}_{\text{G,lift}} + \mathbf{R}_{\text{G,vm}} \tag{5.8}$$

where the subscript G denotes the dispersed phase. Dispersed Phase Element (DPE) is generally applied for bubbles, droplets and particles, and in this case it mirrors the total bubbles. The inter-phase momentum transfer is determined by assembling the forces acting on the DPEs. In DPEs generic term, particles could be refereed to bubbles. $\mathbf{R}_{\text{G,drag}}$, $\mathbf{R}_{\text{G,lift}}$ and $\mathbf{R}_{\text{G,vm}}$ represent the instantaneous drag, lift and virtual mass.

In most two-fluid calculation the following functional forms are utilized:

$$\mathbf{R}_{\text{G,drag}} = \frac{3}{4} \rho_{\text{L}} \alpha_{\text{G}} \frac{C_{\text{D}}}{d_{32}} \mid \mathbf{U}_{\text{G}} - \mathbf{U}_{\text{L}} \mid (\mathbf{U}_{\text{G}} - \mathbf{U}_{\text{L}}) \tag{5.9}$$

$$\mathbf{R}_{\text{G,lift}} = \alpha_{\text{G}} C_{\text{l}} \rho_{\text{L}} \mathbf{U}_{\mathbf{r}} \times (\nabla \times \mathbf{U}_{\mathbf{L}}) \tag{5.10}$$

$$\mathbf{R}_{\text{G,vm}} = \alpha_{\text{L}} C_{\text{vm}} \rho_{\text{L}} \big(\frac{D_L \mathbf{U}_{\mathbf{L}}}{Dt} - \frac{D_G \mathbf{U}_{\mathbf{G}}}{Dt} \big) \tag{5.11}$$

where, $\mathbf{U}_{\mathbf{r}} = \mathbf{U}_{\mathbf{L}} - \mathbf{U}_{\mathbf{G}}$ is the relative velocity, and $\frac{D_i}{Dt}$ stands for the substantive derivative which is defined as:

$$\frac{D_i}{Dt} = \frac{\partial}{\partial t} + \mathbf{U}_{\text{i}} \cdot \nabla \tag{5.12}$$

The coefficient C_D, C_L and $C_{\nu m}$ are usually determined, empirically.

Population Balance Modelling (PBM)

Particles have a huge impact on the flow behaviour of a particular system. The size distribution of secondary phase, which may be constituted of gas bubbles, liquid drops or solid particles, can evolve in conjunction with the transport of the secondary phase in this type of flow system. These evolutionary processes may include a combination of different phenomena such as nucleation, growth, dispersion, dissolution, aggregation or coalescence, and breakage or break-up creating the dispersion [50]. To investigate the effects of particles in the flow, a balance equation based on population balance approach can be considered as more adequate examination of the behaviour of population of particles. Nowadays, the coupling of computational fluid dynamic and population balance models is increasingly utilized to predict how the particles properties, such as size, is distributed. Property distributions of particles helps to improve gas evolution electrodes system [1].

The dispersed phase include the discrete elements. Each element is generally identified by a number of properties known as coordinates. If the coordinates become specified, the elements will be distinguished. There are two kinds of coordinates, internal and external. External coordinates correspond to the spatial status, while internal coordinates correspond to the properties of the elements, for instance, their momentum (or velocities), their enthalpies (or temperatures), their volumes, surface area or sizes [46]. According to the Eulerian-Eulerian approach, the dispersed phase can be explained by the number density function (NDF). The NDF provides information about how the population of elements inside a control volume varies through the proposed properties. The NDF is an average quantity of the dispersed phase. In fact, it has the mathematical feature of an averaged function. It undergoes changes versus time, physical space and internal-coordinate space. In order to study the evolution of the NDF with respect to time, internal-coordinate and physical space, a focus should be given to the population balance equation [46].

$$\frac{\partial n_\zeta}{\partial t} + \nabla_x.(U_p n_\zeta) + \nabla_\zeta.(\dot{\zeta} n_\zeta) = h_\zeta \tag{5.13}$$

where ζ is the internal-coordinate vector, $n_\zeta(\zeta; x, t)$ the expected number of bubbles in a physical volume dx, in the phase-space volume $d\zeta$, U_p the velocity vector for the particular system, $\dot{\zeta}$ the continuous rate of change in the space of internal-coordinate and h_ζ mirrors the discrete events including breakage/break-up and aggregation/coalescence.

In the Eq.5.13, the first term reveals accumulation. The second term shows the net flux of number density because of convection in the physical space. The third term illustrates

convection in the internal-coordinate space. As a matter of fact, bubbles move in physical space because the bubble velocity $U_p = \frac{dx}{dt}$ and in the internal-coordinate space due to a internal-coordinate velocity $\dot{\zeta} = \frac{d\zeta}{dt}$.

The method of classes (CM)

The class method solves the particle number density, directly [47]. In CM, the continuous size range of particles can be realized through the discretization of the particle size distribution into a number of classes of discrete sizes. For each class, the equation of the number density of particles is solved and coalescence and breakup rates are transformed into birth and death rates for each class. The population balance equation for the ith bubble class is represented as:

$$\frac{\partial n_i}{\partial t} + \nabla.(\mathbf{U}n_i) = B_{i_C} - D_{i_C} + B_{i_B} - D_{i_B} \tag{5.14}$$

where n_i is the number of the bubbles from group i per unit volume, $\mathbf{U}$ is the velocity of carrier flow which is obtained by single-phase approach or E-E approaches. B_B and B_C are the birth rates caused by breakup and coalescence, respectively, and D_C and D_B the relevant death rates, from coalescence and break-up, respectively.

The number density is referred to each bubble volume through the gas volume fraction.

$$n_i = \frac{\alpha_i}{\nu_i} \tag{5.15}$$

where ν_i is the volume of class i.

$$\sum \alpha_i = \alpha_G \tag{5.16}$$

where α_a is the volume fraction of the dispersed phase.

To solve population balance equation using the scalars f_i, Eq.5.14 is changed to the following equation:

$$\frac{\partial \alpha_G f_i}{\partial t} + \nabla.(\alpha_G \mathbf{U} f_i) = B_{i_C} - D_{i_C} + B_{i_B} - D_{i_B} \tag{5.17}$$

$$f_i = \frac{\alpha_i}{\alpha_G} \tag{5.18}$$

$$\sum f_i = 1 \tag{5.19}$$

Here, f_i is the bubble volume fraction of group of size i. As Eq.5.17 shows, all particles move with a same velocity **U**. This approach is called by homogeneous MUSIG model (MUlti SIze Group) [51]. The MUSIG model approximates the continuous particle size distribution by a given number of size fraction. If a large range of particles sizes is considered in multiphase flow, the number of conservation equations may become impractical. To overcome the mentioned problem, a simplified class method, based on homogeneous and inhomogeneous MUSIG models, is performed. In a system with substantial large particles, the inhomogeneous MUSIG model developed by Krepper et al. [52] is more feasible. In homogeneous MUSIG model, the whole diameter range of dispersed phase is divided into M size groups and only one common momentum equations is solved for all size groups. Alternatively, in the inhomogeneous MUSIG model the dispersed phase is divided firstly into N velocity groups where each group is characterized by its own velocity field. Furthermore, each velocity group j is divided into a number of sub-size groups M_j, j=1, 2, ... N.

Method of classes calculates the Sauter Mean Diameter L_{32} as follows:

$$L_{32} = \frac{\sum_i f_i}{\sum_i f_i/d_i} \tag{5.20}$$

The Sauter mean diameter represents the average particle size, and it is defined as the diameter of a sphere that has the same volume/surface area ratio as a particle interest. The importance of Sauter mean diameter is relied on active surface area [46].

Bubble coalescence

In this work, only coalescence component of source term in the equation of number density function is taken into account and no breakage event is considered. This assumption is due to presence of small bubbles in the system and laminar regime of the flow. Hence, the source term are as follows:

$$S_i = B_{i_C} - D_{i_C} \tag{5.21}$$

Ramkrishna [47] proposed an approach named as fixed pivot, in order to discretize the source terms of particles. The approach assumes that the population of bubbles is distributed on pivotal grid points x_i with $x_{i+1} = sx_i$ and $s > 1$. Breakage and aggregation may create bubbles with volume ν such that $x_i < \nu < x_{i+1}$. This bubble must be split by assigning respectively fraction γ_i and γ_{i+1} to x_i and x_{i+1}. The following limitations, preserve the number balance and mass balance.

$$\begin{cases} \gamma_i x_i + \gamma_{i+1} x_{i+1} = \nu \\ \gamma_i + \gamma_{i+1} = 1 \end{cases} \tag{5.22}$$

Ramkrishna [47] has also reported the birth in class i due to coalescence in this way:

$$\begin{aligned} B_{i_C} = & \sum_{k=0}^{n} \sum_{j=0}^{n} \left[\theta(x_{i-1} < x_j + x_k < x_i) \times (1 - \frac{1}{2}\delta_{jk}) \right] \\ & \times \gamma_{i-1}(x_j + x_k)\beta(x_k, x_j) \frac{36\alpha_g^2}{\pi^2} \frac{f_j f_k}{(d_j d_k)^3} \\ & + \sum_{k=0}^{n} \sum_{j=k}^{n} \left[\theta(x_i < x_j + x_k < x_{i+1}) \times (1 - \frac{1}{2}\delta_{jk}) \right] \\ & \times \gamma_i(x_j + x_k)\beta(x_k, x_j) \frac{36\alpha_g^2}{\pi^2} \frac{f_j f_k}{(d_j d_k)^3}, \end{aligned} \tag{5.23}$$

where θ is a test function expressed as:

$$\theta(test) = \begin{cases} 0 & \text{test is false} \\ 1 & \text{test is true} \end{cases} \tag{5.24}$$

and

$$\gamma_{i-1}(\nu) = \frac{\nu - x_{i-1}}{x_i - x_{i-1}}; \gamma_i(\nu) = \frac{x_{i+1} - \nu}{x_{i+1} - x_i}$$

The death rates D_{i_C} in class i due to coalescence is defined as follows:

$$D_{i_C} = \frac{36 f_i \alpha_G^2}{\pi^2 d_i^3} \sum_{k=0}^{n} \beta(x_i, x_k) \frac{f_k}{d_k^3} \tag{5.25}$$

The Coalescence model

The third contribution to the collision rate results from laminar shear in the liquid phase. Collisions occur in this situation due to the development of a gross circulation pattern in a reactor at sufficiently high gas rates. This mechanism of collision will not play a significant role at the relatively low gas rates employed. The functional form of the collision rate due to laminar shear is expressed by [64]:

$$\omega_{ij}(d_i : d_j) = n_i n_j \frac{4}{3}(\frac{d_i + d_j}{2})^3 (\frac{d\nu_c}{dr}) \qquad \left(\frac{1}{sm^3}\right) \tag{5.26}$$

where ν_c is the continuous phase circulation velocity. The term $\frac{d\nu_c}{dr}$ is the average shear rate.

5.2.4 Result and Discussion

The use of the OpenFOAM tool for Computational Fluid Dynamic (CFD) is widely spread across industrial and academic environments. Compared to using commercial CFD codes, the advantage of using OpenFOAM lies on the Open-Source General Public License (GPL) which allows the user to use and freely modify a modern advanced CFD code. Single-phase approach (pimpleFOAM) and Two-fluid model (twoPhaseEulerFOAM) in OpenFOAM were customized for coupling two phase flow model and population balance model (CFD-PBM)(Fig.5.2). The new OpenFOAM solver was developed with considering entire governing equations mentioned in modelling part. The new solver was written based on the CM and it allows us to take into account every size distribution function instead of constant size in boundaries of computational field.

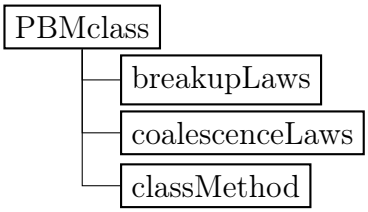

Figure 5.2 Construction of the PBM class implemented in OpenFOAM solver

The developed solver was applied in simulation for the IRDE reactor whose specifications are presented in Fig.5.3. A grid with 34,300 hexahedra yielded sufficiently accurate results for the proposed problem and was selected for the IRDE study (Fig.5.3a). In this system, the cathode which is considered as inlet boundary, and it is rotating. Thus, the velocity was configured in a cylindrical system. Angular component of liquid velocity is according to rotational speed of working electrode (rpm=100 and 250). According to the applied rotational speeds, calculated Reynolds number are less than the critical ones [86]. Hence, the flow regime is laminar which results in neglecting of breakage in population balance model because of $\epsilon = 0$. In the present study, Behzadi and colleague's set of interfacial force

[39] closure were used. First challenge of the study is the gas phase fraction determination because it is produced by electrochemical reaction and there is no sparger to inject the gas. To identify the value of gas phase fraction in inlet, the amount of gas residual on electrode is calculated. Gas residual is the ratio of hydrogen mass flux produced by electrochemical reaction to hydrogen mass flux caused by detached bubbles. This ratio is shown below [86]:

$$\alpha_{H_2} = \frac{\dot{m}_{H_2}}{\pi r_{cyl}^2 u_T \rho_{H_2}} = 0.88 \times 10^{-3} \tag{5.27}$$

where u_T is terminal velocity of rising hydrogen bubbles, $\dot{m}_{H_2}$ obtained by Eq.5.2, r_{cyl} electrode radius and ρ_{H_2} hydrogen density.

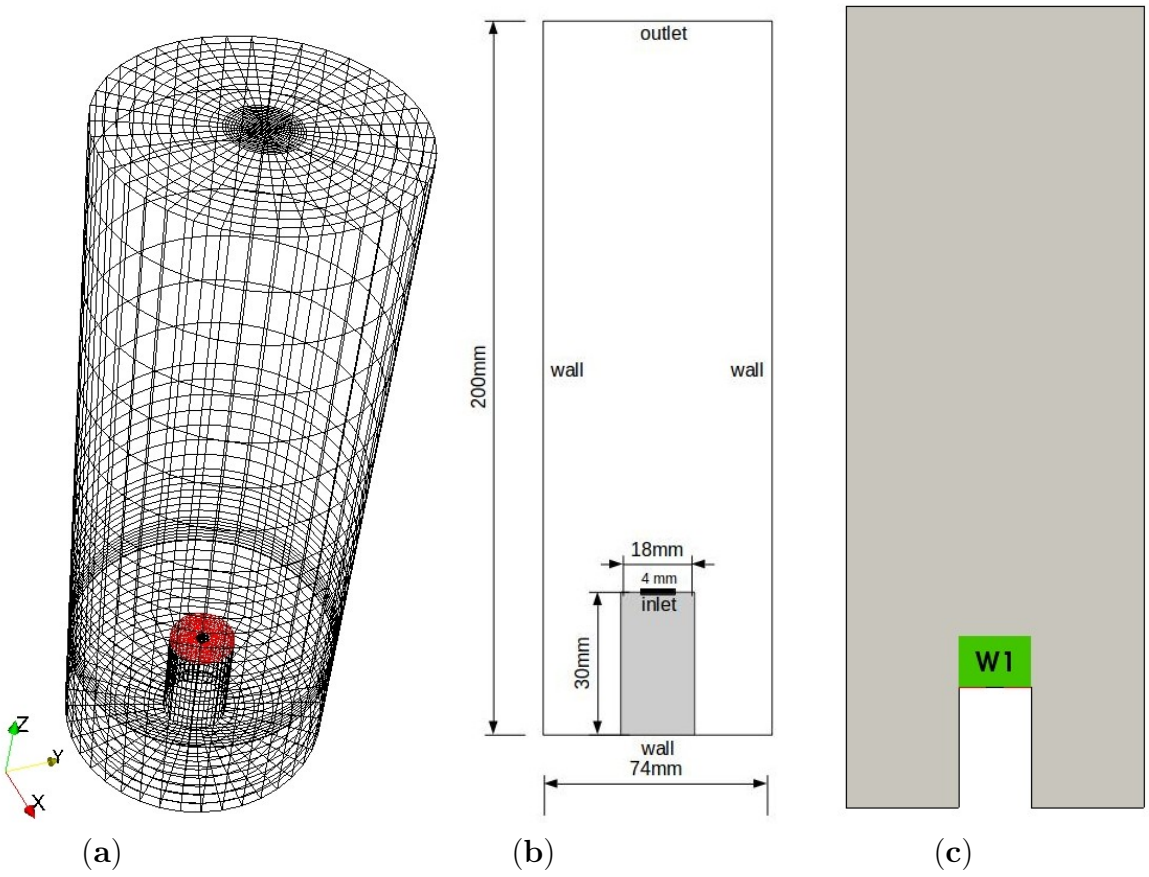

Figure 5.3 (**a**) Schematic of hexahedral mesh. (**b**) The specifications of the reactor and (**c**) the location of volume W1.

Figure 5.4 indicates instantaneous gas phase fraction in three different times through a vertical cut in the middle of the IRDE reactor. As it can be seen from contour plots, a rising bubble plume is gradually generated. To see the transient behaviour of gas phase versus time, the reader is referred to first animation file (video.1).

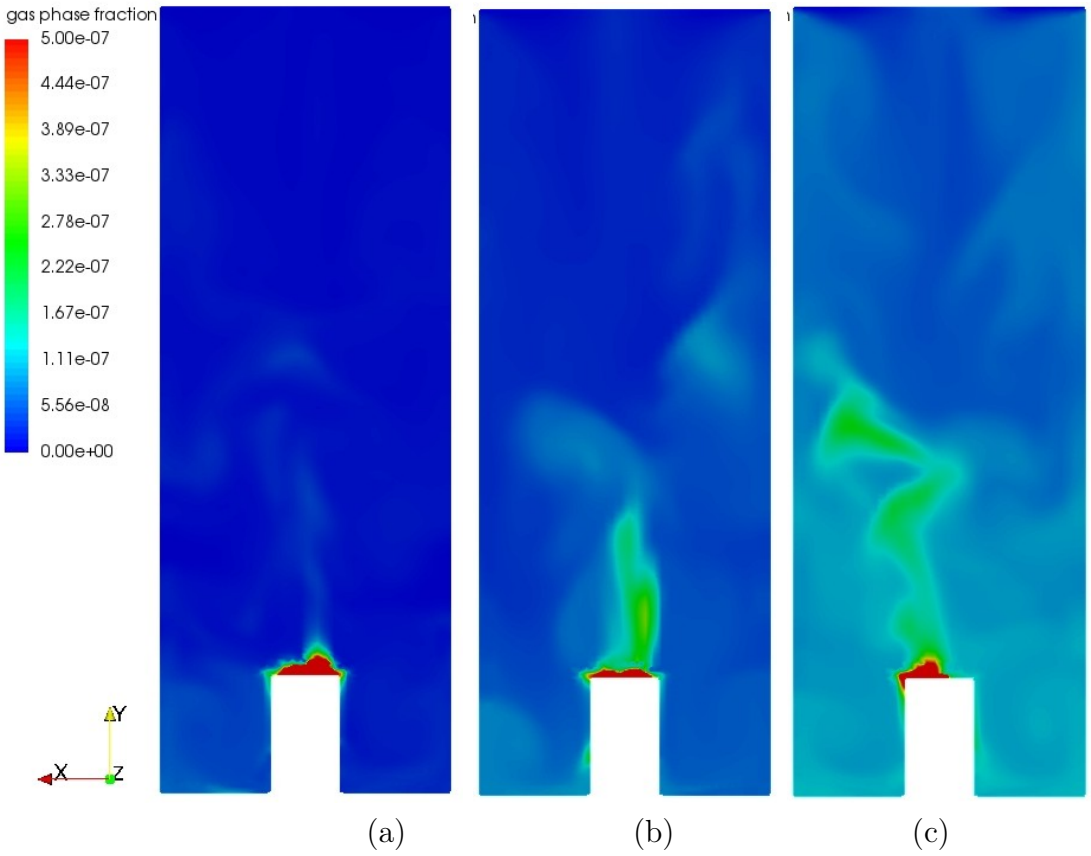

Figure 5.4 Gas phase fraction in vertical cut at (a) t=9s, (b) t=30s, (c) t=60s

As Figure 5.4 illustrates, gas hold-up is extremely low. The bubbles follow the bulk flow and are affected by the continuous phase (water), but not vice versa. Hence, the flow field was calculated with a single-phase solver to reduce the computational effort. The flow field obtained from the single-phase approach was then imported in the population balance solver, in order to advect the bubble size distribution imposed at the inlet and study how bubbles distribute in the IRDE.

A distribution of bubble sizes is observed at the electrodes of the IRDE reactor. For this reason, the continuous distribution function reported by Nierhaus et al. [86] was used in the simulation and imposed at the electrode surface, which is treated as an inlet boundary for the gas phase (Figure 5.5a). Nierhaus et al. [86] reported the experimental bubble size distributions in an optical window (W1) for two different rotating velocities, 100 rpm and 250 rpm. Figure 5.3.c illustrates how the $W1$ volume has been configured in the IRDE reactor. W1 was located above the electrode to enable tracking bubbles in the rising plume.

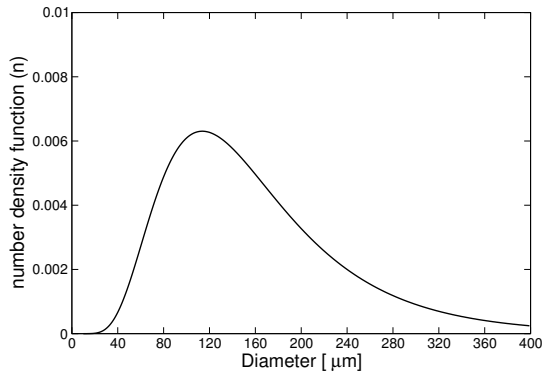

(**a**)

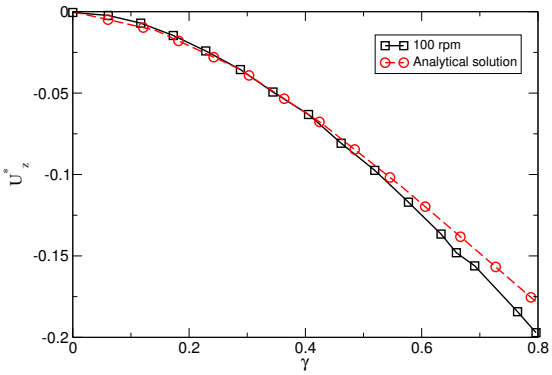

(**b**)

Figure 5.5 (**a**) The continuous distribution function imposed at the electrode surface (Nierhaus et al. [86]); (**b**) mean axial velocity component profile $u_z{}^* = \frac{u_z}{\sqrt{\omega_z \nu}}$ and comparison to the analytical solution.

Figure 5.5b compares the computed axial velocity component profile $u_z{}^*(= \frac{u_z}{\sqrt{\omega_z \nu}})$ as a function of the dimensionless height ($\gamma = \frac{z}{\delta}$) with analytical solution, where δ is the displacement thickness of the fluid boundary layer ($\delta = \sqrt{\frac{\nu}{\omega_z}}$). The comparison shows that the numerical results match with the analytical solution [88] in the region close to the electrode. The confirmed flow field applied in population balance calculations for its NDF consists of the accumulation, convection term (physical space) and coalescence due to laminar shear rate.

To validate the CFD-PBM solver in IRDE, an analysis is applied to investigate the bubble size distribution in volume W1. The comparison of the bubble size distribution between the experimental study and current CFD-PBM using CM (19 classes) is presented in Table 5.1. The results considering log-normal approximation thus match better experimental measurements. The fair agreement confirms the assumptions in the PBM model, particularly for 100 rpm. In fact, since the bubble size is too small (low Stokes number) and no significant

changes are observed between Fig. 5.6 and 5.5a, most of the effect is due to advection, and no considerable segregation occurs.

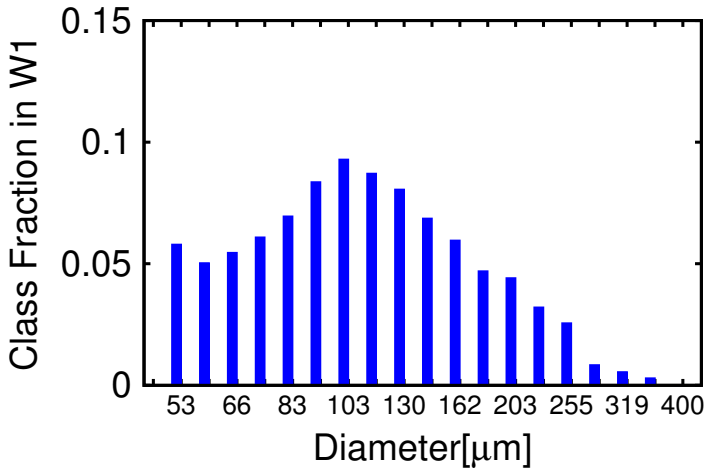

(**a**)

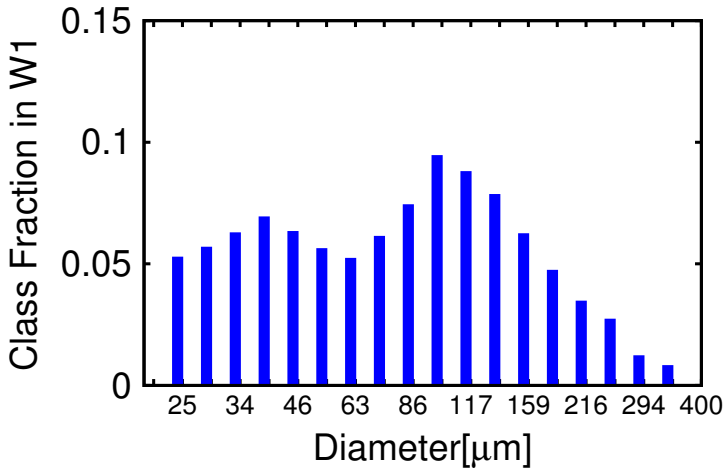

(**b**)

Figure 5.6 Bubble size distribution in W1 for (**a**) CM (19 classes) and rpm = 100; (**b**) CM (19 classes) and rpm = 250.

It can be observed in Table 5.1, for 100 rpm, simulation data match better experimental ones while there is a slight disagreement for higher speed of rotation. The prime causes of the discrepancy is a result of the constant current density I and the neglection of growth effect in number density function. As mentioned, constant value of current density was assumed for the calculation of hydrogen mass flux (Eq.5.2). The variation of current density modifies hydrogen mass flux and consequently, it changes the gas phase fraction above the electrode.

Case	arithmetic				log-normal			
	E	SD	E	SD	μ	σ	μ	σ
	EXP		SIM		EXP		SIM	
100 rpm	145	85	122	58	4.82	0.54	4.7	0.45
250 rpm	153	80	100	65	4.9	0.49	4.4	0.60

Table 5.1 The comparison between experiment and simulation results in terms of arithmetic and log-normal mean and standard deviation (E: arithmetic mean; SD:arithmetic standard deviation; μ: log-normal mean; σ: log-normal standard deviation)

Fig.5.6 depicts with increasing rotational speed from 100 to 250, bubble size distribution moves slightly towards large size of bubbles. This trend is due to the fact that bubble detachment is favored for higher rotation speed and laminar shear rate is increased.

The originality of our simulation lies on the fact that bubble size distribution can be obtained for all regions of the reactor. The most important zone of an electrochemical reactor is usually above the electrodes. As shown in Fig.5.6, the particle size spectrum for W1 can be obtained by the CFD-PBM solver. Regarding to this issue and shape of the plot, a unimodal log-normal distribution function for 100 rpm and bimodal log-normal distribution function for 250 rpm are captured as well as experimental observations [86].

Fig.5.7 shows the small bubbles are dragged away and down. However, a very small amount of large bubbles might be entrained in the downward flow as well as shown in an snapshot of the experiment (Fig.5.7(d)).

If the multiphase approach is considered, the movement trend of each phase can be explained by gas-velocity contour and vector. Figure 5.8 illustrates three dominant zones existing in the IRDE reactor as follows:

1. Downward flow motion (rotation-induced suction).
2. Circulation patterns (rotational movement of the electrode)
3. Upward flow motion (rising bubble plume)

The mere presence of gas-phase results in the creation of a third region. As mentioned earlier, the flow regime is laminar in the system. Thus, the breakage in population balance equation (Eq.5.17) is ignored and only the effect of convective term and coalescence due to laminar shear rate are considered. In other words, the convective and aggregation terms in physical space is the cause of the variation of bubbles size in laminar two phase flows. In

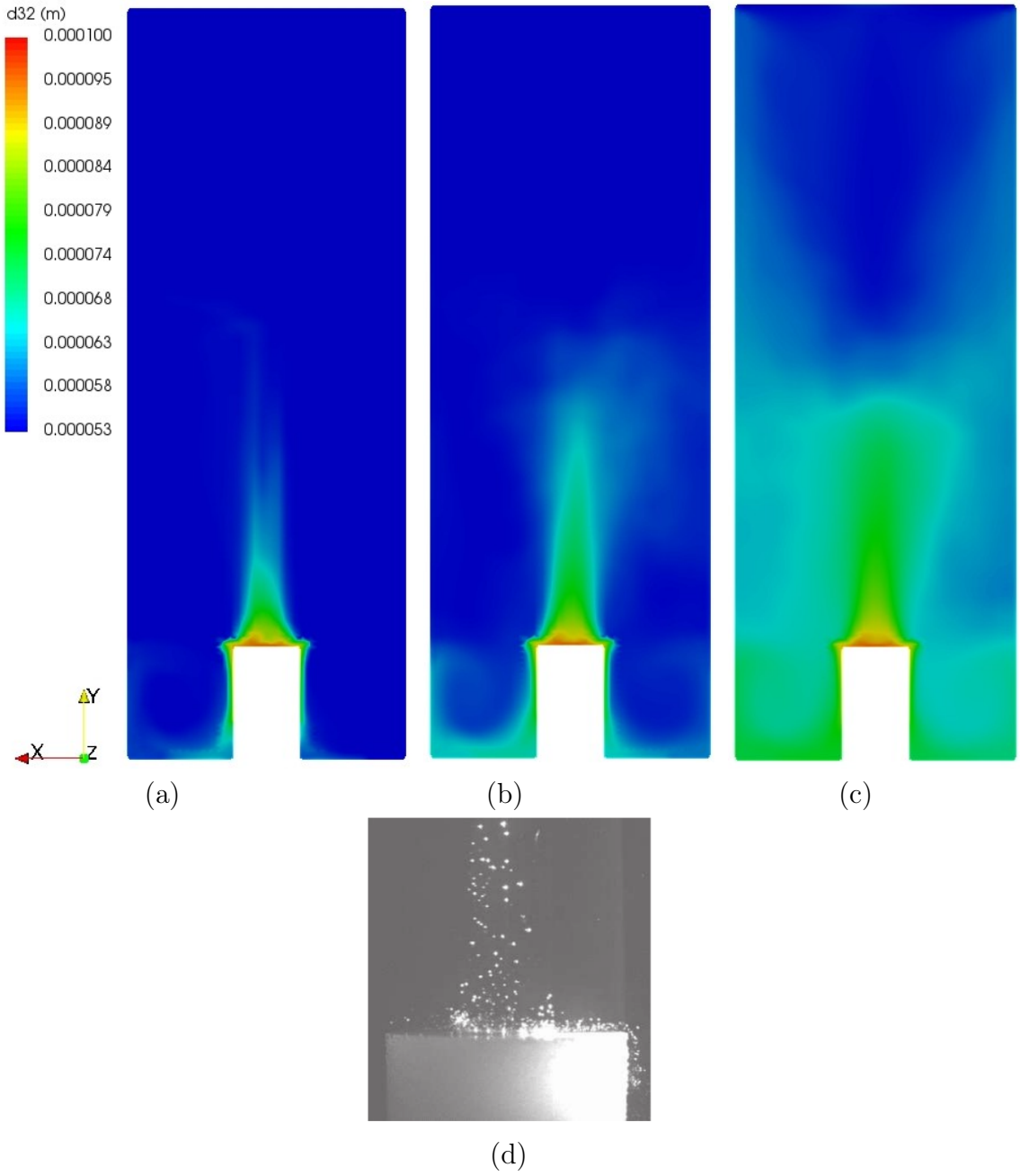

Figure 5.7 Sauter mean diameter at (a) t=9s, (b) t=30s, (c) t=60s

fact, bubble breakage do not exist in the laminar system because there are no eddies able to cause breakage indeed.

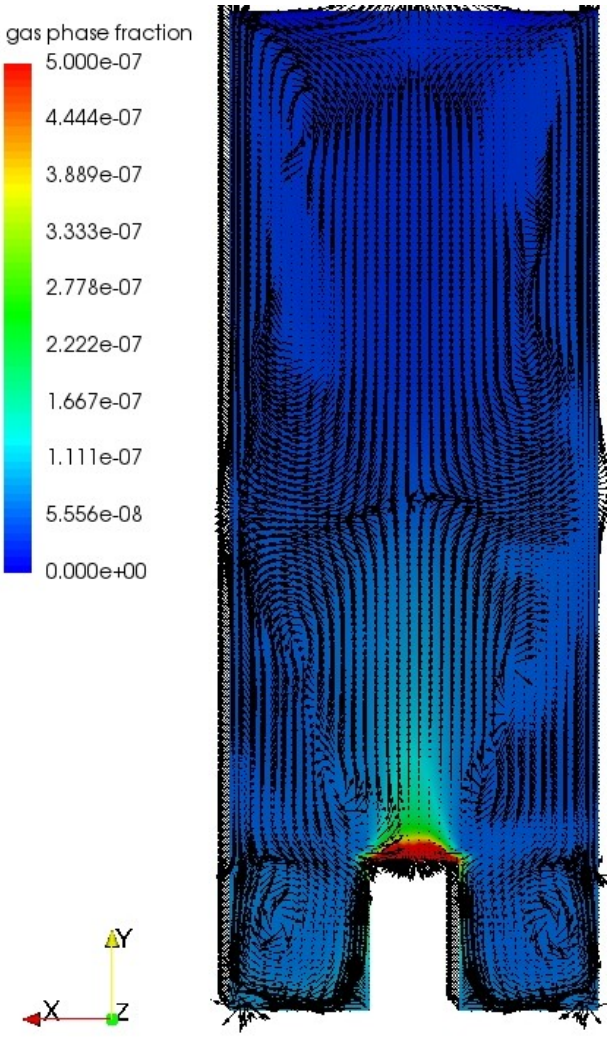

Figure 5.8 Time averaged velocity and vector field for gas phase

5.2.5 Conclusion

In this paper we performed a simulation study for a water electrolysis reactor (IRDE). The purpose of the paper is to validate the CFD-PBM solver which can be applied for an electrochemical reactor to predict the bubble size distribution. The originality of our OpenFOAM solver lies on the fact that it could accept a bubble size distribution as boundary condition and it is able to export distribution function for a specified region in an arbitrary time based on class method. The authors's attention was concentrated on the validation of the implemented OpenFOAM solver with available experimental bubbles distribution. Our results described for the first time the simulations using single-phase approach (dilute system) and Euler-Euler model accompanied with a population

balance method in an electrochemical reactor including gas-evolution electrodes. From the research that has been carried out, it is possible to conclude that big bubbles tend to move upward and small bubbles follow the flow behavior. Based on the laminar results of IRDE simulations, it is evident the convective term addition to coalescence due to laminar shear rate play an important role for the transport of the number density function (NDF). The main limitations of the performed simulation was the assumption of a constant current density and ignorance of growth term which lead to a discrepancy between our results and experimental data with increasing rotational velocity of working electrode. Particular attention was paid to the hydrodynamic study of the IRDE reactor. It was demonstrated that there are three different regions in the IRDE reactor. In our future research we intent to concentrate on the coupling electrochemical part and inclusion of bubbles growth in the current solver in order to enhance the results.

CHAPTER 6

Study of Local Population Balance Models: CM,QMOM,DQMOM and EQMOM

6.1 Avant-propos

Auteurs et affiliation :

Ehsan Askari : Étudiant au doctorat*

Pierre Proulx : Professeur*

Alberto Passalacqua : Professeur agrégé **

* Université de Sherbrooke, Faculté de Génie, Département de Génie Chimique et de Génie Biotechnologique

** Mechanical Engineering Department, Iowa State University, IA, USA

Date de soumission : 8 janvier 2018
Date de publication : 27 février 2018

Revue : ChemEngineering-Open Access Journal

Titre français :

Étude des modèles de bilan de population locale et de la méthode des moments en quadrature étendue

Contribution au document :

Dans le présent article, deux colonnes à bulles rectangulaires et un réacteur d'électrolyse de l'eau sont modélisés à l'aide de OpenFoam avec différentes techniques de PBM. En outre, la méthode des classes (CM) et la méthode des moments en quadrature (QBMM) sont comparées à l'aide du solveur CFD-PBM développé.

Résumé français :

Prévoir le comportement des bulles et leurs propriétés est crucial pour la conception de réacteurs performants. La taille des bulles peut varier dans un écoulement gaz-liquide. Pour les écoulements homogènes, la distribution de taille et le déplacement des bulles sont assez bien définis. Cependant, dans les écoulements hétérogènes, les bulles forment des grappes et de grandes bulles se forment rapidement. Afin d'analyser ces systèmes d'écoulements hétérogènes, il est possible de décrire mathématiquement le volume, la taille et les autres propriétés de dispersion des bulles. Le modèle de bilan de populations (Population Balance Model) fait partie des modèles mathématiques permettant de prédire les fonctions de distribution du déplacement des bulles et la variation de leurs propriétés. Dans cette publication, la méthode des classes (CM) et la méthode basée sur la quadrature des moments (QBMM) sont décrites et leurs implémentations sont comparées avec le programme de résolution CFD-PBM, nouvellement développé dans la boîte à outils pour l'étude numérique d'écoulement dynamique (CFD) libre OpenFOAM. Ces méthodes de résolution numérique ont été testées dans plusieurs cas: deux colonnes rectangulaires permettant d'observer l'écoulement des bulles et un réacteur d'électrolyse de l'eau. Tous les résultats numériques sont comparés avec des résultats observés en laboratoire, disponibles dans la littérature. Grâce à ces comparaisons, il est possible d'observer que l'utilisation de la méthode de la quadrature des moments (EQMOM) permet une légère amélioration de la prédiction des résultats obtenus en laboratoire. La méthode EQMOM permet aussi de reconstruire une fonction de densité numérique (NDF) continue, qui est utile pour établir un modèle de l'évolution des gaz dans un réacteur d'électrolyse de l'eau.

6.2 Study of Local Population Balance Models and Extended Quadrature Method of Moments Applications

In order to optimize and design new bubbly flow reactors, it is necessary to predict the bubble behavior and properties with respect to the time and location. In gas-liquid flows, it is easily observed that the bubble sizes may vary widely. The bubble size distribution is relatively sharply defined, and bubble rises are uniform in homogeneous flow; however bubbles aggregate, and large bubbles are formed rapidly in heterogeneous flow. To assist in the analysis of these systems, the volume, size and other properties of dispersed bubbles can be described mathematically by distribution functions. Therefore, a mathematical modeling

tool called the Population Balance Model (PBM) is required to predict the distribution functions of the bubble motion and the variation of their properties. In the present paper, two rectangular bubble columns and a water electrolysis reactor are modeled using the open-source Computational Fluid Dynamic (CFD) package OpenFOAM. Furthermore, the Method of Classes (CM) and Quadrature-based Moments Method (QBMM) are described, implemented and compared using the developed CFD-PBM solver. These PBM tools are applied in two bubbly flow cases: bubble columns (using a Eulerian-Eulerian two-phase approach to predict the flow) and a water electrolysis reactor (using a single-phase approach to predict the flow). The numerical results are compared with measured data available in the scientific literature. It is observed that the Extended Quadrature Method of Moments (EQMOM) leads to a slight improvement in the prediction of experimental measurements and provides a continuous reconstruction of the Number Density Function (NDF), which is helpful in the modeling of gas evolution electrodes in the water electrolysis reactor.

6.2.1 Introduction

In recent years, there has been a growing interest in two-phase flows as they can be observed in various industries such as petroleum, mining, chemical and biotechnology [19, 49, 68, 89]. In a two-phase flow, the dispersion of the particles (bubbles) in the continuous phase plays an important role in the process. One of the main challenges is to use the population balance model to predict the evolution of the number of bubbles and of their size in bubbly flow. To give an example, in order to optimize and enhance the efficiency of electrochemical reactors, the evolved bubbles should be under control, since the presence of bubbles has favorable and unfavorable effects, such as a resistive film for the electric current flow and ions supply heading to the electrode to participate in the electrode reaction. Bubbles can also play a role as a turbulence promoter and inducer of convection over the electrode surface [1, 90–92]. The accurate description of bubble size evolution is then beneficial to formulate predictive models for design optimization.

In the literature concerning the simulation of gas-liquid systems, several authors have used a monodisperse model only accounting for a mean bubble size (Holzinger [9], Deen et al. [93], Friberg [94], Morud and Hjertager [95], Ranade and Deshpande [96], Schwarz and Turner [97], Schwarz [98]). While these models reduce the computational cost of the numerical simulation, they are unable to predict the evolution of the bubble size

distribution, limiting their applicability and reliability for industrial design purposes [99]. One of the main problems in modeling of multiphase dispersion is the prediction of bubble size distribution. Global polydisperse models, in which a spatially-varying field of bubble sizes is considered, can globally account for the polydispersity of the bubbles, in addition to the phase continuity equation. As global polydispersity models yield a non-constant bubble size, the disperse phase is global polydisperse with a locally monodispersed size distribution (Kerdouss et al. [100], Ishii et al. [101]). However, by applying this approach, the local probability distribution of the bubble size is not considered. Detailed models using the locally polydisperse approach give more information on the secondary phase behavior (Dhanasekharan et al. [102], Venneker et al. [103]). The most used methods of locally polydisperse models are the Method of Classes (CM)(Bannari et al. [68], Balakin et al. [104], Becker et al. [105], Kumar and Ramkrishna [106, 107], Puel et al. [108]), Quadrature Method of Moments (QMOM) (Marchisio et al. [44, 45], McGraw [55], Marchisio et al. [109], Sanyal et al. [110]) and Direct Quadrature Method of Moments (DQMOM) (Marchisio and Fox [58], Selma et al. [59], Silva and Lage [111]). The method of classes, while intuitive and accurate, is computationally intensive due to the large number of classes required to finely discretize the Number Density Function (NDF) with a large number of classes. Compared with CM, the QMOM can consider a wide range of bubble sizes with a reduced number of equations for the moments of the NDF. However, in some evaporation and combustion problems (Nguyen et al. [5], Yuan et al. [6]), the value of the NDF for null internal coordinates needs to be known, which is not the case if the QMOM method is used. DQMOM solves the equations for weights and abscissae directly. Shortcomings related to the conservation of moments affect the DQMOM approach since weights and abscissas are not conserved quantities (Yuan et al. [6]). In order to overcome these limitations, Yuan et al. [6] introduced the Extended Quadrature Method of Moments (EQMOM), which enables the shape of NDF to be reconstructed from a moment set using continuous kernel density functions instead of Dirac delta functions.

QMOM and EQMOM have been recently compared in the study of liquid-liquid dispersion in a stirred tank Selma et al. [59], Li et al. [112]. Li et al. [112] performed a comparison between QMOM and EQMOM in turbulent liquid-liquid dispersion, and they observed that these two methods provided similar predictions. They managed to reconstruct the droplet size distribution by using EQMOM. CM and DQMOM have been compared in bubbly flow by Selma et al. [59], as well. Their study was carried out based on two test cases, one involving a bubble column and the other a stirred tank. They reported that it is more computationally efficient to use DQMOM compared to CM even with a relatively

low number of classes. A summary of some works concerning the coupling of E-E with Population Balance Model (PBM) and the comparison among PBMs are provided in Table 6.1 and Table 6.2, respectively.

Reference	**Test Case**	**PBM**	**Hypotheses**	**Remarks**
Bannari et al. [68]	bubble column	CM	accumulation, advection, coalescence, breakage	Constant mean bubble size does not give satisfactory results compared to those based on PBM; 25 classes give better results
Gimbun et al. [113]	gas-liquid stirred tank	QMOM	accumulation, coalescence, breakage	Better agreement is achieved using PBM compared to a uniform bubble size
Li et al. [112]	liquid-liquid stirred tank	EQMOM and QMOM	accumulation, advection, coalescence, breakage	Similar predictions for EQMOM and QMOM; EQMOM provides a continuous BSD
Selma et al. [59]	gas-liquid stirred tank; bubble column	DQMOM and CM	accumulation, advection, coalescence, breakage	High number of classes is required; CM is computationally heavy; DQMOM is much more efficient (computationally) compared to CM
Gupta and Roy [114]	bubble column	DQMOM and QMOM	accumulation, coalescence, breakage	A summary of studies done on bubble columns flow modeling using PBM; no significant difference between DQMOM and QMOM
Askari et al. [115]	gas-liquid stirred tank	EQMOM	accumulation, coalescence, breakage	The agreement between experimental data and simulation results using EQMOM; reconstruction of bubble size distribution

Table 6.1 The most remarkable studies in the field of bubbly flow modeling using Population Balance Model (PBM). Method of Classes (CM); Quadrature Method of Moments (QMOM); Extended Quadrature Method of Moments (EQMOM); Direct Quadrature Method of Moments (DQMOM)

In the present work, we simulate a gas-liquid flow in two rectangular bubble columns using CM, QMOM, DQMOM and EQMOM. The numerical results obtained in these two cases are used to compare the four solution methods for the PBE. The implementation of EQMOM provided by OpenQBMM [78] is coupled to a two-fluid solver in OpenFOAM to describe the bubble evolution in bubble columns. The EQMOM approach, coupled with a single-phase CFD solver in OpenFOAM, is then used to describe the evolution of the bubble phase in an electrochemical cell. This simplification, in the case of the electrochemical system, is possible because the bubble sizes of interest in this system are of the order of

PBM	Advantages	Disadvantages
CM	Intuitive and accurate	Computationally intensive
QMOM	Wide range of bubble sizes with a reduced computational cost	Disabled in case of null internal coordinates
DQMOM	Wide range of bubble sizes with a reduced computational cost	Shortcomings related to non-conservative quantities (weights and abscissas)
EQMOM	Wide range of bubble sizes with a reduced computational cost (ONLYcompared to CM) and reconstruction capability of continuous NDF	Heavy computation compared to QMOM and DQMOM

Table 6.2 An overview of locally polydisperse PBMs. NDF, Number Density Function.

a micron, significantly smaller and having a lower Stokes number than in the case of the bubble column. In this case, then, a one-way coupling approach is sufficient.

The remainder of this article is organized as follows. First, the modeling approach and numerical solution method of population balance equations are explained in Section 6.2.2. The numerical results obtained for the bubble columns and the electrochemical cell are presented in Section 6.2.6, comparing them to the experiments for validation purposes. Conclusions are drawn in Section 6.2.7.

6.2.2 Numerical model

The governing equations of single-phase and two-phase system (two-fluid model) used in this model are shown in Table 6.3. This discussion is limited to a brief review of the PBMs.

6.2.3 Population Balance Modelling

The evolution of the size distribution of a particle population, which may consist of solid particles, bubbles or droplets, is described studying the changes in space and time of the Number Density Function (NDF) $n(\zeta; \mathbf{x}, t)$. Here, ζ indicates the internal coordinate

Table 6.3 Governing Equations of CFD-PBM model

Equation	Formulation
Continuity (single-phase)	$\frac{\partial \rho}{\partial t} + \nabla \cdot (\rho \mathbf{U}) = 0$
Momentum (single-phase)	$\frac{\partial}{\partial t}(\rho \mathbf{U}) + \nabla \cdot (\rho \mathbf{U}\mathbf{U}) = -\nabla p + \nabla \cdot \bar{\bar{\tau}}_{\text{effi}}$
Continuity (multi-phase)	$\frac{\partial}{\partial t}(\rho_{\text{i}} \alpha_{\text{i}}) + \nabla \cdot (\alpha_{\text{i}} \rho_{\text{i}} \mathbf{U}_{\text{i}}) = 0.0$
Reynolds stress tensor	$\bar{\bar{\tau}}_{\text{effi}} = (\mu_{\text{lam}} + \mu_{\text{t}}) \left(\nabla \mathbf{U} + \nabla \mathbf{U}^T\right) - \frac{2}{3}(\rho k + (\mu_{\text{lam}} + \mu_{\text{t}}) \nabla \cdot \mathbf{U}) \bar{\bar{I}}$
Momentum (multi-phase)	$\frac{\partial}{\partial t}(\rho_{\text{i}} \alpha_{\text{i}} \mathbf{U}_{\text{i}}) + \nabla \cdot (\alpha_{\text{i}} \rho_{\text{i}} \mathbf{U}_{\text{i}} \mathbf{U}_{\text{i}}) = -\alpha_{\text{i}} \nabla p + \nabla \cdot (\alpha_i \bar{\bar{\tau}}_{\text{effi},i}) + \mathbf{R}_{\text{i}} + \mathbf{F}_{\text{i}} + \alpha_{\text{i}} \rho_{\text{i}} \mathbf{g}$
Interfacial momentum exchange	$\mathbf{R}_{\text{G}} = -\mathbf{R}_{\text{L}} = \mathbf{R}_{\text{G,drag}} + \mathbf{R}_{\text{G,lift}} + \mathbf{R}_{\text{G,vm}}$
Liquid-gas exchange coefficient	$K = \frac{3}{4} \rho_{\text{L}} \alpha_{\text{G}} \frac{C_{\text{D}}}{d_{32}} \mid \mathbf{U}_{\text{G}} - \mathbf{U}_{\text{L}} \mid (\mathbf{U}_{\text{G}} - \mathbf{U}_{\text{L}}) + \alpha_{\text{G}} C_{\text{l}} \rho_{\text{L}} \mathbf{U}_{\mathbf{r}} \times (\nabla \times \mathbf{U}_{\mathbf{L}}) + \alpha_{\text{L}} C_{\text{vm}} \rho_{\text{L}} \left(\frac{D_L \mathbf{U}_{\mathbf{L}}}{Dt} - \frac{D_G \mathbf{U}_{\mathbf{G}}}{Dt}\right)$
Schiller Naumann drag coefficient [28]	$C_D = \begin{cases} \frac{24}{\text{Re}}\left(1 + 0.15\text{Re}^{0.687}\right) & \text{Re} \leq 1000 \\ 0.44 & \text{otherwise} \end{cases}$
Ishii-Zuber drag coefficient [30]	$C_D = \max\{\min[\frac{2}{3}\sqrt{\text{Eo}}, \frac{8}{3}], \frac{24}{\text{Re}}(1 + 0.1\text{Re}^{0.75})\}$
Tomiyama lift coefficient [116]	$C_l = \begin{cases} \min(0.288 \tanh(0.121\text{Re}), f(\text{Eo}_G)) & \text{Eo}_G < 4 \\ f(\text{Eo}_G) & 4 \leq \text{Eo}_G \leq 10.7 \end{cases}$
Mixture k-ϵ model [39]	$\frac{\partial}{\partial t}(\rho_{\text{m}} k_{\text{m}}) + \nabla \cdot (\rho_{\text{m}} \mathbf{U}_{\text{m}} k_{\text{m}}) = \nabla \cdot \left(\frac{\mu_{\text{t,m}}}{\sigma_{\text{k}}} \nabla k_{\text{m}}\right) + P_k^{\text{m}} - \rho_{\text{m}} \epsilon_{\text{m}} + S_k^{\text{m}}$
	$\frac{\partial}{\partial t}(\rho_{\text{m}} \epsilon_{\text{m}}) + \nabla \cdot (\rho_{\text{m}} \mathbf{U}_{\text{m}} \epsilon_{\text{m}}) = \nabla \cdot \left(\frac{\mu_{\text{t,m}}}{\sigma_\epsilon} \nabla k_{\text{m}}\right) + \frac{\epsilon_m}{k_m}(C_{1\epsilon} G_{\text{k,m}} - C_{2\epsilon} \rho_{\text{m}} \epsilon_{\text{m}}) + C_{\epsilon 3} \frac{\epsilon_m}{\epsilon_k} S_k^{\text{m}}$
Break-up rate function [67]	$\Omega_B(d_j : d_i) = \frac{-3k_1(1-\alpha)}{11 b^{8/11}} n_j \left(\frac{\epsilon}{d_j^2}\right)^{1/3} \{\Gamma(8/11, t_m) - \Gamma(8/11, b) + 2b^{3/11}(\Gamma(5/11, t_m) - \Gamma(5/11, b)) + b^{6/11}(\Gamma(2/11, t_m) - \Gamma(2/11, b))\}$
Coalescence rate [65]	$\beta(d_i, d_j) = \theta_{ij} P_c$
Coalescence frequency [117]	$\theta(i,j) = \frac{\pi}{4} n_i n_j (d_i + d_j)^2 \epsilon^{1/3} \left(d_i^{2/3} + d_j^{2/3}\right)^{1/2}$
Coalescence efficiency [65]	$P_C(d_i, d_j) = \exp\left(-c \frac{\left[0.75(1+\xi_{ij}^2)(1+\xi_{ij}^3)\right]^{1/2}}{(\rho_d/\rho_c + 0.5)^{1/2}(1+\xi_{ij})^3} \text{We}_{ij}^{1/2}\right)$

representing the size of the discrete element of the disperse phase, $\mathbf{x}$ is the position vector in physical space and t is time.

Assuming the velocity of the disperse phase is known, the evolution of the NDF is defined by the population balance equation (Marchisio et al. [44, 45], Marchisio and Fox [46], Ramkrishna [47]):

$$\begin{aligned}\frac{\partial n(\zeta;\mathbf{x},t)}{\partial t} + \nabla_{\mathbf{x}} \cdot [\mathbf{U}_G n(\zeta;\mathbf{x},t)] - \nabla_{\mathbf{x}} \cdot [\Gamma \nabla_x n(\zeta;\mathbf{x},t)] \\ +\nabla_{\zeta} \cdot [G(\zeta) n(\zeta;\mathbf{x},t)] = \overline{B}_{ag}(\zeta;\mathbf{x},t) - \overline{D}_{ag}(\zeta;\mathbf{x},t) \\ +\overline{B}_{br}(\zeta;\mathbf{x},t) - \overline{D}_{br}(\zeta;\mathbf{x},t) + N(\zeta;\mathbf{x},t),\end{aligned} \tag{6.1}$$

where $\mathbf{U}_G$ is the velocity of the disperse phase, Γ is the diffusivity and $G(\zeta)$ the continuous rate of change in the space of internal-coordinate. The first term of Equation (6.1) represents accumulation; the second term describes convection; and the third diffusion in physical space. The source terms $\overline{B}_{\mathrm{br}}(\zeta;\mathbf{x},t)$, $\overline{B}_{\mathrm{br}}(\zeta;\mathbf{x},t)$, $\overline{D}_{\mathrm{ag}}(\zeta;\mathbf{x},t)$ and $\overline{D}_{\mathrm{ag}}(\zeta;\mathbf{x},t)$ are birth rate due to breakage, birth rate due to coalescence, death rate due to breakage and death rate due to coalescence, respectively. Finally, $N(\zeta;\mathbf{x},t)$ is the rate of change of the NDF due to nucleation. In the present study, the NDF has the form of being length-based and $G(\zeta)$ is defined as growth rate.

Bubbles may nucleate when the liquid is supersaturated with gas. When the dissolved gas concentration reaches a critical value, bubbles nucleate. This critical value might be theoretically obtained from Classical Nucleation Theory (CNT) (Abraham [48]). The nucleation theory provides information about the generation of nuclei (the formation of cluster of molecules after reaching some critical size) per unit time and volume of the liquid as a function of the local parameters. The bubbles can grow in size if the liquid is saturated with dissolved gas. The remaining gas is transported into the liquid on a molecular level and gives rise to supersaturation that causes an increases of the growth of bubbles that move through liquid. In this case, the growth term is included in the PBE as a source term. In some systems such as a gas-evolving electrode, bubble growth and nucleation terms might be treated as boundary conditions, since the sources of nucleation are usually irregularities of the electrode surfaces, and once a nucleus exists, the bubble growth occurs on the electrode surface in a concentration boundary layer. Gas bubbles develop at nucleation sites on the electrode surface, grow in size until they reach a critical break-off diameter and detach into the electrolyte afterwards (Nierhaus [49], Tomasoni [50]). In other words, the bubble formation happens on the electrode. Consequently, it can be described by means of a boundary condition (an ingoing flux boundary).

Growth, nucleation and diffusivity were not taken into account in the example applications presented in this work, since the focus is on bubble coalescence and breakage. Therefore, the final form of the evolution equation of the NDF is:

$$\frac{\partial n(\zeta;\mathbf{x},t)}{\partial t}+\nabla_{\mathbf{x}}\cdot[\mathbf{U}_G n(\zeta;\mathbf{x},t)] = \overline{B}_{ag}(\zeta;\mathbf{x},t)-\overline{D}_{ag}(\zeta;\mathbf{x},t)+\overline{B}_{br}(\zeta;\mathbf{x},t)-\overline{D}_{br}(\zeta;\mathbf{x},t). \quad (6.2)$$

The breakage and coalescence source terms are modeled as (Marchisio et al. [44, 45], Marchisio and Fox [46]):

$$\overline{B}_{\mathrm{ag}} = \frac{\zeta^2}{2}\int_0^{\zeta} \frac{\beta\left(\left(\zeta^3-\zeta'^3\right)^{1/3},\zeta'\right)}{\left(\zeta^3-\zeta'^3\right)^{2/3}} n\left(\left(\zeta^3-\zeta'^3\right)^{1/3};\mathbf{x},t\right) n(\zeta';\mathbf{x},t)d\zeta', \quad (6.3)$$

$$\overline{D}_{\mathrm{ag}} = n(\zeta;\mathbf{x},t)\int_0^{\infty} \beta(\zeta,\zeta')n(\zeta';\mathbf{x},t)d\zeta', \quad (6.4)$$

$$\overline{B}_{\mathrm{br}} = \int_{\zeta}^{\infty} a(\zeta')b(\zeta|\zeta')n(\zeta;\mathbf{x},t)d\zeta', \quad (6.5)$$

$$\overline{D}_{\mathrm{br}} = a(\zeta)n(\zeta;\mathbf{x},t). \quad (6.6)$$

Here, $\beta(\zeta,\zeta')$ is the coalescence rate between bubbles of size ζ and ζ'; $a(\zeta)$ is the breakup frequency of a bubble with size ζ; $b(\zeta|\zeta')$ represents daughter distribution function generated from the breakup of a bubble of size ζ'.

6.2.4 Class Methods

The class method solves the bubble' number density, directly Ramkrishna [47]. In CM, the continuous size range of bubbles can be realized through the discretization of the bubbles size distribution into a number of classes of discrete sizes. For each class, the equation of the number density of bubbles is solved and coalescence and breakup rates are transformed into birth and death rates. The population balance equation for the i-th bubble class is

represented as:

$$\frac{\partial n_i}{\partial t} + \nabla \cdot (\mathbf{U}_G n_i) = \overline{B}_{i,agr} - \overline{D}_{i,agr} + \overline{B}_{i,br} - \overline{D}_{i,br} \tag{6.7}$$

where n_i is the number of the bubbles from group i per unit volume. $\overline{B}_{br}$ and $\overline{B}_{agr}$ are the birth rates caused by breakup and coalescence, respectively, and $\overline{D}_{agr}$ and $\overline{D}_{br}$ the corresponding death rates, from coalescence and breakage, respectively.

The relationship between the volume fraction and the number density is:

$$n_i = \frac{\alpha_i}{\nu_i} \tag{6.8}$$

where ν_i is the volume of a bubble of class i.

$$\sum \alpha_i = \alpha_G \tag{6.9}$$

where α_G is the volume fraction of the dispersed phase.

To solve the population balance equation using the scalars f_i, Equation (6.7) is changed to the following equation:

$$\frac{\partial \alpha_G f_i}{\partial t} + \nabla \cdot (\alpha_G \mathbf{U}_G f_i) = \overline{B}_{i,agr} - \overline{D}_{i,agr} + \overline{B}_{i,br} - \overline{D}_{i,br} \tag{6.10}$$

$$f_i = \frac{\alpha_i}{\alpha_G} \tag{6.11}$$

$$\sum f_i = 1 \tag{6.12}$$

Here, f_i is the bubble volume fraction of group of size i. As Equation (6.10) shows, all bubbles in a computational cell move with the same velocity $\mathbf{U}_G$. This approach is called the MUlti SIze Group (MUSIG) [51]. It is worth observing that assuming all the bubbles in a computational cell move with the same velocity is a limitation of the approach, which may be acceptable for narrow bubble size distributions, but not in general. A class of Quadrature-based Moments Methods (QBMM) that is not affected by this limitation was proposed by [118], and its adoption will be the topic of future work.

The method of classes calculates the Sauter mean diameter d_{32} as follows:

$$d_{32} = \frac{\sum_i f_i}{\sum_i f_i / d_i} \tag{6.13}$$

The Sauter mean diameter represents the average bubble size, and it is defined as the diameter of a sphere that has the same volume to surface area ratio as the bubble under consideration. The Sauter diameter is often used in problems where the active surface area is the relevant parameter [57].

[47] proposed an approach named fixed pivot in order to discretize the source terms in the PBE. The approach assumes that the population of bubbles is distributed on pivotal grid points x_i with $x_{i+1} = sx_i$ and $s > 1$, where i refers to the class i with $i < n$. Assuming spherical bubbles, $(4/3)\pi(d_{i+1}/2)^3 = (4s/3)\pi(d_i/2)^3$, where s is calculated to ensure $d_n = d_{2r+1} = d_{\max} = d_{\max}$ and $d_r = d_{mean}$.

In the CM technique, the bubble size is divided into $n = 2r + 1$ classes, where n is odd in order to have symmetrical divisions. This gives the following relation:

$$d_i = s^{(i-r-1/3)} d_{mean} \quad s = \left(\frac{d_{\max}}{d_{mean}} \right)^{3/r} \tag{6.14}$$

Bannari et al. [68] evaluated the the values of r and s for different classes assuming $d_{\max} = 5$ mm and $d_{mean} = 10$ mm (Table 6.4).

Number of Classes	**7**	**11**	**15**	**25**
Value of r	3	5	7	12
Value of s	2	1.5157	1.3459	1.1892

Table 6.4 Values of r and s used in different classes.

Breakage and aggregation may create bubbles with volume ν such that $x_i < \nu < x_{i+1}$. This bubble must be split by assigning respectively fraction γ_i and γ_{i+1} to x_i and x_{i+1}. The following limitations preserve the number balance and mass balance.

$$\begin{cases} \gamma_i x_i + \gamma_{i+1} x_{i+1} = \nu \\ \gamma_i + \gamma_{i+1} = 1 \end{cases} \tag{6.15}$$

Ramkrishna [47] has also reported the birth in class i due to coalescence in this way:

$$\begin{aligned}\overline{B}_{i,agr} = &\sum_{k=0}^{n}\sum_{j=0}^{n}\left[\theta(x_{i-1} < x_j + x_k < x_i) \times (1 - \frac{1}{2}\delta_{jk})\right] \\ &\times \gamma_{i-1}(x_j + x_k)\beta(x_k, x_j)\frac{36\alpha_g^2}{\pi^2}\frac{f_j f_k}{(d_j d_k)^3} \\ &+ \sum_{k=0}^{n}\sum_{j=k}^{n}\left[\theta(x_i < x_j + x_k < x_{i+1}) \times (1 - \frac{1}{2}\delta_{jk})\right] \\ &\times \gamma_i(x_j + x_k)\beta(x_k, x_j)\frac{36\alpha_g^2}{\pi^2}\frac{f_j f_k}{(d_j d_k)^3},\end{aligned} \tag{6.16}$$

where θ is a test function expressed as:

$$\theta(\varphi) = \begin{cases} 0 & \varphi \text{ is false} \\ 1 & \varphi \text{ is true} \end{cases}. \tag{6.17}$$

and:

$$\gamma_{i-1}(\nu) = \frac{\nu - x_{i-1}}{x_i - x_{i-1}}, \quad \gamma_i(\nu) = \frac{x_{i+1} - \nu}{x_{i+1} - x_i}. \tag{6.18}$$

The death rates $\overline{D}_{i,agr}$ in class i due to coalescence is defined as follows:

$$\overline{D}_{i,agr} = \frac{36 f_i \alpha_G^2}{\pi^2 d_i^3}\sum_{k=0}^{n}\beta(x_i, x_k)\frac{f_k}{d_k^3}, \tag{6.19}$$

while the birth rate $\overline{B}_{i_{br}}$ in class i due to breakup as:

$$\overline{B}_{i_{br}} = \frac{6\alpha_G}{\pi}\sum_{k=i}^{n} b(x_k|x_i)a(x_k)\pi_{i,k}\frac{f_k}{d_k^3}, \tag{6.20}$$

and the death rate $\overline{D}_{i,br}$ in class i due to break-up:

$$\overline{D}_{i,br} = \frac{6\alpha_G f_i}{\pi d_i^3}a(x_i), \tag{6.21}$$

where:

$$\pi_{i,k} = \int_{x_{i-1}}^{x_i}\frac{\nu - x_{i-1}}{x_i - x_{i-1}}p(\nu, \nu_k)d\nu + \int_{x_i}^{x_{i+1}}\frac{x_{i+1} - \nu}{x_{i+1} - x_i}p(\nu, \nu_k)d\nu \tag{6.22}$$

The mentioned integrals are solved by the Gaussian quadrature integration as follows:

$$\pi_{i,k} \simeq \sum_{j=1}^{5} \frac{(1+W_j)^3}{(j+1)^2 p_5^2 p(W_j)} p\left(\frac{x_i - x_{i-1}}{2}(1+W_j) - x_{i-1}, x_k\right) + \sum_{j=1}^{5} \frac{(1+W_j)^2(1-W_j)}{(j+1)^2 p_5^2 p(W_j)} p\left(\frac{x_{i+1} - x_i}{2}(1+W_j) - x_i, x_k\right) \tag{6.23}$$

P_n is a Legendre polynomial and can be formulated using the recurrence relation:

$$P_n = \frac{(2n-1)xP_{n-1} - (n-1)P_{n-2}}{n}; \quad P_0 = 1; \quad P_1 = x \tag{6.24}$$

W_j is the weighting function of the orthogonal polynomials as shown in Table 6.5. If j equals five, adequate accuracy is achieved.

$\boldsymbol{W_1}$	$\boldsymbol{W_2}$	$\boldsymbol{W_3}$	$\boldsymbol{W_4}$	$\boldsymbol{W_5}$
$\sqrt{\frac{35+2\sqrt{70}}{63}}$	$\sqrt{\frac{35-2\sqrt{70}}{63}}$	0	$-\sqrt{\frac{35-2\sqrt{70}}{63}}$	$-\sqrt{\frac{35+2\sqrt{70}}{63}}$

Table 6.5 Values of weights used in Gaussian quadrature.

Boundary and initial conditions to solve CM equations are shown in Table 6.6. It is assumed that the bubble size at the inlet is monodispersed and spatially uniform, equal to the mean diameter (d_{2r}). The first-order upwind scheme is used to discretize the advection term of the f_i equations.

Boundary Conditions			**Initial Condition**
Inlet	Wall	Outlet	Inlet value
$f_i = \begin{cases} 1 & i = 2\text{r} \\ 0 & i \neq 2\text{r} \end{cases}$	Neumann	Neumann	

Table 6.6 Boundary and initial condition for f_i equations

6.2.5 Quadrature-Based Moments Method

Quadrature-based Moment Methods (QBMM) consider the evolution of a set of moments of the NDF. If integer moments are considered, their definition is:

$$M_k = \int_0^\infty n(L;\mathbf{x},t)L^k dL, \quad k = 0, 1, \ldots \tag{6.25}$$

Evolution equations for the moments of the NDF read:

$$\frac{\partial M_k(t,x)}{\partial t} + \nabla \cdot [\mathbf{U}_G M_k(t,x)] = \overline{B}_{ag,k} - \overline{D}_{ag,k} + \overline{B}_{br,k} - \overline{D}_{br,k} \tag{6.26}$$

By solving Equation (6.26) for a set of at least four moments, the Sauter mean diameter $d_{32} = m_3/m_2$ can be calculated.

Quadrature Method of Moments

In the QMOM technique, the unknown NDF is represented by a weighted summation of Dirac delta distributions $\delta(L - L_\alpha)$[55]:

$$n(L) \approx \sum_{\alpha=1}^{N} W_\alpha \delta(L - L_\alpha) \tag{6.27}$$

where W_i are non-negative weights of each kernel density function, L_i are the corresponding quadrature abscissae and N is the number of kernel density functions to approximate the NDF. Source terms in the moment Equation (6.26) become:

$$\overline{B}_{ag,k} = \frac{1}{2}\sum_{\alpha=1}^{N} W_\alpha \sum_{\beta=1}^{N} W_\beta (L_\alpha^3 + L_\beta^3)^{k/3} \beta(L_\alpha, L_\beta), \tag{6.28}$$

$$\overline{D}_{ag,k} = \sum_{\alpha=1}^{N} W_\alpha L_\alpha^k \sum_{\beta=1}^{N} W_\beta \beta(L_\alpha, L_\beta), \tag{6.29}$$

$$\overline{B}_{br,k} = \sum_{\alpha=1}^{N} W_\alpha \overline{b}_\alpha^{(k)} a(L_\alpha), \tag{6.30}$$

$$\overline{D}_{br,k} = \sum_{\alpha=1}^{N} W_\alpha L_\alpha^k a(L_\alpha), \tag{6.31}$$

where the N is the number of weights w_α, and the corresponding abscissae L_α are determined from the first $2N$ integer moments of the NDF. $\beta_{\alpha\beta}$ is the aggregation kernel for the bubbles of size L_α and L_β; a_α is the breakage kernel for the bubble size of L_α; and $\overline{b}_\alpha^{(k)}$ represents daughter bubble distribution function.

Boundary conditions and initial conditions to solve the moment equations are shown in Table 6.7. Gauss upwind is utilized as the divergence scheme. If the bubble size, which can be represented by a constant value or a distribution function, is known, the moments will be easily calculated. The moments for constant bubble size are found by:

$$M_i = \begin{cases} \alpha_G & i = 0 \\ M_0 \zeta^i & i \neq 0 \end{cases} \tag{6.32}$$

where ζ is bubble size and α_G is gas phase fraction.

Boundary Conditions			**Initial Condition**
Inlet	Wall	Outlet	Inlet value
Equation (6.32)	Neumann	Neumann	

Table 6.7 Boundary conditions, initial conditions and divergence scheme corresponding m_i equations.

Direct Quadrature Method of Moments

DQMOM is based on the direct solution of the transport equations for weights and abscissas of the quadrature approximation Fan et al. [60]. The transport equations for weights and abscissas are written as:

$$\frac{\partial}{\partial t} W_\alpha + \nabla(\phi W_\alpha) = a_\alpha \tag{6.33}$$

$$\frac{\partial}{\partial t} L_\alpha + \nabla(\phi L_\alpha) = b_\alpha \tag{6.34}$$

where a_i and b_i are found by the solution of the following linear system in terms of the unknown a_i and b_i Bove et al. [119]:

$$\sum_{\alpha=1}^{N}[(1-k){L_\alpha}^{k}a_\alpha + k{L_\alpha}^{k-1}b_\alpha] = \frac{1}{2}\sum_{\alpha=1}^{N}W_\alpha\sum_{\beta=1}^{N}W_\beta(L_\alpha^3+L_\beta^3)^{k/3}\beta(L_\alpha,L_\beta) - \sum_{\alpha=1}^{N}W_\alpha L_\alpha^k\sum_{\beta=1}^{N}W_\beta\beta(L_\alpha,L_\beta) + \sum_{\alpha=1}^{N}W_\alpha\overline{b}_\alpha^{(k)}a(L_\alpha) - \sum_{\alpha=1}^{N}W_\alpha L_\alpha^k a(L_\alpha) \quad k=0,...,2N-1. \tag{6.35}$$

The source terms $S^{(k)}$ are taken to be the as same as for the QMOM method. Boundary and initial conditions to solve for weights and abscissae are shown in Table 6.8. The first-order upwind scheme is used to discretize the advection term in both Equations (6.33) and (6.34). The linear system obtained from Equation (6.35) is solved using the Gauss–Seidel technique.

Boundary Conditions			**Initial Condition**
Inlet	Wall	Outlet	Inlet value
L_i and W_i corresponding to m_i	Neumann	Neumann	

Table 6.8 Boundary conditions and initial condition for DQMOM equations.

Extended Quadrature Method of Moments

The EQMOM approach approximates the unknown NDF with a weighted sum of smooth, non-negative kernel density functions $\delta_\sigma(L,L_\alpha)$ (Nguyen et al. [5], Yuan et al. [6]):

$$n(L) \approx p_N(L) = \sum_{\alpha=1}^{N}W_\alpha\delta_\sigma(L,L_\alpha) \tag{6.36}$$

In this work, the log-normal kernel density is used [79]:

$$\delta_\sigma(L,L_\alpha) = \frac{1}{L\sigma\sqrt{2\pi}}\exp\left(-\frac{(L-L_\alpha)^2}{2\sigma^2}\right), \tag{6.37}$$

Source terms are then closed in terms of the primary and secondary quadrature found with the EQMOM procedure, leading to:

$$\overline{B}_{ag,k} = \frac{1}{2}\sum_{\alpha_1=1}^{N}\sum_{\gamma_1=1}^{N_\alpha}W_{\alpha_1}W_{\alpha_1\gamma_1}\sum_{\alpha_2=1}^{N}\sum_{\gamma_2=1}^{N_\alpha}W_{\alpha_2}W_{\alpha_2\gamma_2}(L_{\alpha_1\gamma_1}^3+L_{\alpha_2\gamma_2}^3)^{k/3}\beta_{\alpha_1\gamma_1\alpha_2\gamma_2}, \tag{6.38}$$

$$\overline{D}_{ag,k} = \sum_{\alpha_1=1}^{N} \sum_{\gamma_1=1}^{N_\alpha} L_{\alpha_1\gamma_1}^{k} W_{\alpha_1} W_{\alpha_1\gamma_1} \sum_{\alpha_2=1}^{N} \sum_{\gamma_2=1}^{N_\alpha} W_{\alpha_2} W_{\alpha_2\gamma_2} \beta_{\alpha_1\gamma_1\alpha_2\gamma_2}, \tag{6.39}$$

$$\overline{B}_{br,k} = \sum_{\alpha_1=1}^{N} \sum_{\gamma_1=1}^{N_\alpha} W_\alpha W_{\alpha\gamma} \overline{b}_{\alpha\gamma}^{(k)} a_{\alpha\gamma}, \tag{6.40}$$

$$\overline{B}_{br,k} = \sum_{\alpha_1=1}^{N} \sum_{\gamma_1=1}^{N_\alpha} W_\alpha W_{\alpha\gamma} L_{\alpha\gamma}^{k} a_{\alpha\gamma}, \tag{6.41}$$

where the N primary weights W_α, the corresponding primary abscissae L_α, together with the parameter σ are determined from the first $2N+1$ integer moments of the NDF. The $2N_\alpha$ quantities $W_{\alpha\gamma}$, called secondary weights and abscissae, respectively, are computed using the standard Gaussian quadrature formulae for known orthogonal polynomials to the kernel NDF (Nguyen et al. [5], Yuan et al. [6]). $\beta_{\alpha_1\gamma_1\alpha_2\gamma_2}$ is the aggregation kernel for the bubbles of size $L_{\alpha_1\gamma_1}$ and $L_{\alpha_2\gamma_2}$; $a_{\alpha\gamma}$ is the breakage kernel for the bubbles size of $L_{\alpha\gamma}$; and $\overline{b}_{\alpha\gamma}$ represents the daughter distribution function. Boundary conditions and initial conditions used to solve the moment equations are the same as those used for the QMOM approach (Table 6.7).

6.2.6 Results and Discussion

Test Case 1: Pseudo-2D Bubble Column

The first test case for the coupled Population Balance Model and Two Fluid Model (PBM-TFM) approach is a simple geometry (a rectangular bubble column [68]). The same test case was used in [59] to compare CM and DQMOM. Consequently, only the simulations with EQMOM were necessary to allow the comparison.

The dimensions and boundary conditions used to perform the simulations are shown in Figure 6.1, while Table 6.9 summarizes the models used in the simulations for this test case. Tables 6.10-6.12 demonstrates the boundary and initial conditions applied in CM, QMOM, EQMOM and DQMOM, respectively.

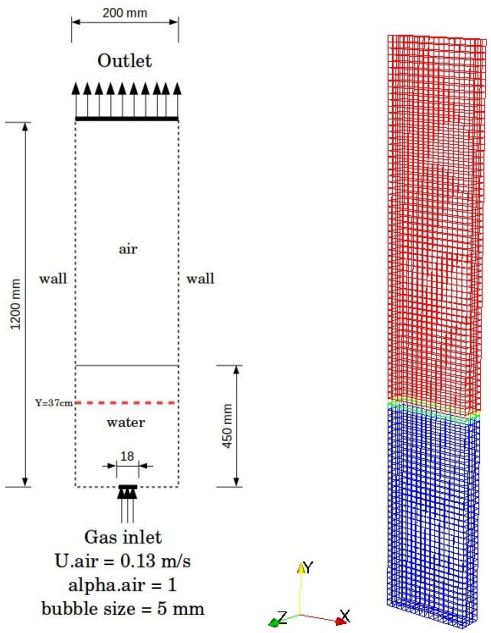

(**a**) (**b**)

Figure 6.1 (**a**) Dimension and boundary conditions in the bubble column [68] and (**b**) mesh.

Settings	**Model**
Two-phase flow	Two-fluid model (TFM)
Drag	Schiller and Naumann [28]
Lift	Tomiyama et al. [116]
Virtual mass	$C_{vm} = 0.25$ [59]
Turbulence	Standard k-ϵ model
Population balance	CM and EQMOM
Coalescence	Hagesather et al. [65]
Breakage	Luo and Svendsen [67]

Table 6.9 Models used in the simulation of the bubble column of Pfleger et al. [120]

Boundary Conditions			**Initial Condition**
Inlet	Wall	Outlet	Inlet value
$f_i = \begin{cases} 1 & i = 12 \\ 0 & i \neq 12 \end{cases}$	Neumann	Neumann	

Table 6.10 Boundary and initial conditions for f_i equations (25 classes).

Figure 6.2 depicts a comparison between experimental measurements [120] and axial liquid velocity provided by the CFD-PBM solver on a line along y = 37 cm. The comparison

Boundary Conditions			**Initial Condition**
Inlet	Wall	Outlet	Inlet value
$m_i = \begin{cases} 1 & i = 0 \\ 5 & i = 1 \\ 25 & i = 2 \\ 125 & i = 3 \\ 625 & i = 4 \\ 3125 & i = 5 \\ 15,625 & i = 6 \end{cases}$	Neumann	Neumann	

Table 6.11 Boundary and initial conditions for m_i equations used in the QMOM and EQMOM methods (Test Cases I and II).

Boundary Conditions			**Initial Condition**
Inlet	Wall	Outlet	$W_i = \begin{cases} 0.33 & i = 0 \\ 0.33 & i = 1 \\ 0.34 & i = 2 \end{cases}$ $L_i = \begin{cases} 0.001 & i = 0 \\ 0.002 & i = 1 \\ 0.003 & i = 2 \end{cases}$
$W_i = \begin{cases} 0.1667 & i = 0 \\ 0.6667 & i = 1 \\ 0.1667 & i = 2 \end{cases}$ $L_i = \begin{cases} 3.26 & i = 0 \\ 5.00 & i = 1 \\ 6.73 & i = 2 \end{cases}$	Neumann	Neumann	

Table 6.12 Boundary and initial conditions for W_i and L_i equations used in the DQMOM method [59]

confirms that the solver using EQMOM works properly for the bubble column. Figure 6.2a shows that the variation of secondary nodes does not have a significant impact. However, the increase of primary nodes from two to three provides better accuracy, as was expected. Figure 6.2b demonstrates the differences among population balance models. It is observed that EQMOM using three nodes represents a slight improvement in comparison with CM (25 classes) and DQMOM (three nodes). It is noteworthy that the CM (25 classes) computationally is very expensive [59]. By contrast, DQMOM and EQMOM have less computational demand.

Figure 6.3 demonstrates the radial bubble segregation based on the Sauter mean diameter contour. In fact, the bubble size decreases heading toward the wall due to breakage phenomena. However, the high gas phase fraction and coalescence events at the center of column lead to the creation of larger bubble sizes. As Figure 6.3 shows, Sauter mean diameter distributions predicted by the applied PBMs (DQMOM, EQMOM, CM) are qualitatively confirmed by comparison with experimental observation.

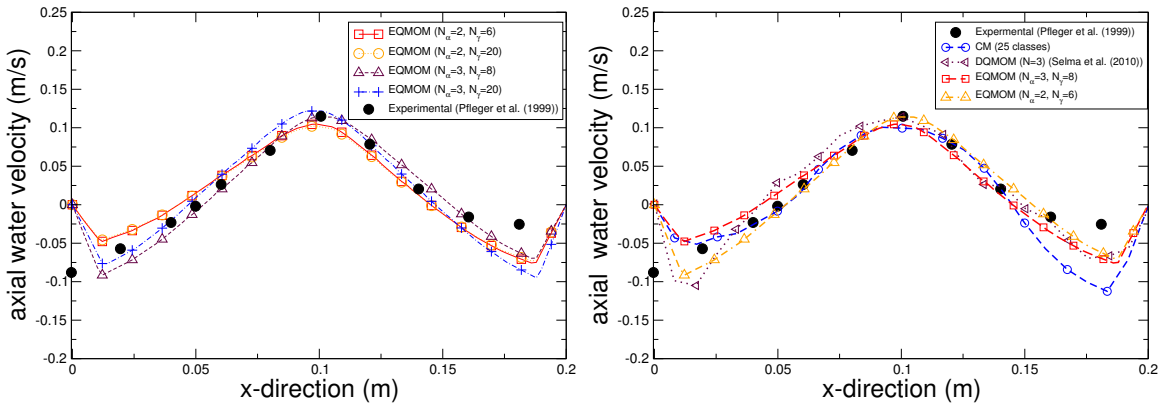

(**a**) (**b**)

Figure 6.2 Profile of axial liquid velocity through a line at y = 37 cm from the bottom of the bubble column. (**a**) The variation of primary and secondary nodes and their effects on the predicted velocity profile. (**b**) The comparison among CM (classes), DQMOM (3 nodes), EQMOM (3 nodes) and EQMOM (2 nodes).

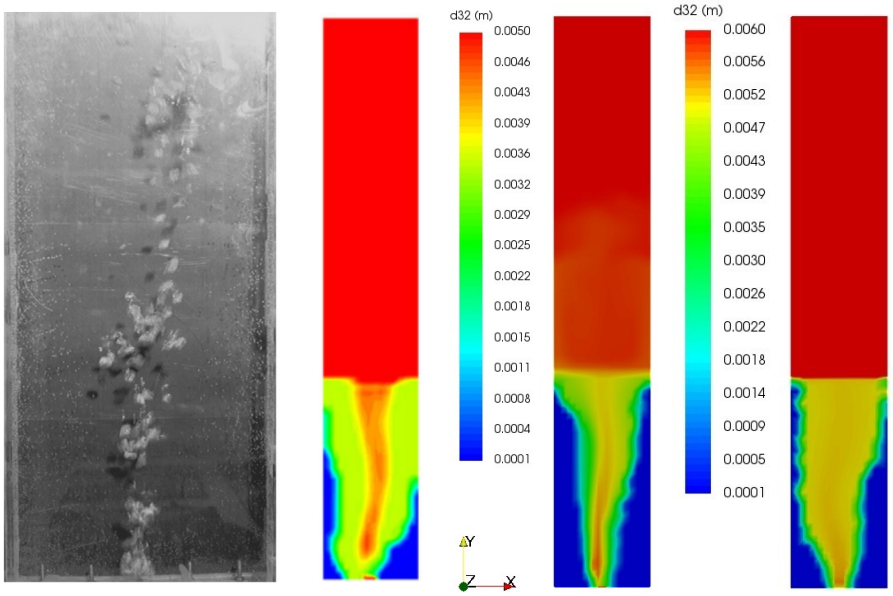

Experiment DQMOM [59] EQMOM CM

Figure 6.3 Experimental snapshot of a meandering bubble plume by Buwa et al. [121] and the predicted Sauter mean diameter using DQMOM (Selma et al. [59]), EQMOM and CM.

EQMOM is capable of providing a smooth reconstruction of the NDF for each arbitrary zone or cell in the computational domain. While this reconstruction is not unique for the set of transported moments, examining the reconstructed NDF can provide a better insight into the behavior of the dispersed phase. In order to plot NDF, weights and abscissae calculated by EQMOM and extracted from CFD-PBM solver are utilized to approximate

Equation (8.20). Figure 6.4 indicates the shape of NDF in the liquid phase (water zone) at $t = 60$ s. It can be observed that the mean bubble diameter ranges from 1 mm to 6 mm, and thus, the monodispersity is not a suitable approximation. As can be observed from Figure 6.4a, the NDF is represented by a Dirac delta function for $N = 2$, while Figure 6.4b exhibits a continuous NDF for $N = 3$. This means the increase of the nodes in EQMOM configuration applied in the bubble column leads to the creation of a spread in bubble sizes, even locally.

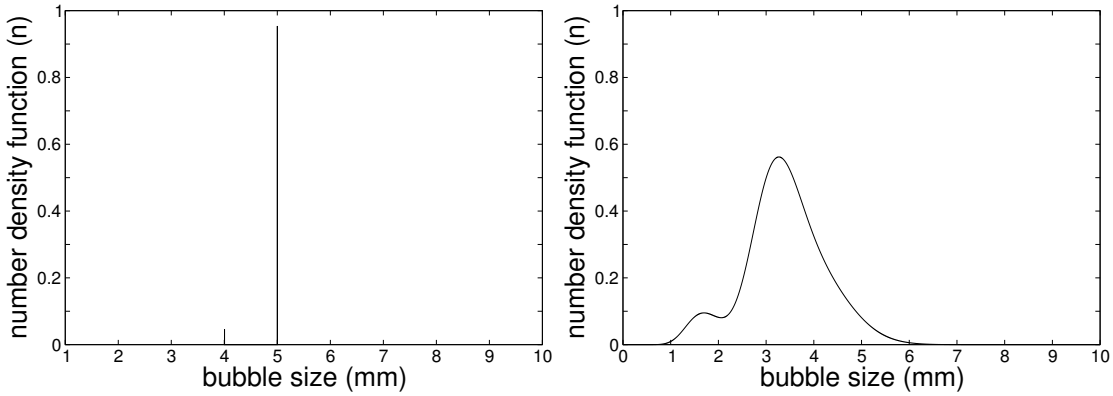

(**a**) (**b**)

Figure 6.4 Number density function in water zone (liquid phase) using EQMOM (**a**) $N_\alpha = 2$ and (**b**) $N_\alpha = 3$.

Test Case 2: 3D Bubble Column

For the second case, the coupled PBM-TFM solver was tested in a square bubble column (Deen [122]). The models used in the simulations are summarized in Table 6.13. This configuration is based on the work of Holzinger [9] in which the same test case was studied using a monodisperse bubble size distribution. In Test Case 2, QMOM and EQMOM simulations were performed.

The column has a square cross-section with W (width) $= D$(depth) $= 0.15$ m. The sparger is in the form of a square, the are of which is $A_{in} = 0.03 \times 0.03$ m. The dimensions and boundary conditions are shown in Figure 6.5. The domain is discretized into $15 \times 15 \times 60$ control volumes, a total of 13,500 cells. Figure 6.6 shows the comparison between QMOM and EQMOM with the experimental measurements reported by Deen [122] Three nodes were used for QMOM, and three primary nodes were used for EQMOM. The EQMOM approach yielded a minor improvement in the gas velocity profile, while no change was observed through the liquid velocity profile. Likewise, the color maps of the Sauter mean diameter are similar for both methods, as shown in Figure 6.7. In spite of the similarity, the computational cost of EQMOM is higher than the QMOM method, as Madadi-Kandjani

and Passalacqua [79] reported for a zero-dimension case, as well as the current simulation process.

Settings	Model
Two-phase flow	Two-fluid model
Drag	Ishii and Zuber [30]
Lift	$C_l = 0.5$
Virtual mass	$C_{vm} = 0.5$
Turbulence	Behzadi et al. [39]
Population balance	EQMOM and QMOM
Coalescence	Hagesather et al. [65]
Breakage	Luo and Svendsen [67]

Table 6.13 Overview of the models used in the solver.

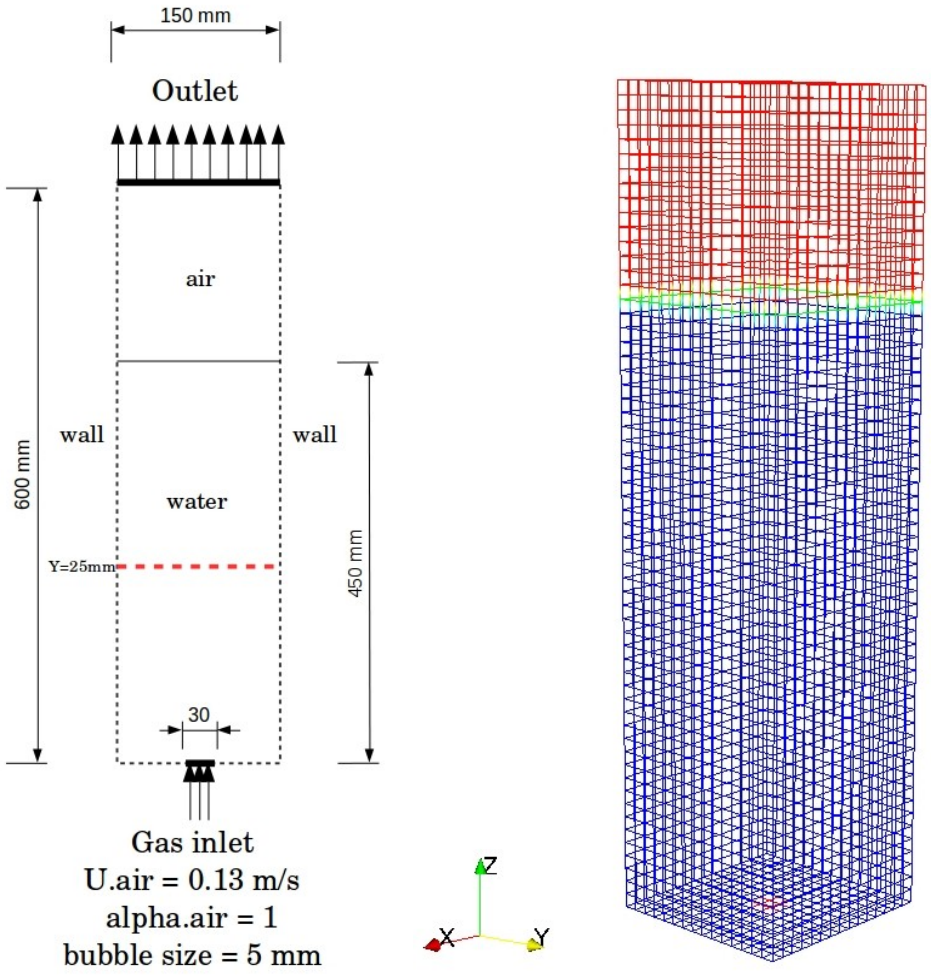

(**a**) (**b**)

Figure 6.5 (**a**) Dimension and boundary condition in the bubble column (Deen [122]) and (**b**) the mesh (13,500 cells) in the case of Deen [122].

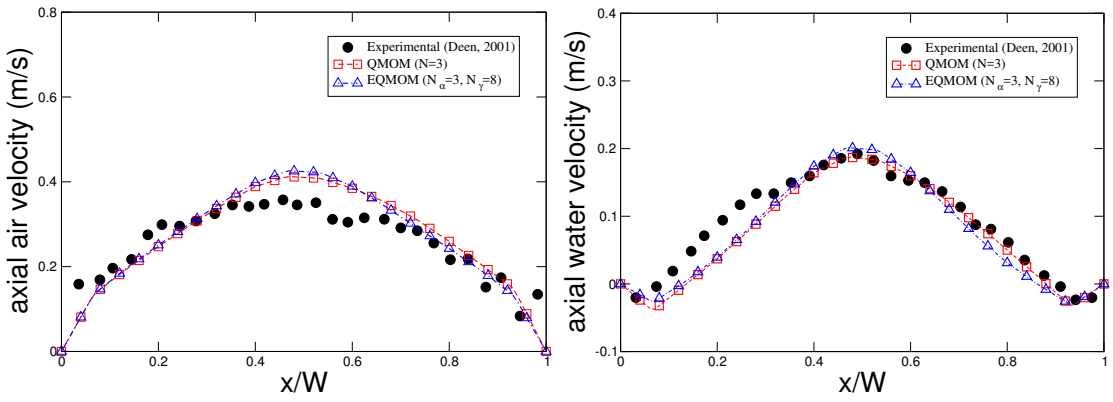

(**a**) (**b**)

Figure 6.6 Comparison between EQMOM and QMOM against experimental data: (**a**) axial gas velocity and (**b**) axial liquid velocity for the case of Deen [122]

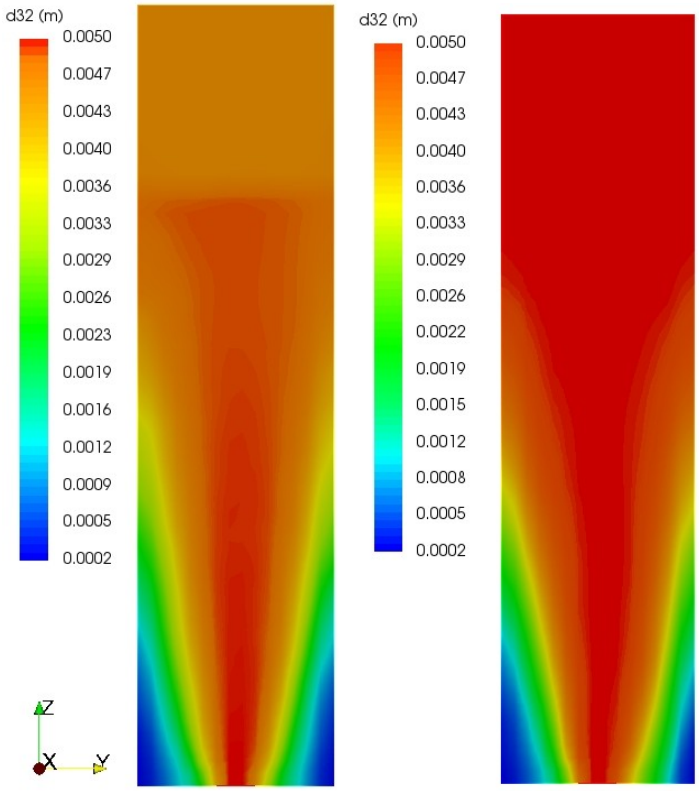

EQMOM QMOM

Figure 6.7 Color maps of time-averaged Sauter diameter along the plane located in the middle of the column of Deen [122].

Test Case 3: Water Electrolysis Reactor

The bubbly flow in a water electrolysis reactor consisting of a gas evolution electrode was chosen as the third case. This decision is based on the simplicity of the case and

on the availability of experimental data for the bubble size distribution. It was decided to investigate the Inverted Rotating Disk Electrode (IRDE) proposed by Parys et al. [2], which is composed of three electrodes as follows:

- Reference electrode: Ag/AgCl saturated with KCl
- Counter electrode: platinum grid
- Working electrode (rotating electrode): made by embedding a platinum rod in an insulating Poly Vinylidene Fluoride (PVFD) cylinder.

When a potential difference is applied between electrodes, hydrogen is produced at the cathode and oxygen at the anode in the form of bubbles. In this case, we put aside the influence of the anode, because the experimental bubble distribution is only available over cathode and hydrogen bubbles. Consequently, the impact of oxygen bubbles is not taken into account in the simulation. The specifications of the IRDEreactor are presented in Figure 6.8. In this system, the rotating cathode is considered as an inlet boundary with imposed velocity, volume fraction and bubble size distribution. The angular component of the liquid velocity is set according to the rotational speed of working electrode ($\omega = 100$ and 250 rpm). According to the applied rotational speeds, the calculated Reynolds number is less than the critical ones [49]. Therefore, the flow regime is laminar, which allows neglecting source terms in the population balance model because of $\epsilon = 0$. In the present study, gas hold-up is extremely low. The bubbles follow the bulk flow and are affected by the continuous phase (water), but not vice versa. Hence, the flow field was calculated with a single-phase solver. The flow field obtained from the single-phase approach was then imported in the population balance solver, in order to advect the bubble size distribution imposed at the inlet and study how bubbles distribute in the IRDE. The settings, boundary and initial conditions used in the simulation are summarized in Tables 6.14-6.15.

Settings	**Model**
single-phase flow	-
laminar	-
population balance	EQMOM
coalescence	no
breakage	no

Table 6.14 Models used in the simulations of Test Case 3.

A distribution of bubble sizes is observed at the electrodes of the IRDE reactor. For this reason, the continuous distribution function reported by Nierhaus [49] was used in the simulation and imposed at the electrode surface, which is treated as an inlet boundary for the gas phase (Figure 6.9a).

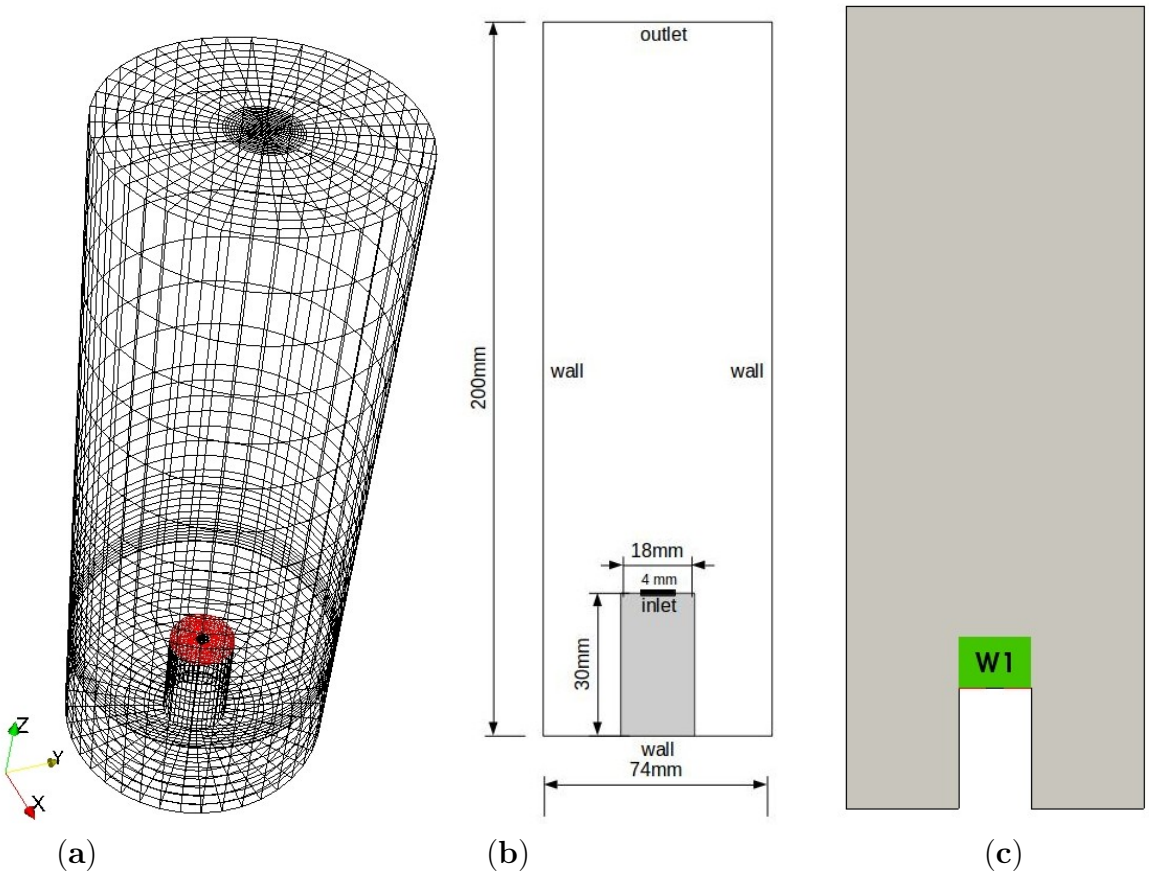

Figure 6.8 (**a**) Schematic of hexahedral mesh [123]. (**b**) The specifications of the reactor and (**c**) the location of volume W1.

A grid with 34,300 hexahedra yielded sufficiently accurate results for the proposed problem and was selected for the IRDE study.

Nierhaus [49] reported the experimental bubble size distributions in an optical window (W1) for two different rotating velocities, 100 rpm and 250 rpm. Figure 6.8 illustrates how the $W1$ volume has been configured in the IRDE reactor. W1 was located above the electrode to enable tracking bubbles in the rising plume. Figure 6.9b compares the computed axial velocity component profile $u_z{}^*(= \frac{u_z}{\sqrt{\omega_z \nu}})$ as a function of the dimensionless height ($\gamma = \frac{z}{\delta}$), where δ is the displacement thickness of the fluid boundary layer ($\delta = \sqrt{\frac{\nu}{\omega_z}}$). The comparison shows that the numerical results match with the analytical solution [88] in the region close to the electrode. The confirmed flow field applied in population balance calculations for its NDF consists of the accumulation and convection term (physical space).

To validate the CFD-PBM solver in IRDE, an analysis is applied to investigate the bubble size distribution in volume W1. The comparison of the bubble size distribution

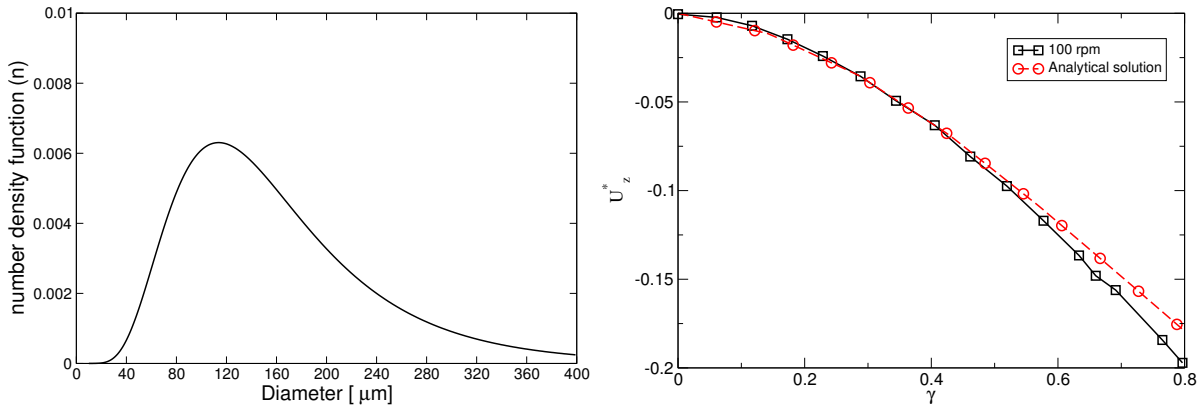

(**a**) (**b**)

Figure 6.9 (**a**) The continuous distribution function imposed at the electrode surface (Nierhaus [49]); (**b**) mean axial velocity component profile $u_z{}^* = \frac{u_z}{\sqrt{\omega_z \nu}}$ and comparison to the analytical solution.

	Boundary Conditions			**Initial Condition**
	Inlet	Wall	Outlet	Inlet value
$m_i =$	1 $i=0$			
	145 $i=1$			
	$26,801$ $i=2$			
	6.31×10^{6} $i=3$	Neumann	Neumann	
	1.89×10^{9} $i=4$			
	7.26×10^{11} $i=5$			
	3.54×10^{14} $i=6$			

Table 6.15 Boundary and initial condition for m_i equations used in Test Case 3.

between the experimental study and current CFD-PBM using EQMOM (three nodes) is presented in Figure 6.10. The results thus obtained are compatible with experimental measurements (Figure 6.10a,b). The fair agreement confirms the assumptions in the PBM model, particularly for 150 rpm. In fact, since the bubble size is so small (low Stokes number), most of the effect is due to advection, and no segregation occurs.

In the case of 150 rpm, simulation data better match experimental data, while there is a disagreement for a higher rotational speed. The prime cause of the discrepancy might be the result of the neglect of size change effects in the PBM model.

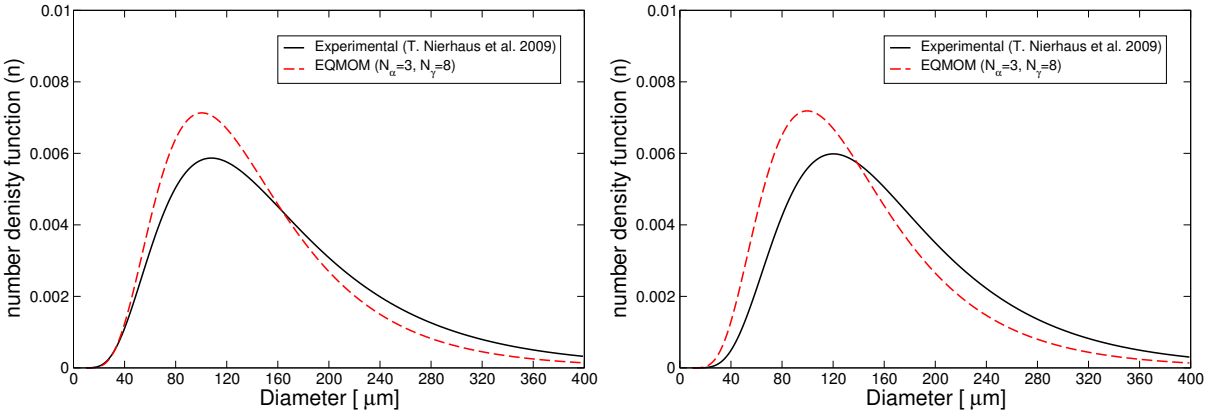

(**a**) (**b**)

Figure 6.10 Bubble size distribution in W1 for (**a**) EQMOM (three nodes) and rpm = 100; (**b**) EQMOM (three nodes) and rpm = 250.

6.2.7 Conclusions

In this paper, an analysis was performed for comparison among local Population Balance Models (PBM), CM, QMOM, DQMOM and EQMOM, based on three cases in the presence of bubbly flow. The purpose of the paper is to validate the CFD-PBM solver, which was applied for two different bubble columns and a water electrolysis reactor to predict the bubble size distribution. The originality of the OpenFOAM solver lies on the fact that it employs the novel method of PBM, which can accept the continuous bubble size distribution as a boundary condition. Moreover, the solver is able to export the distribution function for a specified region in an arbitrary time based on the EQMOM method. It was observed that the CFD-PBM using EQMOM provides a reasonable prediction, as well as CM consisting of 25 classes, but requires less computational demand compared with CM (Table 6.16).

Case	**DQMOM [59]**	**CM (25 Classes)**	**QMOM ($n = 3$)**	**EQMOM ($n = 2$)**	**EQMOM ($n = 3$)**
Test Case 1	1	5	-	1.3	1.4
Test Case 2	-	-	1	-	1.5

Table 6.16 Normalized computational costs of applied PBMs in Test Cases 1 and 2.

From the research that has been carried out, it is possible to conclude that QMOM and EQMOM have similar predictions. EQMOM is computationally more expensive than QMOM, although it is able to obtain a continuous NDF of the model. In order to simulate bubbly flow in the bubble column, it is proposed to use at least three nodes in the EQMOM

technique. This minimum value is required to acquire a continuous NDF function. It is evident that the experimental and numerical NDF can be compared in the water electrolysis reactor (IRDE). Agreement is achieved using EQMOM in the IRDE reactor. The results proved that the most dominant term is advection in the PBM model.

CHAPTER 7

Application of EQMOM in Turbulent Gas-liquid stirred tank (part 1)

7.1 Avant-propos

Auteurs et affiliation :

Ehsan Askari : Étudiant au doctorat*

G. St-Pierre Lemieux : Étudiant au doctorat*

C. Braga Vieira : Étudiante au post-doctorat*

G. Litrico : Étudiante au doctorat*

Pierre Proulx : Professeur*

* Université de Sherbrooke, Faculté de Génie, Département de Génie Chimique et de Génie Biotechnologique

Date de soumission : 8 juin 2017
Date de acceptance : 9 août 2017
Date de publication : 31 juillet 2018

Revue : AIP Conference Proceedings (ICNAAM 2017)

Titre français :

Simulation de l'écoulement et du transfert de masse dans un réservoir agité turbulent gaz-liquide avec le solveur CFD-PBM dans OpenFOAM (première partie)

Contribution au document :

Dans cet article, un modèle CFD-PBM utilisant la méthode EQMOM est développé dans OpenFOAM et appliqué dans un réservoir agité turbulent gaz-liquide.

Résumé français :

Dans cette publication, un modèle pour la diffusion de l'oxygène dans un réacteur de 3 litres est établi à l'aide de la boîte à outils pour l'étude numérique d'écoulement dynamique (CFD) OpenFOAM. Ce modèle utilise la première implémentation de la méthode des quadratures de moments, EQMOM permettant d'effectuer des bilans de population (PBM). La modélisation tridimensionnelle du réacteur utilise des cadres référentiels multiples (MRF), une méthode développée pour représenter le déplacement des pales de l'agitateur. La diffusion des gaz et les turbulences sont évaluées dans un contexte Euler-Euler (E-E). Le modèle de turbulence employé est k-ϵ. Une version modifiée du coefficient de traînée de Tomiyama est utilisée pour évaluer l'échange de momentum. Pour accélérer les calculs, des grappes de calculs parallèles ont été utilisées pour évaluer la distribution spatiale de la phase gazeuse, la moyenne des diamètres des bulles de Sauter (d_{32}), la fonction de densité numérique (NDF), la fraction massique d'oxygène dans l'eau et la structure de l'écoulement.

7.2 Simulation of bubbly flow and mass transfer in a turbulent gas-liquid stirred tank with CFD-PBM solver in OpenFOAM: EQMOM application

In the present paper, the oxygen dispersion in a laboratory scale (3 litres) bioreactor is modelled using open source Computational Fluid Dynamic (CFD) package OpenFOAM (Open Source Operation and Manipulation). The combined effect of the bubble breakup and coalescence in the tank is accounted by a novel method of Population Balance Model (PBM) called Extended Quadrature Method of Moments (EQMOM). The three dimensional simulation is made within a Multiple Reference Frame (MRF), which is a well established method for the modelling of mixers. Dispersed gas and bubbles dynamics in the turbulent flow are modelled using Eulerian-Eulerian (E-E) approach with mixture k-ϵ turbulent model. A modified Tomiyama drag coefficient was used for the momentum exchange, as well. Parallel computing is employed to make efficient use of computational power to predict the spatial distribution of gas phase fraction, Sauter mean bubble diameter (d32),

Number Density Function (NDF), oxygen mass fraction in water and flow structure. The numerical results are compared with experimental data, and good agreement is achieved.

7.2.1 Introduction

Modelling of the complex flow in a chemical or bioprocessing reactor in the presence of a rotating impeller, is a formidable computational challenge. The scientific and technical literature on the subject has rapidly evolved from single-phase rotating impeller systems (Holzinger [9]; Lane [124]) to population balance methods aiming at the prediction of the disperse phase bubble sizes (Kerdouss et al. [125, 126]; [127, 128]; Gimbun et al. [113]; Holzinger [9]). Gimbun et al. [113] applied a CFD mass transfer model to simulate gas-liquid stirred tanks agitated by Rushton impeller using Quadrature Method of Moments (QMOM) method. Their model was established for a high speed of impeller which leads to remove the convective and diffusion terms in mass transfer equation of oxygen. Hence, their comparison was based on overall two-phase mass transfer coefficient. Kerdouss et al. [126] reported the same approach but in different stirred tank reactor named "laboratory scale New Brunswick BioFlo " using Method of Classes (CM). These two studies confirm monodispersity of the bubbles is not a good choice in gas-liquid stirred tanks and Population Balance Model (PBM) gives better accuracy. The most used PBMs are CM (Kumar Krishna [106, 107]), QMOM (McGraw [55]), and Direct Quadrature Method of Moments (DQMOM)(Marchisio and Fox [58]). In spite of the fact that the CM is intuitive and accurate, it is computationally heavy due to a large number of required bins to discretize Number Density Function (NDF), properly. Additionally, this way requires a bubble size range to solve the Population Balance Equation (PBE). Compared to CM, QMOM can consider a broad range of bubble size with reduced number of equations. However, in some evaporation and combustion problems (Fox et al. [129]; Yuan et al. [6]) the value of the NDF is needed to be known for null internal coordinates, which is not the case if the QMOM method is used (E. Madadi-Kandjani and A. Passaloacqua [79]). Another most severe restrictions of QMOM is the implicit use of a discontinuous reconstructed NDF which is assumed to be the summation of Dirac delta functions. This limitation can be an obstacle through the simulation of combustion problems, as well as processes involving oxygen dissolution due to mass transfer. DQMOM solves the equations for weights and abscissae directly. Shortcomings related to the conservation of moments affect the DQMOM approach due to the fact that weights and abscissas are not conserved quantities (Yuan et

al. [6]). To overcome these limitations, Yuan et al. [6] introduced an Extended Quadrature Method of Moments (EQMOM) which enables the shape of NDF to be reconstructed from a moment set using continuous kernel density functions instead of Dirac delta functions. Additionally, E. Madadi-Kandjani and A. Passaloacqua [79] reported EQMOM procedures ensure the reconstructed NDF preserves all the moments used for its reconstruction. The formulation of EQMOM equations involves transport by convection and source/sink terms for the coalescence or breakup. In present work, we simulate gas-liquid flow and oxygen transfer from air to water in a laboratory scale (3 litres) New Brunswick bioreactor. The experimental set-up corresponds to the one used by Kerdouss et al. [126]. We employ CFD-PBM solver using EQMOM to reconstruct the bubble size distribution in water zone (liquid phase). In this study, EQMOM was for the first time implemented in the CFD code OpenFOAM to simulate coalescence and breakage of gas-liquid systems in stirred tanks. Moreover, we solved the equation of oxygen mass fraction by our CFD-PBM OpenFOAM solver to achieve the concentration distribution of oxygen as a dissolved component in water. The implementation and use of EQMOM with a log-normal NDF in a two phase CFD solver based on open source CFD code OpenFOAM and validation of flow regime, for a rotational speed of impeller (flooding behaviour), are the main novelties of this work.

7.2.2 Numerical model

The flow model is based on solving Navier-Stokes equations for The Eulerian-Eulerian (E-E) multiphase model along with mixture k-ϵ turbulent model [39]. Tomiyama drag coefficient has been selected in the model [130]. Other forces such as lift and added mass force have not been included in this paper. We applied the EQMOM method using log-normal kernel density function with two primary nodes and six secondary nodes which is implemented in the CFD program. The breakup model of Luo and Svendsen [67] and coalescence model of Hagesather et al. [65], were used in population balance library. Dissolved oxygen concentration equation is added to the system regarding mass concentration fraction. The saturation concentration fraction is calculated by Henry's law and Danckwerts volumetric mass transfer coefficient (Dhanasekharan et al. [102]) was applied to model oxygen transfer between gas and liquid.

7.2.3 Tank specifications and numerical technique

The solution domain for experimental system investigated in this work, is shown in Fig. 7.1. The Salome and snappyHexMesh as open source tools are used as geometry and mesh generator, respectively. Figs.7.1.b-c show essential features of the 482'422 cells generated for the tank consisting of hexahedral, prisms, tetrahedral and polyhedral. The final mesh resolution is based on Kerdouss et al. [126] which allows us to consider 2-3 bubbles per each computational cell. The domain of tank is discretized by an unstructured finite volume method obtained using CFD-PBM OpenFOAM solver to convert the governing equations to algebraic equations that can be solved numerically. In this work, reactinhTwoPhaseEulerFoam solver of the Open source CFD code OpenFOAM-4.0 was added to simulate the gas-liquid dispersion. The solver was integrated and fully coupled with open-source implementation of Quadrature-Based Moment Methods (OpenQBMM) [131].

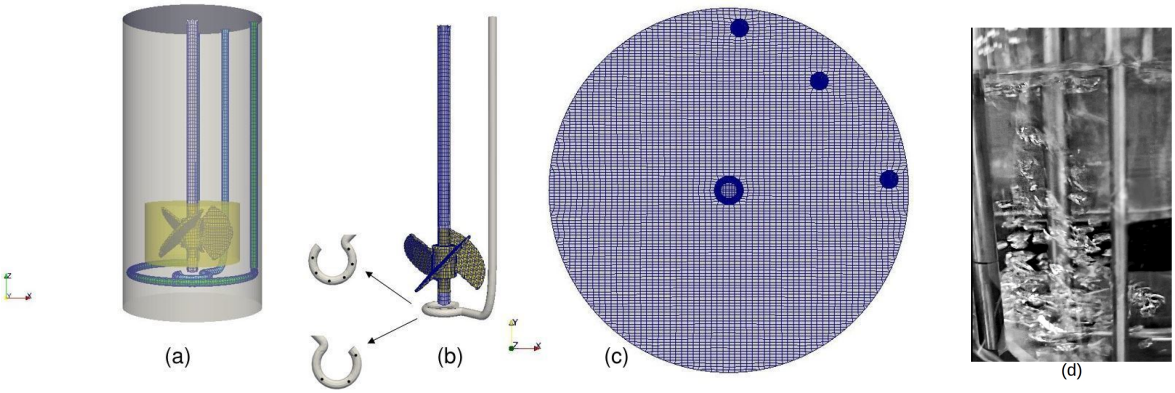

Figure 7.1 From left to right: (a) solution domain and MRF zone, (b) unstructured mesh in impeller and shaft with sparger location and (c) front view of unstructured mesh and (d) experimental image in the reactor for 50 rpm

7.2.4 Discussion and results

The current case 50 rpm falls into the flooding regime which is close to borderline between loading and flooding regime according to the prediction based on Froud and Flow dimensionless numbers ($Fr = \frac{n^2 D}{g}$, $Fl = \frac{Q_G}{nD^3}$) [132]. The Froud number is the ratio of the impeller driven acceleration and gravity, and flow number is the ratio of gas flow rate and impeller driven flow rate. Flooding behavior has been observed in the experiment (Fig.7.1.d) and simulation (Fig.7.2.c) concerning gas phase fraction. This similarity verifies the

CFD-PBM solver, qualitatively. For quantitative validation, the evolution of the dissolved oxygen concentration ([DO]) calculated using Danckwerts volumetric mass transfer coefficient (surface renewal theory) was tracked versus time and compared with experimental measurements. Fig.7.2.c shows predicted oxygen concentration profile is in good agreement with our experimental data.

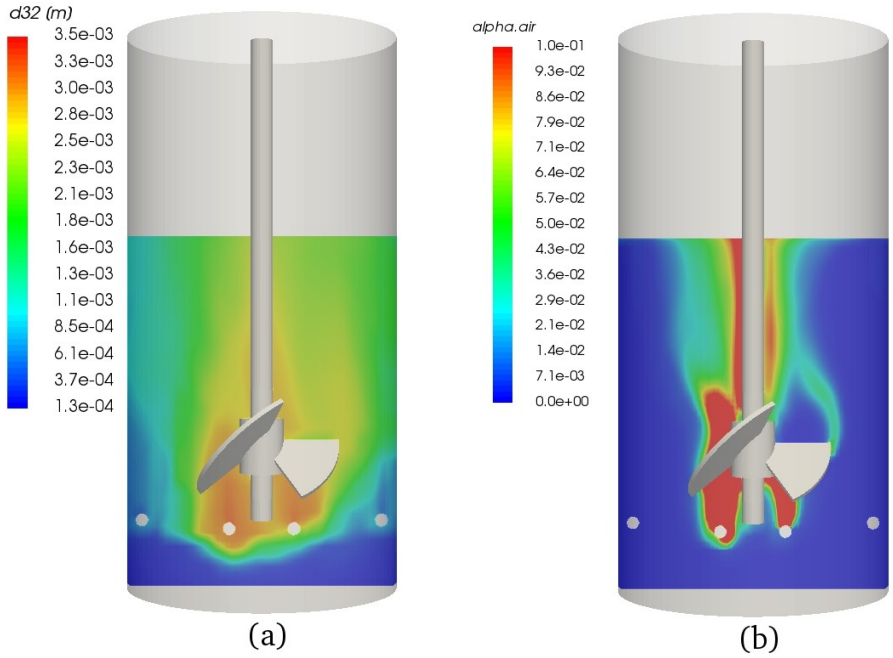

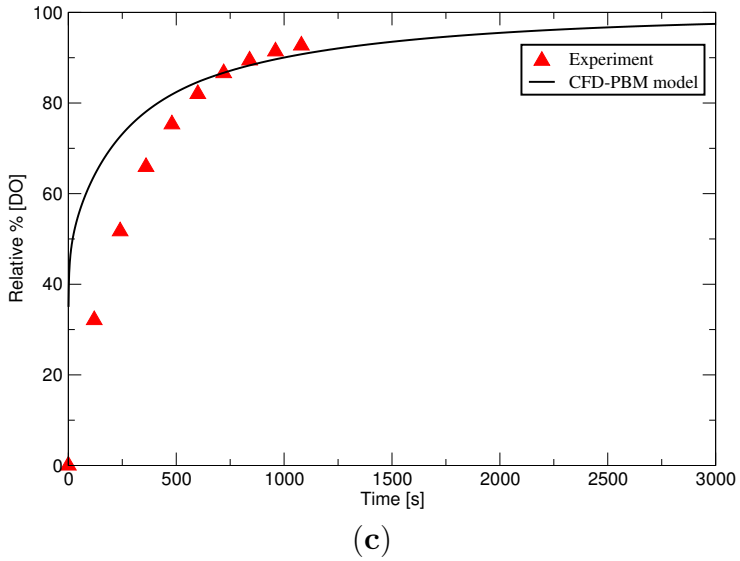

Figure 7.2 From left to right: (a) contour of Sauter mean diameter (b) contour of gas phase fraction and (c) Prediction of the evolution of the dissolved oxygen [DO]

The results obtained in Fig.7.2.a, local Sauter mean bubble diameter (d32) is reduced along the axial direction. When bubbles move upward and pass the impeller zone, the vortex caused by rotation of impeller affects the bubbles. The strong eddies decrease the bubble size in impeller region due to breakage event.

EQMOM is capable of reconstructing continuous NDF and provide more detailed information about dispersed phase and bubble particles. Fig. 7.3 indicates the shape of NDF in the liquid phase for a five- second period. The reason behind of using of PBM is to capture the physics of the problem accurately. Even from the size distribution, it can be observed that there are bubbles with different mean values. The mean bubble diameter nearly ranges from 0.1mm-4 mm and thus the monodispersity is not a good approximation.

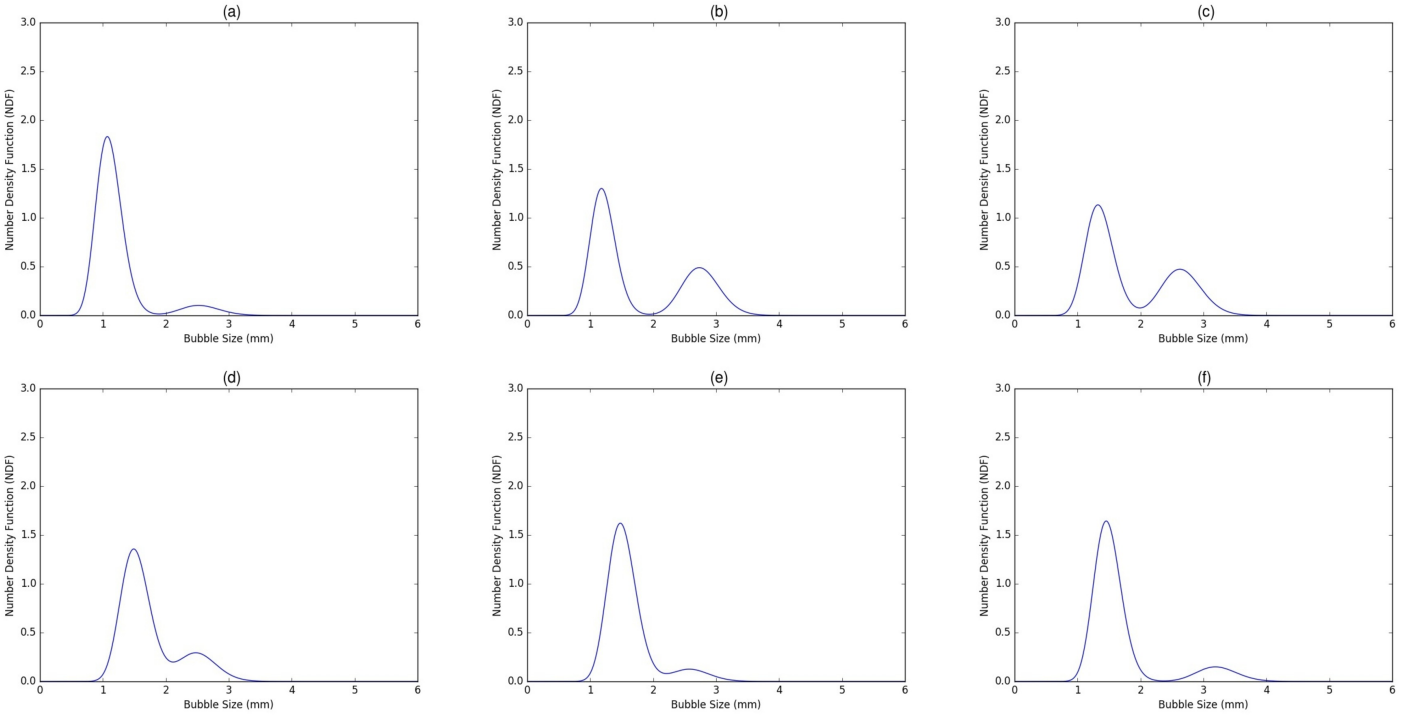

Figure 7.3 Number Density Function (NDF) in water at time= (a) 10s, (b) 11s, (c) 12s, (d) 13s, (e) 14s and (f) 15s

7.2.5 Conclusion

In this work, E-E model coupled with EQMOM to simulate turbulent gas-liquid flow in a stirred tank reactor and concentration distribution of dissolved oxygen in the water. The low speed of impeller (50 rpm) was selected to simulate in which was operated under

flooding regime condition. The comparison between CFD result and the experimental observations indicated the flooding regime is well-predicted by CFD-PBM solver in terms of gas phase fraction and dissolved oxygen evolution. The solver is able to extract the continuous bubble NDF for each arbitrary zone of the domain because of the capability of EQMOM approach in capturing the mean values along with the deviation from the mean. It is seen when gas bubbles pass impeller, their size is reduced. In our future investigations, we will study the effect of rotational speed of impeller on NDFs in different flow regimes of stirred tank reactor.

CHAPTER 8

Application of Extended Quadrature Method in Gas-Liquid Stirred Tanks (part 2)

8.1 Avant-propos

Auteurs et affiliation :

Ehsan Askari: Étudiant au doctorat*

G. St-Pierre Lemieux: Étudiant au doctorat*

Pierre Proulx: Professeur*

* Université de Sherbrooke, Faculté de Génie, Département de Génie Chimique et de Génie Biotechnologique

Date de soumission : 1 juin 2018
Date de acceptance : 13 septembre 2018

Revue : The Canadian Journal of Chemical Engineering

Titre français :

Simulation d'écoulement de bulles et du transfert de masse dans une cuve agitée et turbulente avec le solutionneur CFD-PBM dans OpenFOAM (2ième partie).

Contribution au document :

Dans cet article, le modèle CFD-PBM utilisant EQMOM est appliqué et validé dans deux réservoirs agités gaz-liquide. Les résultats de la turbine axiale sont discutés sur la base de quatre vitesses de rotation de la turbine avec différents coefficients de transfert de masse volumétrique.

Résumé français :

Dans cette publication, un modèle pour la diffusion de l'oxygène dans un réacteur de 3 litres utilisant une agitation axiale est établi à l'aide de la boîte à outils pour l'étude numérique

d'écoulement dynamique (CFD) OpenFOAM. L'effet combiné de la fragmentation et de la coalescence dans le réacteur est évalué grâce à la première implémentation de la méthode des quadratures de moments (EQMOM). Il s'agit d'une méthode permettant d'effectuer des bilans de populations (PBM). La modélisation tridimensionnelle du réacteur utilise des cadres référentiels multiples (MRF), une méthode développée pour représenter le déplacement des pales de l'agitateur. La diffusion des gaz et les turbulences sont évaluées dans un contexte Euler-Euler (E-E). Le modèle de turbulence employé est k-ϵ. Une version modifiée du coefficient de traînée de Tomiyama est utilisée pour évaluer l'échange de momentum. Pour accélérer les calculs, des grappes de calculs parallèles ont été employées pour évaluer la distribution spatiale de la phase gazeuse, la moyenne des diamètres des bulles de Sauter (d_{32}), la fonction de densité numérique (NDF), la fraction massique d'oxygène dans l'eau et la structure de l'écoulement. Les résultats numériques produits sont comparés avec des données obtenues en laboratoire. Ces comparaisons permettent d'évaluer les performances du modèle à quatre vitesses angulaires différentes, par conséquent à différents coefficients de transfert de masse.

8.2 Application of Extended Quadrature Method of Moments for Simulation of Bubbly Flow and Mass Transfer in Gas-Liquid Stirred Tanks (part 2)

In the present paper, two gas-liquid stirred tanks, one agitated by a radial impeller and another by an axial impeller, are modelled using the open-source Computational Fluid Dynamic (CFD) package OpenFOAM (Open Source Field Operation And Manipulation). The combined effect of the bubble breakup and coalescence in the tank is considered by a Population Balance Model (PBM) called Extended Quadrature Method of Moments (EQMOM). The three-dimensional simulation is made using a Multiple Reference Frame (MRF), a well-established method for the modelling of mixers. Dispersed gas and bubble dynamics in the turbulent flow are modelled using Eulerian-Eulerian approach (E-E) with mixture k-epsilon turbulent model and the modified Tomiyama drag coefficient for the momentum exchange. The model is developed to predict the spatial distribution of gas phase fraction, Sauter mean bubble diameter (d_{32}), Number Density Function (NDF), Dissolved Oxygen (DO) evolution and flow structure. The numerical results are compared with experimental data and a fair agreement is achieved. The results of the axial impeller

are discussed based on four impeller rotational speeds with different volumetric mass transfer coefficients.

8.2.1 Introduction

Mixing of gas-liquid systems is important in numerous processes such as absorption, desorption, floatation and biochemical fermentations. A good interfacial contact area between gas and liquid obtained by effective and efficient mixing is required to maximize the mass transfer. The modelling of the complex flow in mixing devices is a formidable computational challenge. Although Computational Fluid Dynamics (CFD) methods have significantly advanced with significant contributions from fundamental and applied research in the last 30 years, it still remains a difficult task to use these methods to help in the design and analysis of stirred tanks. The scientific and technical literature on the subject has rapidly evolved from single-phase rotating impeller systems (Luo et al. [133]; Tabor et al. [134]; Micale et al. [135]; Holzinger [9]; Lane et al. [128]) to population balance methods aiming at the prediction of the disperse phase bubble sizes (Luo et al. [133]; Venneker et al. [103]; Kerdouss et al. [100, 125, 126]; Lane et al. [127, 128]; Gimbun et al. [113]; Holzinger [9]).

According to literature available, the modeling of gas-liquid stirred tanks can be made simpler to target overall parametric study, or more complex to describe the bubble size distribution. Single bubble size models can be used to decrease the computational effort while maintaining a local description of the two-phase flow details (Deen et al. [93]; Friberg [94], Morud and Hjertager [95]; Ranade and Deshpande [96]; Ranade [136]). However, this type of model cannot provide reliable information for industrial designs[99]. The prediction of bubble size distribution is an important problem in modeling of the multiphase dispersion. Local monodisperse models in addition to the phase continuity equation, can globally account for polydispersity of the bubbles. As local monodisperse models yield a non-constant bubble size, the disperse phase is local monodisperse with a locally constant diameter of the particles (Kerdouss et al. [100] and Ishii et al. [101]). However, with this approach the local probability distribution of the bubble size is not considered. Detailed models using locally polydisperse approach give more information on the secondary phase behavior (Dhanasekharan et al. [102]; Venneker et al. [103]). The most used methods of locally polydisperse models are Classes Method (CM)(Balakin et al. [104]; Bannari et al. [68], Becker et al. [105]; Kumar and Ramkrishna [106, 107];Puel et al. [108]), Quadrature

Method of Moments (QMOM) (McGraw [55]; Marchisio et al. [44, 45, 109]; Sanyal et al. [110]), and Direct Quadrature Method of Moments (DQMOM)(Silva and Lage [111]; Selma et al. [59];Marchisio and Fox [58]).

The MUSIG (MultiSize Group) model of CM developed by Helmholtz-Zentrum Dresden-Rossendorf (HZDR) [137] for gas-liquid systems has recently become a favourite choice and was released in the latest versions of Open Source CFD Toolbox (OpenFOAM). CM is intuitive and accurate, while computationally intensive. The higher computational cost comes from the large number of classes required to discretize the Number Density Function (NDF). Additionally, this method needs the user to input a bubble size range to solve the Population Balance Equation (PBE).

Comparing with CM, QMOM can consider a wide range of bubble sizes with a reduced number of equations. However, the value of the NDF for null internal coordinates needs to be known. This is not the case when QMOM method is used. Another restriction of QMOM is the implicit use of a discontinuous reconstructed NDF which is assumed to be summation of Dirac delta functions. This limitation can be an obstacle through the simulation of combustion problems, as well as processes involving reaction and dissolution due to mass transnfer. DQMOM directly solves the equations for weights and abscissas. Shortcomings related to the conservation of moments affect DQMOM approach since weights and abscissas are not conserved quantities (Yuan et al. [6]). In order to overcome these limitations, Yuan et al. [6] introduced an Extended Quadrature Method of Moments (EQMOM) which enables the shape of NDF to be reconstructed from a moment set using continuous kernel density functions instead of Dirac delta functions. Additionally, Madadi-Kandjani and Passalacqua [79] reported that EQMOM procedure ensures that the reconstructed NDF preserves all the moments used for its reconstruction. The formulation of EQMOM equations involves transport by convection and source/sink terms for the coalescence or breakup.

Locally polydisperse population balance models have been recently applied to model stirred tanks. Gao et al. [138] simulated droplet breakage in turbulent liquid-liquid dispersion by using a two-fluid model and QMOM method implemented in OpenFoam. They focused on breakage kernels corresponding to several different test cases. Their model predictions validated against experimental data. Li et al. [112] performed a comparison between QMOM and EQMOM in turbulent liquid-liquid dispersion and they observed these two methods provided similar predictions. They performed the reconstruction of the droplet size distribution with the use of EQMOM. Gimbun et al. [113] applied a CFD mass transfer model to simulate gas-liquid stirred tanks agitated by Rushton impeller using QMOM

method. Their model was established for a high speed mixing. In such circumstance, the convective and diffusion terms can be ignored. Hence, their comparison was based on overall two-phase mass transfer coefficient. In their PBM model (QMOM), the convective term in physical space was removed. Kerdouss et al. [126] reported the same approach but in different stirred tank reactor named "laboratory scale New Brunswick BioFlo" using Class Method (CM). These two studies confirm monodispersity of the bubbles is not a suitable choice in gas-liquid stirred tanks and Population Balance Model (PBM) gives better accuracy.

The previous work (Askari et al. [115]) provided a comparison of computational time for different PBM methods, including DQMOM, QMOM, CM and EQMOM applied in bubble columns. The results indicated the CFD-PBM using EQMOM provides a reasonable prediction in bubbly flow reactors as well as CM consisting of large number classes, but requires less computational demand compared with CM. From that research, it was possible to conclude that EQMOM is computationally more expensive than QMOM. However, the advantage is the reconstruction of the continuous NDF with the same number of nodes.

In the present investigation, the combined Computational Fluid Dynamics (CFD) and Population Balance Model (PBM) approach is applied on two mixer tanks. The first case is a gas-liquid stirred tank containing a radial impeller, so-called Rushton reactor. The second one is a laboratory scale (3 litres) New Brunswick bioreactor agitated by an axial impeller. The experimental set-up corresponds to the one used by Kerdouss et al. [126] for the axial impeller and Deen et al. [93] for the Rushton turbine. The CFD-PBM solver is employed using EQMOM to reconstruct the bubble size distribution in liquid phase. In this study, EQMOM was, to the authors' knowledge, for the first time implemented in the CFD code OpenFOAM to simulate coalescence and breakage of gas-liquid systems in stirred tanks. Moreover, the equation of oxygen mass fraction is solved in bioreactor simulation by the developed CFD-PBM OpenFOAM solver to achieve the concentration distribution of oxygen as the dissolved component in water. The implementation and use of EQMOM with a log-normal NDF in a two phase CFD solver based on open source CFD code OpenFOAM and validation dissolved oxygen evolution, are the main novelties of this research. The principle goal of the present research is relied on the application of EQMOM in gas-liquid stirred tank which leads to achieve and investigate the continuous bubble size distribution for different speeds of rotation. The paper is organized as follows. First, The experimental measurements conditions are described. Then modeling method is explained. After that modeling results are validated by comparing them to experimental data. The simulation results are presented and discussed, afterwards.

8.2.2 Experimental setup

Rushton stirred tank with a volume of 14 L, studied by Gimbun et al. [113], was selected for the CFD-PBM modelling of an air-water flow with the presence of radial impeller. The reader is referred to [113] for the configuration details. A 3 L New Brunswick BioFlo 110 bioreactor ($T = 125$ cm) with 2 L working volume is used in this study for the second case. This reactor is equipped with automatic feedback controllers for temperature. The mixing is driven by a 45 degree pitched blade impeller with 3 blades ($D = 7.1$ cm) mounted on a 1 cm diameter shaft placed at the centerline of the bioreactor and located at 22 cm from the head plate of the vessel. The gas is supplied through a ring sparger (with 6 holes of 0.1 cm in diameter) located 5 cm under the center of the impeller. The dissolved oxygen concentration was measured with a polarographic-membrane dissolved oxygen probe (InPro 6800 series O_2 sensors from *Mettler Toledo*). The bioreactor was de-aerated by sparging with N_2 until only minimum levels of dissolved oxygen remained. At this point, air was diffused into the reactor until saturation was achieved.

In the present paper, numerical simulations are compared to the experimental data (conducted at 20°C) of a stirred tank filled with tap water with a total height of $H = 4/3T$, gas flow rate of $2.3 \cdot 10^{-5}$ m$^3\cdot$ s^{-1} for bioreactor and 0.7 VVM for Rushton impeller. Four impeller rotation speeds of 50 rpm, 150 rpm, 300 rpm and 600 rpm correspond respectively to Reynolds number, $Re = \rho_{\mathrm{L}} N D^2/\mu_{\mathrm{L}} \simeq 2.8 \times 10^4$ to 3.5×10^5, for bioreactor and one rotation speed of 513 rpm for radial impeller in Rushton mixer are applied. According to the applied rotational speeds of bioreactor and Rushton turbine, calculated Reynolds number are more than the critical ones reported in the literature for mixers. The water properties is set as $\rho_{\mathrm{L}} = 998.2$ kg $\cdot$ m^{-3}, $\mu_{\mathrm{L}} = 0.00089$ kg $\cdot$ m $^{-1}\cdot$ s $^{-1}$ and σ=0.073 N $\cdot$ m^{-1}. The properties of air are set as ρ_{G}=1.225 kg $\cdot$ m^{-3}, $\mu_{\mathrm{G}} = 1.789 \cdot 10^{-5}$ kg $\cdot$ m$^{-1}\cdot$ s^{-1}.

8.2.3 Numerical model

Governing flow equations

The gas and liquid are described as interpenetrating continua and equations for conservation of mass and momentum are solved for each phase.The flow model is based on solving Navier-Stokes equations for the Eulerian-Eulerian multiphase model along mixture k-ϵ

turbulent model. The continuity equation for the volume fraction of the dispersed phase is written as:

$$\frac{\partial}{\partial t}\left(\rho_G \alpha_G\right) + \nabla \cdot \left(\alpha_G \rho_G \vec{U}_{\mathrm{G}}\right) = 0 \tag{8.1}$$

Where ρ_G, α_G and $\vec{U}_{\mathrm{G}}$ represent the density, volume fraction and average velocity, respectively, of the dispersed phase (Gas). The continuous phase (Liquid) L and the gas phase G are assumed to share space in proportion to their volume such that their volume fractions sum to unity in the cells domain. Hence, the volume fraction of the continuous phase α_L is calculated by:

$$\alpha_{\mathrm{L}} + \alpha_{\mathrm{G}} = 1.0 \tag{8.2}$$

The momentum conservation equation for the phase i after averaging is written as:

$$\begin{aligned} &\frac{\partial}{\partial t}\left(\rho_{\mathrm{i}} \alpha_{\mathrm{i}} \vec{U}_{\mathrm{i}}\right) + \nabla \cdot \left(\alpha_{\mathrm{i}} \rho_{\mathrm{i}} \vec{U}_{\mathrm{i}} \vec{U}_{\mathrm{i}}\right) = \\ &\quad -\alpha_{\mathrm{i}} \nabla p + \nabla \cdot \bar{\bar{\tau}}_{\mathrm{effi}} + \vec{R}_{\mathrm{i}} + \vec{F}_{\mathrm{i}} + \alpha_{\mathrm{i}} \rho_{\mathrm{i}} \vec{g} \end{aligned} \tag{8.3}$$

p is the pressure shared by the two phases and $\vec{R}_{\mathrm{i}}$ are the inter-phase momentum exchange terms. The term $\vec{F}_{\mathrm{i}}$ expresses the Coriolis and centrifugal forces applied in the rotating reference frame for the MRF model and is written as:

$$\vec{F}_{\mathrm{i}} = -2\alpha_{\mathrm{i}} \rho_{\mathrm{i}} \vec{N} \times \vec{U}_{\mathrm{i}} - \alpha_{\mathrm{i}} \rho_{\mathrm{i}} \vec{N} \times \left(\vec{N} \times \vec{r}\right) \tag{8.4}$$

The Reynolds stress tensor $\bar{\bar{\tau}}_{\mathrm{effi}}$ is related to the mean velocity gradients using Boussinesq hypothesis:

$$\begin{aligned} \bar{\bar{\tau}}_{\mathrm{effi}} &= \alpha_{\mathrm{i}} \left(\mu_{\mathrm{lam,i}} + \mu_{\mathrm{t,i}}\right) \left(\nabla \vec{U}_{\mathrm{i}} + \nabla \vec{U}_{\mathrm{i}}^{T}\right) \\ &\quad -\tfrac{2}{3}\alpha_{\mathrm{i}} \left(\rho_{\mathrm{i}} k_{\mathrm{i}} + \left(\mu_{\mathrm{lam,i}} + \mu_{\mathrm{t,i}}\right) \nabla \cdot \vec{U}_{\mathrm{i}}\right) \bar{\bar{I}} \end{aligned} \tag{8.5}$$

Interfacial momentum exchange

The most important interfacial force is the drag force acting on the bubbles resulting from the mean relative velocity between the two phases. Other forces such as lift and turbulent dispersion may in some instances be significant under the velocity gradient of the surrounding liquid and acceleration of bubbles, respectively. Both these forces have not been included in the present study. Scargiali et al. [139] reported turbulent dispersion and lift force are almost negligible in gas-liquid stirred tanks. The term $\vec{R}_{\mathrm{i}}$ is reduced only to the drag force proportional to the mean velocity difference, given by the following form:

$$\vec{R_{\mathrm{L}}} = -\vec{R_{\mathrm{G}}} = K(\vec{U_{\mathrm{G}}} - \vec{U_{\mathrm{L}}}) \tag{8.6}$$

K is the liquid-gas exchange coefficient written as:

$$K = \frac{3}{4}\rho_{\mathrm{L}}\alpha_{\mathrm{L}}\alpha_{\mathrm{G}}\frac{C_{\mathrm{D}}}{d} \mid \vec{U_{\mathrm{G}}} - \vec{U_{\mathrm{L}}} \mid \tag{8.7}$$

Here, d is the bubble diameter.

For calculation of the drag coefficient, the standard correlation of Tomiyama et al. [130] is used to take into account the bubble shape and tap water as fully contaminated liquid:

$$C_D = \max\left\{\frac{24}{\mathrm{Re_p}}(1 + 0.15\mathrm{Re_p^{0.687}}), \frac{8}{3}\frac{\mathrm{Eo}}{\mathrm{Eo}+4}\right\} \tag{8.8}$$

where $\mathrm{Re_p}$ is the relative Reynolds number and Eo is the Eötvös number. The current form of drag model takes into account the effect of turbulence in liquid phase using the definition of Eq.8.9 [140]:

$$\mathrm{Re_p} = \frac{\rho_{\mathrm{L}} \mid \vec{U_{\mathrm{G}}} - \vec{U_{\mathrm{L}}} \mid d}{\mu_{\mathrm{L}} + \mathrm{C}\mu_{\mathrm{t,L}}} \tag{8.9}$$

Here, C is set to 0.3 for capturing the effect of the turbulence [100]. The Eötvös number is ratio of buoyancy force to surface tension and formulated as:

$$\mathrm{Eo} = \frac{g(\rho_L - \rho_G)d^2}{\sigma} \tag{8.10}$$

Turbulence model equations

When the secondary phase is not dilute, primary and secondary phases tend to fluctuate as one entity at high phase fractions. The use of one set of equations for k and ϵ is suggested for the mixture of the continuous and disperse phases [39].

The transport equations for the k_m and ϵ_m are:

$$\frac{\partial}{\partial t}\left(\rho_\mathrm{m} k_\mathrm{m}\right) + \nabla \cdot \left(\rho_\mathrm{m} \vec{U_\mathrm{m}} k_\mathrm{m}\right) = \nabla \cdot \left(\frac{\mu_{\mathrm{t,m}}}{\sigma_\mathrm{k}} \nabla k_\mathrm{m}\right) + P_k^\mathrm{m} - \rho_\mathrm{m}\epsilon_\mathrm{m} + S_k^\mathrm{m} \tag{8.11}$$

$$\begin{aligned}&\frac{\partial}{\partial t}\left(\rho_\mathrm{m}\epsilon_\mathrm{m}\right) + \nabla \cdot \left(\rho_\mathrm{m} \vec{U_\mathrm{m}} \epsilon_\mathrm{m}\right) = \\ &\quad \nabla \cdot \left(\tfrac{\mu_{\mathrm{t,m}}}{\sigma_\epsilon} \nabla k_\mathrm{m}\right) + \tfrac{\epsilon_m}{k_m}\left(C_{1\epsilon} P^{\mathrm{m}_k} - C_{2\epsilon}\rho_\mathrm{m}\epsilon_\mathrm{m}\right) + C_{2\epsilon}\tfrac{\epsilon_m}{k_m} S_k^\mathrm{m}\end{aligned} \tag{8.12}$$

where m refers to the mixture of the two phases. G_kL is the rate of production of turbulent kinetic energy. Further details about the definition of the model parameters are provided by Behzadi et al. [39].

Population balance models and CFD implementation

The prediction of bubble sizes in the stirred tank is required for the calculation of the interfacial area and interphase momentum exchange. In the stirred tank, the gas undergoes a complex phenomenon that tends to break up and coalescence the gas bubbles as they move through the liquid. Breakup tends to occur when disruptive forces in the liquid are large enough to overcome surface tension. Coalescence occurs when two or more bubbles collide and the film of liquid between them becomes thin and eventually ruptures. The approach used here is the change in bubble number density n due to breakage and coalescence mechanisms using population balances equations (PBE). In this work, the EQMOM method using log-normal kernel density function is used. The number density function (NDF) is written as [141]:

$$\frac{\partial n}{\partial t} + \nabla \cdot \left(\vec{U_{\mathrm{G}}} n \right) = \overline{B}_{\mathrm{ag}} - \overline{D}_{\mathrm{ag}} + \overline{B}_{\mathrm{br}} - \overline{D}_{\mathrm{br}} \tag{8.13}$$

where n is the number of bubbles per unit volume, B_{br} and B_{ag} are the birth rates due to break-up and coalescence, respectively. The corresponding death rates are D_{br} and D_{ag}.

The breakage and coalescence source terms are modeled as (Marchisio et al. [44, 45], Marchisio and Fox [46]):

$$\overline{B}_{\mathrm{ag}} = \frac{\zeta^2}{2} \int_0^{\zeta} \frac{\beta \left(\left(\zeta^3 - \zeta'^3 \right)^{1/3}, \zeta' \right)}{\left(\zeta^3 - \zeta'^3 \right)^{2/3}} n \left(\left(\zeta^3 - \zeta'^3 \right)^{1/3}; \mathbf{x}, t \right) n(\zeta'; \mathbf{x}, t) d\zeta', \tag{8.14}$$

$$\overline{D}_{\mathrm{ag}} = n(\zeta; \mathbf{x}, t) \int_0^{\infty} \beta(\zeta, \zeta') n(\zeta'; \mathbf{x}, t) d\zeta', \tag{8.15}$$

$$\overline{B}_{\mathrm{br}} = \int_{\zeta}^{\infty} a(\zeta') b(\zeta|\zeta') n(\zeta; \mathbf{x}, t) d\zeta', \tag{8.16}$$

$$\overline{D}_{\mathrm{br}} = a(\zeta) n(\zeta; \mathbf{x}, t). \tag{8.17}$$

Here, $\beta(\zeta, \zeta')$ is the coalescence rate between bubbles of size ζ and ζ'; $a(\zeta)$ is the breakup frequency of a bubble with size ζ; $b(\zeta|\zeta')$ represents daughter distribution function generated from the breakup of a bubble of size ζ'.

The EQMOM method requires the moment transport equation to be obtained from the NDF equation. The moment definition of order k of the NDF is:

$$M_k = \int_0^{+\infty} n(L; \mathbf{x}, t) L^k dL \tag{8.18}$$

If the moment definition is applied on NDF equation, it leads to:

$$\frac{\partial M_k(t,x)}{\partial t} + \nabla.(\vec{U_G} M_k(t,x)) = \overline{B}_{ag,k} - \overline{D}_{ag,k} + \overline{B}_{br,k} - \overline{D}_{br,k} \tag{8.19}$$

Since the NDF is unknown, it is approximated from the transport moments. Yuan et al. [6] approximated the NDF with a weighted sum of non-negative kernel density functions $\delta_{\sigma_{(NDF)}}(L, L_\alpha)$:

$$n(L) \approx p_N(L) = \sum_{\alpha=1}^{N} W_\alpha \delta_{\sigma_{(NDF)}}(L, L_\alpha) \tag{8.20}$$

where W_α is the non-negative weight of each kernel density function, L_α is the corresponding quadrature abscissae, N is the number of kernel density functions to approximate the NDF and $\sigma_{(NDF)}$ is the variance of the distribution function (NDF).

The coupling with E-E model is done via the Sauter mean diameter:

$$d_{32} = \frac{m_3}{m_2} \tag{8.21}$$

Source terms in the moment transport equations are written as follows:

$$\overline{B}_{ag,k} = \frac{1}{2} \sum_{\alpha_1=1}^{N} \sum_{\beta_1=1}^{N_\alpha} W_{\alpha_1} W_{\alpha_1\beta_1} \sum_{\alpha_2=1}^{N} \sum_{\beta_2=1}^{N_\alpha} W_{\alpha_2} W_{\alpha_2\beta_2} (L^3_{\alpha_1\beta_1} + L^3_{\alpha_2\beta_2})^{k/3} a_{\alpha_1\beta_1\alpha_2\beta_2} \tag{8.22}$$

$$\overline{D}_{ag,k} = \sum_{\alpha_1=1}^{N} \sum_{\beta_1=1}^{N_\alpha} L^k_{\alpha_1\beta_1} W_{\alpha_1} W_{\alpha_1\beta_1} \sum_{\alpha_2=1}^{N} \sum_{\beta_2=1}^{N_\alpha} W_{\alpha_2} W_{\alpha_2\beta_2} a_{\alpha_1\beta_1\alpha_2\beta_2} \tag{8.23}$$

$$\overline{B}_{br,k} = \sum_{\alpha_1=1}^{N} \sum_{\beta_1=1}^{N_\alpha} W_\alpha W_{\alpha\beta} \bar{b}^{(k)}_{\alpha\beta} \beta_{\alpha\beta} \tag{8.24}$$

$$\overline{D}_{br,k} = \sum_{\alpha_1=1}^{N} \sum_{\beta_1=1}^{N_\alpha} W_\alpha W_{\alpha\beta} L_{\alpha\beta}^k \beta_{\alpha\beta} \tag{8.25}$$

where the N primary weights W_α, the corresponding primary abscissas L_α, together with the parameter σ are determined from the first $2N+1$ integer moments of the NDF. The $2N_\alpha$ quantities $\mathrm{W}_{\alpha\beta}$ and $\mathrm{L}_{\alpha\beta}$ called secondary weights and abscissas are computed using the standard Gaussian quadrature formulae for known orthogonal polynomials to the kernel NDF. The breakage kernel is shown by $\beta_{\alpha\beta}$ which is for the bubbles of size $L_{\alpha\beta}$, $a_{\alpha_1\beta_1\alpha_2\beta_2}$ is the aggregation kernel for the bubble size of $L_{\alpha_1\beta_1}$ and $L_{\alpha_2\beta_2}$. The fragmentation distribution function is represented by $\overline{b}_{\alpha\beta}$ which is symmetric in the present work.

These equations have the form of the transport equations of a scalar variable in the dispersed phase and are solved using an open-source quadrature-based population balance solver for OpenFOAM (OpenQBMM). In the current work, two primary nodes and six secondary nodes have been chosen to apply EQMOM approach. A more detailed overview of EQMOM method has been reported in the literature (Madadi-Kandjani and Passalacqua [79], Gao et al. [138], Passalacqua et al. [131]).

Coalescence and breakup kernels

The choice of the coalescence and breakage kernels is a controversial issue in population balance modelling. At the moment there is little information in the literature stating which kernels can be chosen for different systems. It is recommended to examine their suitability and performance for each particular system. In the current investigation, the main focus has been given to general population balance framework (EQMOM) and mass transfer. Thus, the study of different breakage and coalescence functions left for our future work. In the present CFD model, the kernels are chosen based on the ones applied in the previous work for the same reactor and operational condition [126].

Breakup kernel:

A breakup model by [67], derived from theories of isotropic turbulence, is used in this work. In a turbulent flow, bubble break-up occurs when eddies hit the bubbles surface with enough energy to overcome the surface tension. The bombarding eddies must be equal to or smaller than the bubble size as well. The model assumes the break-up is binary. The turbulent break-up mechanism can be modelled as the product of break-up probability and

collision frequency. The probability is due to the energy contained in eddies and collisions happens between bubbles and turbulent eddies.

The breakage density of one bubble of size d_i that breaks into bubbles of sizes d_j and $(d_i^3 - d_j^3)^{1/3}$ is given by [7]:

$$\Omega_{br}(d_i : d_j) = \int_{\lambda_{min}}^{d} \omega_{br}^T(d_i, \lambda) p_{br}(d_i : d_j, \lambda) d\lambda \qquad \left(\frac{1}{sm^3}\right) \tag{8.26}$$

The eddy-bubble collision probability density $\omega_{br}^T(d_i, \lambda)$ has units $(1/sm^3[m])$. The upper integration limit for the eddy size is based on the model assumption that only eddies of size smaller than or equal to the bubble diameter can cause bubble breakage [67].

The breakage density of one particle of size d_i that breaks into particles of sizes d_j and $(d_i^3 - d_j^3)^{1/3}$ is given by [67]:

$$\Omega_{br}(d_i : d_j) = 0.861 \alpha_L n_i (\frac{\epsilon}{d_i^2})^{\frac{1}{3}} \int_{\xi_{min}}^{1} \frac{(1+\xi)^2}{\xi^{11/3}} Exp(-\frac{12 c_f \sigma}{2\rho_L \epsilon^{2/3} d_i^{5/3} \xi^{11/3}}) d\xi \tag{8.27}$$

The increase energy in the surface area is obtained by:

$$c_f = f_{BV}^{2/3} + (1 - f_{BV}^{2/3})^{2/3} - 1 \tag{8.28}$$

where f_{BV} ($= 0.5$ [67]) is breakage volume fraction which equals to $\frac{\nu_j}{\nu_i}$, ξ is the ratio of eddy size to bubble size (dimensionless eddy size) when a bubble splits into two equal bubbles.

Coalescence kernel:

The coalescence rate is usually written as the product of collision rate $\omega_{agr}(d_i : d_j)$ and coalescence efficiency p_c:

$$\Omega_{agr}(d_i : d_j) = \omega_{agr}(d_i : d_j) p_C(d_i : d_j) \tag{8.29}$$

The collision rate of bubbles per unit volume, is given by Saffman and Turner [117] and can be written as:

$$\omega_{agr}(d_i : d_j) = 0.088\pi n_i n_j (d_i + d_j)^2 \epsilon^{1/3} (d_i^{2/3} + d_j^{2/3})^{1/2} \tag{8.30}$$

where ϵ is the turbulent energy dissipation rate per unit volume of liquid and d_i and d_j are the diameter of bubbles of abscissae i and j with their number density been given by n_i and n_j, respectively.

The coalescence probability of bubbles of sizes d_i and d_j is expressed as Luo and Svendsen [67]:

$$p_C(d_i, d_j) = exp\left(-c\frac{\left[0.75(1+\xi_{ij}^2)(1+\xi_{ij}^3)\right]^{1/2}}{(\rho_d/\rho_c + 0.5)^{1/2}(1+\xi_{ij})^3} We_{ij}^{1/2}\right) \tag{8.31}$$

where $C = 0.5$, $\eta_{ij} = \frac{d_i}{d_j}$,$u_{ij} = (u_i^2) + u_j^2)^{1/2}$, $u_i = \beta^{1/2}(\epsilon d_i)^{1/2}$,$\beta$ equals 2.05. In addition, u_i and u_j are bubble velocity and σ is surface tension.

Interphase Oxygen Mass Transfer

In order to model the interphase oxygen mass transfer, the oxygen transport equations are solved along with the phase mass, momentum and population balance equations. The transport equation for the local mass fraction of oxygen in the liquid phase is:

$$\begin{aligned}\frac{\partial}{\partial t}(\rho_L \alpha_L {Y_L}^{O_2}) + \nabla \cdot (\alpha_L \rho_L \vec{U}_L {Y_L}^{O_2}) = \\ \nabla \cdot (\alpha_L \left[\rho_L {D_{L,m}}^{O_2} + \frac{\mu_t}{Sc_t}\right] \nabla {Y_L}^{O_2}) + K_L a(\rho_{L,e}{}^{O_2} - \rho_L{}^{O_2})\end{aligned} \tag{8.32}$$

Where ρ_L, ${D_{L,m}}^{O_2}$, Sc_t, $\rho_{L,e}{}^{O_2}$, $\rho_L{}^{O_2}$, K_L and a are liquid phase density, the mass diffusion coefficient for oxygen in liquid phase, turbulent Schmidt number, equilibrium mass concentration of oxygen in water, mass concentration of oxygen in liquid phase, mass transfer coefficient and interfacial area, respectively.

$\rho_{L,e}{}^{O_2}$ is calculated by using Henry's Law as follows:

$$P_{O_2} = H.{\rho_{L,e}}^{O_2} \tag{8.33}$$

The Henry's constant and diffusion coefficient of oxygen at 20°C, are respectively 4010 Pa kg^{-1} m^3 and 2.01 $\times$ 10^{-9} m^2 s^{-1}. Using the CFD simulation, the volumetric mass transfer coefficient K_La is calculated as the product of the liquid mass transfer coefficient K_L and the interfacial area a. Four theories for the mass transfer coefficient calculation are well knwown from the mass transfer litterature, they are outlined in Table 8.1. The interfacial area is given as function of the local gas volume fraction and local Sauter mean diameter d_{32} which is computed by PBM:

$$a = \frac{6\alpha_G}{d_{32}} \tag{8.34}$$

Label	Theory	Correlation
(1)	Frossling	$Sh = 2 + 0.552 * Re^{0.5} * Sc^{0.33}$
(2)	Higbie	$Sh = 1.13 * Re^{0.5} * Sc^{0.5}$
(3)	Penetration Theory	$K_L = \frac{2}{\sqrt{\pi}}\sqrt{\frac{D_{O_2}U_{slip}}{d_{32}}}$
(4)	Surface Renewal Theory	$K_L = 0.4\sqrt{D_{O_2}}\left(\frac{\epsilon_L}{\nu_L}\right)^{0.5}$

Table 8.1 Overview of mass transfer coefficients used in the model

8.2.4 Tank specifications and numerical technique

The solution domain is shown in Figures 8.1-8.2. BlockMesh as a toolbox of OpenFOAM is employed for the first case and Salome and snappyHexMesh open source tools are used as the geometry and mesh generator in the second case.

Figures 8.1b-c demonstrate 446'341 hexahedral mesh in Rushton turbine. Figures 8.2b-c show essential features of the 482'422 cells generated for the bioreactor tank consisting of hexahedral, prisms, tetrahedral and polyhedral. The final mesh resolution is based on [126] which allows to consider 2-3 bubbles per each computational cell.

In this work, original reactingTwoPhaseEulerFoam solver of the Open source CFD code OpenFOAM-4.0 was used as a base to develop a new CFD-PBM solver called "react-

ingTwoPhaseEulerQBMMFoam". First, the coalescence and breakage kernels and their connection with the turbulence model (k.water and ϵ.water) was developed in Open Quadrature-Based Moment Methods (OpenQBMM) [131]. Then OpenQBMM was fully integrated and coupled in reactingTwoPhaseEuelrFoam. Next, the link between PBM and interfacial momentum exchange was established. Subsequently, the connection among mass transfer library (K_L), PBM (d_{32}) and turbulence (ϵ) was completed. In order to investigate the rotational speed of impeller and mass transfer coefficient in the tank, the sixteen cases described in Table.8.2 were simulated.

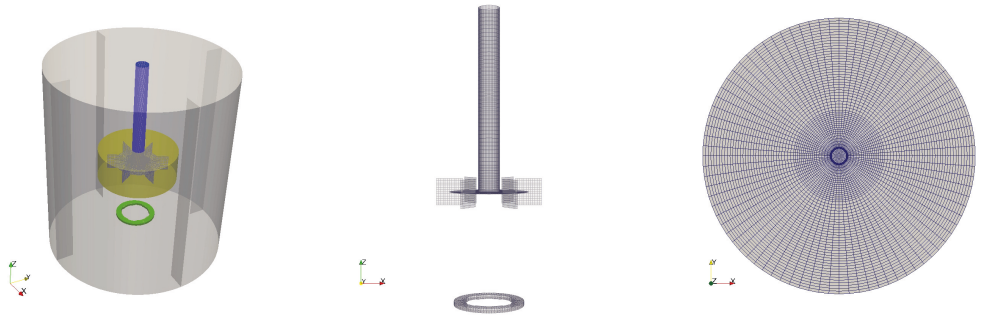

(a) (b) (c)

Figure 8.1 Schematic of Rushton turbine: (a) solution domain and MRF zone, (b) structured mesh in impeller and shaft with location of the sparger ring and (c) front view of the structured mesh

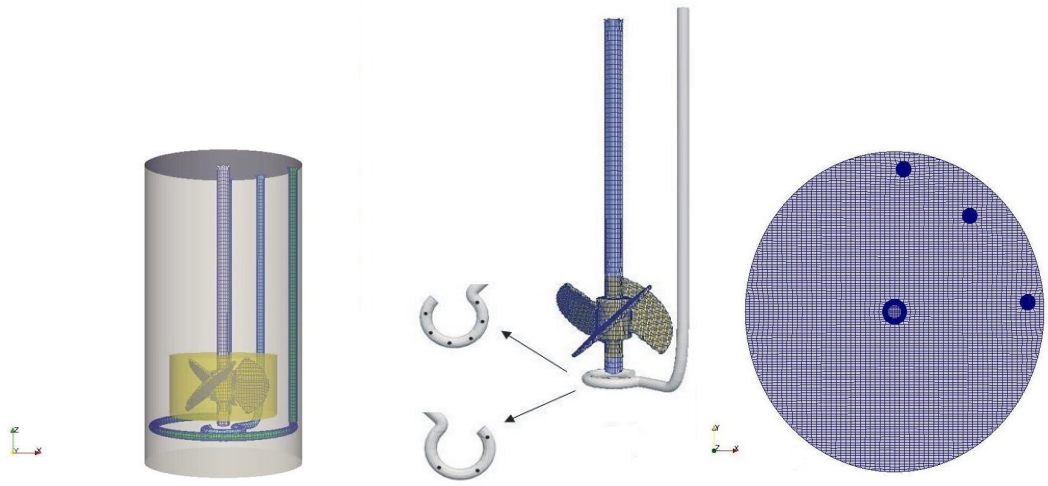

(a) (b) (c)

Figure 8.2 Schematic of bioreactor: (a) solution domain and MRF zone, (b) unstructured mesh in impeller and shaft with sparger location and (c) front view of the unstructured mesh

Test cases	ω	Re	K_L	Test cases	ω	Re	K_L
Case 1	50	3×10^4	(1)	Case 9	300	17.63×10^4	(1)
Case 2	50	3×10^4	(2)	Case 10	300	17.63×10^4	(2)
Case 3	50	3×10^4	(3)	Case 11	300	17.63×10^4	(3)
Case 4	50	3×10^4	(4)	Case 12	300	17.63×10^4	(4)
Case 5	150	8.8×10^4	(1)	Case 13	600	35.2×10^4	(1)
Case 6	150	8.8×10^4	(2)	Case 14	600	35.2×10^4	(2)
Case 7	150	8.8×10^4	(3)	Case 15	600	35.2×10^4	(3)
Case 8	150	8.8×10^4	(4)	Case 16	600	35.2×10^4	(4)

Table 8.2 The main characteristics of the test cases investigated in this study where ω, the rotational speed (rpm) and K_L, the mass transfer coefficient (m/s)

The gas flow rate at the sparger is defined via inlet-velocity boundary condition with gas volume fraction equals to unity. The bubble diameter at gas orifice (the sparger) is assumed to be uniform and is calculated from the following correlation [142] for low gas flow rates:

$$d_b = \left(\frac{6\sigma d_o}{g(\rho_l - \rho_g)} \right)^{1/3} \tag{8.35}$$

where d_o is the orifice diameter.

For simulation performed without the PBE model, the size of all bubbles inside the tank was determined by the same correlation. In this system, the orifices of the sparger are considered as inlet boundary. Shaft, as wall type boundary, separated from the impeller, is rotating. Thus, the velocity was configured in a cylindrical system. Angular component of shaft rotation is according to the rotational speed of impeller (rpm=50 to 600).

An overview of the boundary conditions used in the system is shown in Table 8.3. Multiple Reference Frame (MRF) is employed to model the impeller region. The MRF method represents a good compromise between physical accuracy and reasonable computational effort and is used with the population equations in the present work. To avoid numerical difficulties often encountered in such complex multiphase flows, the calculations were made for two-phase flow starting with the converged quasi steady-state single bubble size flow field. Converged quasi steady-state two-phase flow field with constant bubble size and MRF was used for the calculation of the steady-state two-phase flow with the MRF model and population balance model. Since our experimental observation shows the

oxygen dissolution is a long-term process (between 500-3000 **sec**), a shortcut strategy is adopted. The transient solver of mass transfer is launched with fixed fluid flow provided by steady-state solution of the solver coupling two-fluid model and population balance model. This method greatly accelerates the solution process and enables the user to reach the end time of water saturation. However, it cannot perfectly resolve the time-space evolution in early times of the saturation.

Variable	gas inlet (sparger)	outlet	shaft	impeller	walls
α_G	1	zero grad.	zero grad.	zero grad.	zero grad.
$\vec{U}_G$	$U_{G,inlet}$	inletOutlet	rot. wall vel.	noSlip	noSlip
$\vec{U}_L$	0	inletOutlet	rot. wall vel.	noSlip	noSlip
$k_{L,G}$	k_{inlet}	inletOutlet	kqRWallFunc.	noSlip	noSlip
$\epsilon_{L,G}$	ϵ_{inlet}	inletOutlet	epsilonWallFunc.	noSlip	noSlip
m_i	$m_{i,inlet}$	zero grad.	zero grad.	zero grad.	zero grad.
$Y_L{}^{O_2}$	0	zero grad.	zero grad.	zero grad.	zero grad.

Table 8.3 Overview of divergence schemes used in fvScheme dictionary

8.2.5 Result and Discussion

- **Rushton turbine**

The time-averaged of axial and radial components of water velocity are compared with Deen et al. [93] PIV measurements. The results for the mean velocities were normalized using the impeller tip velocity (V_{tip}). The results predicted by CFD-EQMOM modelling match slightly the experimental data (Figure 8.3).

Figure 8.4 shows the local gas hold-up, the gas velocity vectors and the local bubble sizes obtained by the CFD-PBM simulation for the Rushton stirred tank. The smallest bubbles can be observed around and above the impeller whereas largest bubbles are found between the impeller and the sparger ring. The main reason for this event might be the combination of gas phase fraction and size of turbulent eddies. A large accumulation of the air phase is observed below the impeller. The dissipation rates in the regions close to impeller reach a maximum reducing the bubble size.

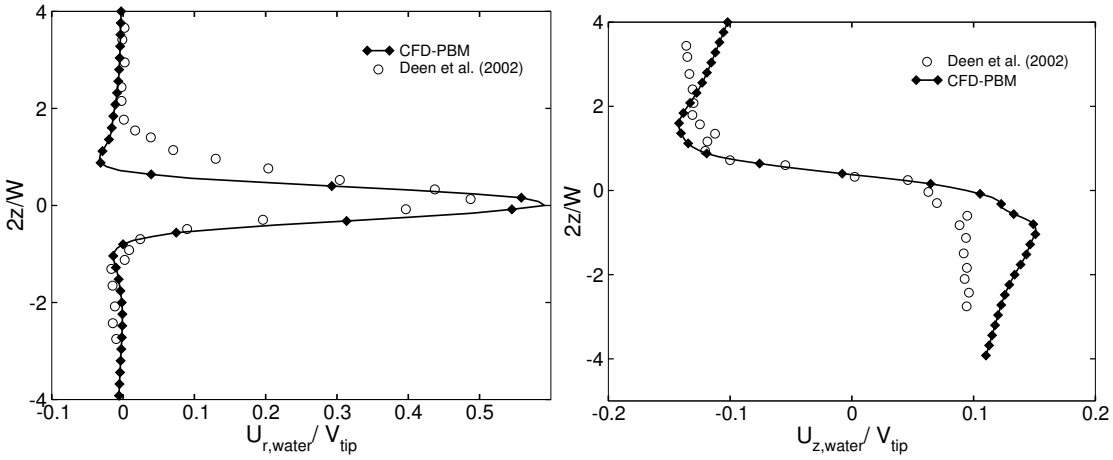

Figure 8.3 Prediction of water axial (u_z) and radial velocity (u_r) at r/R = 0.37 for Rushton turbine

Figure 8.5 demonstrates the 513 rpm case falls into the loading regime. This prediction was made using the Froud and the Flow dimensionless numbers ($\mathrm{Fr} = \frac{N^2 D}{g}$ and $\mathrm{Fl} = \frac{Q_G}{ND^3}$) [132]. The Froud number is the ratio of the impeller driven acceleration and gravity, and flow number is the ratio of gas flow rate and impeller driven flow rate. The type of flow for the current exercise has been observed in simulation (Figures 8.4a-b) concerning the gas phase fraction and gas velocity vectors as well.

- **New Brunswick bioreactor**

The developed CFD-PBM solver was used to simulate the gas-liquid stirred tank as presented in section 2. Here, the validation process is carried out using transient behavior of oxygen concentration in the water due to lack of experimental information on velocity field.

The evolution of the dissolved oxygen concentration (DO) was tracked versus time using transient solver of mass transfer with fixed flow field and compared with the experimental measurements. Figure 8.6 illustrates the above mentioned comparison for 50 rpm, 150 rpm, 300 rpm and 600 rpm. The obtained results are nearly compatible with experimental measurements at final period of time or close to complete saturation. In all cases the shape of the dissolved oxygen concentration versus time is not well described in the first seconds. Experiments show a sigmoid curve followed by a rapid increase, and concluded by a slow final increase. The primary cause of this discrepancy might be due the chosen strategy (transient mass transfer with fixed velocity field) to solve the equation of oxygen concentration.

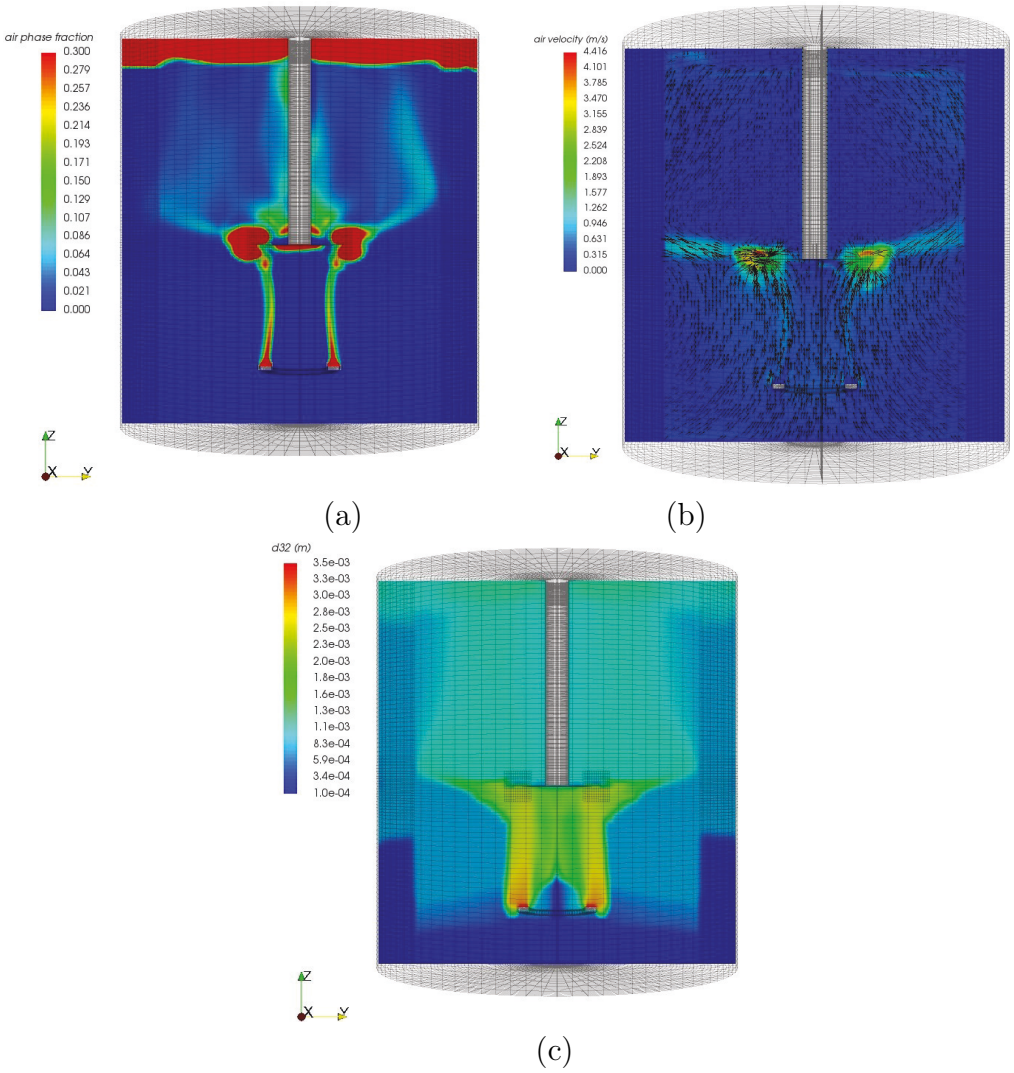

Figure 8.4 Contour map provided by CFD-PBM in Rushton reactor at $\omega = 513$ rpm (a) air phase fraction, (b) air velocity vectors, (c) bubble size (Sauter diameter)

As it can be seen from Figure 8.6a-d, while a slight disagreement is found within initial minutes of oxygenation, a fair agreement is also observed using surface renewal theory in 50 rpm and penetration theory in 150, 300 and 600 rpm.

The presence of discrepancy observed in the model using surface renewal theory might be a result of the prediction of turbulence model which was coupled in the CFD-PBM solver. Since the key variable in the formulation of surface renewal theory is the turbulent kinetic energy dissipation rate (ϵ), the theory failed to predict the oxygen concentration in high turbulent cases. As has been shown in the literature, this problem is very common in the turbulent two-phase flows in mixers. Lane [124] has recently studied this shortcoming

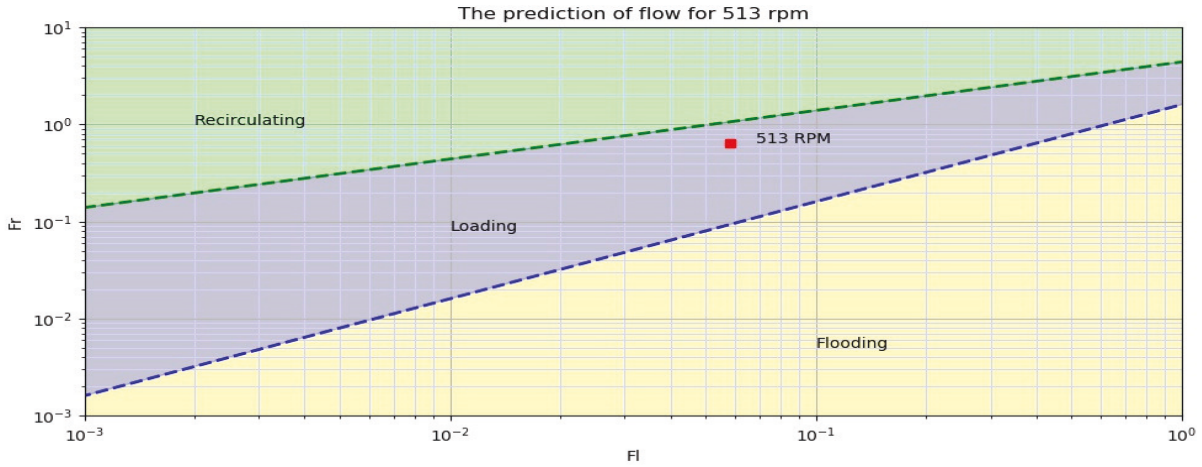

Figure 8.5 The flow condition in Rushton reactor based on [132] for ω=513 rpm

in the modelling of mixer tanks. According to his study, a fine and hybrid mesh can be employed to overcome those difficulties.

As Figure 8.7 represents, the cases 50 rpm, 150 rpm, 300 rpm and 600 rpm fall into the flooding regime, loading regime, borderline of loading and recirculation and recirculation regime, respectively. The type of flow for each exercise has been observed in the experiment (Figure 8.8) and simulation (Figures 8.9-8.10) considering gas phase fraction and gas velocity vectors.

As Figure 8.8 illustrates, the impeller speed increases from 50 rpm to 600 rpm at a constant gas flow rate, the behaviour of the gas-liquid flow in the reactor is undergone considerable changes. Firstly, the gas sparging dominates and creates a bubble column type flow with gas rising in the center. Next, the impeller begins to have an effect and then the circulation patterns of the stirred tank just begin to form. Finally, the circulation loops are partially developed and the impeller dominates the effects of the gas sparging. This similar transition can be predicted by the model which verifies the CFD-PBM solver, qualitatively. Figures 8.9-8.10 display time-averaged gas phase fraction and gas vector velocity in four different rotational speed through a vertical cut in the middle of the reactor.

In spite of the fact that increases in the rotational speed of the impeller lead to higher mixedness and air dispersion, it is still not enough to overcome the gas buoyancy. In the presence of the axial flow impeller, the gas bubbles rise near the shaft where shear forces are small, so that the flow pattern and discharging effect is disrupted. At 600 rpm, the gas dispersion is greater than other cases due to this fact that mixer power is greater than

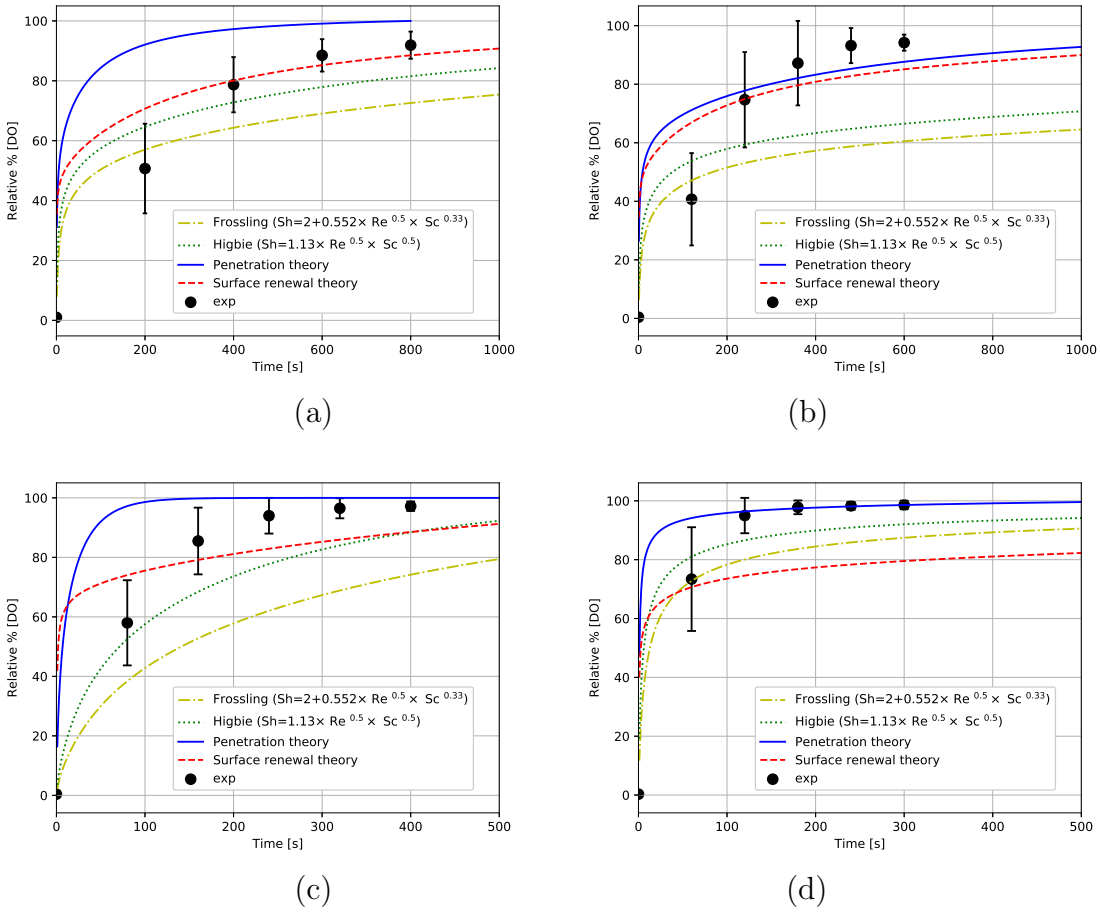

Figure 8.6 DO evolution for (a) ω=50 *rpm*, (b) ω=150 *rpm*, (c) ω=300 *rpm*, (d) ω=600 *rpm*

gas stream energy. However, the strong vortex caused by 600 rpm and water splash pull the injected air into the center of the reactor and the rotating zone. These phenomena bring about more gas accumulation in the middle as well. By contrast (Figures 8.9d and 8.4), the air widely spread through the tank in the Rushton reactor with larger volume and lower rotation speed of the impeller. This issue will be discussed in one reactor with a different configuration of impellers in our future study.

Figure 8.11 exhibits the predicted contours of the local Sauter mean diameter in four different rotational speed along the plane located in the middle of the tank. When the bubbles move upward and pass the impeller zone, the vortex caused by rotation of the impeller affects the bubbles. The strong eddies decrease the bubble size in the impeller region due to breakage event. This phenomenon becomes more intensive with a rise in rotational speed.

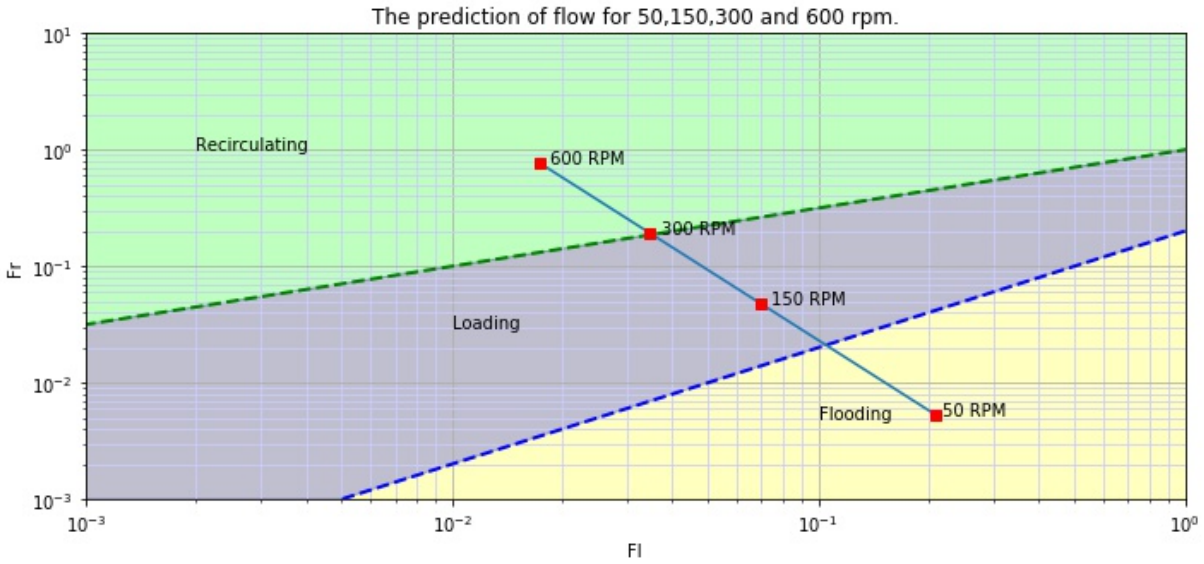

Figure 8.7 The flow condition in reactor based on [132] for ω=50 rpm, ω=150 rpm, ω=300 rpm and ω=600 rpm

(a) (b) (c) (d)

Figure 8.8 Experimental images in stirred tank for (a) ω=50 rpm, (b) ω=150 rpm, (c) ω=300 rpm, (d) ω=600 rpm

EQMOM is capable of reconstructing continuous Number Density Function (NDF) for each arbitrary zone or any cell in a computational domain. This approach allows the acquiring of detailed information about dispersed phase and bubble particles. In order to plot NDF, two weights and two abscissas ($N = 2$) have to be calculated by EQMOM. The extracted values of weights and abscissas from CFD-PBM solver are utilized to approximate Eq.8.20 . Figs.8.12-8.15 indicates one of the possible shapes of the NDF in the liquid phase

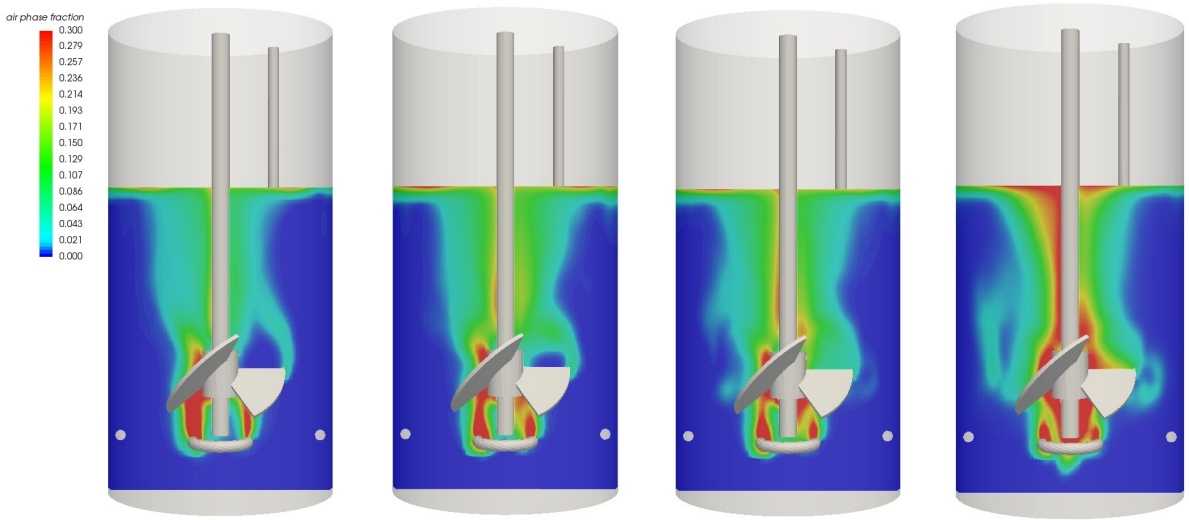

Figure 8.9 Contour of averaged-time gas hold-up along the plane located in the middle of the reactor (a) ω=50 rpm, (b) ω=150 rpm, (c) ω=300 rpm, (d) ω=600 rpm

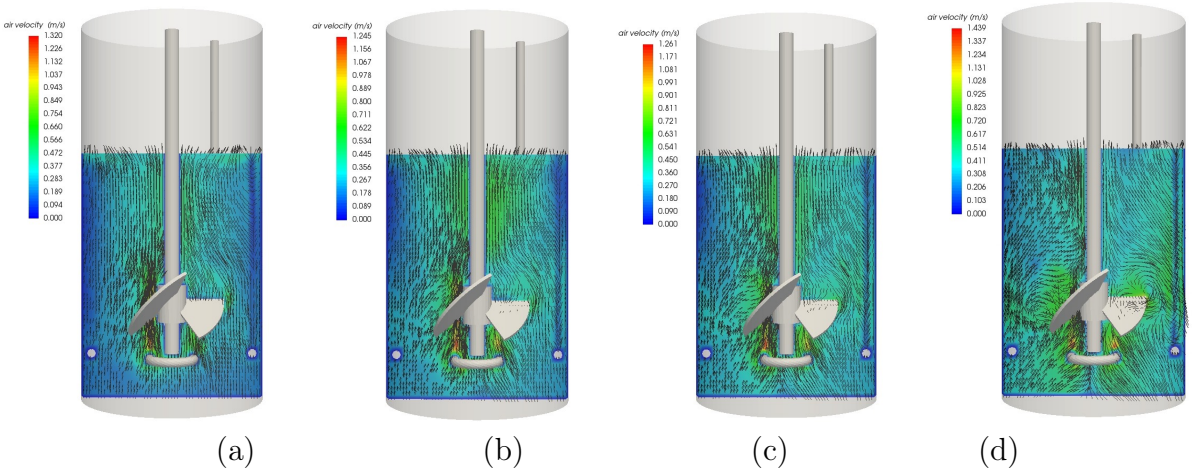

Figure 8.10 Averaged-time gas velocity vector along the plane located in the middle of the reactor ((a) ω=50 rpm, (b) ω=150 rpm, (c) ω=300 rpm, (d) ω=600 rpm

(water zone) corresponding to the considered moments for a four-second period after the achievement of quasi steady-state condition (excluding mass transfer) in the system for different rotational speed of the impeller. To achieve the continuous NDF the average moments through the entire domain was computed and then the spectrum of NDF was reconstructed based on the averaged moments.

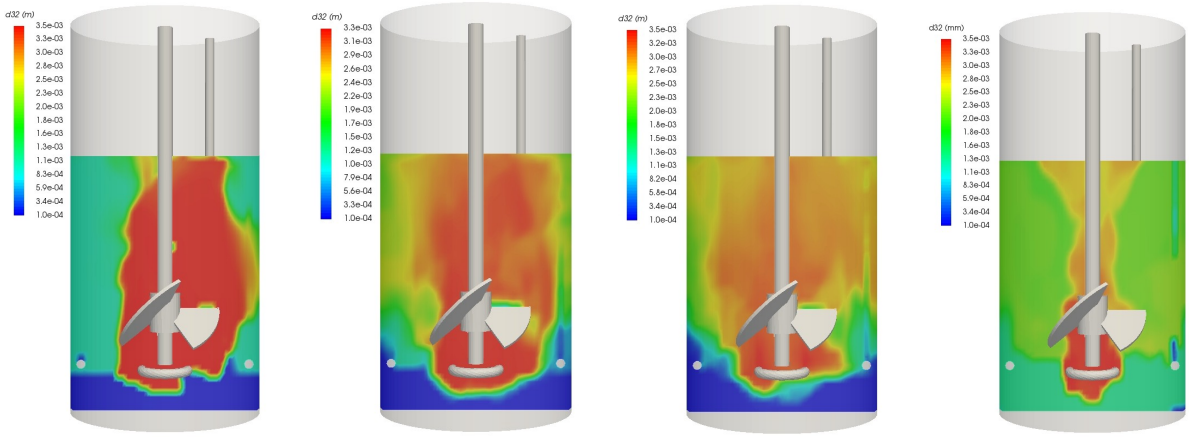

Figure 8.11 Contour of averaged-time local sauter diameter along the plane located in the middle of the reactor (a) ω=50 *rpm*, (b) ω=150 *rpm*, (c) ω=300 *rpm*, (d) ω=600 *rpm*

The reason behind the use of PBM is to capture the physics of the problem accurately. The size distribution shows bubbles with different mean values. The mean bubble diameter ranges from 0.1 mm-4 mm and the monodispersity is not a good approximation. As it can be observed from Figs.8.12-8.14, the NDF is bi-modal for 50 rpm and 150 rpm cases and practically for 300 rpm. This might be due to the limited interaction among bubbles and between bubbles and continuous phase. In these cases, the energy is limited to mixer action. This input is not strong enough to create a smooth trend in the NDF. It was observed that there is only one snapshot in 300 rpm that exhibits a unimodal distribution. As Figs.8.15 demonstrates, the spectrum was totally converted into unimodal distribution and the bimodal trend has disappeared at 600 rpm. This is because of the energy which is spread out through the flow field by the gas stream and the mixer. The released energy generates strong eddies which result in more coalescence and breakage among bubbles compared to the lower speed of the impeller. Another reason might be due to the presence of large polydispersity in high turbulent cases.

8.2.6 Conclusion

In this paper, a study was carried out for two aerated stirred tanks, called Rushton turbine and bioreactor, containing axial and radial impellers, respectively. The CFD-PBM solver which can be applied for a stirred tank to predict the bubble size distribution and local

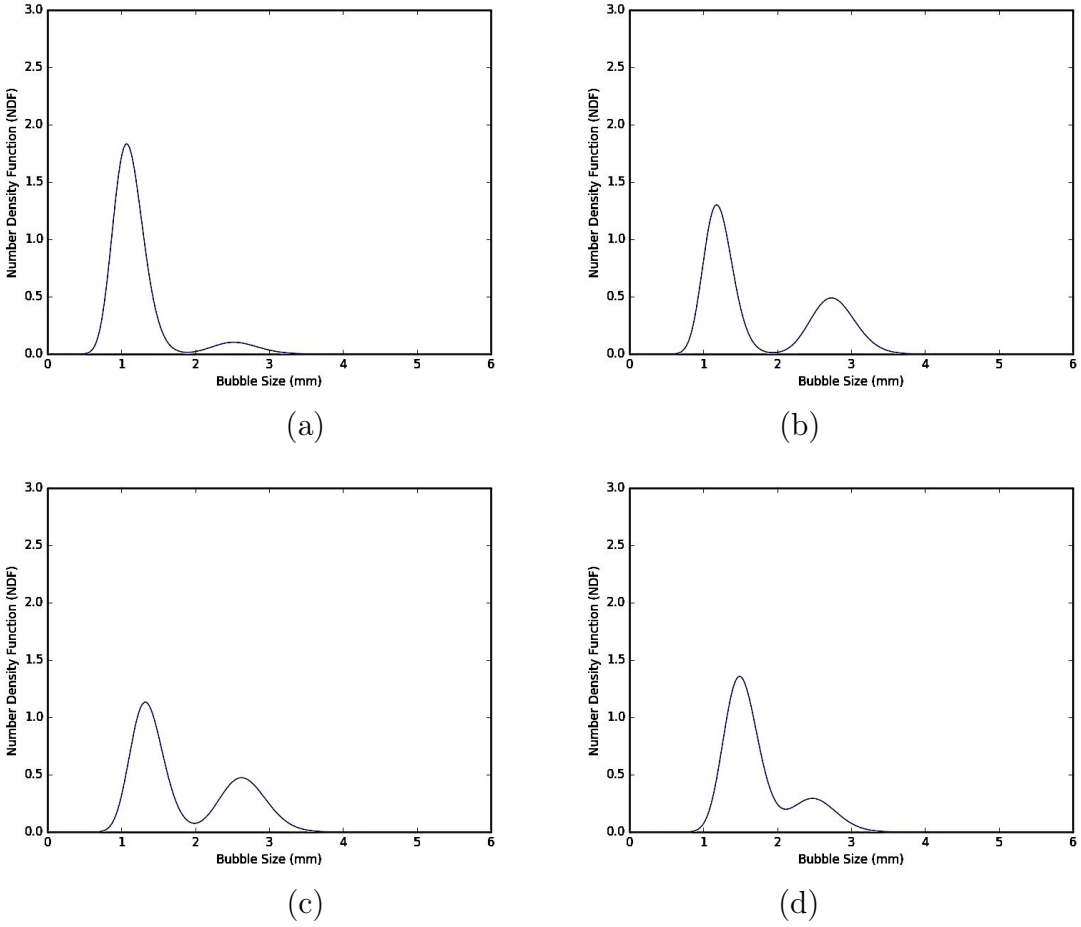

Figure 8.12 Dynamic Number Density Function (NDF) in water zone for 50 *rpm* in (a) δt=1 *s*, (b) δt=2 *s*, (c) δt=3 *s*, (d) δt=4 *s*

oxygen mass concentration in water was fairly validated by the results obtained. The originality of the OpenFOAM solver lies on EQMOM application as PBM model. The implemented PBM can accept the continuous bubble size distribution as the boundary condition and is able to export a distribution function for a specified region in an arbitrary time. For the first time, the described model has been carried out in a stirred tank reactor including gas-liquid flow agitated by an axial impeller. The study of bioreactor shows that the two-phase mass transfer model using surface renewal theory obtains superior predictions (DO) for 50 rpm (the lowest rotational speed of impeller in this work for bioreactor). However, the model using penetration theory appears to be more appropriate (DO) for 150, 300 and 600 rpm. From the numerical results, it is evident the NDF is bimodal for 50,150 and nearly 300 rpm and unimodal for 600 rpm. The proposed model also shows that the prediction of (DO) have a slight discrepancy in early times between the numerical results and experimental data. This aspect of the model should be further

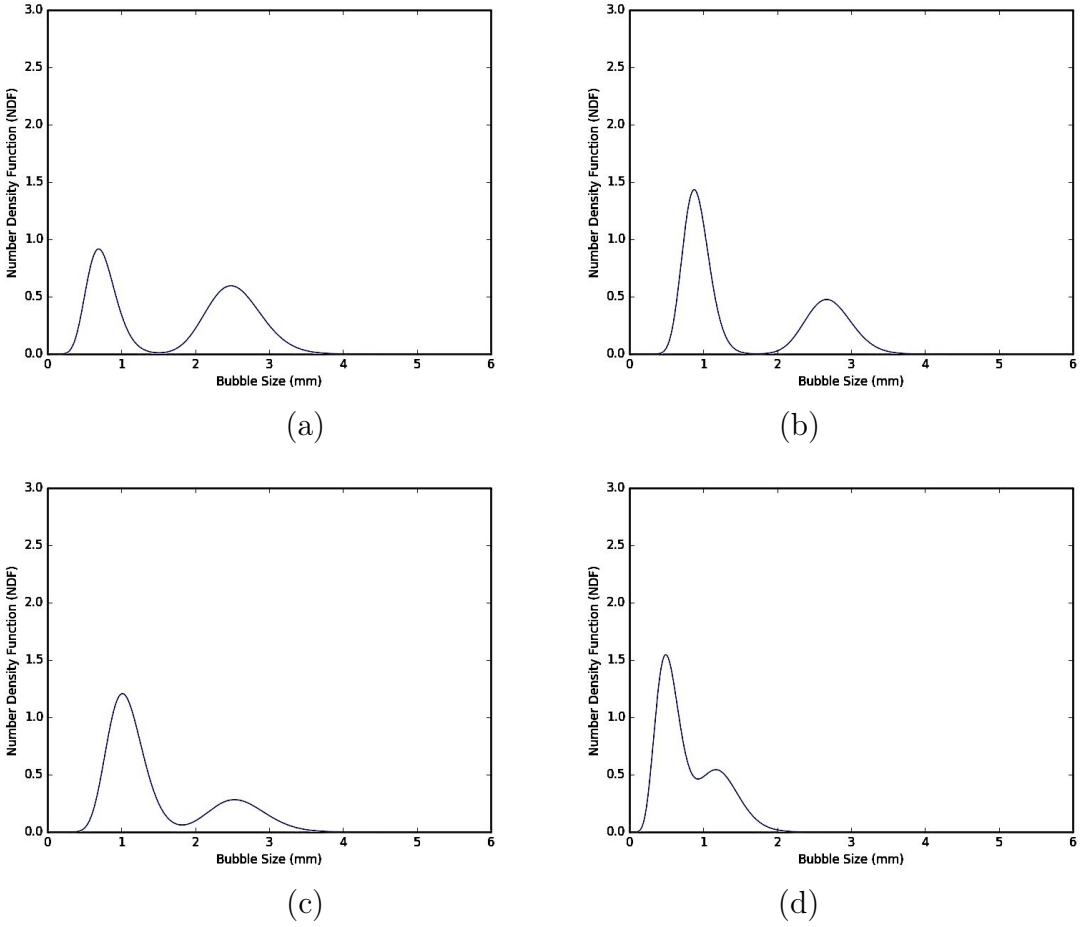

Figure 8.13 Dynamic Number Density Function (NDF) in water zone for 150 rpm in (a) δt=1 s, (b) δt=2 s, (c) δt=3 s, (d) δt=4 s

investigated by improving the applied transient strategy, the validation of the bubble size distribution and turbulent dissipation rates. The model exhibits that the use of an axial impeller in aerated tanks is not satisfactory and the use of a Rushton agitator is more efficient for more gas dispersion.

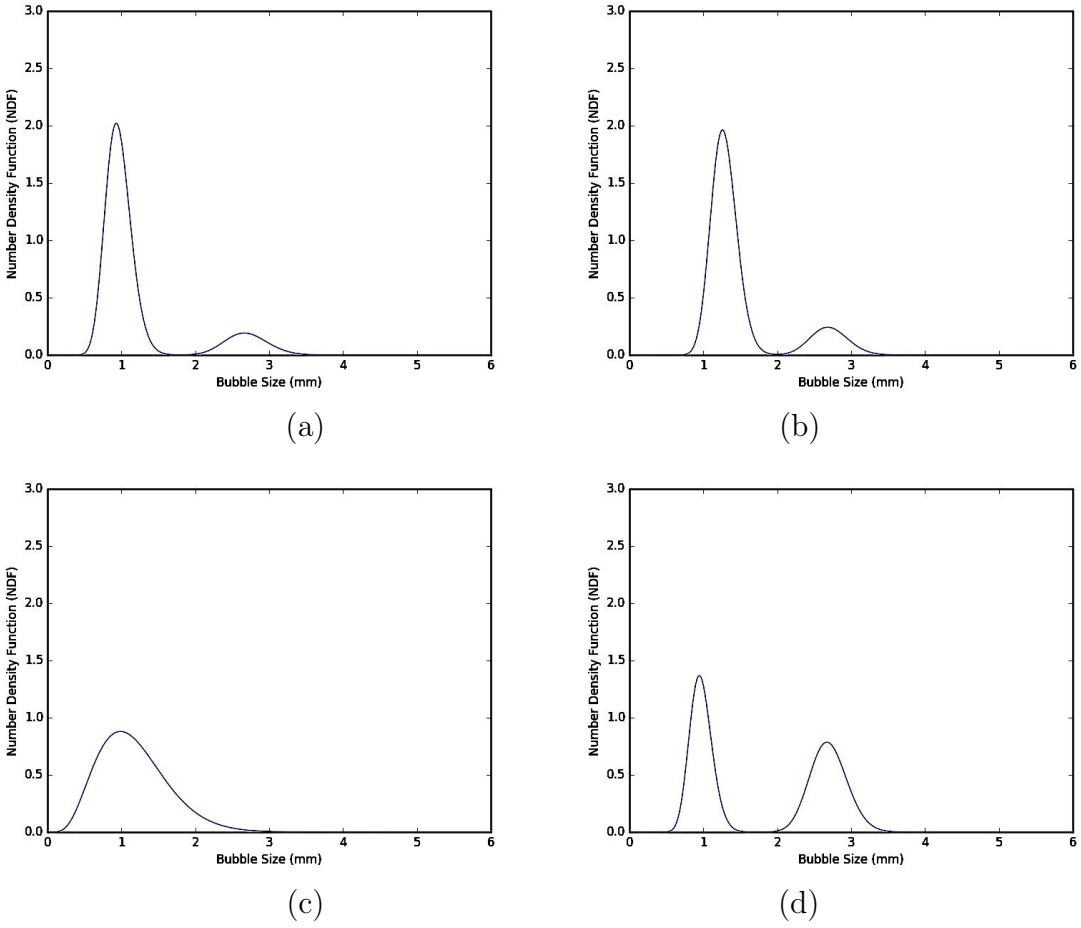

Figure 8.14 Dynamic Number Density Function (NDF) in water zone for 300 rpm (a) δt=1 s, (b) δt=2 s, (c) δt=3 s, (d) δt=4 s

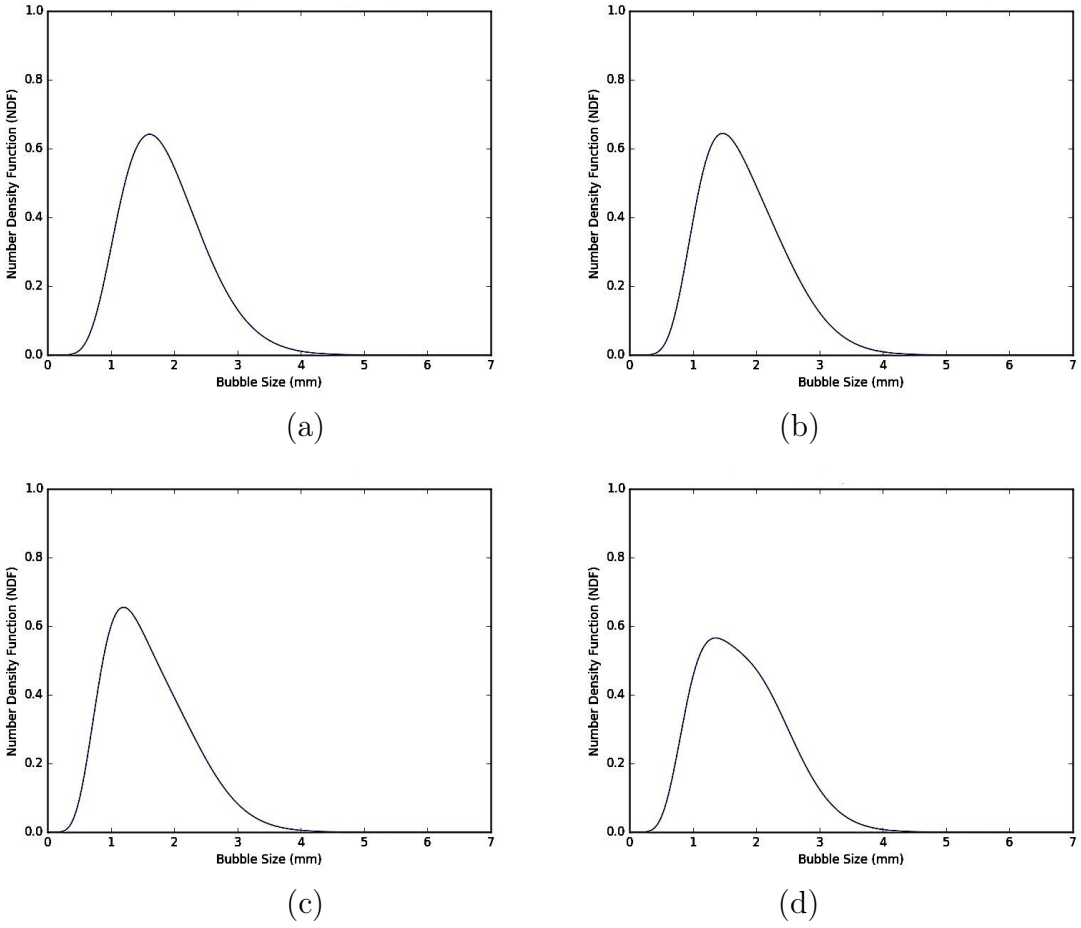

Figure 8.15 Dynamic Number Density Function (NDF) in water zone for 600 *rpm* (a) δt=1 *s*, (b) δt=2 *s*, (c) δt=3 *s*, (d) δt=4 *s*

CHAPTER 9

Summary and conclusion

The current Ph.D project aims to develop a model to optimize the bubbly flow reactors taking into account the motion and behavior of the evolved bubbles. The model is based on the coupling of the fluid mechanics of multiphase flows using a modern, open-source numerical toolbox for Computational Fluid Mechanics (CFD) known as OpenFOAM with the equations describing the evolution of the secondary phase (bubbles). The method used to describe the evolution of the secondary phase (the bubbles) in multiphase flows is known as Population Balance Modelling (PBM) and has grown very fast in the last two decades. The model is developed and validated first using some simple physical examples found in the scientific literature. The validation of the model is further applied to more complex environments such as the stirred tank reactor (STR), a unit very often used industrially that has attracted great interest. The application of the model to such system enables us to predict the time-dependent physical space distribution of the bubbles in the reactor as well as their size distribution. Using these results we can predict the local and overall mass transfer between the bubbles and the liquid, that result being a critical factor in the determination of the characteristics of industrial reactors. The use of a recently developed form of the Quadrature Method of Moments, the base method used to predict the size characteristics of the bubbles enabled us to predict in a much more accurate way the bubbles size distributions. The Extented QMOM (EQMOM) method indeed enabled us to obtained continuous size distributions.

In short, the developed model enables us to predict:

1. The velocity and concentration profiles of species in both liquid and gas-phase
2. The local void fraction, Sauter mean diameter and number of bubbles
3. The local transient size distribution of bubbles in the reactor
4. The local and overall two-phase mass transfer coefficients

This last chapter concludes the thesis and is divided in two sections. The first section summarizes the conclusions already made along this thesis and the second one makes suggestions for future work.

9.1 Conclusions

The results of the present study have been extensively discussed in the previous chapters. In the following, the most important conclusions are summarized.

- The development of the CFD-PBM solver was successful. The solver was applied for two different bubble columns, a water electrolysis reactor and gas-liquid stirred tank to predict the bubble size distribution. The originality of the OpenFOAM solver lies on the fact that it employs the various population balance approach (CM, QMOM), especially the novel method of PBM (EQMOM), which can accept the continuous bubble size distribution as a boundary condition. Moreover, the solver is able to export the distribution function for a specified region in an arbitrary time based on the EQMOM and CM methods.
- It was observed that the CFD-PBM using EQMOM provides a reasonable prediction, as well as CM consisting of 25 classes, but requires less computational demand compared with CM. From the research that has been carried out, it is possible to conclude that QMOM and EQMOM have similar predictions. EQMOM is computationally more expensive than QMOM, although it is able to obtain a continuous NDF of the model. EQMOM can deal with the value of the NDF for null internal coordinates, as well. Although this capability has not been used in the present work, this could be of importance when the secondary phase bubbles are absorbed and disappear in the liquid.
- The main focus of the project was about the application of the solver in the gas-liquid stirred tank for oxygen absorption. The CFD-PBM solver which can be applied for a stirred tank to predict the bubble size distribution and local oxygen mass concentration in water was largely validated by the results obtained. It was observed that the solver is able to extract the continuous bubble NDF for each arbitrary zone of the domain because of the capability of EQMOM approach in capturing the mean values along with the deviation from the mean. It is seen when either gas bubbles pass impeller or rotational speed of impeller is increased, their size is reduced.
- The current study in the proposed mixing tank shows that the two-phase mass transfer model using surface renewal theory obtains superior predictions of dissolved oxygen [DO] for 50 rpm (the lowest rotational speed of impeller in this work). However, the model using penetration theory appears to be more appropriate to predict [DO] for 150, 300 and 600 rpm. From the numerical results, it is evident the NDF is bimodal for 50,150 and nearly 300 rpm and uni-modal for 600 rpm. The proposed model

also shows that the prediction of the two-phase turbulence seems to lead to a slight discrepancy between the numerical results and experimental data with increasing rotational speed of impeller, this aspect of the model should be further investigated. The model's results clearly show that the use of an axial impeller in the present tank configuration is not satisfactory.

9.2 Future works

Future research may try to find ways to consider of nucleation and growth terms in population balance equation. The addition and integration of electrochemical equations in the developed solver could yield new insights. The present study should be regarded as another step towards the accurate simulation of dispersed two-phase flows in electrochemical systems. The impact of the porous electrodes on the bubble formation in the electrochemical system should be studied, as well. It should be pointed out that turbulent two-phase flows are still poorly understood and there is more room to explore and investigate, particularly, in mixing two-phase reactors where the flow is extremely complex. The improvement of turbulence models results in the enhancement of the prediction of other phenomena which are integrated in the overall model such as breakage and coalescence models in population balance part.

CHAPTER 10

Conclusion

Le projet vise à développer un modèle pour optimiser les écoulements de bulles dans des réacteurs. Il se concentre sur le déplacement et l'évolution des bulles. Pour commencer, des cas simples ont été modélisés, puisque les résultats expérimentaux sont connus et disponibles dans la littérature scientifique. Ces cas simples consistent en la modélisation de deux colonnes de bulles et une cellule électrolytique. Ils ont permis de comprendre la complexité de certains des phénomènes physiques implémentés. Par la suite, un cas plus compliqué a été modélisé. Il s'agissait d'un réacteur deux-phases agité par une hélice marine. Ce cas est approprié pour démontrer l'application des méthodes de CFD-PBM implémentées. En employant des algorithmes modernes de bilan de population, le nombre de bulles et la variation de leurs propriétés, comme leur diamètre, ont été modélisés dans tous les cas, simple ou complexe, avec une précision satisfaisante. Les nouvelles implémentations des approches de bilan de population, CM, QMOM et EQMOM vont permettre des suivis plus rapides et plus précis pour le développement de réacteurs optimaux.

10.1 Sommaire

- L'implémentation de nouveaux solveurs basés sur le modèle de bilan des populations est réussie. La méthode a été appliquée à deux colonnes d'écoulement de bulles, une cellule électrolytique et à un réacteur gaz-liquide. Dans ces trois cas, les solveurs ont été capables de prédire la distribution de taille de bulles de manière satisfaisante.
- Ces travaux sont originaux, car ils approchent le problème de l'écoulement de bulles avec plusieurs modèles de bilan de population nouvellement implémentés dans OpenFOAM: CM, QMOM et EQMOM.
- Toutes les méthodes de bilan de population peuvent être employées avec des distributions de taille comme condition aux limites. Ceci est une amélioration par rapport aux autres méthodes ne permettant que l'utilisation d'une taille unique.
- Le modèle EQMOM permet d'obtenir des prédictions raisonnables avec moins de temps de calcul que CM. Le modèle EQMOM est plus demandant que QMOM, mais permet d'obtenir des fonctions de densité numérique continues.

- L'application des nouveaux solveurs pour déterminer l'absorption d'oxygène dans l'eau dans un réacteur agité par une hélice marine a été faite avec succès. Le modèle a pu prédire la solubilisation de l'oxygène dans le réacteur. De plus, il a été possible d'extraire les fonctions de densités statistiques (NDF) pour des zones arbitraires grâce à l'approche EQMOM.
- De plus, plusieurs modèles de transfert de masse ont été comparés lors des essais sur le réacteur gaz-liquide. Le modèle de renouvellement des surfaces [1] obtient de meilleures prédictions d'oxygène dissous lorsque le réacteur est agité à 50 tours par minutes. Toutefois, le modèle utilisant la théorie de pénétration [2] semble plus approprié lors que les vitesses d'agitation sont de 150, 300 et 600 tours par minute.
- L'utilisation des méthodes CFD-PBM a aussi permis d'observer les distributions statistiques de la taille des bulles. La distribution observée à 50 et 150 tours par minute est bimodale. La distribution est uni modale à 600 tours par minute. À 300 tours par minute, la distribution semble varier dans le temps, mais est généralement bimodale.

10.2 Travaux futurs

Des futurs travaux pour l'intégration des termes de nucléation et de croissance dans les équations de bilan de pourraient apporter des prédictions encore plus précises. L'emploi d'équation électrochimique, utilisée conjointement avec les méthodes CFD-PBM, pourrait permettre de simuler avec une grande précision des cas complexes de cellules électrolytiques. Un de ces cas pourrait être celui d'une électrode poreuse. Les modèles pourraient y permettre l'étude des écoulements et de la formation des bulles dans le système. Il est aussi important de souligner que les écoulements turbulents comportant deux phases possèdent encore quelques mystères. Il est toujours possible d'améliorer les modèles de turbulence, ce qui améliorerait aussi la précision des modèles de fission et de coalescence dans les équations de bilan de population.

1. surface renewal theory
2. penetration theory

LIST OF REFERENCES

[1] C. A. Sequira, D. M. F. Santos, D. M. F., B. Sljukie, and L. Amaral. Physics of electrolytic gas evolution. *Brazilian Journal of Physics*, 43:199–208, 2013.

[2] H. Vay Parys, S. Van Damme, P. Maciel, T. Nierhaus, F. Tomasoni, A. Hublin, H. Deconinck, and J. Deconinck. Eulerian-lagrangian model for gas-evolving process based on supersaturation. *WIT Transaction on Engineering Science*, 65:109–118, 2009.

[3] P. Marciel, T. Nierhaus, S. V. Damme, H. V. Parys, J. Deconinck, and A. Hubin. New model for gas evolving electrodes based on supersaturation. *Electrochemistry Communications*, 11(4):875–877, 2009.

[4] Sh. Zhan, M. Li, J. Zhou, J. Yang, and Y. Zhou. CFD simulation of dissolution process of alumina in an aluminum reduction cell with two-particle phase population balance model. *Applied Thermal Engineering*, 73(1):805 – 818, 2014.

[5] T. T. Nguyen, F. Laurent, R. O. Fox, and M. Massot. Solution of population balance equations in applications with fine particles: Mathematical modeling and numerical schemes. *Journal of Computational Physics*, 325:129–156, 2016.

[6] C. Yuan, F. Laurant, and R. O. Fox. An extended quadrature method of moments for population balance equations. *Journal of Aerosol Science*, 32:1111–1116, 2012.

[7] H. A. Jakobsen. *Chemical Reactor Modelling*. Springer-Verlag, Verlag Berlin Heidelberg, 2008.

[8] W. D. Deckwer. *Bubble Column Reactors*. John Wiley & Sons, New York, 1992.

[9] G. Holzinger. *Eulerian Two-Phase Simulation of the Floating Process with OpenFOAM*. PhD thesis, Johannes Kepler Universitat Linz, 2016.

[10] F. H. Harlow and J. E. Welch. Numerical calculation of time-dependent viscous incompressible flow of fluid with free surface. *Physics and Fluids*, 8:2182–2189, 1965.

[11] A. A. Amsden and F. H. Harlow. A simplified mac technique for incompressible fluid flow calculations. *Journal of Computational Physics*, 6:322–325, 1970.

[12] C. W. Hirt and B. D. Nichols. Volume of fluid (VOF) method for the dynamics of free boundaries. *Journal of Computational Physics*, 39:201–225, 1981.

[13] M. Sussman, P. Smereka, and S. Osher. A level-set approach for computing solutions to incompressible two-phase flow. *Journal of Computational Physics*, 114:146–159, 1994.

[14] F. Beux and S. Banerjee. Numerical simulation of three-dimensional two-phase flows by means of a level set method. *ECCOMAS 96 Proceedings*, John Wiley, 1996.

[15] J. A. Sethian. *Level Set Methods*. Cambridge University Press, Cambridge, 1996.

[16] S. O. Unverdi and G. Tryggvason. A front-tracking method for viscous, incompressible, multi-fluid flows. *Journal of Computational Physics*, 100:25–37, 1992.

[17] G. Tryggvason, B. Bunner, A. Esmaeeli, and S. Mortazavi. Direct numerical simulations of dispersed flows. In *Third International Conference on Multiphase Flow (ICMF 98)*, France, 1998.

[18] R. Clift, J. R. Grace, and M. E. Weber. *Bubbles, Drops and Particles*. Academic Press, New York, 1978.

[19] H. Rusche. *Computational Fluid Dynamics of Dispersed Two-Phase Flows at High Phase Fractions*. PhD thesis, Imperial College of London, 2002.

[20] Y. A. Buyevich. Statistical hydrodynamics of dispersed systems, physical background and general equations. *Journal of Fluid Mechanics*, 49:489–507, 1971.

[21] M. Ishii. *Thermofluid Dynamic Theory of Two-phase Flow*. Eyrolles, Paris, 1975.

[22] Y. A. Buyevich and T. G. Theofanous. Ensemble averaging technique in the mechanics of suspensions. In *Proceeeing of ASME IMECE Meeting*, Dallas, Texas, 1997.

[23] D. A. Drew and S. L. Passman. *Theory of Multicomponent Fluids*. Springer-Verlag, New York, 1999.

[24] D. Z. Zhang and A. Prosperetti. Ensemble phase-averaged equations for bubbly flows. *Physics and Fluids*, 6:2956–2970, 1994.

[25] H. G. Weller. The development of a new flame aera combustion model using conditional averaging. *Thermo-Fluids Section Report*, 1993.

[26] H. G. Weller. Modelling and solution of the conditionally averaged two-phase flow equations. Technical report, 2005.

[27] C. Bartels, M. Breuer, K. Wechsler, and F. Durst. Computational fluid dynamics applications on parallel-vector computers: computations of stirred vessel flows. *Computers and Fluids*, 31:69–97, 2002.

[28] L. Schiller and Z. Naumann. A drag coefficient correlation. *Zeitschrift des Vereines Deutscher Ingenieure*, 77:318, 1935.

[29] A. Tomiyama, I. Kataoka, and T. Sakaguchi. Drag coefficients of bubbles. 1st report. drag coefficients for a single bubbles in a stagnant liquid. *Nippon Kikai Gakkai Ronbunshu*, 61:2357–2364, 1995.

[30] M. Ishii and N. Zuber. Drag coefficient and relative velocity in bubbly, droplet and particulate flows. *AIChE Journal*, 25:843–855, 1995.

[31] A. Tomiyama, H. Tamaia, I. Zunb, and Sh. Hosokawaa. Transverse migration of single bubbles in simple shear fows. *Chemical Engineering Science*, 57:1849–1858, 2002.

[32] H. Marschall. *Towards the Numerical Simulation of Multi-Scale Two-Phase Flows*. Ph.D. thesis, Technische Universitat Munchen, 2011.

[33] Mandar V. Tabib, B. Jyeshtharaj A. Swarnendu, and B. Joshi. CFD simulation of bubble column: An analysis of interphase forces and turbulence models. *Chemical Engineering Journal*, 139:589–614, 2008.

[34] R. O. Fox. *Turbulence in Multiphase Flows*. Springer, Singapore, 2017.

[35] Evenio. Choosing the right turbulence model for your CFD simulation, 2017. URL `http://blog.envenio.com/turbulencemodelscfd`.

[36] D. Corson, R. Jaiman, and F. Shakib. Industrial application of rans modelling: capabilities and needs. *International Journal of Computational Fluid Dynamics*, 2009.

[37] A. D. Gosman, R. I. Lekakou, S. Politis, R. I. Issa, and M. K. Looney. Multidimensional modeling of turbulent two-phase flows in stirred vessels. *AIChE Journal*, 38: 1946—1956, 1992.

[38] R. T. Lahey. The simulation of multidimensional multiphase flows. *Nuclear Engineering and Design*, 235:1043–1060, 2005.

[39] B. Behzadi, R. I. Issa, and H. Rusche. Modelling of dispersed bubble and droplet flow at high phase fractions. *Chemical Engineering Science*, 59:759–770, 2004.

[40] H. K. Versteeg and W. Malalasekera. *An Introduction to Computational An Introduction to Computaional Fluid Dynamics*. Pearson Education Limited, second edition edition, 2007.

[41] *Ansys Fluent Theory Guide*. ANSYS, USA, 2016.

[42] G. H. Yeoh, Ch. Cheung, and J. Tu. *Multiphase Flow Analysis Using Population Balance Modeling: Bubbles, Drops and Particles*. Elsevier, 2014.

[43] A. D. Randolph. A population balance for countable entities. *The Canadian Journal of Chemical Engineering*, 42, 1964.

[44] D. L. Marchisio, R. D. Vigil, and R. O. Fox. Quadrature method of moments for aggregation-breakage processes. *Journal of Colloid and Interface Science*, 258: 322–334, 2003.

[45] D. L. Marchisio, J. T. Pikturna, R. O. Fox, and R. D. Vigil. Quadrature method of moments for population-balance equations. *AIChE Journal*, 49:1266–1276, 2003.

[46] D. L. Marchisio and R. O. Fox. *Multiphase Reacting Flows: Modelling and Simulation.* SpringerWienNewYork, 2007.

[47] D. Ramkrishna. *Population Balances.* Academic Press, San Diego, 2000.

[48] F. Abraham. *Homogeneous nucleation theory.* Academic Press New York, 1974.

[49] T. Nierhaus. *Modeling and Simulation of Dispersed Two-Phase Flow Transport Phenomena in Electrochemical Processes.* Ph.D. thesis, von Karman Institute for Fluid Dynamics, 2009.

[50] F. Tomasoni. Non-intrusive assessment of transport phenomena at gas-evolving electrodes. Master's thesis, Von Karman Institute for Fluid Dynamics, 2010.

[51] S.M. Lo. *Application of Population Balance to CFD Modeling of Bubbly Flow via the MUSIG Model*, page 1096. AEA Technology, Harwell, UK, 1996.

[52] E. Krepper, D. Lucas, and H. Prasser. On the modelling of bubbly flow in vertical pipes. *Nuclear Engineering and Design*, 235:597–611, 2005.

[53] A. D. Randoph and M. A. Larson. Theory of particulate processes, analysis and techniques of continuous crystallization. *AIChE Journal*, 18:670–670, 1972.

[54] H. M. Katz Hulburt and S. Katz. Some problems in particle technology: A satisfied mechanical formulation. *Chemical Engineering Science*, 19, 1964.

[55] R. McGraw. Description of aerosol dynamics by the quadrature method ofmoments. *Aerosol Science and Technology*, 27:255–265, 1997.

[56] B. Carnahan. *Applied numerical methods.* Krieger Publishing Company,, 1990.

[57] D. L. Marchisio and R. O. Fox. *Computational Models for Polydisperse Particulate and Multiphase Systems.* Cambridge University Press, 2013.

[58] D. L. Marchisio and R. O. Fox. Solution of population balance equations using the direct quadrature method of moments. *Journal of Aerosol Science*, 36:43–73, 2004.

[59] B. Selma, R. Bannari, and P. Proulx. Simulation of bubbly flows: Comparison between direct quadrature method of moments (dqmom) and method of classes. *Chemical Engineering Science*, 65:1925–9141, 2010.

[60] R. Fan, D. L. Marchisio, and R. O. Fox. Application of the direct quadrature method of moments to polydisperse gas-solid fluidized beds. *Powder Technology*, 139:7–20, 2004.

[61] B. Selma. *Contribution to complex gas-liquid fows: Development and validation of a mathematical model.* PhD thesis, Sherbrooke University, 2009.

[62] Yixiang Liao and Dirk Lucas. A literature review of theoretical models for drop and bubble breakup in turbulent dispersions. *Chemical Engineering Science*, 64: 3389–3406, 2009.

[63] Y. Liao and D. Lucas. A literature review on mechanisms and models for the coalescence process of fluid particles. *Chemical Engineering Science*, 65:2851–2864, 2010.

[64] M. J. Prince and H. W. Blanch. Bubble coalescence and break-up in air-sparged bubble columns. *AIChE Journal*, 36:1485–1499, 1990.

[65] L. Hagesather, H. A. Jakobsen, K. Hjarbo, and H. Svendsen. A coalescence and breakup module for implementation in CFD codes. *European Symposium on Computer Aided Process Engineering-10*, 8:367–372., 2000.

[66] R. Kubot, I. Komasawaa, and T. Otake. Behavior of dispersed particles in turbulent liquid flow. *Journal of Chemical Engineering of Japan*, 5(4):349–355, 1972.

[67] H. Luo and H. F. Svendsen. Theoretical model for drop and bubble breakup in turbulent dispersions. *AIChE Journal*, 42:1225–1233, 1996.

[68] R. Bannari, F. Kerdouss, B. Selma, A. Bannari, and P. Proulx. Three-dimensional mathematical modeling of dispersed two-phase flow using class method of population balance in bubble columns. *Computers and Chemical Engineering*, 32(12):3224–3237, 2008.

[69] F. Kerdouss, A. Bannari, P. Proulx, R. Bannari, M. Skrga, and Y. Labrecque. Two-phase mass transfer coefficient prediction in stirred vessel with a CFD model. *Computers and Chemical Engineering*, 32(8):1943–1955, 2008.

[70] P. Chen, J. Sanyal, and M. P. Duduković. Numerical simulation of bubble columns flows: effect of different breakup and coalescence closures. *Chemical Engineering Science*, 60(4):1085–1101, 2005.

[71] S. V. Patankar. *Numerical Heat Transfer and Fluid Flow*. Taylor and Francis, USA, 1980.

[72] J. H. Ferziger and M. Peric. *Computational Methods for Fluid Dynamics*. Springer-Verlag, Berlin, 1996.

[73] C. Hirsch. *Numerical Computation of Internal and External Flows, volume I and II*. John Wiley & Sons, 1991.

[74] F. Moukalled, L. Mangani, and M. Darwish. *The Finite Volume Method in Computational Fluid Dynamics*. Springer, 2016.

[75] R. Courant, E. Isaacson, and M. Rees. On the solution of non-linear hyperbolic differential equations by finite differences. *Communications on Pure and Applied Mathematics*, 5:243–255, 1952.

[76] K. Mooney, T. Maric, and J. Hopken. *The OpenFOAM Technology Primer*. Sourceflux, 2014.

[77] The open source integration platform for numerical simulation, 2018. URL `http://www.salome-platform.org`.

[78] OpenQBMM. An open-source implementation of Quadrature-Based Moment Methods, 2017. URL `https://www.openqbmm.org/`. DOI: 10.5281/zenodo.591651.

[79] E. Madadi-Kandjani and A. Passalacqua. An extended quadrature-based moment method with log-normal kernel density functions. *Chemical Engineering Science*, 131: 323–339, 2015.

[80] Paraview: an open-source, multi-platform data analysis and visualization application, 2018. URL `http://www.paraview.org/`.

[81] Mammouth parallèle 2, 2015. URL `http://www.calculquebec.ca`.

[82] A.N. Colli and J.M. Bisang. The effect of a perpendicular and cumulative inlet flow on the mass-transfer distribution in parallel-plate electrochemical reactors. *Electrochimica Acta*, 13:758–766, 2014.

[83] H. Van Parys, E. Tourwe, T. Breugelmans, M. Depauw, J. Deconinck, and A. Hubin. Modeling of mass and charge transfer in an inverted rotating disk electrode (irde) reactor. *Journal of Electroanalytical Chemistry*, 622:44–50, 2009.

[84] F. Jomard, J. P. Feraud, J. Morandini, Y. Du Terrail Couvat, and J. P. Caire. Hydrogen filter press electrolyser modelled by coupling Fluent and flux expert codes. *Journal of Applied Electrochemistry*, 38:297–308, 2008.

[85] S. Charton, J. Janvier, P. Rivalier, E. Chainet, and J. P. Caire. Hybrid sulfur cycle for h2 production: A sensitivity study of the electrolysis step in a filter-press cell. *International Journal of Hydrogen Energy*, 35:1537–1547, 2010.

[86] T. Nierhaus, H. V. Parys, S. Dehaeck, J. V. Beeck, H. Deconinck, J. De-coninck, and A. Hubinc. Simulation of the two-phase flow hydrodynamics in an irde reactor. *Journal of Electrochemical Society*, 156:139–148, 2009.

[87] H. G. Weller, G. Tabor, H. Jasak, and C. Fureby. A tensorial approach to computational continuum mechanics using object-oriented techniques. *Computers in Physics*, 12:620–631, 1998.

[88] W. G. Cochran. The flow due to a rotating disc. *Mathematical Proceedings of the Cambridge Philosophical Society*, 30:365–375, 1934.

[89] M. Karimi, H.Droghetti, and D. L. Marcisio. PUFoam : A novel open-source CFD solver for the simulation of polyurethane foams. *Computer Physics Communications*, 217:138–148, 2017.

[90] MJ. Leahy and M. P. Schwarz. Modeling natural convection in copper electrorefining: Describing turbulence behavior for industrial-sized systems. *Metallurgical and Materials Transactions B*, 42:875–890, 2011.

[91] MJ. leahy and M. P. Schwarz. Experimental validation of a computational fluid dynamics model of copper electrowinning. *Metallurgical and Materials Transactions B*, 41:1247–1260, 2010.

[92] MJ. Leah and M. P. Schwarz. Computational fluid dynamics modelling of natural convection in copper electrorefining. *16th Australasian Fluid Mechanics Conference, Gold Coast, Australia*, pages 112–116, 2007.

[93] N. G. Deen, T. Solberg, and B. H. Hjertager. Flow generated by an aerated rushton impeller: Two-phase PIV experiments and numerical simulations. *The Canadian Journal of Chemical Engineering*, 80:1–15, 2002.

[94] P. C. Friberg. *Three-dimensional modeling and simulations of gas-liquid flows processes in bioreactors*. PhD thesis, Norwegian University of Science and Technology, 1998.

[95] K. E. Morud and B. H. Hjertager. LDA measurements and CFD modeling of gas-liquid flow in a stirred vessel. *Chemical Engineering Science*, 51:233–249, 1996.

[96] V. V. Ranade and V. R. Deshpande. Gas-liquid flow in stirred vessels: trailing vortices and gas accumulation behind impeller blades. *Chemical Engineering Science*, 54:2305–2315., 1999.

[97] M. P. Schwarz and W. J. Turner. Applicability of the standard k-ϵ turbulence model to gas-stirred baths. *Applied Mathematical Modelling*, 12:273–279, 1988.

[98] M. P. Schwarz. Simulation of gas injection into liquid melts. *Applied Mathematical Modelling*, 20:41–51, 1996.

[99] S. M. Kresta, A. W. Etchells III, D. S. Dickey, and V. A. Atiemo-Obeng. *Advances In Industrial Mixing*. John Wiley & Sons, USA, 2016.

[100] F. Kerdouss, A. Bannari, and P. Proulx. CFD modeling of gas dispersion and bubble size in a double turbine stirred tank. *Chemical Engineering Science*, 61:3313–3322, 2006.

[101] M. Ishii, S. Kim, and J. Uhle. Interfacial area transport equation: model development and benchmark experiments. *International Journal of Heat and Mass Transfer*, 45: 3111–3123, 2002.

[102] K. Dhanasekharan, J. Sanyal, A. Jain, and A. Haidari. A generalize approach to model oxygen transfer in boreactors using population balances and computational fluid dynamics. *Chemical Engineering Science*, 60:213–218, 2005.

[103] B. C. H. Venneker, J. J. Derksen, and H. E. A. Van Den Akker. Population balance modeling of aerated stirred vessels based on CFD. *AIChE Journal*, 48:673–684, 2002.

[104] B. V. Balakin, A. C. Hoffmann, and P. Kosinski. Coupling star-cd with a population balance technique based on the classes method. *Powder Technol*, 257:47–54, 2014.

[105] P. J. Becker, F. Puel, R. Henry, and N. Sheibat-Othman. Investigation of discrete population balance models and breakage kernels for dilute emulsification systems. *Industrial and Engineering Chemistry Research*, 50:11358–11374, 2011.

[106] S. Kumar and D. Ramkrishna. On the solution of population balance equations by discretization-I. a fixed pivot technique. *Chemical Engineering Science*, 51:1311–1332, 1996.

[107] S. Kumar and D. Ramkrishna. On the solution of population balance equations by discretization-II. a moving pivot technique. *Chemical Engineering Science*, 51: 1333–1342, 1996.

[108] F. Puel, G. Fvotte, and J. P. Klein. Simulation and analysis of industrial crystallization processes through multidimensional population balance equations. *Chemical Engineering Science*, 58:3715–3727, 2003.

[109] D. L. Marchisio, R. D. Vigil, and R. O. Fox. Implementation of the quadrature method of moments in CFD codes for aggregation-breakage problems. *Chemical Engineering Science*, 139:3337–3351., 2003.

[110] J. Sanyal, D. L. Marchisio, R. O. Fox, and K. Dhanasekharan. On the comparaison between population balance models for CFD simulation of bubble columns. *Industrial and Engineering Chemistry Research*, 44:5063–5072, 2005.

[111] L. Silva and P. Lage. Development and implementation of a polydispersed multiphase model in OpenFOAM. *Computer and Chemical Engineering*, 35:2653–2666, 2011.

[112] D. Li, Z. Gao, A. Buffo, W. Podgorska, and D. L. Marchisio. Droplet breakage and coalescence in liquid-liquid dispersions: Comparison of different kernels with eqmom and qmom. *AIChE Journal*, 63:2293–2311, 2017.

[113] J. Gimbun, C. D. Rielly, and Z. K. Nagy. Modelling of mass transfer in gas-liquid stirred tanks agitated by rushton turbin and cd-6 impeller: A scale up study. *Chemical Engineering Research and Design*, 87:437–451, 2017.

[114] A. Gupta and Sh. Roy. Euler–euler simulation of bubbly flow in a rectangular bubble column: Experimental validation with radioactive particle tracking. *Chemical Engineering Journal*, 225:818–836, 2013.

[115] E. Askari, G. S. Lemieux, C. Braga Vieira, G. Litrico, and P. Proulx. Simulation of bubbly flow and mass transfer in a turbulent gas-liquid stirred tank with CFD-PBM solver in OpenFOAM: EQMOM applicationg. *15th International Conference of Numerical Analysis and Applied Mathematics, Thessaloniki, Greece*, Sep 2017.

[116] A. Tomiyama, G.P. Celata, S. Hosokawa, and S. Yoshida. Terminal velocity of single bubbles in surface tension force dominant regime. *International Journal of Multiphase Flow*, 28:1497–1519, 2002.

[117] P. G. Saffman and J. S. Turner. On the collision of drops in turbulent clouds. *Journal of Fluid Mechanics*, 1:16–30, 1956.

[118] C. Yuan, B. Kong, A. Passalacqua, and R. O. Fox. An extended quadrature-based mass-velocity moment model for polydisperse bubbly flows. *The Canadian Journal of Chemical Engineering*, 92:2053–2066, 2014.

[119] S. Bove, T. Solberg, and B. H. Hjertager. A novel algorithm for solving population balance equations: the parallel parent and daughter classes. derivation , analysis and testing. *Chemical Engineering Science*, 60:1449–1464, 2005.

[120] D. Pfleger, S. Gomes, N. Gilbert, and H. G. Wagner. Hydrodynamic simulations of laboratory scale bubble columns. fundamental studies of the eulerian–eulerian modeling approach. *Chemical Engineering Science*, 54:5091–5099, 1999.

[121] Vivek V. Buwa, Dhanannjay S. Deo, and Vivek V. Ranade. Eulerian–lagrangian simulations of unsteady gas–liquid flows in bubble columns. *International Journal of Multiphase Flow*, 32:864–885, 2006.

[122] N. G. Deen. *An experimental and computational study of fluid dynamics in gas-liquid chemical reactors*. Ph.D. thesis, Aalborg University Esbjerg, 2001.

[123] Super marine, 2017. URL `https://github.com/Spationaute/SuperMarine`.

[124] G. L. Lane. Improving the accuracy of CFD predictions of turbulence in a tank stirred by a hydrofoil impeller. *Chemical Engineering Science*, 169:188–211, 2017.

[125] F. Kerdouss, L. Kiss, P. Proulx, J. F. Bilodeau, and C. Dupuis. Mixing characteristics of an axial flow rotor: Experimental and numerical study. *International Journal of Chemical Reactor Engineering*, 3:1542, 2005.

[126] F. Kerdouss, A. Bannari, and P. Proulx. Two-phase mass transfer coefficient prediction in stirred vessel with a CFD model. *Computers and Chemical Engineering*, 32:1943–1955, 2007.

[127] G. L. Lane, M. P. Schwarz, and G. M. Evans. Predicting gas-liquid flow in a mechanically stirred tank. *Applied Mathematical Modelling*, 26:223–235, 2002.

[128] G. L . Lane, M. P. Schwarz, and G. M. Evans. Numerical modelling of gas-liquid flow in stirred tank. *Chemical Engineering Science*, 60:2203–2214, 2005.

[129] R. O. Fox, F. Laurant, and M. Massot. Numerical simulation of spray coalescence in an eulerian framework: direct quadrature method of moments and multi-fluid method. *Journal of Computational Physics*, 227:3058–3088, 2008.

[130] A. Tomiyama, I. Kataoka, I. Zun, and T. Sakaguchi. Drag coefficient of single bubble under normal and micro gravity conditions. *JSME International Journal*, 41:472–479, 1998.

[131] A. Passalacqua, F. Laurent, E. Madadi-Kandjani, J.C. Heylmun, and R.O. Fox. An open-source quadrature-based population balance solver for OpenFOAM. *Chemical Engineering Science*, 176:306 –318, 2018.

[132] B. W. Lee and M. P. Dudukovic. Determination of flow regime and gas holdup in gas-liquid stirred tanks. *Chemical Engineering Science*, 109:264–275, 2014.

[133] J. Y. Luo, R. I. Issa, and A. D. Gosman. Prediction of impeller induced flows in mixing vessels using multiple frames of reference. *IChemE Symposium Series*, 136: 549–556, 1994.

[134] G. Tabor, A. D. Gosman, and R. I. Issa. Numerical simulation of the flow in a mixing vessel stirred by a rushton turbine. *IChemE Symposium series*, 140:25–34, 1996.

[135] G. Micale, A. Brucato, and F. Grisafi. Prediction of flow fields in a dual-impeller stirred tank. *AIChE Journal*, 45:445–464, 1999.

[136] V. V. Ranade. An efficient computational model for simulating flow in stirred vessels: A case of rushton turbine. *Chemical Engineering Science*, 52:4473–4484, 1997.

[137] Y. Liao, R. Oertel, S. Kriebitzsch, F. Schlegel, and D. Lucas. A discrete population balance equation for binary breakage. *International Journal for Numerical Methods in Fluids*, 87:202–215, 2018.

[138] Z. Gao, D. Li, A. Buffo, W. Podgorska, and D. L. Marchisio. Simulation of droplet breakage in turbulent liquid-liquid dispersions with CFD-PBM: Comparison of breakage kernels. *Chemical Engineering Science*, 142:277 – 288, 2016.

[139] F. Scargiali, A. D'Orazio, F. Grisafi, and A. Brucato. Modelling and simulation of gas?liquid hydrodynamics in mechanically stirred tanks. *Chemical Engineering Research and Design*, 85(5):637–646, 2007.

[140] A. Bakker and H. E. A. VanDenAkker. A computational model for the gas-liquid flow in stirred reactors. *Transaction of IChemE*, 72:594–606, 1994.

[141] M. Vanni. Approximate population balance equations for aggregation-breakage processes. *Journal of Colloid and Interface Science*, 221:143–160, 1999.

[142] M. Moo-Young and W. Blanch H. Design of biochemical reactors. *Advanced Biochemical Engineering*, 19:1–69, 1981.